List-mode proton CT reconstruction

Feriel Khellaf

To cite this version:

Feriel Khellaf. List-mode proton CT reconstruction. Medical Imaging. Université de Lyon, 2020. English. NNT : 2020LYSEI074 . tel-03131226v2

HAL Id: tel-03131226
https://theses.hal.science/tel-03131226v2

Submitted on 10 Feb 2021

N°d'ordre NNT : 2020LYSEI074

THÈSE de DOCTORAT DE L'UNIVERSITÉ DE LYON
opérée au sein de
l'INSA LYON

École Doctorale N° 160
ÉLECTRONIQUE, ÉLECTROTECHNIQUE, AUTOMATIQUE

Spécialité/ discipline de doctorat :
Traitement du Signal et de l'Image

Soutenue publiquement le 21/09/2020, par :
Feriel Khellaf

List-mode proton CT reconstruction

Devant le jury composé de :

Schulte, Reinhard	Professeur des Universités, Loma Linda University, Loma Linda	Rapporteur
Comtat, Claude	Ingénieur chercheur, CEA, Orsay	Rapporteur
Parodi, Katia	Professeure des Universités, Ludwig-Maximilians-Universitat, Munich	Examinatrice
Peyrin, Françoise	Directrice de recherche, INSERM, Lyon	Examinatrice
Létang, Jean Michel	Maître de conférences, INSA-LYON, Lyon	Directeur de thèse
Rit, Simon	Chargé de recherche, CNRS, Lyon	Co-directeur de thèse
Krah, Nils	Post-doctorant, CNRS, Lyon	Invité
Rinaldi, Ilaria	Physicienne médicale, Maastro Clinic, Maastricht	Invitée

Département FEDORA – INSA Lyon - Ecoles Doctorales – Quinquennal 2016-2020

SIGLE	ECOLE DOCTORALE	NOM ET COORDONNEES DU RESPONSABLE
CHIMIE	**CHIMIE DE LYON** **http://www.edchimie-lyon.fr** Sec. : Renée EL MELHEM Bât. Blaise PASCAL, 3e étage **secretariat@edchimie-lyon.fr** INSA : R. GOURDON	**M. Stéphane DANIELE** Institut de recherches sur la catalyse et l'environnement de Lyon IRCELYON-UMR 5256 Équipe CDFA 2 Avenue Albert EINSTEIN 69 626 Villeurbanne CEDEX **directeur@edchimie-lyon.fr**
E.E.A.	**ÉLECTRONIQUE, ÉLECTROTECHNIQUE, AUTOMATIQUE** **http://edeea.ec-lyon.fr** Sec. : M.C. HAVGOUDOUKIAN **ecole-doctorale.eea@ec-lyon.fr**	**M. Gérard SCORLETTI** École Centrale de Lyon 36 Avenue Guy DE COLLONGUE 69 134 Écully Tél : 04.72.18.60.97 Fax 04.78.43.37.17 **gerard.scorletti@ec-lyon.fr**
E2M2	**ÉVOLUTION, ÉCOSYSTÈME, MICROBIOLOGIE, MODÉLISATION** **http://e2m2.universite-lyon.fr** Sec. : Sylvie ROBERJOT Bât. Atrium, UCB Lyon 1 Tél : 04.72.44.83.62 INSA : H. CHARLES **secretariat.e2m2@univ-lyon1.fr**	**M. Philippe NORMAND** UMR 5557 Lab. d'Ecologie Microbienne Université Claude Bernard Lyon 1 Bâtiment Mendel 43, boulevard du 11 Novembre 1918 69 622 Villeurbanne CEDEX **philippe.normand@univ-lyon1.fr**
EDISS	**INTERDISCIPLINAIRE SCIENCES-SANTÉ** **http://www.ediss-lyon.fr** Sec. : Sylvie ROBERJOT Bât. Atrium, UCB Lyon 1 Tél : 04.72.44.83.62 INSA : M. LAGARDE **secretariat.ediss@univ-lyon1.fr**	**Mme Sylvie RICARD-BLUM** Institut de Chimie et Biochimie Moléculaires et Supramoléculaires (ICBMS) - UMR 5246 CNRS - Université Lyon 1 Bâtiment Curien - 3ème étage Nord 43 Boulevard du 11 novembre 1918 69622 Villeurbanne Cedex Tel : +33(0)4 72 44 82 32 **sylvie.ricard-blum@univ-lyon1.fr**
INFOMATHS	**INFORMATIQUE ET MATHÉMATIQUES** **http://edinfomaths.universite-lyon.fr** Sec. : Renée EL MELHEM Bât. Blaise PASCAL, 3e étage Tél : 04.72.43.80.46 **infomaths@univ-lyon1.fr**	**M. Hamamache KHEDDOUCI** Bât. Nautibus 43, Boulevard du 11 novembre 1918 69 622 Villeurbanne Cedex France Tel : 04.72.44.83.69 **hamamache.kheddouci@univ-lyon1.fr**
Matériaux	**MATÉRIAUX DE LYON** **http://ed34.universite-lyon.fr** Sec. : Stéphanie CAUVIN Tél : 04.72.43.71.70 Bât. Direction **ed.materiaux@insa-lyon.fr**	**M. Jean-Yves BUFFIÈRE** INSA de Lyon MATEIS - Bât. Saint-Exupéry 7 Avenue Jean CAPELLE 69 621 Villeurbanne CEDEX Tél : 04.72.43.71.70 Fax : 04.72.43.85.28 **jean-yves.buffiere@insa-lyon.fr**
MEGA	**MÉCANIQUE, ÉNERGÉTIQUE, GÉNIE CIVIL, ACOUSTIQUE** **http://edmega.universite-lyon.fr** Sec. : Stéphanie CAUVIN Tél : 04.72.43.71.70 Bât. Direction **mega@insa-lyon.fr**	**M. Jocelyn BONJOUR** INSA de Lyon Laboratoire CETHIL Bâtiment Sadi-Carnot 9, rue de la Physique 69 621 Villeurbanne CEDEX **jocelyn.bonjour@insa-lyon.fr**
ScSo	**ScSo*** **http://ed483.univ-lyon2.fr** Sec. : Véronique GUICHARD INSA : J.Y. TOUSSAINT Tél : 04.78.69.72.76 **veronique.cervantes@univ-lyon2.fr**	**M. Christian MONTES** Université Lyon 2 86 Rue Pasteur 69 365 Lyon CEDEX 07 **christian.montes@univ-lyon2.fr**

*ScSo : Histoire, Géographie, Aménagement, Urbanisme, Archéologie, Science politique, Sociologie, Anthropologie

Abstract

Proton therapy is used for cancer treatment to achieve better dose conformity by exploiting the energy-loss properties of protons. Proton treatment planning systems require knowledge of the stopping-power map of the patient's anatomy to compute the absorbed dose. In clinical practice, this map is generated through a conversion from X-ray computed tomography (CT) Hounsfield units to proton stopping power relative to water (RSP). This calibration generates uncertainties as photon and proton physics are different, which leads to the use of safety margins and the reduction of dose conformity. In order to reduce uncertainties, proton CT (pCT) was proposed as a planning imaging modality since the reconstructed quantity is directly the RSP. In addition to energy loss, protons also undergo multiple Coulomb scattering (MCS) inducing non-linear paths, thus making the pCT reconstruction problem different from that of X-ray CT.

The objective of this thesis is to improve image quality of pCT list-mode reconstruction. The use of a most likely path (MLP) formalism for protons to account for the effects of MCS has improved the spatial resolution in pCT. This formalism assumes a homogeneous medium. The first contribution of this thesis is a study on proton paths in heteregeneous media: the accuracy of the MLP was evaluated against a Monte Carlo generated path in different heterogeneous configurations. Results in terms of spatial, angular, and energy distributions were analyzed to assess the impact on reconstruction. The second contribution is a 2D directional ramp filter used for pCT data reconstruction. An intermediate between a filtered backprojection and a backproject-filter approach was proposed, based on the extension of the usual ramp filter to two dimensions, in order to preserve the MLP spatial information. An expression for a band-limited 2D version of the ramp filter was derived and tested on simulated pCT list-mode data. Then, a comparison of direct reconstruction algorithms in terms of spatial resolution and RSP accuracy was conducted. Five algorithms, including the 2D directional ramp, were tested to reconstruct different simulated phantoms. Results were compared between reconstructions from data acquired using idealized or realistic trackers. Finally, the last contribution is a deconvolution method using the information on the MLP uncertainty in order to improve spatial resolution of pCT images.

Résumé

La thérapie proton est utilisée dans le cadre du traitement contre le cancer afin de parvenir à une meilleure distribution de dose en exploitant les propriétés du proton. Les systèmes de planification de thérapie proton requièrent une carte du pouvoir d'arrêt des tissus du patient afin de pouvoir calculer la dose absorbée. En clinique, cette image est générée à partir d'une conversion des unités Hounsfield d'une image tomodensitométrique (CT) rayons X au pouvoir d'arrêt relatif (RSP) du proton. Cette calibration induit des incertitudes étant donné que les interactions physiques des photons et des protons sont différentes, ce qui va mener à l'utilisation de marges de sécurité et à la réduction de la conformité de dose. Afin de réduire ces incertitudes, l'imagerie proton CT a été proposée pour la planification de la thérapie proton puisque la quantité reconstruite est directement le RSP. En plus de la perte d'énergie, les protons interagissent également via la diffusion multiple de Coulomb (MCS) qui induit des trajectoires non linéaires, ce qui rend le problème de reconstruction en proton CT différent de la reconstruction CT rayons X.

L'objectif de cette thèse est l'amélioration de la qualité d'image en reconstruction proton CT en mode liste. L'utilisation du formalisme du chemin le plus vraisemblable (MLP) afin de prendre en compte les effets du MCS a permis d'améliorer la résolution spatiale en proton CT. Ce formalisme suppose un milieu homogène. La première contribution de cette thèse est une étude sur les trajectoires des protons en milieux hétérogènes: la justesse du MLP a été évaluée en comparaison avec un MLP obtenu par simulations Monte Carlo dans différentes configurations. Les résultats en matière de distribution spatiale, angulaire, et énergétique ont été analysés afin d'évaluer l'impact sur l'image reconstruite. La seconde contribution est un filtre rampe directionnel 2D utilisé dans le cadre de la reconstruction proton CT. Il s'agit d'une méthode intermédiaire entre la rétroprojection filtrée et le filtrage de la rétroprojection, basée sur l'extension du filtre rampe en 2D afin de préserver l'information spatiale sur le MLP. Une expression pour une version 2D limitée en bande de fréquence du filtre rampe a été dérivée et testée sur des données pCT simulées. Ensuite, une comparaison de différents algorithmes de reconstruction directs en matière de résolution spatiale et justesse du RSP a été menée. Cinq algorithmes, incluant le filtre rampe directionnel, ont été testés afin de reconstruire différents fantômes. Les résultats obtenus à partir de données acquises avec des détecteurs idéaux ou réalistes ont été comparés. Enfin, la dernière contribution est une méthode de déconvolution qui utilise l'information sur l'incertitude du MLP afin d'améliorer la résolution des images proton CT.

Acknowledgments

Over the course of the last three years, I have received the help and support of several people, whom I would like to acknowledge here.

First of all, I would like to thank my three advisors, official and unofficial: Jean Michel Létang, Simon Rit, and Nils Krah. They form a very competent multidisciplinary team, and I am grateful for being given the chance to work with them. I have especially appreciated their availability and promptness to review my work and give me useful feedback, and their constant involvement and interest in my work. Nils has been a great "unofficial" advisor, whose help I have requested quite a lot, especially during the first year or two, as we were sharing an office then. Thank you to all three for bearing with me for the last three years.

I would like to acknowledge the other committee members — Reinhard Schulte, Claude Comtat, Katia Parodi, Françoise Peyrin, and Ilaria Rinaldi — for reading my manuscript, attending my defense, asking relevant questions and making useful comments.

I would like to express my gratitude to all my colleagues of the CLB group, led by David Sarrut, cited without particular order: Ane, Thomas, Joey, Antoine, Aurélien, Mélanie, Ahmad, David, Olga, Adrien, Cyril, Laure, Madalina, Francesca, and all others. Your presence has made this adventure much more enjoyable. A special mention goes to Thomas for his precious help with IT-related issues, especially my Monte Carlo simulations and reconstructions on the IN2P3 cluster.

I must not forget my friends outside academia for believing in me more than I do myself, for encouraging me and helping me unwind every now and then. Finally, I thank my parents, my grandmother, my aunt, and the rest of my family in Algeria and France for their lifelong support.

Contents

List of Figures

Acronyms

APS active pixel sensors
AQUA Advanced QUality Assurance
ART algebraic reconstruction technique

BPF backproject first
BTF backprojection-then-filtering

CCD charge-coupled device
CMOS complementary metal oxide semi-conductor
CSDA continuous slowing down approximation
CSP cubic spline path
CT computed tomography

DBP differentiated backprojection
DD distance-driven
DECT dual energy computed tomography
DFT discrete Fourier transform
DNA deoxyribonucleic acid
DR directional ramp
DROP diagonally relaxed orthogonal projections
DRR digitally reconstructed radiography

ESF edge spread function

FBP filtered backprojection
FOV field of view
FT Fourier transform

HPGe hyperpure geranium detector
HU Hounsfield units

ICRP International Commission on Radiological Protection
ICRU International Commission on Radiation Units and measurements
iMPACT innovative Medical Protons Achromatic Calorimeter and Tracker
IMPT intensity modulated proton therapy
IMRT intensity modulated radiation therapy
IVI interaction vertex imaging

LBL Lawrence Berkeley Laboratory
LLUMC Loma Linda University Medical Center
LSF line spread function

MAPS monolithic active pixel sensor
MCS multiple Coulomb scattering
MGH Massachusetts General Hospital
ML maximum likelihood
MLP most likely path
MRI magnetic resonance imaging
MTF modulation transfer function
MWPC multiwire proportionnal chamber

NIU Northern Illinois University

pCT proton computed tomography
PET positron emission tomography
PMMA poly(methyl methacrylate)
pRad proton radiography
PRaVDA Proton Radiotherapy Verification and Dosimetry Applications
PRIMA PRoton IMAging
PSDs position sensitive detectors
PSI Paul Sherrer Institut
PTCOG Particle Therapy Co-Operative Group
PTV planning target volume

RBE radiobiological effectiveness
RERD residual energy-range detector
RMS root mean square
ROI region of interest
RSP relative stopping power

SLP straight line path
SOBP spread-out Bragg peak
SSDs silicon-strip detectors
SVD singular value decomposition

TOF time-of-flight
TPS treatment planning system
TSVD truncated singular value decomposition
TVS total variation superiorization

UCSC University of California Santa Cruz

WEPL water equivalent path length
WET water equivalent thickness

xCT X-ray CT

Introduction

Cancer is one of the most widespread and deadliest diseases worldwide, with about 18 million new cases and 9.5 million deaths in 2018 (*Global Cancer Observatory*). About half of cases would require radiation therapy, either alone or in combination with other treatments such as surgery and/or chemotherapy. Standard radiation therapy uses high energy X-rays to damage cancerous cells. The use of protons instead of X-rays for cancer therapy has been proposed as it offers advantages in terms of dose conformity, i.e. maximizing the dose to the target while minimizing the dose to healthy tissues. Exploiting the proton's Bragg peak – a localized dose peak shortly before the protons come to rest – allows to treat deep-seated tumors while sparing critical structures, which is essential for head and neck cancers, prostate cancers, pediatric cancers, etc. The position of the Bragg peak, and therefore of the proton range, can be adjusted via the proton-beam energy.

Planning a proton therapy requires the acquisition of a CT image in order to predict the range and therefore the absorbed dose in the patient. Specifically, a proton stopping power map of the traversed tissues is necessary to estimate the proton range. Unfortunately, using an X-ray CT to compute the stopping power is prone to uncertainties as photon and proton interactions with matter are quite different. This uncertainty, along with other errors due to patient alignment, movements, etc., compels practitioners to use safety margins around the treatment volume at the expense of the sparing of healthy tissues. In this context, proton CT is an attractive solution as the reconstructed quantity is directly the proton stopping power, i.e. no calibration is needed from an X-ray CT. The use of proton CT for treatment planning can help lowering range uncertainties and thus improve dose conformity.

The objective of this PhD was to improve image quality of list-mode proton CT reconstruction. In a list-mode setup, each proton is tracked individually, and its energy, position and direction are measured upstream and downstream from the patient. As proton paths are non-linear due to multiple Coulomb scattering, this allows for a better estimation of the proton path and an improvement of spatial resolution. Tomographic reconstruction algorithms for proton CT must be adapted to take into account the non-linearity of proton paths. The reconstruction problem consists in recovering a stopping power map from the list-mode data.

Chapter 1 starts by presenting the different interactions of protons with matter, namely the energy loss, multiple Coulomb scattering, and nuclear interactions. Chapter 2 presents the bases of proton therapy and the clinical rationale of proton imaging in the context of proton therapy planning. Chapter 3 is a review of proton CT imaging from the early days of proton imaging to the contemporary hardware developments and reconstruction techniques. Chapters 4 to 7 present the contributions of this work. First, a study on the impact of heterogeneities on the proton path, is carried out using Monte Carlo simulations. Specifically, the theoretical most likely path (MLP) is compared to a simulated path in different heterogeneous configurations. In chapter 5, an extension of the ramp filter to two dimensions to improve spatial resolution of pCT is proposed. This method, along with four other direct reconstruction algorithms, is assessed in terms of spatial resolution and stopping power accuracy in chapter 6. A last contribution is presented in chapter 7, a shift-variant deconvolution method taking into account the uncertainty on the proton path to improve spatial resolution.

Part I

State of the art

Chapter 1

Proton interactions with matter

A proton is a positively charged subatomic particle, often denoted p or p^+. For protons in the energy regime typically used for proton imaging (60-300 MeV), we distinguish three interaction processes (Figure 1.1):

1. Energy loss: non-elastic Coulomb interactions with atomic electrons;
2. multiple Coulomb scattering (MCS): deflection of the proton via elastic Coulomb repulsion between the charge of the proton and the charge of the nuclei;
3. Nuclear interactions: elastic and non-elastic interactions with the nuclei involving nuclear forces.

The first two interactions involve electromagnetic forces between the charge of the particle and the charge of the electrons or nuclei of the atoms, while the last type of interaction involves nuclear forces. Each interaction can be categorized as (a) elastic when kinetic energy is conserved or (b) non-elastic when kinetic energy is not conserved. In this chapter, we introduce these interactions and the associated theoretical models, and briefly discuss their implementation for Monte Carlo simulations.

1.1 Energy loss

1.1.1 Stopping power

Protons lose energy through electromagnetic interactions with atomic electrons and nuclei. At a clinical energy range, they predominantly lose energy due to inelastic collisions with electrons, resulting in their excitation and ionization. The multiplication of these microscopic interactions ($\sim$ 20 eV lost per interaction (Berger et al., 1993)) will cause the proton to lose energy until it stops. In the continuous slowing down approximation (CSDA), it is assumed that protons lose their energy continuously along their tracks at a rate given by the stopping power S, expressed as the average energy loss per unit path length:

$$S = -\frac{\mathrm{d}E}{\mathrm{d}x}. \tag{1.1}$$

The stopping power depends on the target medium as well as the proton energy, and is given by the Bethe-Bloch formula, including correction terms, for protons with $E > 2$ MeV:

$$S = 4\pi r_e^2 m_e c^2 \rho_e \frac{1}{\beta^2}\left[\ln\left(\frac{2m_e c^2\beta^2}{I(1-\beta^2)}\right) - \beta^2 - \frac{\delta}{2} - \frac{C}{Z} + F\right], \tag{1.2}$$

with r_e the electron radius, $m_e c^2$ the electron energy at rest, ρ_e the electronic density, $\beta = v/c$ the particle velocity relative to the velocity of light c, and I the mean excitation energy of the medium. The last three terms are corrections to the original

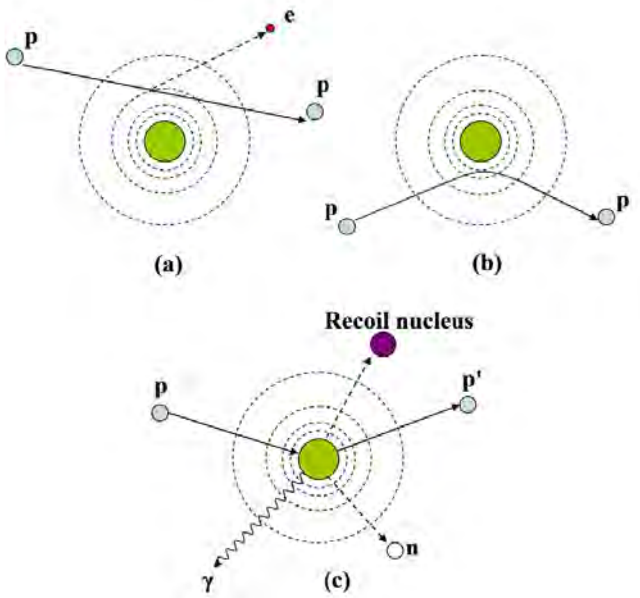

FIGURE 1.1 – Main proton interactions: (a) energy loss via Coulomb interactions with electrons, (b) scattering via Coulomb interactions with nucleus, (c) non elastic nuclear reactions producing secondary particles (figure from Newhauser and Zhang (2015)).

Bethe-Bloch formula: $\delta/2$ is the density-effect correction, C/Z is the shell correction, and F represents higher order corrections (Barkas, Bethe and Mott corrections). The density-effect correction is only large for high energies (its contribution reaches 1% above 500 MeV). The shell correction is significant at low energies (10% for protons at 2 MeV). All correction terms can be ignored in the proton imaging energy regime. An overview of the different terms in equation 1.2 can be found in Berger et al. (1993). Note that this is the formula for the electronic stopping power, and we omit energy loss due to electromagnetic interactions with the nucleus as it is not significant in the clinical regime (contribution of < 0.1 % to the energy loss (Janni, 1982)).

The dose delivered by the protons is directly related to the mass stopping power by

$$D = \phi \frac{S}{\rho}, \tag{1.3}$$

with ϕ the fluence of the protons and ρ the mass density of the target. As the stopping power is roughly proportional to $1/\beta^2$, the more protons lose kinetic energy, the more the stopping power – and therefore the dose – increases (see Figure 1.2). As the protons progress in the medium, they lose more and more energy, which will give rise to a peak of dose at the end of the proton path, called the Bragg peak (see section 2.2).

According to Equation 1.2, the stopping power also depends on the target medium via the electronic density ρ_e and the I value. The electronic density of a mixture or compound of N elements is defined as

$$\rho_e = \rho N_A \sum_{i=1}^{N} w_i \frac{Z_i}{A_i}, \tag{1.4}$$

with N_A Avogadro's number, and Z_i, A_i and w_i the atomic number, atomic mass,

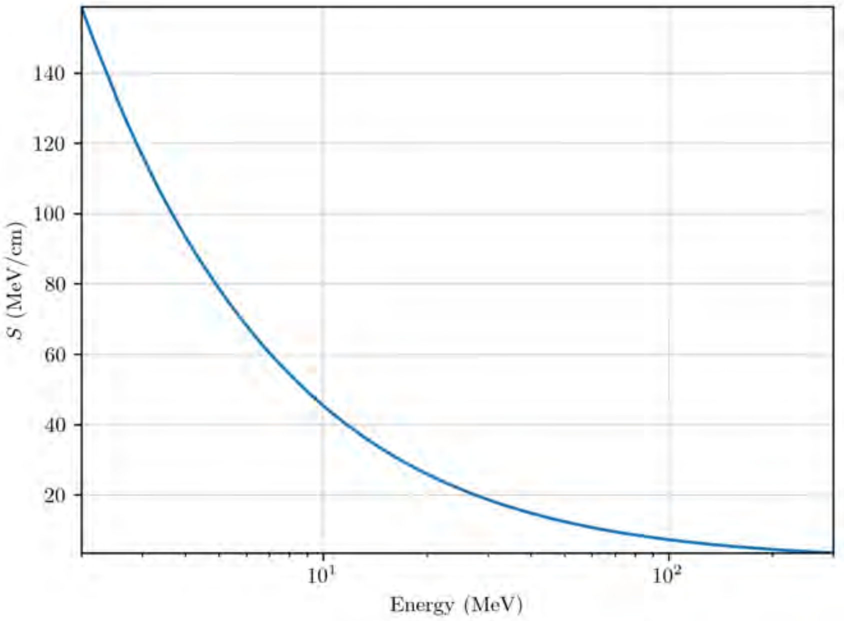

FIGURE 1.2 – Stopping power of protons with energy between 2 MeV and 300 MeV in water (data retrieved from Geant4 v10.6).

and fraction by weight of the i^{th} element of the target. On the other hand, the mean excitation energy I is not easily obtained. In fact, there is no consensus on how to establish reference values. It is estimated that a 10% variation on the mean excitation energy introduces about 1% variation on the stopping power of water (Yang et al., 2012). The value currently recommended by International Commission on Radiation Units and measurements (ICRU) is $I = 78$ eV for water.

1.1.2 Range

The proton stops once it loses all of its kinetic energy. The depth at which a proton will stop is called the CSDA range and is defined as

$$R = \lim_{E_f \to 0} \int_{E_f}^{E_i} \frac{1}{S(E)} \, \mathrm{d}E, \tag{1.5}$$

with E_i and E_f the initial and final energy of the proton, respectively. Often, the term *range* is also used to refer to the mean projected range. As protons undergo elastic scattering and deviate from their initial direction, it is easier to observe the projections of the CSDA range on the initial direction of the protons. The mean projected range is related to the dose using

$$R = d_{80} \tag{1.6}$$

where d_{80} is the depth corresponding to the distal 80% point of the Bragg peak. The mean projected range is smaller than the CSDA range by a detour factor due to multiple Coulomb scattering. However, in the clinical energy range, the detour factor is about 0.999 (Berger et al., 1993), such that the mean projected range and the CSDA range are interchangeable. The range can also be approximated from the energy of the proton using the Bragg-Kleeman rule

$$R = \alpha E^p \tag{1.7}$$

with the parameters $\alpha = 2.2 \times 10^{-3}$ and $p = 1.77$ obtained by fitting Equation 1.7 to the range in cm for beam energies up to 200 MeV (Bortfeld, 1997).

1.1.3 Energy/range straggling

Energy loss is a statistical process as protons lose energy in discrete amounts through a myriad of collisions, and the stopping power represents only the average of this stochastic quantity. The energy lost by each proton depends on the type and number of interactions it undergoes. Therefore, a perfectly monoenergetic proton beam will have an energy spread after traversing an absorber. This is called energy straggling, and induces range straggling as well. The straggling function is not always symmetrical, such that the most probable energy loss is not necessarily equal to the average energy loss used to define the stopping power.

We consider the case of "thick" absorbers, when the proton path length is long and many collisions occur. When the total energy loss is small ($<$ 20% of the initial energy), the energy loss spectrum for a single collision does not depend much on the energy of the proton before the collision. We can therefore consider the energy losses in individual collisions to be independent. According to the central limit theorem, the sum of independent stochastic variables is normally distributed. Consequently, the energy loss distribution after traversing a given thickness is Gaussian, with a variance given by (Bohr, 1948)

$$\frac{\mathrm{d}}{\mathrm{d}x}\sigma_B^2(x) = \kappa_2(x) = 4\pi r_e^2 m_e c^2 \rho_e \left[\frac{1-\frac{1}{2}\beta^2(x)}{1-\beta^2(x)}\right]. \tag{1.8}$$

For energy losses larger than 20% of the initial energy of the proton (which is usually the case in proton imaging), the collision spectrum depends more strongly on the energy before the collision, i.e. the energy lost in a collision will depend on previous collisions. In this case, the energy distribution after the target is no longer Gaussian, i.e. the moments of order > 2 are different from zero (Symon, 1948; Tschalär, 1968b,a; Tschalär and Maccabee, 1970). The variance of the distribution can be obtained by solving the following differential equation

$$\frac{\mathrm{d}}{\mathrm{d}x}\sigma_T^2(x) = \kappa_2(x) - 2\left(\frac{\mathrm{d}}{\mathrm{d}E}\kappa_1(E(x))\right)\sigma_T^2(x) + \text{higher order terms}, \tag{1.9}$$

with $\kappa_1(E(x)) = S$, the stopping power.

1.2 Multiple Coulomb Scattering

1.2.1 Molière's theory

Due to multiple elastic electromagnetic interactions with atomic nuclei, protons are deflected from their original direction. While the angular deflection from a single interaction is almost always negligible, the multiplication of such interactions causes a deflection of typically a few degrees (see Figure 1.3). The angular scattering distribution is approximately Gaussian, with a tail towards large angles due to some rare large angle scattering events. A comprehensive theory of MCS was proposed by Molière (1947, 1948). He gives the following expression for the angular distribution

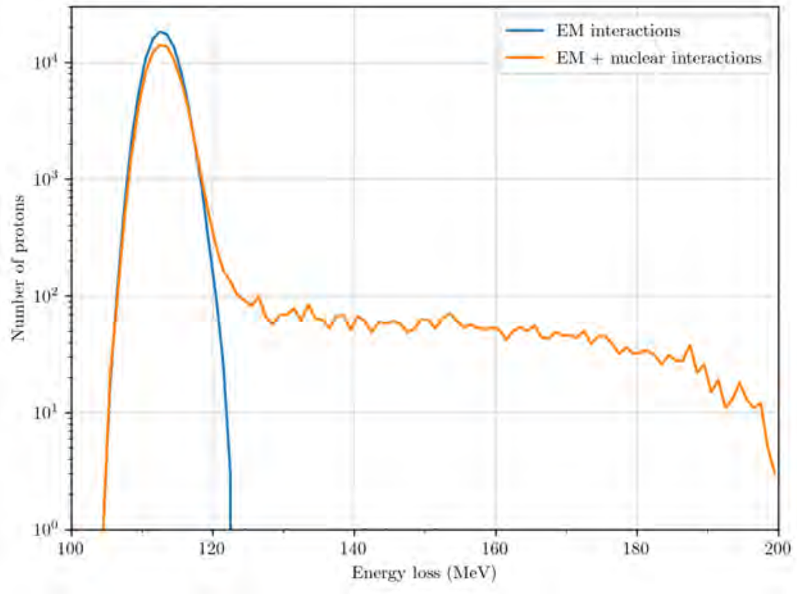

(A)

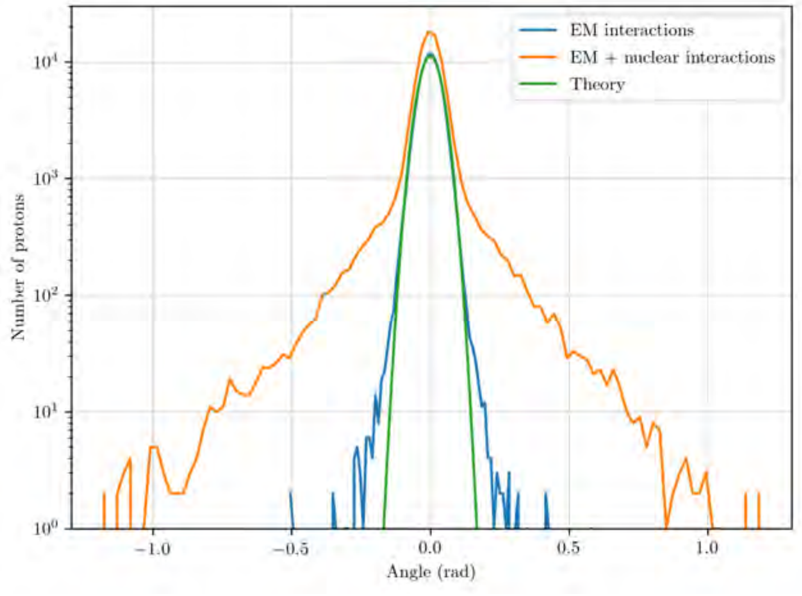

(B)

FIGURE 1.3 – Energy loss and angular distribution of protons with initial energy 200 MeV traversing 20 cm of water, obtained from 10^5 protons simulated with Geant4 v10.6. The *emstandard_opt4* physics list was used for EM interactions and *QGSP_BIC_EMZ* for the full physics.

$$f(\theta) = \frac{1}{2\pi\theta_M}\left(f^{(0)}(\theta') + B^{-1}f^{(1)}(\theta') + B^{-2}f^{(2)}(\theta') + ...\right) \tag{1.10}$$

with θ_M the characteristic multiple scattering angle, θ' a reduced angle, and B the root of the equation

$$B - \ln B = b, \tag{1.11}$$

where b is the natural logarithm of the effective number of collisions in the target. The first term is a Gaussian

$$f^0(\theta') = 2\exp(-\theta'^2), \tag{1.12}$$

the second term models large angle scattering and the third term is a correction. Formulas for θ_M, θ', b, $f^{(n)}(\theta')$ and tables for $f^{(n)}(\theta')$ can be found in Bethe (1953). The contribution to scattering from electromagnetic interactions with the electrons was neglected in Molière's original theory as scattering is limited by the small mass of the electron. It was later taken into account by Bethe by replacing Z^2 by $Z(Z+1)$ in all formulas of Molière's theory. The sum of the three first terms in Equation 1.10 allows an accuracy better than 1%.

1.2.2 Gaussian approximation

For the purpose of proton imaging and therapy, a simple Gaussian model is sufficient as 98% of protons fall within this model. The distribution of scattering angles is therefore approximated by

$$f(\theta) \propto \exp\left(-\frac{1}{2}\frac{\theta^2}{\sigma_\theta^2}\right) \tag{1.13}$$

with θ the projected scattering angle along the initial direction of the proton and σ_θ the width of the Gaussian. For a thin slab of material, Highland (1975) gives the following formula for σ_θ

$$\sigma_\theta = \frac{E_0}{pv}\sqrt{\frac{l}{X_0}}\left[1 + \varepsilon \ln\left(\frac{l}{X_0}\right)\right] \tag{1.14}$$

with l the thickness of the slab traversed by the protons, X_0 the radiation length of the material, ε a constant, and p and v the momentum and celerity of the protons, respectively. This equation only works for thin scatterers, i.e. when pv does not vary much. It was obtained by fitting Bethe's version of Molière's theory (Bethe, 1953) to a handier formula given by Rossi and Greisen (1941). Lynch and Dahl (1991) propose to set $E_0 = 13.6$ MeV and $\varepsilon = 0.038$ instead of the original values in Highland's paper by performing the fit for different values of Z. A generalization of this formula to thick scatterers is proposed by Gottschalk et al. (1993) by performing a quadratic integral and extracting the factor $[1 + \varepsilon \ln(l/X_0)]$ from the integral, which yields

$$\sigma_\theta = E_0\left(1 + 0.038 \ln \frac{L}{X_0}\right)\sqrt{\int_0^L \frac{1}{p^2v^2}\frac{\mathrm{d}l}{X_0}} \tag{1.15}$$

with L the total thickness of the scatterer. The exit angular distribution $f(\theta)$ for 200 MeV protons in water is shown in Figure 1.3. The simulated results, including or excluding nuclear interactions, are compared with the distribution computed from Equation 1.13. The distributions are similar except for the non Gaussian tails of the

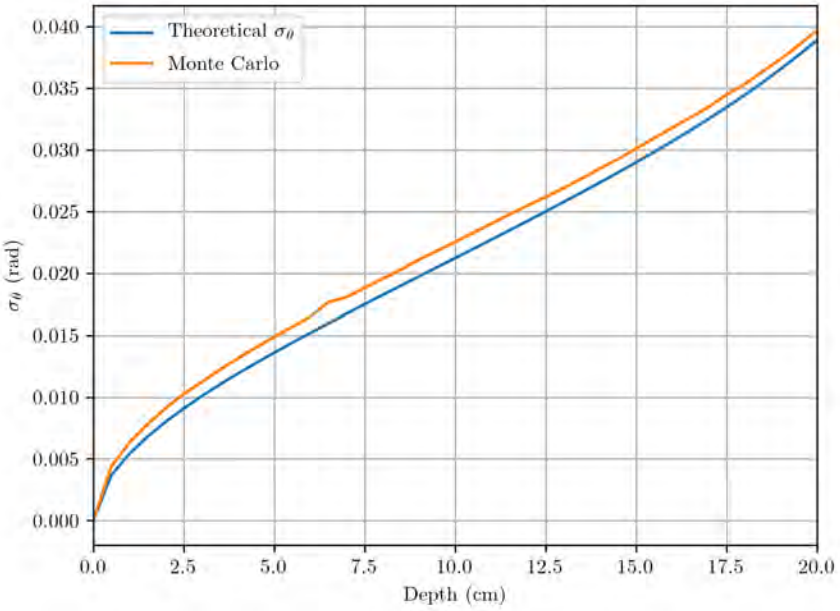

FIGURE 1.4 – Standard deviation of the scattering angles in function of depth, computed with Equation 1.15 and simulated with Geant4 v10.6 excluding nuclear reactions using the *emstandard_opt4* physics list.

simulated distributions. These tails are larger when nuclear interactions are taken into account. In practice, in the context of proton imaging, protons with unusually large scattering angles are filtered out to comply with the Gaussian approximation (see section 3.6.1.1). The width σ_θ against the depth in water is plotted in Figure 1.4. There is a good agreement between σ_θ predicted by Equation 1.15 and Monte Carlo simulations without nuclear reactions, although the simulated scattering width is larger as large angle scattering is not taken into account in the Gaussian approximation.

1.3 Nuclear interactions

While electromagnetic interactions are quite well-understood, it is harder to model interactions involving nuclear forces. Although they are not as frequent as electromagnetic interactions, they are not rare enough to be neglected. We categorize nuclear reactions as in (Barschall et al., 1999):

- elastic nuclear reactions in which “the incident projectile scatters off the target nucleus, with the total kinetic energy being conserved.” For example,

  $$p +^{16} O \rightarrow p +^{16} O \tag{1.16}$$

  is an elastic reaction as the internal state of both the target nucleus and the projectile are unchanged.
- non-elastic nuclear reactions in which kinetic energy is not conserved. “For instance, the target nucleus may undergo break-up, it may be excited into a higher quantum state, or a particle transfer reaction may occur”, as in

  $$p +^{16} O \rightarrow p + p +^{15} N, \tag{1.17}$$

Secondary	n	p	d	t	α	γ	recoils
Multiplicities	1.27	2.17	0.43	0	0.85	0.37	-
Energy fraction	0.23	0.47	0.098	0	0.04	0.008	0.002

TABLE 1.1 – Mutiplicities and energy transfer fraction for 200 MeV $p +^{16} O$ reaction, from Barschall et al. (1999).

or

$$p +^{16} O \rightarrow p +^{16} O^*, \tag{1.18}$$

where $^{16}O^*$ denotes the excited oxygen nucleus. Possible secondaries (products of non-elastic collisions) include secondary protons, neutrons, γ rays, alpha particles and recoil nuclei. Secondaries can be used for verification of proton therapy treatments (see section 2.3.4).

Non-elastic nuclear interactions, where the proton enters the nucleus and knocks off its constituents as in reaction 1.17, cause large abrupt energy losses, inducing a tail to the straggling distribution, and large scattering angles (Figure 1.3). Elastic interactions also contribute to large scattering angles.

The cross section for non-elastic interactions for the main elements in the human body is almost constant for energies larger than 100 MeV, it reaches a maximum around 30 MeV before falling to zero (Figure 1.5). Table 1.1 shows the multiplicities (average number of particles produced per nuclear reaction) and the fraction of the initial energy transfered to secondary particles. The most frequent secondaries are, in order: protons, neutrons, α particles, deuterons and γ rays. The energy transfer is mostly towards protons and neutrons. Figure 1.6 shows the probability of the 6 most probable reactions in function of depth. As expected, protons and neutrons are the most produced secondaries. Some reactions have a constant probability along the whole depth, but most of them reach a maximum probability near the Bragg peak.

In terms of dose, the dose deposited by deuterons, tritons and α particles contributes less than 0.1% to the total dose, and the distal dose deposited by neutrons is below 0.05% of the prescribed target dose (Paganetti, 2002).

1.4 Geant4

Geant4 (Agostinelli et al., 2003) is a Monte Carlo simulation platform used to simulate the passage of particles through matter. There are different models available to compute the interaction processes described in the previous sections. We give a brief overview of the models selected in the *QGSP_BIC* physics list, that we use later in our simulations.

The class *G4hIonisation* provides the energy loss due to ionisation. For protons with energy greater than 2 MeV, the Bethe-Bloch formula is used via the model in *G4BetheBlochModel*. Stopping power and range values over a large energy range (100 eV $-$ 100 TeV) are precalculated during the initialization of the simulation. At run time, a spline approximation is used to compute the energy loss from the stopping power/range tables. When the energy loss in a step is small (<1%), it is approximated by

$$\Delta E = \frac{\mathrm{d}E}{\mathrm{d}x}\Delta s, \tag{1.19}$$

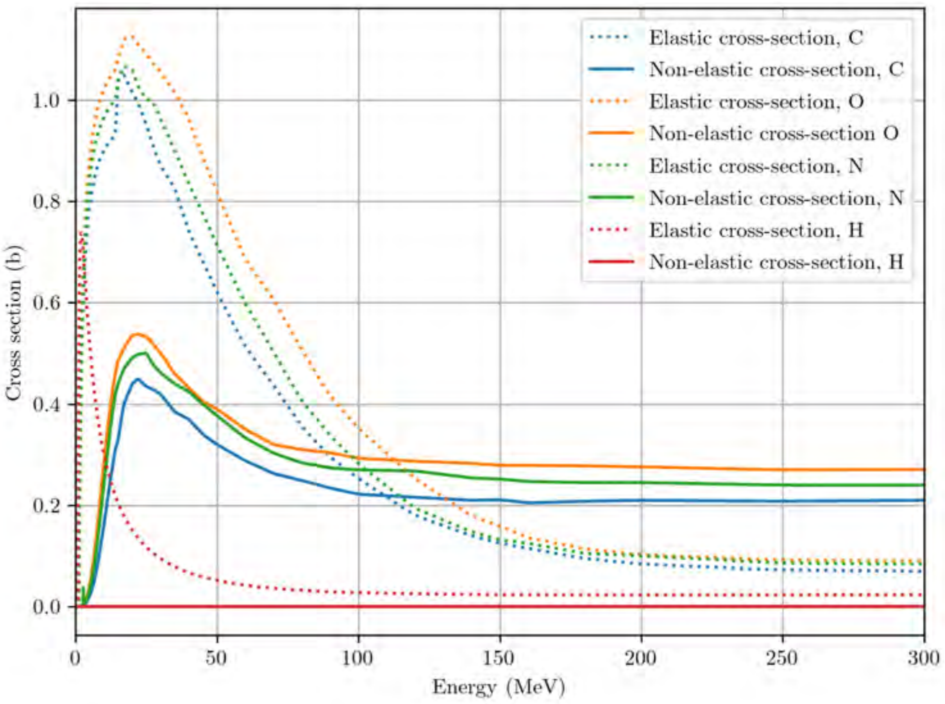

FIGURE 1.5 – Nuclear elastic and non-elastic proton cross-sections for Carbon, Oxygen, Nitrogen, and Hydrogen (data retrieved from Geant4 v10.6).

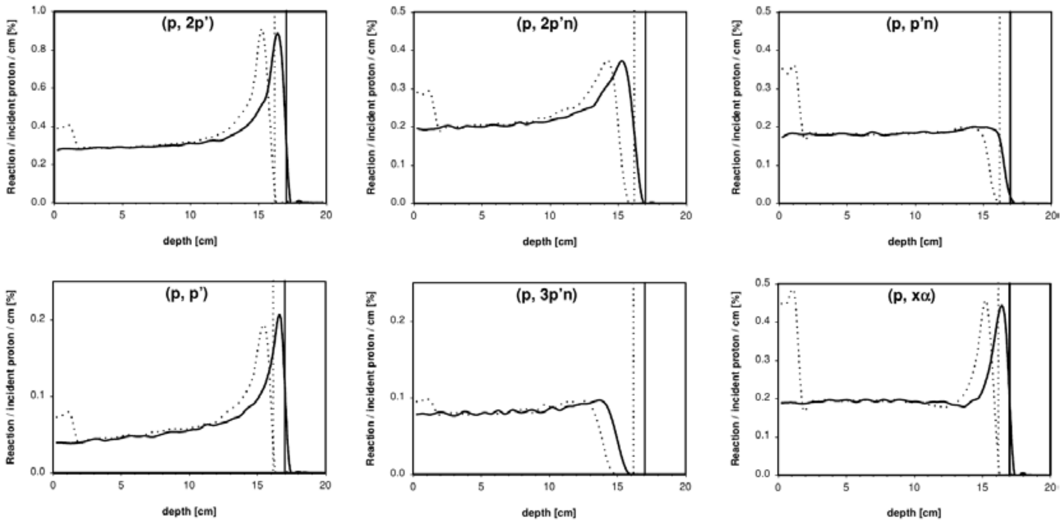

FIGURE 1.6 – Probability per cm per proton for the occurence of a non-elastic nuclear reaction in function of depth, for a 160 MeV beam in water (solid line) and water + bone insert (dotted line). The vertical lines show the position of the Bragg peak (Figure from Paganetti (2002)).

with ΔE the mean energy loss, $\frac{\mathrm{d}E}{\mathrm{d}x}$ the interpolated stopping power at the start of the step, and Δs the step size. Otherwise, the mean loss is computed from

$$\Delta E = E_0 - f(R_0 - \Delta s) \tag{1.20}$$

with R_0 the range at the beginning of the step, and f a function to get the energy from the range.

Energy fluctuations for thick absorbers are computed using a Gaussian model implemented in *G4IonFluctuations*. A thick absorber must verify $k > 10$, with k the number of interactions of the particle in one step. Bohr's variance formula is used when the energy loss is less than 20% of the proton's energy. Otherwise, a multiplicative factor is used to increase fluctuations.

Geant4 uses *G4WentzelVIModel* for MCS (Ivanchenko et al., 2010). It is a mixed model as it combines single and multiple scattering models in order to speed up calculations while keeping a good accuracy and reducing the dependence on the step length (Fernández-Varea et al., 1993). An MCS model is used for scattering angles with $\theta < \theta_{\mathrm{max}} = 0.2$ rad, and a single scattering model otherwise. The model used for MCS is the one proposed by Lewis (1950), and the single scattering is that of Wentzel (1926).

The elastic and non-elastic cross sections for hadron-nucleus reactions are computed according to the Glauber-Gribov model (Grichine, 2009).

1.5 Conclusion

The three main types of interaction of protons with matter have been presented: energy loss due to electromagnetic interactions with atomic electrons, MCS due to electromagnetic interactions with nuclei, and nuclear reactions. The different models used to describe these interactions have been introduced. A good grasp of these interaction processes is necessary to understand proton therapy and proton imaging. For example, in proton CT, spatial resolution is impacted by MCS and density resolution by energy straggling. Regarding proton therapy, the energy loss properties of protons induce an interesting dose profile that can improve dose conformity, as explained in the next chapter.

Chapter 2

Proton therapy

Radiation therapy is a cancer treatment aimed at stopping or slowing down the growth of cancer cells by damaging their deoxyribonucleic acid (DNA). A fundamental point in radiotherapy is dose conformity, i.e. maximize the dose to the tumor and minimize the dose to healthy tissues. The goal of ion therapy (proton, carbon, helium, etc) is to improve dose conformity compared with conventional photon radiation therapy by exploiting the dose profile of charged particles; and to take advantage of the superior radiobiological effectiveness (RBE) of ions compared to photons. In this chapter, we present the history and clinical rationale of proton therapy, before discussing the role of CT imaging in proton therapy treatment planning and the potential use of proton imaging.

2.1 Brief history

The existence of protons was demonstrated by Rutherford (1919) who observed the product of the collision of α particles on nitrogen and oxygen atoms. The development of proton therapy is closely linked to the advancements in particle accelerator technology. In 1930, the first cyclotron was built by Lawrence and Edlefsen (1930) at the Lawrence Berkeley Laboratory (LBL) in California. Later, synchrotrons were proposed by Oliphant (1943), Veksler (1944), and McMillan (1945). While cyclotrons produce protons at one specific energy, synchrotrons are capable of accelerating particles with variable energies.

Wilson (1946) first proposed the use of protons instead of photons for radiation therapy. He suggested to take advantage of their dose profile characterized by a low dose in the shallow region of their path and a high dose at the end of their path (Figure 2.1) to target tumors deep within healthy tissue. The first patients were treated with proton beams targeting the pituitary gland at the LBL in 1955 (Tobias et al., 1955). In the next 35 years, until the early 1990s, proton therapy was based mainly in research institutions in the United States, Russia, Sweden, and Japan, and was used on a modest number of patients. In 1990, the first hospital-based proton therapy facility was built at Loma Linda University Medical Center (LLUMC) in California and equipped with a 250 MeV synchrotron (Slater et al., 1992). The first commercial system, developed by IBA (Ion Beam Applications), was installed at the Massachusetts General Hospital (MGH) in Boston, USA.

By the end of 2018, 221,528 patients had been treated using particle therapy worldwide, mainly protons ($\sim$ 190,000 patients) and carbon ions ($\sim$ 28,000 patients), and new particle therapy centers are being constructed (Figure 2.2). The number of patients treated each year has tripled in the last ten years. While hadron therapy centers have been mainly localized in the USA, Europe, and Japan until now, the rest of Asia is predicted to triple its number of facilities in the next few years.

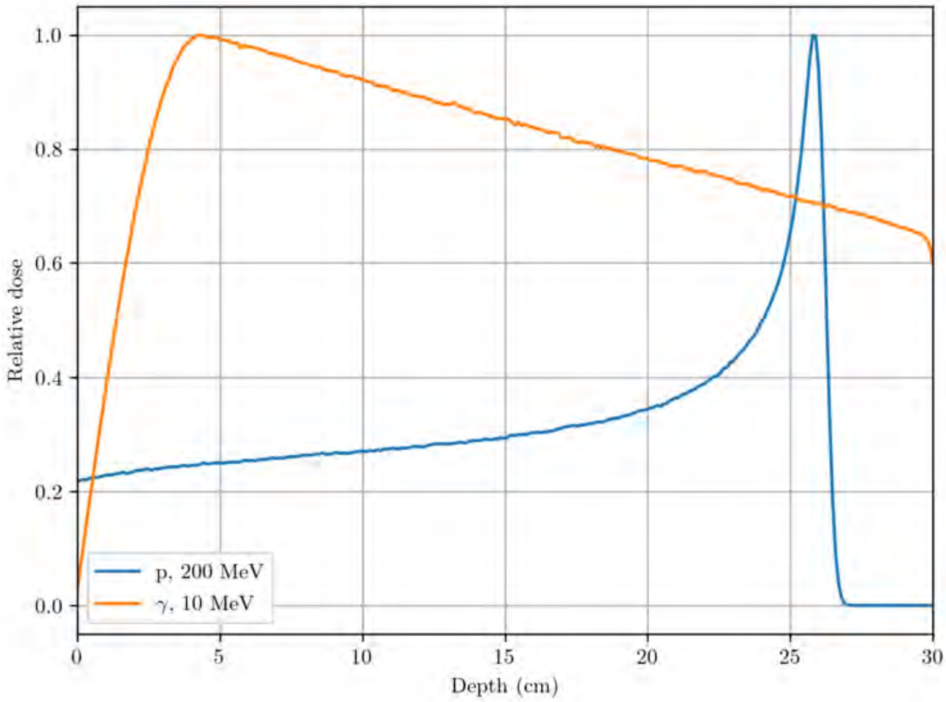

FIGURE 2.1 – Depth dose profiles of 200 MeV protons and 10 MeV photons in water.

2.2 Dose distribution and clinical rationale

Proton interaction processes in matter are different from photons, allowing for a different dose distribution along the particle path (see chapter 1). The dose delivered by photons, after a short build-up, decreases exponentially with depth in the target. Proton dose, on the other hand, is characterized by a peak, called the Bragg peak, localized at the end of the proton path (Figure 2.1). The dose is roughly inversely proportional to proton energy, such that the dose deposited at the entrance of the target, when protons are still highly energetic, is much smaller than the dose deposited near the end of the path, when protons have lost most of their energy. After the peak, the dose decreases to zero such that no dose is delivered to healthy tissues beyond the tumor. By modulating the position of this peak, which depends on the initial energy of the protons and the materials traversed, it is possible to precisely target a deep-seated tumor.

The goal of the treatment is to deliver a uniform dose distribution across the target volume. A single Bragg peak is too narrow (in the depth direction) to cover the whole tumor volume. Therefore, several peaks stopping at different depths are superposed, forming the so-called spread-out Bragg peak (SOBP) (Figure 2.3). SOBPs can be produced by the use of a mechanical device (modulation wheel or ridge filter). Although synchrotrons could theoretically be used for SOBP energy modulation, their acceleration cycles are not fast enough for clinical practice and mechanical modulation in the nozzle is preferred. Synchrotrons are still used to select the maximum energy for each gantry angle.

Furthermore, the beam, which has a typical size of 1 cm, has to be spread in the lateral direction to cover the target. This can be done using either (1) passive scattering where high-Z scatterers are introduced to broaden the proton beam by exploiting MCS; or (2) pencil beam scanning where magnets are used to deflect small

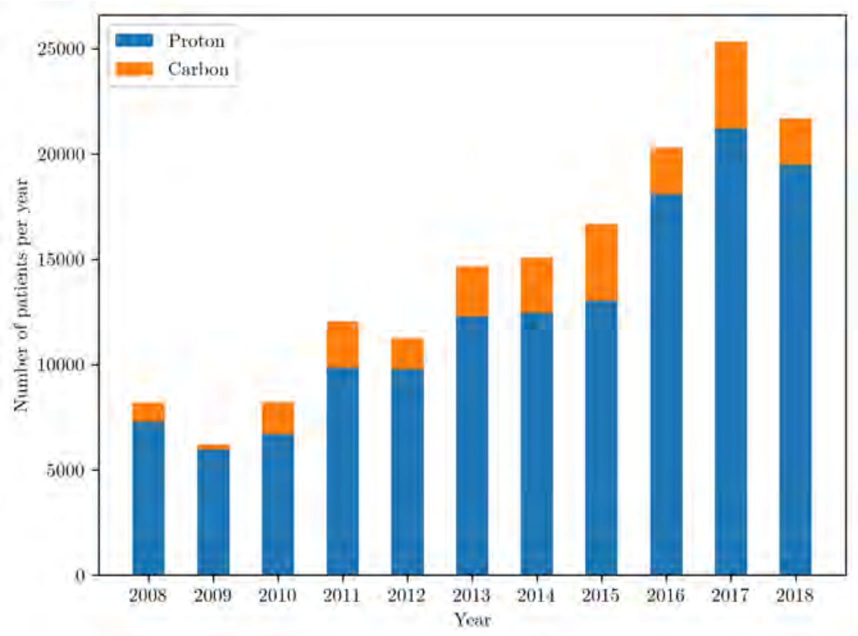

(A) Number of new patients treated per year using proton and carbon ions[a].

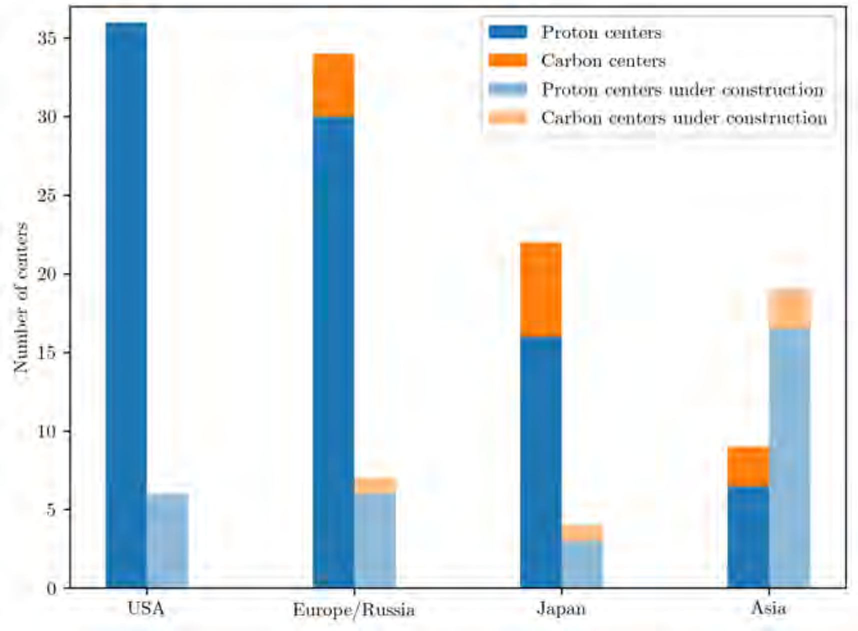

(B) Number of current proton and carbon therapy facilities (updated in February 2020) and under construction facilities (updated in December 2019).

FIGURE 2.2 – Proton and carbon therapy statistics, from PTCOG data[b].

---

[a] Patient data is noisy because the numbers for a few centers are not updated yearly.

[b] Patient and facilities statistics available at `https://www.ptcog.ch/index.php/patient-statistics` and `https://www.ptcog.ch/index.php/facilities-in-operation`

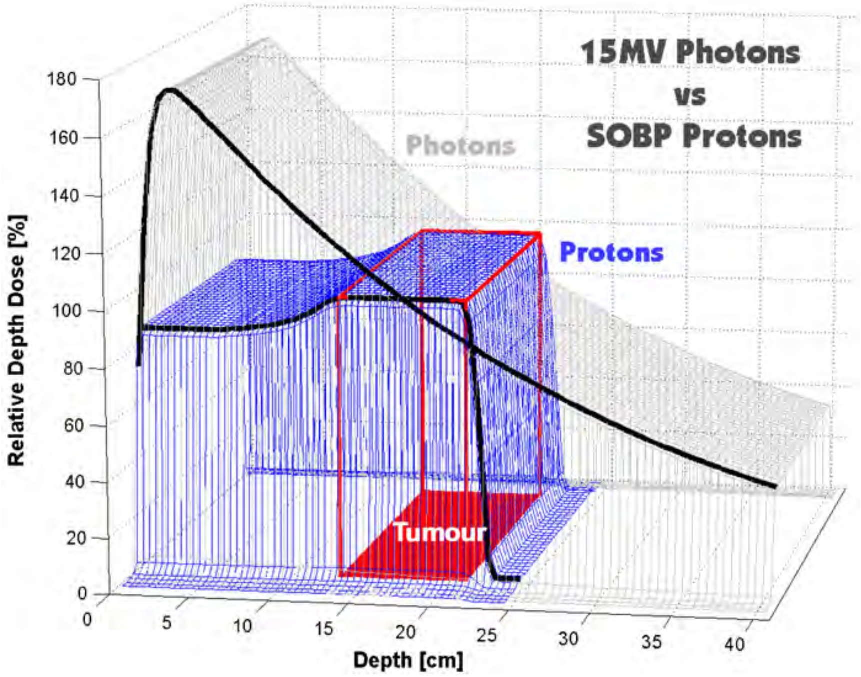

FIGURE 2.3 – Spread out Bragg peak from superposition of energy and intensity modulated protons: the dose is uniform at the target volume and quickly falls to zero beyond the tumor. The red lines indicate the ideal dose distribution. Figure from Smith (2006).

proton beams to precisely shape the dose. A comprehensive review of beam delivery techniques can be found in Paganetti (2012a).

Nowadays, due to intensity modulated radiation therapy (IMRT), the difference in dose conformity between photons and protons has decreased. However, as efforts to develop proton therapy have started later than photon therapy, further improvements in beam scanning technology and intensity modulated proton therapy (IMPT) — which is the superposition of non-uniform distributions from different fields, optimized to produce a uniform dose in the target — can further increase the dose conformity of proton therapy.

There have been many studies showing the dosimetric advantages of proton therapy over photon radiotherapy when both modalities are optimized (Archambeau et al., 1992; Fuss et al., 1999; Lomax et al., 1999; Lin et al., 2000; Clair et al., 2004; Weber et al., 2004; Yock et al., 2005; MacDonald et al., 2008; Vargas et al., 2008; Chan and Liebsch, 2008; Holliday et al., 2016; Zhang et al., 2017b). This benefit is most significant for tumors close to critical structures (head and neck, eye, prostate, etc.) and for pediatric cancers as young individuals are at high risk of developing radiation-induced secondary cancers. Figure 2.4 shows an example of dose distributions using either IMRT or IMPT to treat a brain tumor in a young patient. The integral dose to the brain is decreased with the IMPT plan, with improved sparing of the temporal lobes, orbital structures and both optic nerves.

However, the translation of this dosimetric advantage into a measurable improvement of the clinical outcome (survival rate, reduction of toxicity, improvement of quality of life) has yet to be clearly demonstrated for all treatment sites since high quality clinical studies are scarce (Olsen et al., 2007; Brada, Pijls-Johannesma, and De Ruysscher, 2007; Lodge et al., 2007; De Ruysscher et al., 2012; Weber et al., 2018; Ofuya et al., 2019). At present, several randomized studies are currently ongoing

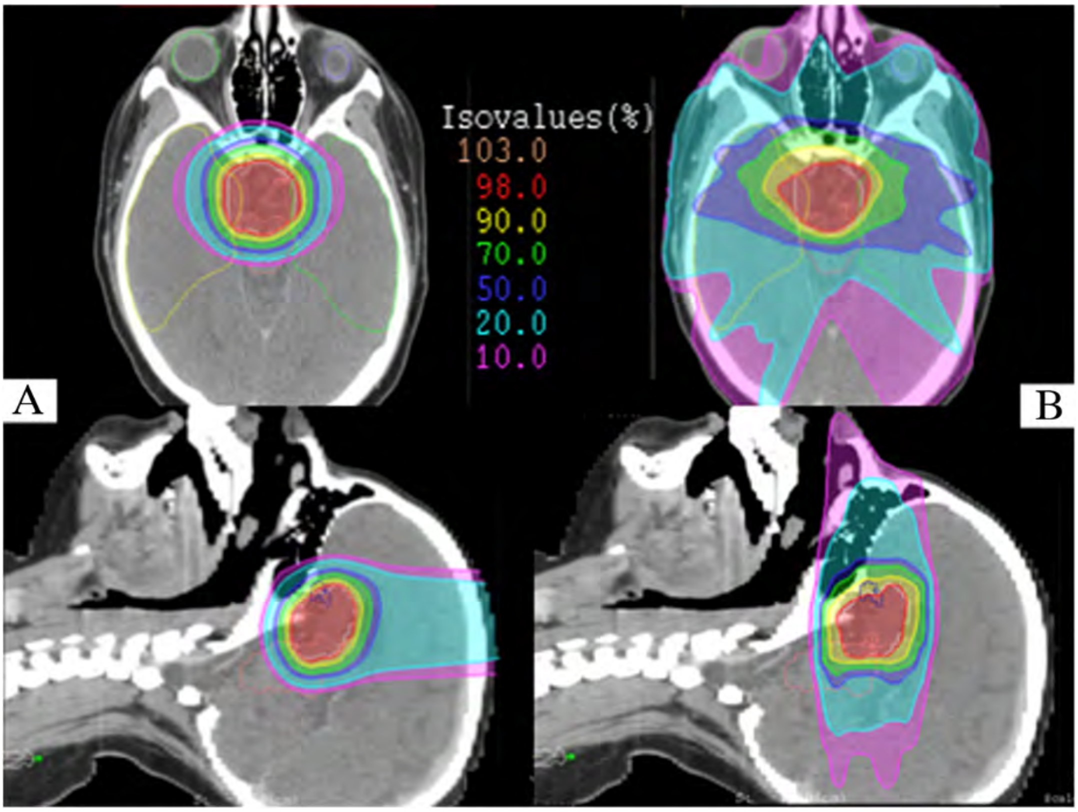

FIGURE 2.4 – Comparison of dose distribution betweem IMPT (A) and IMRT (B) in a young patient with craniopharyngioma. Figure from Rombi et al. (2014).

worldwide to address this issue (Durante, Orecchia, and Loeffler, 2017; Mishra et al., 2017). Such clinical data will allow to carry out robust cost-effectiveness studies of proton therapy. Indeed, economical aspects are crucial since proton facilities are more costly than photon facilities, with a cost per fraction ratio about 2-3, depending on the type of cancer, the fractionation, whether intensity modulation is used, etc. (Peeters et al., 2010; Lievens and Pijls-Johannesma, 2013; Verma, Mishra, and Mehta, 2016).

2.3 Proton therapy treatment planning

It was pointed out in the previous section that the dose distribution must be sculpted in 3D to uniformly cover the tumor. To this end, imaging is essential as dose distributions are altered drastically by inhomogeneities; and failure to account for tissue variations leads to under- and overdosage putting the treatment plan in jeopardy. Proton therapy has made an early use of CT for treatment planning (Goitein, 1978, 1979). The first step of planning a proton therapy treatment is the acquisition of a planning CT to have information on the patient anatomy and take into account heterogeneities along the beam path. Other imaging modalities (MRI, PET) can be used to provide additional information. The planning CT is used by physicians to delineate the target volume and organs at risk. Then, the treatment planning system (TPS) exploits the CT image to compute the absorbed dose by converting the Hounsfield units of the CT into proton stopping power. The TPS then optimizes all treatment parameters to satisfy the prescribed dose. The next section will discuss the different uncertainties that impact the dose computed by the TPS.

2.3.1 Range uncertainties

To fully exploit the advantages of the dose properties of the proton, the position of the Bragg peak — and therefore the range — has to be known precisely. Due to the steepness of the dose gradient at the distal edge of the peak, an error of even a few millimeters can induce gross underdosage of the tumor and/or overdosage of organs at risk. There are several sources of range uncertainty in proton therapy. Some like patient motion, set-up uncertainties, variations in delineation of the tumor, are also found in conventional radiotherapy although they are more critical in proton therapy. Others like the X-ray CT numbers to stopping power calibration are specific to proton therapy, although a similar conversion from CT numbers to relative electron density is used in conventional radiotherapy. To compensate for range uncertainties, safety margins around the tumor volume are added (i.e. the range is increased), producing the planning target volume (PTV). While adding margins might reduce dose conformity, they are necessary to ensure that the prescribed dose has been delivered to the actual volume of the tumor despite treatment uncertainties. In a nutshell, a trade-off between robustness to uncertainties and conformity is made through the choice of the safety margins. A reduction of these uncertainties would allow more conformal treatment plans.

Amongst the different uncertainties, we can distinguish between

- Physics related uncertainties due to
    - CT conversion from HU to stopping power: in order to compute the range of the proton, the stopping power of the tissues in the patient is obtained from the CT image using a calibration curve prone to uncertainties.
    - CT artifacts, resolution, noise, etc.
    - Dose calculation uncertainties due to the choice of the dose calculation algorithm (analytical or Monte Carlo), range degradation due to MCS in heteregeneous regions, I-values, etc.
- Patient related uncertainties due to
    - Organ motion caused by breathing, heartbeats, bowel movements, etc.
    - Anatomical variations, such as weight loss or gain, tumor growth or shrinkage, or bladder or rectal filling.
    - Patient alignment and set-up, as the patient must be positioned in the same way for all treatment fractions.
    - Target delineation.
- Biology related uncertainties: the radiobiological effectiveness (RBE)[1] is assumed to be constant and equal to 1.1 for protons, however it depends on dose, cell type, clinical endpoint and energy deposition characteristics.
- Machine related uncertainties due to
    - Beam delivery technique (passive scattering or scanning).
    - Beam energy spread.

---

[1] The RBE is the ratio of the dose of photons to that of protons to produce a biological response. It is used to compare the biological effects of different particles.

A comprehensive study of range uncertainties can be found in (Paganetti, 2012a,b; McGowan, Burnet, and Lomax, 2013). Different centers use different recipes for the safety margins, for example, the MGH uses 3.5% + 1 mm, LLUMC adds 3.5% + 3 mm, and the University of Florida Proton Therapy Institute applies 2.5% + 1.5 mm (Paganetti, 2012b). These values are subject to adjustments for certain sites near critical structures.

Among all those uncertainties, proton imaging attempts to reduce the error due to the HU to stopping power calibration. The next section will describe the current technique used to perform this conversion before discussing the different imaging solutions to improve the calibration.

2.3.2 X-ray CT conversion

We describe the different procedures used to convert the X-ray CT into a RSP map. The quantity of interest in X-ray CT is the linear attenuation coefficient, expressed in the Hounsfield scale using

$$\mathrm{HU} = 1000 \times \frac{\mu(E) - \mu_{\mathrm{water}}(E)}{\mu_{\mathrm{water}}(E)}, \tag{2.1}$$

where $\mu(E)$ is the linear attenuation coefficient. The Hounsfield scale was defined to have a value of 0 for water. The objective is to convert these HU values (also called CT numbers) into RSP simply defined as

$$\mathrm{RSP} = \frac{S(E)}{S_{\mathrm{water}}(E)}, \tag{2.2}$$

with $S(E)$ the stopping power for a given material at energy E.

2.3.2.1 Tissue substitute method

In the earliest method, the calibration curve was obtained by measuring the HU and RSP values of several tissue substitutes. The HU values can be obtained by scanning a phantom containing tissue equivalent materials; while the RSP can be determined theoretically or experimentally by measuring the shift in the position of the Bragg peak with and without each tissue substitute insert in the path of the proton beam. Then, a piece-wise linear or bi/trilinear curve is fitted to the measured values (Figure 2.5). The calibration curve shows two main slopes, for tissues lower and higher than 0 HU. In the fat-like tissues region (close to 0 HU), the HU-RSP correspondence is not one-to-one, meaning that tissues with a very similar CT number have different RSPs. This calibration method is very dependent on the tissue substitutes chosen for measurement. Different tissue substitutes lead to different calibration curves (see difference between CIRS and Gammex tissue substitutes in Figure 2.5). On the other hand, while they would be ideal to produce the calibration curve, measurements using real human tissues are technically difficult to acquire.

2.3.2.2 Stoichiometric method

To overcome the limitation of the tissue substitute method, Schneider, Pedroni, and Lomax (1996) proposed a stoichiometric method extending the calibration to human tissues. First, a relationship between the linear attenuation coefficient and the atomic number is established from the known elemental composition of the tissue substitutes and the measured CT numbers. The attenuation coefficient is assumed

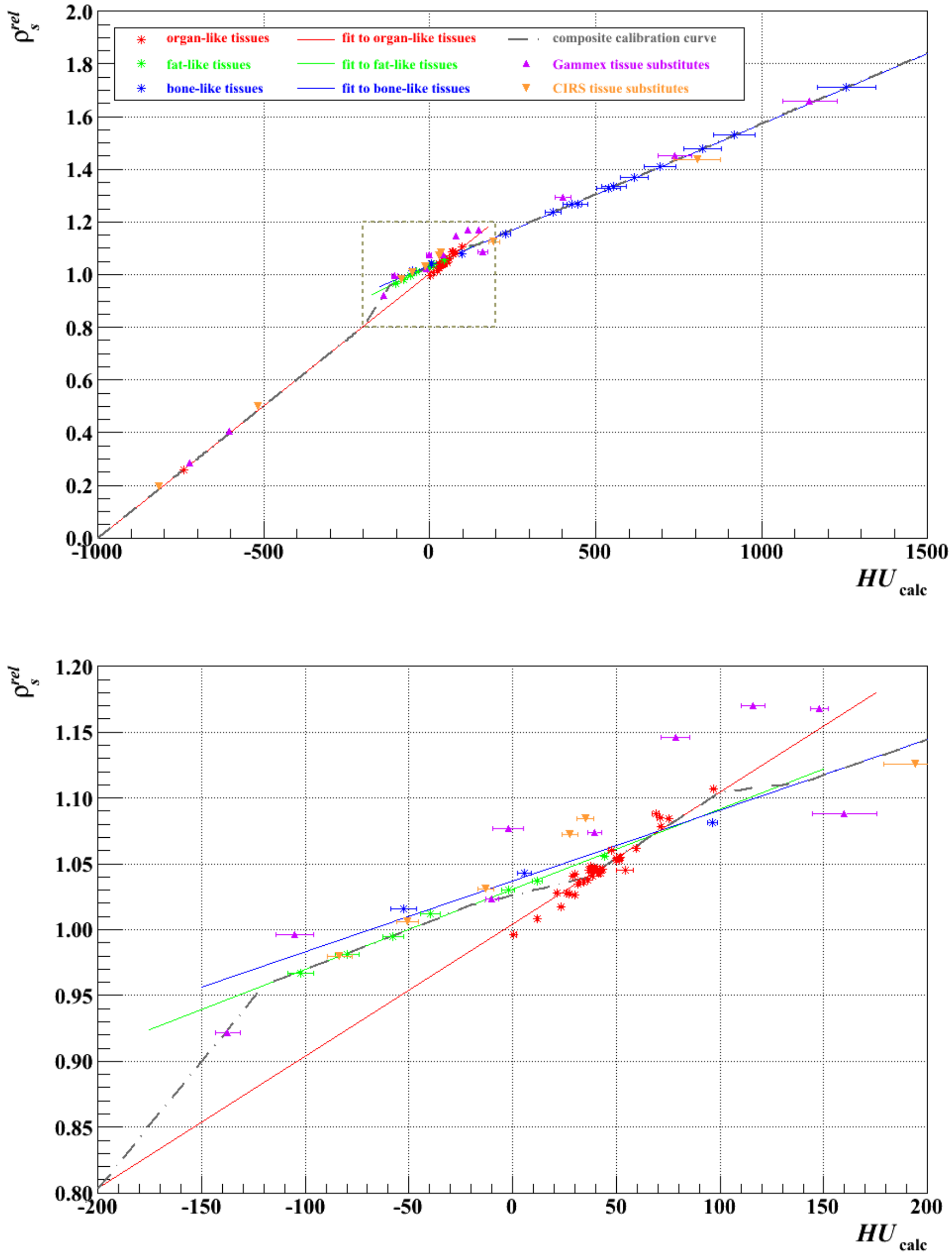

FIGURE 2.5 – Stoichiometric calibration curve of RSP, noted ρ_s^{rel} here, against HU values. The composite calibration curve is pieced together from separate fits to the points for organ-like, fat-like, and bone-like tissues. The data for the Gammex and CIRS tissue substitute phantoms is plotted for comparison with the stoichiometric method. The lower plot magnifies the area of the upper plot in the dashed, boxed region, from -200 HU to +200 HU. Figure from Ainsley and Yeager (2014).

to be related to the sum of three terms corresponding to the photoelectric effect, coherent scattering and incoherent scattering, each with a different Z dependence:

$$\mu = \rho_e (K^{\text{ph}} \tilde{Z}^{3.62} + K^{\text{coh}} \hat{Z}^{1.86} + K^{\text{KN}}), \tag{2.3}$$

with K^{ph} and K^{coh} constants characterizing the photoelectric and coherent scattering cross sections, and K^{KN} the incoherent scattering cross section given by the Klein-Nishina formula. The effective atomic numbers for mixtures are defined as

$$\tilde{Z} = \left[\sum_i \lambda_i Z_i^{3.62} \right]^{1/3.62} \tag{2.4}$$

$$\hat{Z} = \left[\sum_i \lambda_i Z_i^{1.86} \right]^{1/1.86} \tag{2.5}$$

with $\lambda_i = \frac{w_i Z_i}{A_i} \Big/ \sum_i \frac{w_i Z_i}{A_i}$. A fit to the measured μ values is performed to deduce the value of the three constants in Equation 2.3. Then, using this fitted relationship, it is possible to predict the CT number of any human tissue given its chemical composition; while its RSP is given by the Bethe-Bloch formula:

$$\text{RSP} = \rho_e^{\text{rel}} \frac{\ln[2m_e c^2 \beta^2 / I(1-\beta^2)] - \beta^2}{\ln[2m_e c^2 \beta^2 / I_{\text{water}}(1-\beta^2)] - \beta^2}, \tag{2.6}$$

where ρ_e^{rel} is the electron density relative to water and I_{water} is the mean excitation energy of water. Finally, the calibration curve is obtained by plotting the RSP of human tissues against the calculated CT numbers (Figure 2.5). The stoichiometric calibration allows to reduce the error on the estimated RSP values compared with the tissue substitute method, however the HU-RSP degeneracy is still present in the fat-like tissue region.

Uncertainties in the converted RSP result from uncertainties in CT imaging, the stoichiometric formula (Equation 2.3), human tissue composition, the mean excitation energies used to compute the RSP (Equation 2.6), and the energy dependence of the RSP (Yang et al., 2012). According to various studies, range uncertainties due to CT calibration vary from 1.1%-1.8% (Schaffner and Pedroni, 1998), to 3.0%-3.5% (Moyers et al., 2010; Yang et al., 2012).

2.3.3 Imaging alternatives for treatment planning

In order to improve – or even bypass – the calibration, several imaging techniques are being developed as an alternative to X-ray CT.

2.3.3.1 Dual energy CT

In dual energy computed tomography (DECT), an object is scanned using two different energies to allow material discrimination using the energy dependence of the linear attenuation coefficient. The use of DECT for proton therapy was first suggested by Bazalova et al. (2009). A year later, RSP estimation from DECT imaging was demonstrated by Yang et al. (2010). From DECT measurements, the relative electronic density ρ_e^{rel} and the effective atomic number of tissues can be determined. A linear relationship between the effective atomic number and the logarithm of the mean excitation energy can be empirically established (Yang et al., 2010). Knowledge of ρ_e^{rel} and $\ln I$ allows to compute the RSP from Equation 2.6. The superior

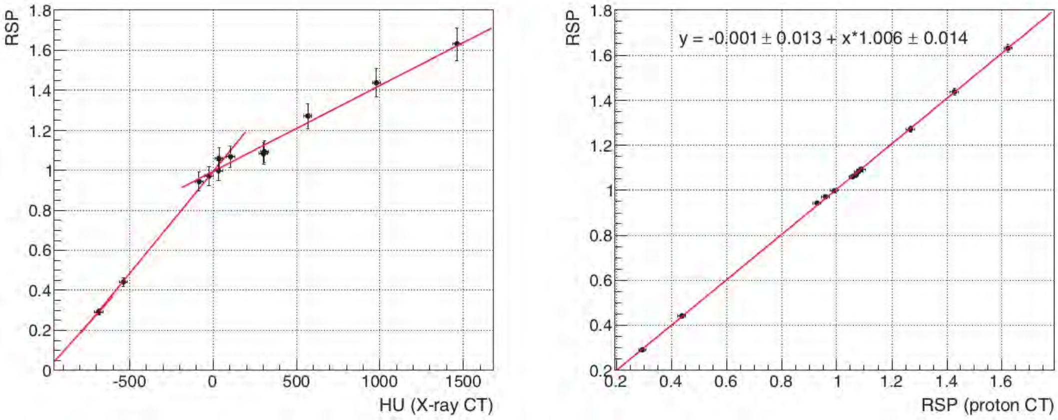

FIGURE 2.6 – Comparison of calibration curves using X-ray CT and proton CT. Figure from Arbor et al. (2015).

accuracy of DECT-based RSP estimation, and its dosimetric advantages, have been demonstrated on commercial TPS (Zhu and Penfold, 2016).

2.3.3.2 Proton radiography

The use of proton radiography (pRad) for patient-specific HU to RSP calibration has been demonstrated (Schneider et al., 2005; Doolan et al., 2015; Collins-Fekete et al., 2017b; Krah et al., 2019). The composition of body tissues varies considerably from patient to patient and introduces inaccuracies in the RSP estimation (Yang et al., 2010), hence the interest in a patient-specific calibration. The principle is to iteratively optimize the calibration curve by minimizing the difference between the measured pRad and a digitally reconstructed radiography (DRR). The DRR is computed from the CT image and the stoichiometric calibration curve using ray tracing methods or Monte Carlo simulations. This method could improve the HU-RSP calibration by using a single radiography and a detector already available in the treatment facility.

2.3.3.3 Proton CT

While the two methods discussed above can improve the quality of the RSP estimation, they still involve a calibration step. In order to fully circumvent the calibration procedure, pCT is the ideal solution as the reconstructed quantity is directly the RSP, as long as the protons have enough energy to traverse the patient, which is a technological challenge. Arbor et al. (2015) have shown that no calibration is required for pCT (Figure 2.6), and that pCT-based range prediction is more accurate and more uniform (less dependent on the localization) than X-ray CT based range prediction. A comprehensive review of proton CT can be found in the following chapter.

2.3.4 Imaging for range monitoring

On another note, there are also imaging modalities for in vivo range and dose verification during or after the radiotherapy treatment (Knopf and Lomax, 2013). We will only discuss the most advanced techniques, although other systems exist. As discussed in section 1.3, inelastic nuclear collisions produce different kinds of secondaries that can be used for range monitoring. Specifically, two types of gamma rays are interesting for treatment verification: (1) coincident gamma rays resulting from the annihilation of the positron produced by the decay of β^+-isotopes (^{11}C or ^{15}N for example, see reaction 1.17) and (2) prompt gammas produced during the de-excitation of the target nuclei (reaction 1.18). The first type of gammas can be used for PET imaging, and the second type for prompt gamma imaging.

2.3.4.1 Positron emission tomography

Possible secondaries of nuclear interactions are positron emission isotopes. The annihilation of the positron with an electron produces two gamma rays emitted at 180° from each other. PET imaging is based on the coincidental detection of these two gammas to reconstruct a 3D activity distribution. Enghardt et al. (1999) first proposed the application of PET imaging to quality assurance in ion therapy. Direct range verification is not possible because the relation between the activity distribution measured by the PET and the dose distribution is not straightforward. Instead, the measured activity is compared with a modeled activity using Monte Carlo simulations. PET imaging of the induced activity can be performed either on-line (during the treatment) or off-line (after the treatment). PET-based range verification is ultimately limited by the knowledge of the elemental composition of the body and the washout (perfusion of positron emitters) processes of human tissues, which are needed to compute the modeled activity distribution.

2.3.4.2 Prompt gamma imaging

Imaging using prompt gammas for proton range verification was first demonstrated by Min et al. (2006). Some nuclear interactions result in the excitation of the target nucleus to a higher energy state, and the subsequent emission of a prompt gamma when the nucleus returns to its ground state. This interaction occurs all along the proton path, until 2-3 mm before the Bragg peak, such that the emission of prompt gammas is correlated with the proton range. Since prompt gammas can be detected within a few nanoseconds after the reaction, this allows real-time range monitoring. Clinical application of prompt gamma imaging is still under development as measuring an adequate signal in the energy range of prompt gammas (2-10 MeV) is challenging. Detection systems for prompt gammas, including the use of a Compton camera (Frandes et al., 2010; Draeger et al., 2018), are actively investigated (Krimmer et al., 2018).

2.4 Conclusion

Proton therapy has the potential to improve dose conformity by taking advantage of the Bragg peak of the proton dose distribution. In order to predict the delivered dose distribution, proton therapy treatment planning systems estimate the proton range using CT imaging. The estimation and reduction of range uncertainties is crucial in proton therapy as they can lead to gross under-dosage of the tumor. One of the main sources of uncertainty is the HU to RSP calibration, with errors up to 3.5% of the range. While different imaging modalities have been proposed to improve the conversion (pRad, DECT), proton CT is the only solution allowing to directly reconstruct an RSP map of the patient. The next chapter will give a comprehensive overview of this technique.

Chapter 3

Proton computed tomography

This chapter offers a broad review of proton transmission imaging: from the historical development of this modality to the the current technology and reconstruction algorithms for proton CT. First, we lay out the principle of pCT.

3.1 Proton CT inverse problem

We state in this section the inverse problem of reconstructing the RSP from proton measurements. The proton stopping power is computed from the Bethe-Bloch formula (Equation 1.2). If we assume that the mean excitation energy I does not vary much in human tissues and has a limited effect on the stopping power due to the logarithmic factor, we can approximate $I = I_{\text{water}} = 78$ eV. In practice, Besemer, Paganetti, and Bednarz (2013) showed that uncertainties in the mean excitation energy might cause proton range variations within the patient up to 4.8 mm. However, under this assumption, we can separate the spatial and energy dependence of the stopping power such that the stopping power at point $\mathbf{x} \in \mathbb{R}^3$ in the object to be reconstructed is given by

$$S(\mathbf{x}, E) = -\frac{\mathrm{d}E}{\mathrm{d}x}(\mathbf{x}) \simeq \rho_e^{\text{rel}}(\mathbf{x}) S_{\text{water}}(E) \tag{3.1}$$

with $\rho_e^{\text{rel}}(\mathbf{x})$ the electron density relative to water and $S_{\text{water}}(E)$ the stopping power of water. From Equation 3.1, we note that while the stopping power depends on both energy and position, the ratio

$$\frac{S(\mathbf{x}, E)}{S_{\text{water}}(E)} \equiv \text{RSP}(\mathbf{x}) \tag{3.2}$$

depends only on the position in the object. Figure 3.1 shows the energy dependence of the RSP of different materials obtained from a Geant4 Monte Carlo simulation. The observed variations are less than 0.7% in the 80-300 MeV energy range, validating the initial assumption. Therefore, we can rearrange and integrate Equation 3.1 to have

$$\int_{\boldsymbol{\Gamma}(t_{\text{in}})}^{\boldsymbol{\Gamma}(t_{\text{out}})} \text{RSP}(\boldsymbol{\Gamma}(t)) \mathrm{d}\boldsymbol{\Gamma}(t) = \int_{E_{\text{out}}}^{E_{\text{in}}} \frac{\mathrm{d}E}{S_{\text{water}}(E)}, \tag{3.3}$$

with $\boldsymbol{\Gamma}(t) \subset \mathbb{R}^3$ the proton trajectory parametrised by $t \in \mathbb{R}$, t_{in} and t_{out} the entrance and exit time, and E_{in} and E_{out} the proton's entrance and exit energies. The right-hand side of Equation 3.3 is equivalent to the water equivalent path length (WEPL), that is the length that the proton would have traversed in water with the same entrance and exit energies (see range Equation 1.5). The pCT inverse problem is to find

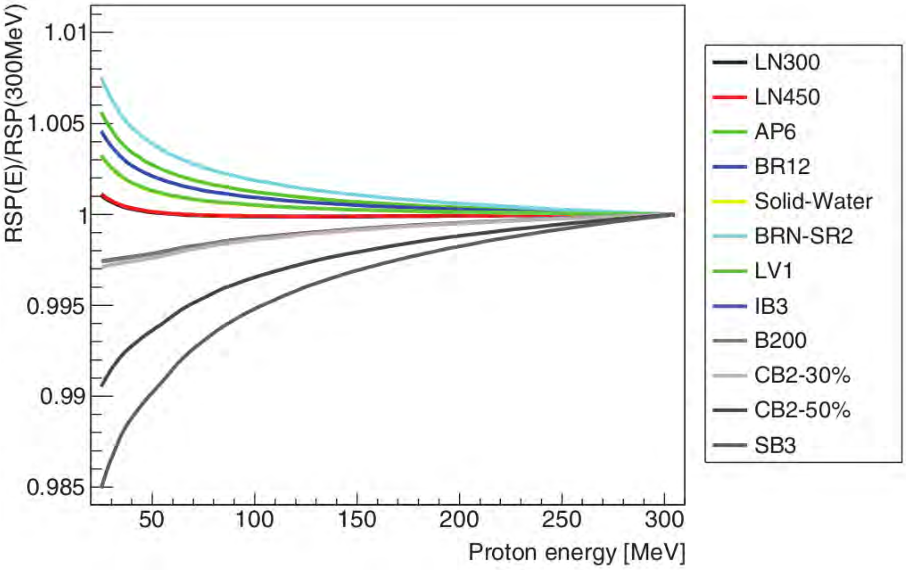

FIGURE 3.1 – Normalized relative stopping power for different materials. Figure from Arbor et al. (2015).

the RSP map from the measured WEPL/energy values, given an estimate $\hat{\Gamma}$ of each proton trajectory.

3.2 Early days of proton CT

The idea of using protons for medical imaging was first proposed by Cormack (1963), more than fifty years ago. In his paper, Cormack proposes a solution to find a function from its line integrals, thus laying the foundation for computed tomography. Amongst possible applications, he describes the determination of X-ray absorption coefficients in 2D and 3D, corresponding to X-ray CT, and the use of the energy loss of protons to guide proton therapy, corresponding to proton CT. He writes

> "The radiotherapist is confronted with the problem of determining the energy of the incident protons necessary to produce the high ionization at just the right place, and this requires knowing the variable specific ionization of the tissue through which the protons must pass."

The first reported proton radiography was made by Koehler (1968). Rather than the energy loss of the protons, their fluence was measured near their range to offer superior contrast. While the steep fall-off of the proton fluence allowed the detection of a very thin piece of aluminium (Figure 3.2a), the spatial resolution was very limited due to multiple Coulomb scattering (MCS). A few years later, West and Sherwood (1972, 1973) performed further experiments (Figure 3.2b) exploring the high contrast capability of proton radiography, due to MCS near edges. Steward and Koehler (1973a,b, 1974a,b) published a series of articles applying proton radiography to the detection of strokes and tumors and some similar works followed (Moffett et al., 1975; Kramer et al., 1978); however, fluence-based proton radiography did not progress much since the 1970s.

The first pCT experiment was conducted by Cormack and Koehler (1976) using a narrow 158 MeV beam and scintillation counters. The density was analytically reconstructed using a calibration of the detector response as a function of absorber thickness to measure the integrated density. The main objective was to detect density

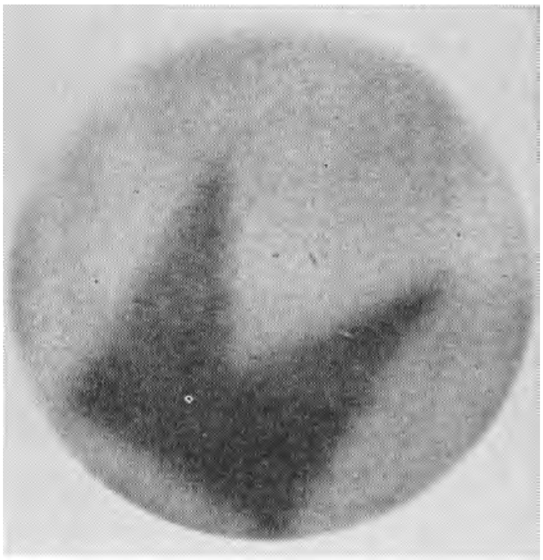

(A) Proton radiography of a stack of aluminum absorbers of thickness 18 g/cm^2 with a pennant-shaped aluminium foil of thickness 0.035 g/cm^2.

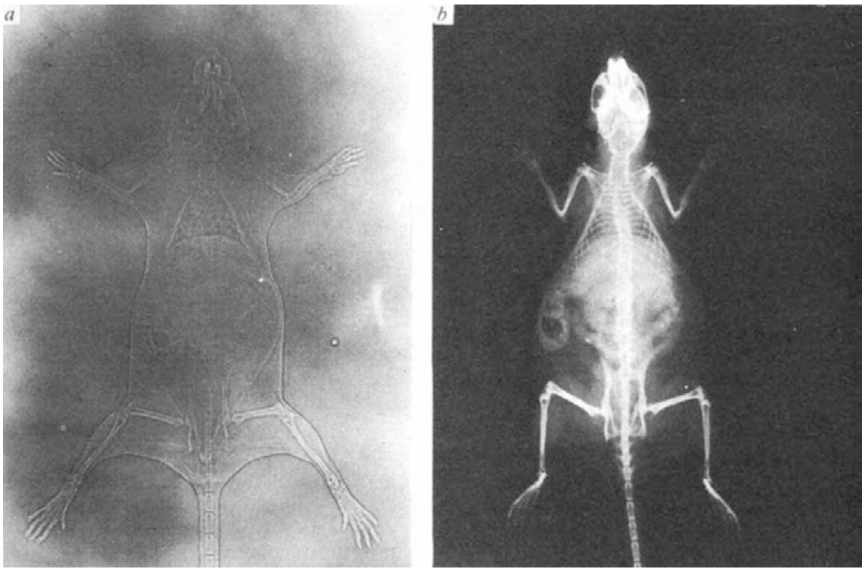

(B) Proton radiography (left) and X-ray radiography (right) of a mouse.

FIGURE 3.2 – Early proton radiography of an object (Koehler, 1968) and of a mouse (West and Sherwood, 1972).

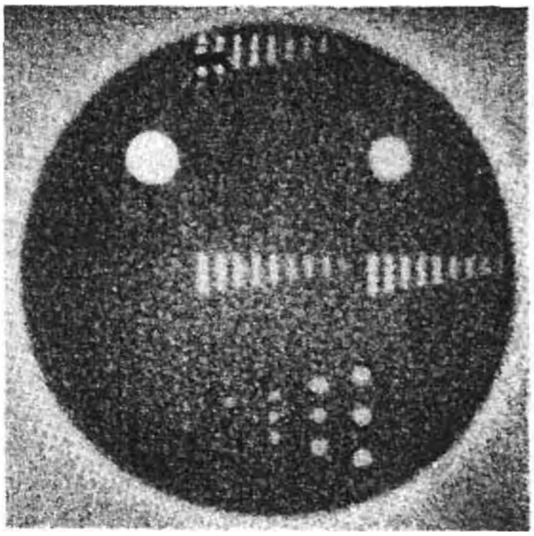

FIGURE 3.3 – Early pCT reconstruction from Hanson et al. (1978)

differences below the detection limit of X-ray CT. Only line profiles were shown in the publication.

In the late 1970s and early 1980s, Hanson continued to explore proton CT at Los Alamos National Laboratory (Hanson et al., 1978; Hanson, 1979; Hanson et al., 1981, 1982). His comparison of X-ray CT and proton CT showed that proton CT can achieve the same density resolution as X-ray CT with a reduced surface dose, although its spatial resolution was limited by MCS (Figure 3.3). It is also free of beam hardening artifacts. In Hanson's experiments, the residual energy, measured using a hyperpure geranium detector (HPGe), and the position, measured with a multiwire proportionnal chamber (MWPC), of each proton was recorded in order to improve spatial resolution. The HPGe detector response was calibrated in terms of residual range in water by scanning a teflon step wedge. Later, the HPGe detector was replaced by a range telescope consisting of a stack of plastic scintillators. The RSP map was reconstructed using a filtered backprojection algorithm. Hanson proposed several other ideas to improve spatial resolution, like the measurement of the exit angle of the protons or the inclusion of curved paths in the reconstruction algorithms to account for MCS, which are nowadays implemented in modern prototypes of pCT scanners.

Early studies focused on the potential dose advantage of pCT rather than its use in treatment planning since proton therapy was still limited at the time. However, due to advancements in low dose X-ray CT and high costs of proton CT due to the particle accelerator, the interest in proton CT dwindled. Hanson et al. (1982) concluded their paper presenting pCT scans of human organs by stating

> "If the only advantage of the proton technique is better dose utilisation, the anticipated extra expense of implementing charged particle CT may not be justified for widespread routine diagnostic studies."

Therefore, while the proof of concept of proton CT was demonstrated in the early 1980s, this was followed by a hiatus period of about a decade in proton imaging research, with a few exceptions (Ito and Koyama-Ito, 1987; Takada and Abe, 1987; Takada et al., 1988), until the 1990s and the expansion of proton therapy.

3.3 General design and detectors

Before proceeding with the modern history of proton CT, this section will give an overview of a pCT scanner design to better understand the current technological developments and grasp the differences between the systems developed by various research groups. We focus on list-mode configurations, i.e. systems where each proton is tracked individually, rather than integrating configurations, given that most current research is focused on list-mode scanners. Figure 3.4 shows a schematic representation of such a proton-tracking scanner. In the following, we summarize the major pCT design requirements, their limitations, and how they can be addressed by appropriate detectors. These key requirements are

- Spatial resolution: a clinically meaningful value for the spatial resolution is 1 mm, given what is achievable in terms of patient positioning and target localization (Schulte et al., 2004). The resolution is physically limited by MCS, in addition to the detector resolution. The RMS error on the trajectory of 200 MeV protons reaches about 0.5 mm at the center of a 20 cm wide homogeneous water phantom (Schulte et al., 2008).
- WEPL resolution: it should be better than 1% (Schulte et al., 2004). It is physically limited by energy/range straggling, as well as incident beam energy spread, detector resolution and MCS (Dickmann et al., 2019). Range straggling is about 1.1% of the proton range, corresponding to 2.85 mm for 200 MeV protons in water.
- Detection rate: in order to scan the patient in a reasonable time, fast data tracking must be achieved. It was estimated that about 100 proton histories per 1 mm^3 voxel per view are needed to achieve a clinically useful image with minimal dose (Sadrozinski et al., 2013). For a head-sized image, this corresponds to a data rate of at least 2 MHz for a 6 min scan. Detection rate can be improved by making faster data acquisition systems, using faster detectors or detectors able to measure multiple events simultaneously.
- Detection efficiency: a high efficiency is essential as undetected protons increase the radiation to the patient without contributing to the image formation. As proton tracking and energy information is measured by several detector layers (see subsections below), efficiency must be excellent in each layer not to discard too many events. In addition, a number of detected events are not used for reconstruction due to nuclear interactions and large angle MCS.

Other requirements include the energy range of the incident beam, the size of the detectors to cover the full imaging area, and the radiation hardness of the detectors. Regarding the energy of the proton beam, it has to be large enough as protons need to pass through the patient in order to be measured. The maximum energy of most medical accelerators is of the order of 230 to 250 MeV. An energy of 200 MeV (corresponding to a 26 cm range in water) is sufficient to traverse the head region, while the abdomen region would need at least 250 MeV (38 cm range). Indeed, the energy dependence of the RSP remains negligible if the residual proton energy is greater than 80 MeV (Arbor et al., 2015), which means that the proton range must exceed by at least 5 cm the maximum thickness crossed.

Two types of detectors are needed to meet the above requirements and produce a pCT image of sufficient quality: a residual energy-range detector (RERD) to measure the proton's WEPL, and position sensitive detectors (PSDs) to measure the position/angle and have a better estimate of the proton trajectory to improve spatial resolution. These detectors are briefly presented in the following sections.

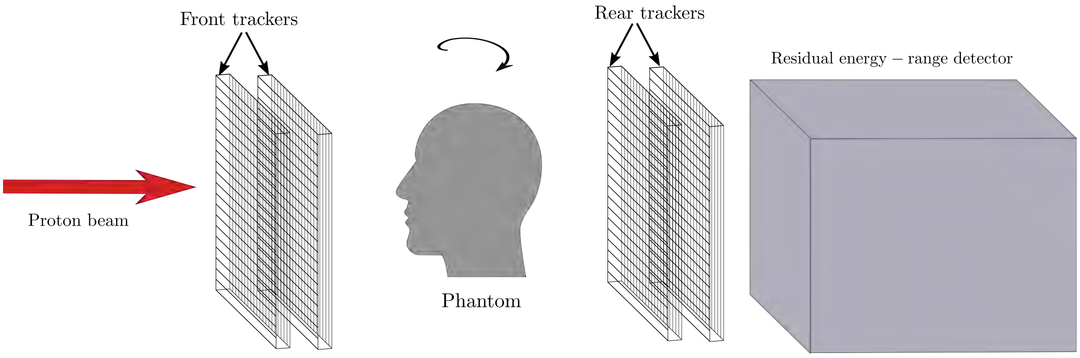

FIGURE 3.4 – Schematic representation of a pCT scanner: the trackers measure the position and direction of the protons, and the energy/range detector measures their WEPL.

3.3.1 Position sensitive detectors

Tracking detectors are used to measure the position and direction of each proton upstream and downstream from the object in order to predict its path. Silicon-strip detectors (SSDs) are usually used for pCT due to their good spatial resolution, efficiency, compactness, and simple calibration. The position information is obtained when the proton hits one of the strips of the detector. Usually, two back-to-back SSDs with orthogonal strip orientation are used to measure the 2D position, although other configurations, like the x-u-v configuration with three tracking planes, are possible (Taylor et al., 2016a). To have the direction information, two of these back-to-back planes are positioned a short distance apart. For example, the SSDs used in one of the state-of-the-art pCT scanners (Bashkirov et al., 2016b) have a sensitive area of about 9×9 cm^2 with a strip pitch of 228 µm, a thickness of 400 µm, and are positioned 50 mm apart. Several such detectors are assembled together to increase the size of the sensitive area, but this has to be done carefully as gaps and non uniformity of the trackers may cause artifacts (Penfold et al., 2011). The RMS spatial resolution of the PSDs is given by

$$\sigma_p^{\text{det}} = \frac{P}{\sqrt{12}}, \tag{3.4}$$

with P the strip pitch; and their angular resolution, neglecting the effects due to the thickness of the PSDs, by

$$\sigma_\theta^{\text{det}} = \frac{P}{\sqrt{6}D}, \tag{3.5}$$

with D the distance between the two tracker planes (Poludniowski, Allinson, and Evans, 2015). The angular resolution is also impacted by the "material budget" of the detectors, i.e. the ratio x/X_0 (see Equation 1.14), as protons scatter when they pass through the trackers. As the radiation length of silicon is constant ($X_0 = 94$ mm), the SSDs should be thin enough to minimize scattering. With the example values for the SSDs given above, the intrinsic spatial resolution is 66 µm and the intrinsic angular resolution, including the scattering effect, is 2.4 mrad for 200 MeV protons (it would be larger for lower energy protons, e.g. at the exit of the object). Overall, the resolution properties of SSDs are satisfactory. The main contributions to the loss of spatial resolution in the reconstructed image are MCS and tracker resolution. While the effects of MCS can be reduced by using a higher beam energy as scattering is inversely proportional to energy, this could negatively impact WEPL resolution (Schulte et al., 2005).

In terms of efficiency, SSDs are close to 100% with very low noise levels, although they can be limited by signal pile-up at very high rates. Other possible PSDs are scintillating fibers, although they have been mostly used for proton radiography as they are less efficient compared with SSDs – Presti et al. (2014) reported an efficiency of 62% and Pemler et al. (1999) only 33%. This low efficiency would be more problematic for the list-mode pCT setup, as the information from 8 independent tracker planes is needed to measure the position and direction of a single proton. In terms of data rate, an x-u-v configuration could help to deal with high proton flux by reducing ambiguity when simultaneous protons are measured.

3.3.2 Residual energy range detectors

There are two main types of RERDs: calorimeters and range telescopes (or range counters). A calorimeter is an unsegmented detector measuring the energy of the protons by converting ionizations into scintillation light, collected by a photomultiplier or photodiode. The measured energy can be converted to range using the Bragg-Kleeman rule for example (Equation 1.7). On the other hand, a range telescope consists of multiple thin sensor stages interleaved with absorbers to stop the proton. The range is directly obtained by the depth of the stage where the proton stops.

For a calorimeter, the WEPL resolution directly depends on the energy resolution of the detector. In order to meet the WEPL resolution requirement, a calorimeter should have an energy resolution better than 1% over a wide energy range, which is not easily achievable (Bashkirov et al., 2016a). The energy resolution of a calorimeter depends on the WEPL, such that resolution is worse for small WEPL values (see Figure 3.5). For a range telescope, the resolution is independent of WEPL. It depends instead on the thickness of the stages as the range is assumed to be equal to the central position of the stopping stage. To achieve a resolution close to the straggling limit, there should be between 60 and 100 stages in the detector (Bashkirov et al., 2016a; Presti et al., 2017). The resolution of a range telescope can be improved depending on how the range is estimated from the measured data (Krah et al., 2018b).

Bashkirov et al. (2016a) proposed a novel detector, the multistage scintillator, which is a hybrid between a calorimeter and a range telescope. It consists of only 5 stages, and its response depends on the position of the stage in which the proton stops as well as the energy deposited in that stage. Compared to a calorimeter, the energy resolution of each stage does not need to be as good to reach a similar WEPL resolution, allowing the use of cheap and fast plastic scintillators. The multistage scintillator has also better resolution and less complexity in terms of assembly and readout than a range counter. However, a major advantage of the range counter is a much simpler calibration compared to a calorimeter or a multistage scintillator (Johnson, 2017).

The detection rate of RERDs, like PSDs, can be improved by simultaneous detection of several events (Esposito et al., 2018).

3.4 Contemporary developments

While early developments focused on the superior contrast capabilities of proton imaging, the so-called "modern era" is characterized by the application of proton imaging to proton therapy treatment planning. In the mid 1990s, supported

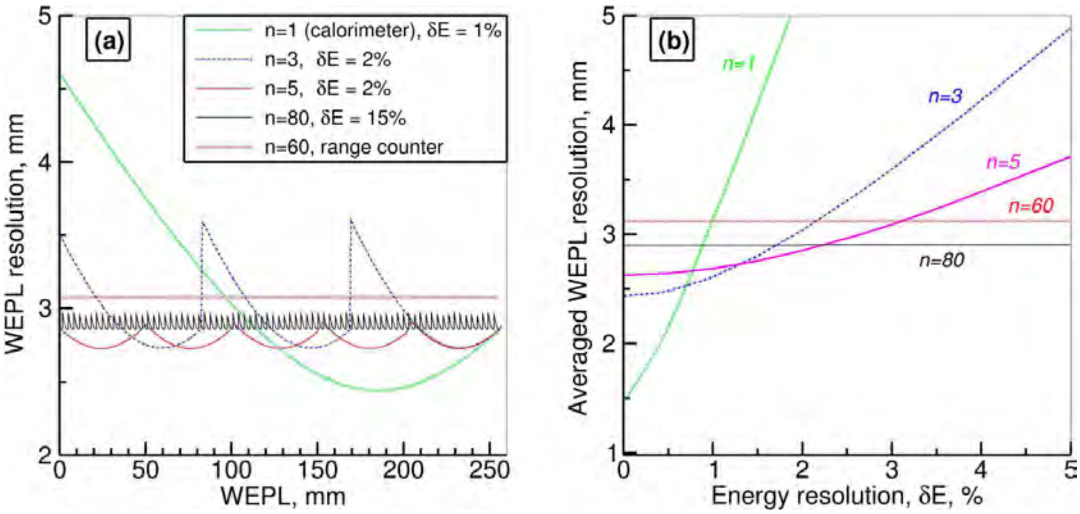

FIGURE 3.5 – Comparison of WEPL resolution between a calorimeter, a range counter, and different multistage scintillators: (a) WEPL resolution in function of WEPL and (b) Average WEPL resolution in function of energy resolution. Figure from Bashkirov et al. (2016a).

by the expansion of proton therapy, interest in proton imaging resurfaced. At the Paul Sherrer Institut (PSI), Schneider and Pedroni (1994, 1995) started investigating proton radiography as a tool for proton therapy. The initial system consisted of two MWPCs to measure each proton's position upstream and downstream from the object, a scintillation counter and a sodium iodide (NaI) energy detector. Due to a low acquisition rate, the exposure time was about 2 hours. Schneider and Pedroni (1995) suggested that proton radiography could be used to check HU-RSP calibration curves by comparing measured radiographs with digitally reconstructed radiographs, a method which was more thoroughly investigated later (section 2.3.3.2). The system at PSI was improved (Pemler et al., 1999) by using two scintillating fiber hodoscopes to measure the position, and a range telescope, allowing to acquire a radiograph within 10 to 20 s. The feasibility of proton radiography under clinical conditions was assessed by scanning an animal patient (Schneider et al., 2004).

In 2000, Zygmanski et al. (2000) experimented with proton CT using a cone beam without recording individual events to reduce acquisition time. The aim was to assess the accuracy of the reconstructed RSP for proton therapy planning. The detection system consisted of a Gd_2O_2S:Tb intensifying screen coupled to a charge-coupled device (CCD) camera. The resulting images offered a good RSP accuracy but suffered from low resolution due to MCS. Indeed, such proton-integrating systems, as they do not track protons individually, offer a limited spatial resolution. Although these systems continue to be studied for pCT (Testa et al., 2013; Rescigno et al., 2015; Krah et al., 2018a) due to their simplicity and lower cost, most developments involve proton-tracking systems, which will be the focus of the rest of this work.

Since 2002, an informal pCT collaboration mostly between LLUMC and University of California Santa Cruz (UCSC) allowed the publication of a number of articles on pCT. In their initial studies (Johnson et al., 2002; Johnson et al., 2003; Sadrozinski et al., 2003, 2004), they investigate the use of SSDs to measure the position and energy of each proton. The pCT collaboration chose SSDs, which were very popular in high-energy physics, because of their excellent spatial resolution at high event rates, mechanical stability, and high efficiency minimizing patient exposure. Soon, a conceptual design for proton CT was proposed by Schulte et al. (2004), and in the next years, several papers followed the progress of the pCT project in terms of technical design (Bashkirov et al., 2007; Bashkirov et al., 2009; Missaghian et al., 2010), particle tracking (Williams, 2004; Schulte et al., 2008) and reconstruction (Li et al., 2003; Mueller et al., 2003; Li et al., 2006; Penfold et al., 2009, 2010b). In 2010, a prototype pCT system, developed by LLUMC/UCSC/Northern Illinois University (NIU), capable of scanning small head-sized phantoms was completed and installed at LLUMC (Hurley et al., 2012). It consisted of 4 SSDs planes, two before and two after the object to measure the position and direction of the protons; and a cesium iodide (CsI) crystal calorimeter chosen for its excellent energy resolution. This system was designed to work at a moderate data rate allowing to acquire a pCT scan in a few hours. It was limited by the data acquisition system, the rate of the CsI detector and the reconstruction time. It was also hindered by the small axial size of the sensitive area of the tracking system (9×18 cm^2).

Hence, in 2011, a collaboration between LLUMC, UCSC and California State University San Bernardino received funding to develop a phase-II pCT scanner (Schulte et al., 2012) to address these limitations. The main difference in terms of design is the use of a multi-stage scintillator, a hybrid between a range counter and a calorimeter (see previous section), instead of the CsI calorimeter (Figure 3.6). By measuring both the range and the energy, the multi-stage scintillator allows a good performance while being inexpensive (Bashkirov et al., 2016a). Several articles documented the progress of the prototype phase-II scanner (Johnson et al., 2014; Zatserklyaniy et al., 2014; Johnson et al., 2015; Bashkirov et al., 2016a; Sadrozinski et al., 2016; Bashkirov et al., 2016b). The phase-II pCT scanner allows to reconstruct high quality data, but is still not fast enough for clinical applications, with a scan time of 6-10 min per acquisition (Bashkirov et al., 2016b). Further hardware improvements should allow the acquisition of a full scan in 2-3 minutes.

An Italian project for proton CT, called PRoton IMAging (PRIMA), emerged in 2007 with the objective of developing a new prototype pCT scanner (Cirrone et al., 2007b; Menichelli et al., 2010; Sipala et al., 2011; Scaringella et al., 2013; Vanzi et al., 2013). Their design resembled the one of the phase-I pCT scanner developed by LLUMC/UCSC/NIU. The calorimeter was made by four YAG:Ce (yttrium aluminium garnet activated by cerium) scintillating crystals, characterized by a fast light decay constant (70 ns) to work in a high particle flux environment. The system was tested with 60 MeV protons at the INFN Laboratori Nazionali del Sud, Catania (Italy) and with 180 MeV protons at Svedberg Laboratory, Uppsala (Sweden). An upgraded system with a larger field of view (5×20 cm^2 instead of 5×5 cm^2) and a better data rate (1 MHz) was planned to be constructed (Civinini et al., 2013; Scaringella et al., 2014; Civinini et al., 2016).

In 2013, the Proton Radiotherapy Verification and Dosimetry Applications (PRaVDA) consortium undertook the development of the first fully solid state proton CT system, based on detector technology built for high energy physics. This system uses position sensitive detectors for both the tracking and the range measurements. The PRaVDA collaboration investigated the use of a stack of complementary metal oxide semi-conductor (CMOS) active pixel sensors (APS) as a range telescope (Poludniowski et al., 2014; Esposito et al., 2015; Taylor et al., 2015; Price and Consortium, 2016), and new silicon trackers (Taylor et al., 2016a). Pixelated sensors allow simultaneous tracking of multiple protons through the range telescope, contrary to scintillator-based calorimeters that are limited by the need for only one proton to pass through the detector per read-out cycle. The PRaVDA collaboration also used the information from the trackers to reconstruct

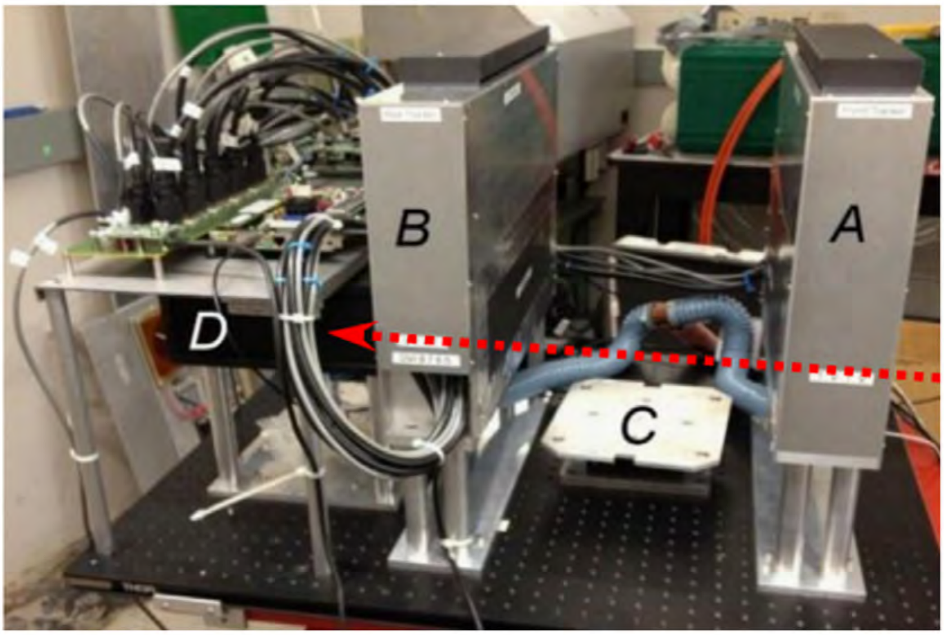

(A) Setup of the phase-II pCT scanner. The front tracker (A), rear tracker (B), phantom rotation stage (C), and 5-stage scintillator (D) are labeled. The red arrow indicates the proton beam direction

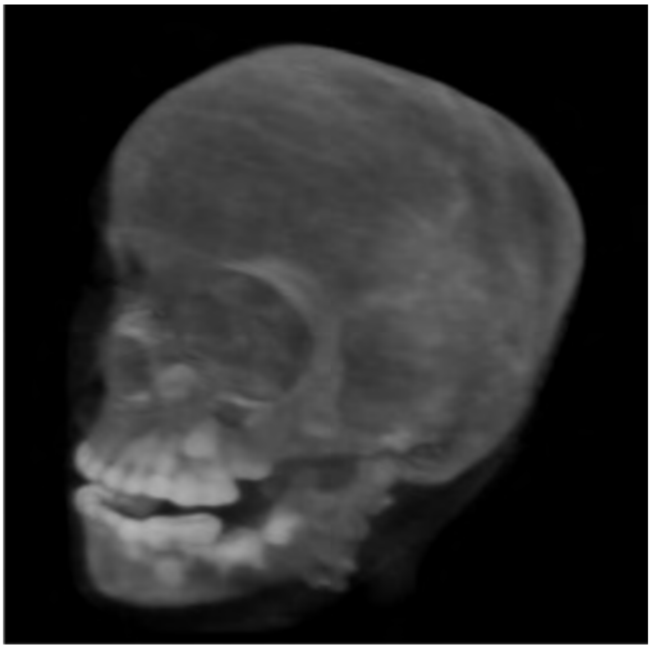

(B) 3D rendering of the reconstructed RSP map of a pediatric head phantom obtained with the phase-II scanner.

FIGURE 3.6 – Phase-II pCT scanner. Figures from Bashkirov et al. (2016a).

proton scattering power maps (Taylor et al., 2016b). In their final design, both the trackers and the range telescope are silicon-based (Esposito et al., 2018). The range telescope used is composed of 21 layers of SSDs interleaved with PMMA absorbers. This system was able to acquire fast pCT scans with 2×10^8 protons/s detectable over the full imaged area.

Other pCT scanners include a system developed and tested in Japan (Saraya et al., 2014), composed of SSDs trackers and a NaI(Tl) calorimeter; and a scanner built by a collaboration between NIU, Fermi National Accelerator Laboratory and Delhi University (Naimuddin et al., 2016). A collaboration between Haukeland University Hospital, the University of Bergen and the Western Norway University of Applied Sciences has been established in order to develop a fast pCT system using a digital tracking calorimeter (Pettersen et al., 2017; Pettersen, 2018; Pettersen et al., 2019). Tracking and energy measurement would be done by the same detector, consisting of multiple layers of monolithic active pixel sensor (MAPS) chips. Also, the innovative Medical Protons Achromatic Calorimeter and Tracker (iMPACT) project aims at building a high speed (100 MHz) scanner using only commercially available solutions for simplicity and cost reduction. A MAPS tracker and an achromatic calorimeter have been developed and successfully tested (Mattiazzo et al., 2018). Finally, ProtonVDA [1] aims at implementing clinical proton imaging systems. A proton radiography system has been developed (Miller et al., 2019) and a pCT platform is in development. First pCT images were presented at the PTCOG 58 conference.

3.5 Alternative proton CT modalities

Although most pCT efforts have been towards energy loss based imaging, some works have attempted to reconstruct pCT images using different information. Bopp et al. (2013, 2015) have studied the use of the angular deviation and the transmission rate of the protons to reconstruct images. They have shown that quantitative information can be extracted from such reconstructions, namely the macroscopic nuclear cross section by exploiting the transmission rate and the inverse scattering length by using the scattering angle. Results have shown such images can help differentiate tissues although reconstruction is challenged by the statistical uncertainty of these observables. Similarly, Quinones, Létang, and Rit (2016) used the transmission information to reconstruct a nuclear cross section map. Statistical noise was quantified, and it was shown to be 400 times higher for transmission based pCT compared with energy loss based pCT for 200 MeV protons. We have previously mentioned the work of Taylor et al. (2016a) who used the angular information from the trackers, without the energy measurement, to reconstruct a proton scattering power map, with the scattering power defined as the rate of change of the mean scattering angle squared per unit of length.

A few decades earlier, Saudinos et al. (1975) proposed to use nuclear scattering of high energy protons (500 MeV to 1 GeV) to reconstruct a 3D map of the object in one exposure, without movement of the beam or the object. The principle is to measure protons that have been scattered via nuclear interactions and to reconstruct the interaction point from the tracker information. This could give quantitative information about the relative concentration of hydrogen in tissues. Further studies on nuclear scattering radiography were conducted (Charpak et al., 1976; Duchazeaubeneix et al., 1980; Saudinos, 1987), but its development was hampered by the need for a high energy medical accelerator, the limited spatial resolution, and

---

[1] `protonvda.com`

the poor signal-to-noise ratio as nuclear events are relatively rare. Interaction vertex imaging (IVI), which is based on the same principle but for range monitoring purposes, has been more recently investigated within the framework of the Advanced QUality Assurance (AQUA)[2] project from the TERA foundation (Amaldi et al., 2010). It was studied for carbon beam therapy as nuclear reactions are more frequent for carbon ions (Henriquet et al., 2012; Finck et al., 2017).

3.6 Reconstruction in proton CT

In the previous sections, the major hardware developments for pCT have been described. This section will deal with the algorithms used to reconstruct pCT data, and how they differ from X-ray CT techniques. First, we present the different methods to estimate the proton path; and second, we explain how this information can be included in usual reconstruction algorithms.

3.6.1 Proton path estimation

3.6.1.1 Most likely path

In order to improve spatial resolution, the most likely path (MLP) of a proton, given complete or partial information about its entry and exit position and direction, can be derived using the Gaussian approximation of the MCS. Schneider and Pedroni (1994) were the first to attempt to model the proton trajectory for use in proton radiography. Later, an expression for the MLP was given by Williams (2004) using χ^2 statistics to simplify the calculation. Finally, Schulte et al. (2008) presented a more compact, matrix-based MLP formalism, and extended it to incomplete track information. A comprehensive study of the most likely path has been conducted by Erdelyi (2009). We will give an outline of Schulte's formalism.

The joint probability that a proton passes through $\mathbf{y}_1 = (u_1, \theta_1)$ and $\mathbf{y}_2 = (u_2, \theta_2)$ given the entrance parameter $\mathbf{y}_{\text{in}}$ (see Figure 3.7) is given by

$$L(\mathbf{y}_1, \mathbf{y}_2 | \mathbf{y}_{\text{in}}) = L(\mathbf{y}_1 | \mathbf{y}_{\text{in}}) L(\mathbf{y}_2 | \mathbf{y}_1), \tag{3.6}$$

where $L(\mathbf{y}_1 | \mathbf{y}_{\text{in}})$ is the probability that the proton passes through $\mathbf{y}_1$ given that it entered in $\mathbf{y}_{\text{in}}$ and $L(\mathbf{y}_2 | \mathbf{y}_1)$ is the probability that it exits with parameter $\mathbf{y}_2$ given that it has passed through $\mathbf{y}_1$. In the case when the proton exit information is measured, we fix $\mathbf{y}_2 = \mathbf{y}_{\text{out}}$. The probabilities in Equation 3.6 are modeled as Gaussian functions

$$L(\mathbf{y}_1 | \mathbf{y}_{\text{in}}) \propto \exp\left[-\frac{1}{2} (\mathbf{y}_1^T - \mathbf{y}_{\text{in}}^T \mathbf{R}_0) \Sigma_1^{-1} (\mathbf{y}_1 - \mathbf{R}_0 \mathbf{y}_{\text{in}}) \right] \tag{3.7}$$

and

$$L(\mathbf{y}_2 = \mathbf{y}_{\text{out}} | \mathbf{y}_1) \propto \exp\left[-\frac{1}{2} (\mathbf{y}_{\text{out}}^T - \mathbf{y}_1^T \mathbf{R}_1) \Sigma_2^{-1} (\mathbf{y}_{\text{out}} - \mathbf{R}_1 \mathbf{y}_1) \right], \tag{3.8}$$

with

$$\mathbf{R}_0 = \begin{pmatrix} 1 & w_1 - w_{\text{in}} \\ 0 & 1 \end{pmatrix}, \ \mathbf{R}_1 = \begin{pmatrix} 1 & w_{\text{out}} - w_1 \\ 0 & 1 \end{pmatrix} \tag{3.9}$$

and

$$\mathbf{\Sigma}_1 = \begin{pmatrix} \sigma_{u_1}^2 & \sigma_{u_1\theta_1}^2 \\ \sigma_{u_1\theta_1}^2 & \sigma_{\theta_1}^2 \end{pmatrix}, \ \mathbf{\Sigma}_2 = \begin{pmatrix} \sigma_{u_2}^2 & \sigma_{u_2\theta_2}^2 \\ \sigma_{u_2\theta_2}^2 & \sigma_{\theta_2}^2 \end{pmatrix}. \tag{3.10}$$

---

[2] `http://project-aqua.web.cern.ch/`

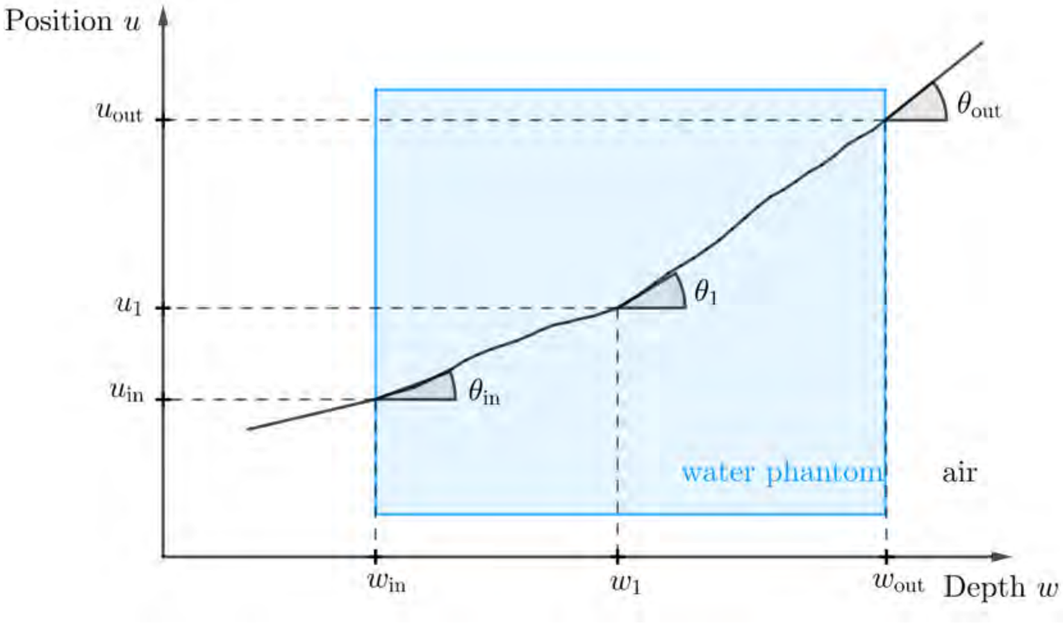

FIGURE 3.7 – Geometry of the proton trajectory used in the MLP formalism.

The angular and spatial scattering variances and covariances can be modeled as (Lynch and Dahl, 1991)

$$\sigma^2_{u_1} = E_0^2\left(1 + 0.038 \ln \frac{w_1 - w_{\text{in}}}{X_0}\right)^2 \int_{w_{\text{in}}}^{w_1} \frac{(w_1 - w)^2}{p^2(w)v^2(w)} \frac{\mathrm{d}w}{X_0} \tag{3.11}$$

$$\sigma^2_{\theta_1} = E_0^2\left(1 + 0.038 \ln \frac{w_1 - w_{\text{in}}}{X_0}\right)^2 \int_{w_{\text{in}}}^{w_1} \frac{1}{p^2(w)v^2(w)} \frac{\mathrm{d}w}{X_0} \tag{3.12}$$

$$\sigma^2_{u_1\theta_1} = E_0^2\left(1 + 0.038 \ln \frac{w_1 - w_{\text{in}}}{X_0}\right)^2 \int_{w_{\text{in}}}^{w_1} \frac{w_1 - w}{p^2(w)v^2(w)} \frac{\mathrm{d}w}{X_0} \tag{3.13}$$

Note that the variance for the scattering angle had already been given in section 1.2.2 (see Equation 1.15). The values for the elements of $\mathbf{\Sigma}_2$ are obtained by replacing w_1 by w_{out} and w_{in} by w_1 in Equations 3.11–3.13. Maximizing Equation 3.6 with respect to $\mathbf{y}_1$ gives the following formulation for the MLP

$$\mathbf{y}_{\text{MLP}}(w_1) = (\mathbf{\Sigma}_1^{-1} + \mathbf{R}_1^T\mathbf{\Sigma}_2^{-1}\mathbf{R}_1)^{-1}(\mathbf{\Sigma}_1^{-1}\mathbf{R}_0\mathbf{y}_{\text{in}} + \mathbf{R}_1^T\mathbf{\Sigma}_2^{-1}\mathbf{y}_{\text{out}}), \tag{3.14}$$

and the corresponding uncertainty matrix

$$\mathbf{\Sigma}_{\text{MLP}}(w_1) = (\mathbf{\Sigma}_1^{-1} + \mathbf{R}_1^T\mathbf{\Sigma}_2^{-1}\mathbf{R}_1)^{-1}, \tag{3.15}$$

where the component in the first row and first column gives the uncertainty on the spatial information. Figure 3.9 shows examples of MLPs and their uncertainty envelopes computed in water using the above equations.

To save computation time, the term $1/p^2v^2$ is approximated by the following polynomial

$$\frac{1}{p^2(w)v^2(w)} = \frac{(E(w) + E_p)^2}{(E(w) + 2E_p)^2E(w)^2} \approx \sum_{i=0}^{N} a_i w^i \tag{3.16}$$

where $E_p = 938$ MeV is the proton rest energy, so that the integrals can be calculated

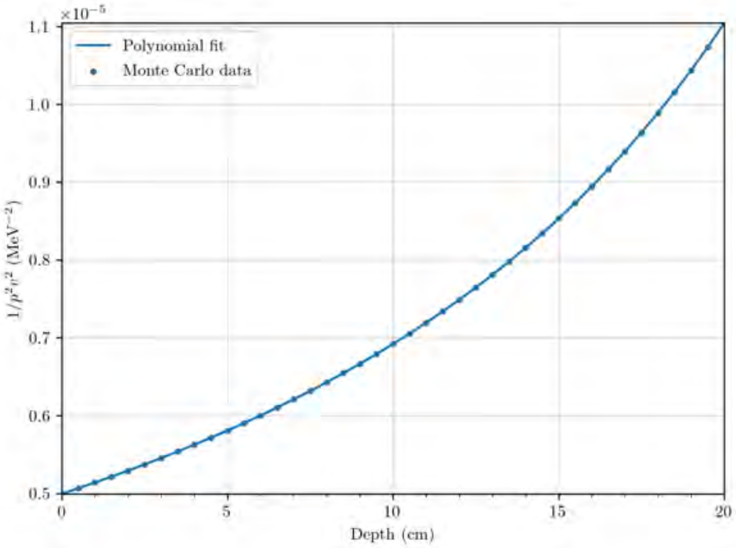

FIGURE 3.8 – Polynomial fit to the energy ratio of protons with an initial energy of 200 MeV in water.

analytically. The a_i coefficients can be estimated by fitting a polynomial (of 5th order as in Schulte et al., 2008) to the energy ratio acquired from a Monte Carlo simulation (Figure 3.8).

In order to comply with the Gaussian approximation of the scattering, large scattering angle events leading to non Gaussian tails must be filtered out. For this purpose, 3σ cuts on the exit angle are performed to exclude nuclear interactions and large angle MCS. In addition, 3σ cuts on the exit energy to filter out non-elastic nuclear interactions allow to improve density resolution. The cuts allow to filter out all protons with large angle and/or energy, lying more than $\pm 3\sigma$ from the mean, with σ the standard deviation of the angle/energy of the exit protons (Schulte et al., 2008). Using these cuts, 1.87% of proton tracks fall outside of the MLP uncertainty envelope, which is close to the expected value of 1% if the distribution was perfectly Gaussian.

3.6.1.2 Other path estimates

While the MLP formalism gives the best estimation of the proton trajectory, it is computationally expensive compared with other simpler methods. The simplest path estimate is the straight line path (SLP) connecting the entrance position to the exit position. It was used by Cirrone et al. (2011) in combination with entry and exit position filtering in order to keep only protons having a quasi-linear path.

Alternatively, a cubic spline path (CSP), defined as

$$\begin{aligned}\mathbf{y}_{\mathrm{CSP}}(w_1) = (2w_1^3 - 3w_1^2 + 1)\mathbf{y}_{\mathrm{in}} + (w_1^3 - 2w_1^2 + w_1)\dot{\mathbf{y}}_{\mathrm{in}} \\ -(2w_1^3 - 3w_1^2)\mathbf{y}_{\mathrm{out}} + (w_1^3 - w_1^2)\dot{\mathbf{y}}_{\mathrm{out}},\end{aligned} \tag{3.17}$$

with $\dot{\mathbf{y}}_{\mathrm{in}}$ and $\dot{\mathbf{y}}_{\mathrm{out}}$ the entrance and exit directions, can be a good alternative. The CSP is less computationally expensive than the MLP and offers a good approximation (RMS difference of less than 10% between the CSP and the MLP according to Li et al. (2006)). Collins-Fekete et al. (2015) proposed to include the energy loss information in the CSP formalism, via a vector magnitude factor, to improve the spatial resolution.

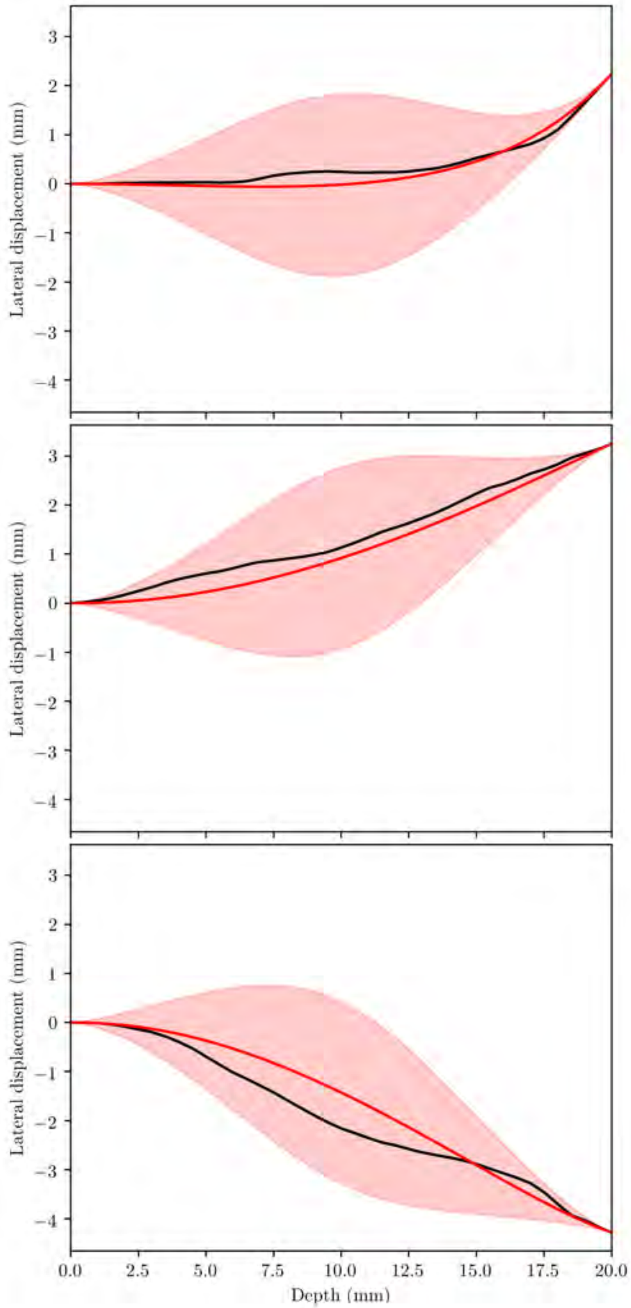

FIGURE 3.9 – Examples of Monte Carlo generated proton trajectories in water (black lines) with estimated MLPs and 3σ uncertainty envelopes (red lines and envelopes).

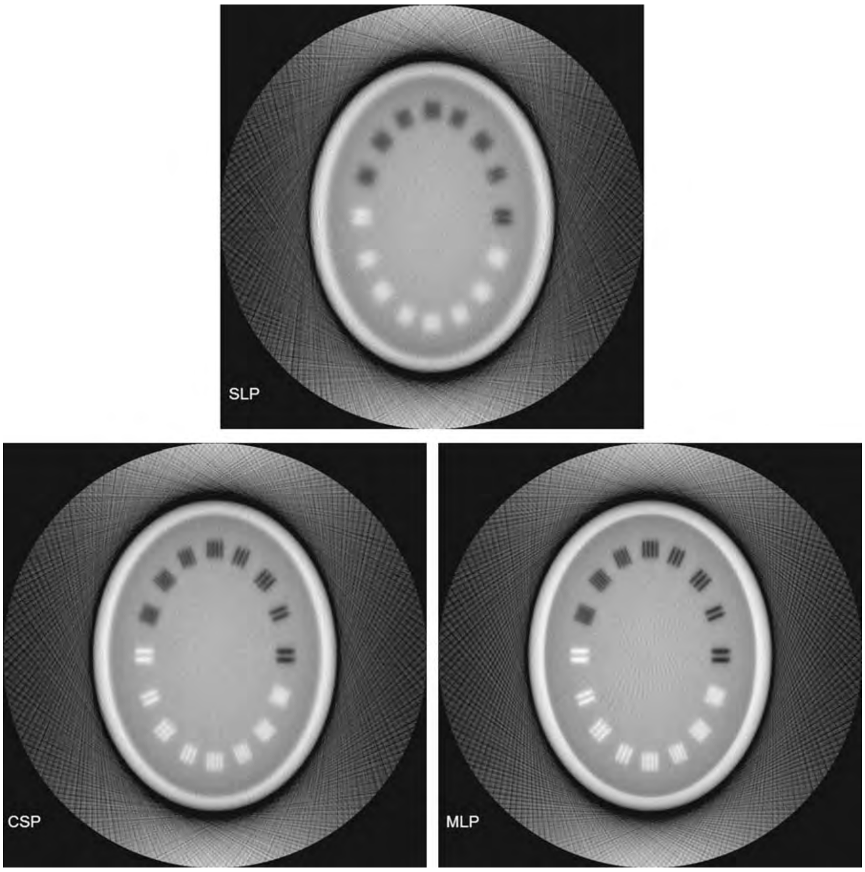

FIGURE 3.10 – Reconstruction with ART algorithm using different path estimates. Figure from Li et al. (2006).

Li et al. (2006) compared the three formalisms in terms of spatial resolution, RMS error and speed, using an ART reconstruction algorithm. The resulting reconstructions using either the SLP, CSP or MLP formalism are shown in Figure 3.10. It was demonstrated that using either a CSP or MLP estimate led to an improvement of the spatial resolution from 2 lp/cm when using the SLP to 5 lp/cm. Additionally, the MLP has the smallest RMS error and the fastest convergence in terms of number of iterations.

Recently, Krah, Létang, and Rit (2019) have shown that, when the energy loss is approximated as a polynomial (as in Equation 3.16), the MLP itself is a polynomial; and that a linear or at most quadric function for the energy loss is sufficient. Furthermore, a mathematically equivalent but slightly more computationally efficient expression for the MLP was given.

3.6.2 Reconstruction algorithms

The problem of reconstructing a 2D function from its projections is well known and has been extensively studied based on the early work of Radon (1917). The acquired data in X-ray CT are integrals of a function $f(x, y)$ over straight lines at different angles. For a mono-energetic X-ray beam, these projections are defined as

$$p_\phi(r) = \int_{\mathcal{L}(\phi,r)} f(x,y)\,\mathrm{d}l, \tag{3.18}$$

with $\mathcal{L}(\phi, r)$ the line parametrized by ϕ, the angle from the y-axis, and r, the distance from the origin; and $\mathrm{d}l$ a small displacement along the line. The complete collection of these integrals is called the Radon transform of $f(x, y)$. The problem of recovering a function from its line integrals can be solved analytically, with the filtered backprojection (FBP) algorithm being the most popular solution as it is fast and efficient (Kak and Slaney, 1988).

Alternatively, iterative methods, although more computationally demanding, offer serious advantages like the reduction of noise and artifacts, and thus are becoming popular to produce low dose CT images. The reconstruction problem is treated as a linear system of equations

$$p_i = \sum_{j=1}^{N} w_{ij} f_j, \quad i = 1...M \tag{3.19}$$

with p_i the integral along the i-th projection ray, f_j the value of f in the j-th pixel or voxel, and w_{ij} the contribution of the j-th pixel/voxel to the i-th ray. This problem cannot be solved by a simple matrix inversion as M and N are very large and the acquired data is subject to noise. Therefore, different kinds of algorithms have been developed to find the values of f, the simplest being the ART (Algebraic Reconstruction Technique) algorithm (Gordon, Bender, and Herman, 1970).

Presumably, iterative methods seem more fit to solve the pCT reconstruction problem. Analytical reconstruction assumes straight line paths, and there is no mathematical solution to the inversion of curved trajectories, with some exceptions such as circles. Therefore, the proton's MLP could not be easily included in a method like the FBP. On the other hand, it is straightforward to redefine Equation 3.19 to solve a list-mode proton CT problem: p_i would be the WEPL of proton i, w_{ij} the length of intersection of the MLP of proton i with pixel j, and f_j the RSP in pixel j.

Different methods have been tested to iteratively reconstruct pCT images, such as the classical ART (Li et al., 2006) or ART including MLP uncertainty via the w_{ij} coefficients (Wang, Mackie, and Tomé, 2010). Other iterative methods have been compared with ART in terms of image quality and speed of convergence (Penfold et al., 2010a; Penfold, 2010). One of these algorithms, called diagonally relaxed orthogonal projections (DROP) was shown to improve convergence rate at the expense of increased image noise. It was therefore combined with a total variation superiorization (TVS) scheme (Penfold et al., 2010b). The addition of TVS resulted in improved spatial and density resolutions. A different type of iterative methods are statistical reconstruction methods. The objective is to reconstruct the image that best fits the data given a statistical model of the noise. Such a method was applied to proton CT (Hansen et al., 2014b; Hansen, Sørensen, and Rit, 2016) by including a model for the energy straggling of protons.

Others have attempted to use analytical methods for pCT reconstruction. For example, FBP can be combined with filtering of protons according to their entry and exit positions or according to their whole MLP trajectory, to keep only particles that have quasi-linear trajectories (Cirrone et al., 2011; Vanzi et al., 2013). This yields images with insufficient spatial resolution and is detrimental in terms of dose and scan time (22% of events were accepted when using a 1 mm acceptance interval and only 1% with a 200 µm interval). Alternatively, the FBP method has been heuristically adapted to work with curved trajectories (Rit et al., 2013) by performing a distance-driven binning in the direction of the proton beam, yielding high resolution images. Also, backproject first approaches, where the order of the filtering and the backprojection are reversed, have been successfully used to account for the proton's MLP (Poludniowski, Allinson, and Evans, 2014; Rit et al., 2015). Finally, a method reconstructing pCT images from optimized proton radiographs was proposed by Collins-Fekete et al. (2016).

A comparison between several algorithms (distance-driven FBP, TVS-DROP and two statistical methods) has been performed by Hansen, Sørensen, and Rit (2016). Their results have shown that the analytical method yields a comparable resolution and image quality to the three tested iterative methods at low dose levels, while being an order of magnitude faster.

3.7 Conclusion

A broad review of proton imaging has been presented in this chapter. From the 1960s until today, proton imaging has evolved in terms of detection technology and reconstruction methods. Several state-of-the-art prototypes have been constructed worldwide using different tracking and energy measurement technologies. In order to become clinically viable, further efforts are underway to make pCT imaging faster and cheaper. Image quality, and particularly spatial resolution, has been improved by using list-mode set-ups and including the MLP formalism in reconstruction algorithms. In the next part, several contributions to list-mode pCT reconstruction will be presented, starting with a study on the accuracy of the MLP formalism.

Part II

Contributions

Chapter 4

Proton path in heteregeneous media

In the previous chapter, the MLP formalism used to estimate the proton path during reconstruction was presented. Several approximations regarding the scattering distribution have been made to derive the MLP expression. In this chapter, we estimate the accuracy of the MLP formalism when the homogeneity assumption is not satisfied. We start by introducing the approximations of the MLP model before presenting our experiments and results. This chapter is adapted from Khellaf et al. (2019).

4.1 Introduction

4.1.1 Assumptions in the MLP model

The MLP formalism assumes a homogeneous material which is approximative for several reasons. First, the radiation length of the traversed materials X_0 is needed to compute the scattering matrices (Equations 3.11–3.13). As the composition of the object to be reconstructed is unknown, we assign a constant value of $X_0 = 36.1$ cm, corresponding to the radiation length of water, as it is a reasonable approximation for soft tissues. However, there is a considerable variability between body tissues, e.g. $X_0 = 14$ cm for cortical bone or $X_0 = 95$ cm for lung tissue (Table 4.1). Using a constant value will therefore inevitably over- or under-estimate scattering in certain regions. Furthermore, the ratio $1/p^2v^2$ must be estimated to take into account the energy dependence of the scattering. It is approximated using the energy loss a proton would undergo in a homogeneous water phantom (Figure 3.8). Given that energy loss depends on the traversed material, this will also introduce inaccuracies in the scattering estimation.

Additionally, heterogeneous configurations also challenge the Gaussian approximation of MCS used to model the scattering angle and position distributions. Even in a homogeneous case, large-angle MCS events and nuclear interactions (elastic and non-elastic) both induce non-Gaussian tails in the scattering distributions. The effect of such events is usually mitigated by applying angle and energy cuts which allow to exclude most protons that have experienced these interactions (Schulte et al., 2008). The Gaussian approximation is therefore valid with appropriate cuts for homogeneous objects. In fact, it is valid as long as tissue properties change only as a function of depth (panel A or B in Figure 4.2), but not along a direction perpendicular to the beam axis. In the case of a transverse heterogeneity (panel C in Figure 4.2), the distribution is expected to be asymmetric as the scattering would differ depending on the lateral coordinate. Such transverse heterogeneities, if they are large enough, could cause systematic errors in the proton path estimate as the MLP assumes a symmetric distribution. Contrary to the approximation made on the values for X_0 or the ratio

Tissue	Raditation length X_0 (cm)	Relative stopping power
Muscle tissue	35.06	1.054
Blood	34.50	1.063
Cortical bone	14.29	1.731
Cartilage	32.49	1.093
Brain	35.06	1.060
Adipose tissue	43.31	0.974
Breast mammary gland	39.22	1.044
Stomach/intestine	35.36	1.047
Heart	35.08	1.056
Kidneys	34.96	1.055
Liver	34.96	1.053
Lung tissue (compressed lungs)	94.94	0.387
Lymph	35.15	1.039
Oesophagus	36.41	1.038
Pancreas	35.28	1.058
Skin	34.27	1.093
Teeth	9.03	2.404
Thyroid	35.25	1.046
Urinary bladder	35.07	1.047

TABLE 4.1 – Radiation length and relative stopping power for some tissues in the ICRP phantom, obtained with Geant4.

$1/p^2v^2$, a spatial asymmetry of the MCS could not be corrected simply by introducing information about the tissues' density and composition in the current Gaussian formalism. A reformulation of the MLP formalism would rather be needed. This effect was mentioned by Williams (2004) who predicted its impact would be small, except for "large objects that have a small dimension perpendicular to the beam (for example, a proton trajectory grazing the surface of a bone plate)".

4.1.2 Previous work

Early observations of unbalanced scattering were reported by West and Sherwood (1972, 1973) who noticed fringes in the intensity distribution when the proton beam would traverse interfaces normal to its direction. This was called the "West-Sherwood effect" by Cormack and Koehler (1976). This effect was exploited in early fluence-based proton CT and radiography to improve density resolution (Figure 3.2). However, in energy-based proton CT, it is rather a cause of deterioration of image quality. In the system described by Tanaka et al. (2016, 2018), the West-Sherwood effect at the edges causes an underestimation of all pixel values inside the object. Zhang et al. (2017a) observed the effects of transverse heterogeneities in the form of range-mixing, i.e. a combination of different dose rate functions around an interface, causing a loss of spatial resolution. These observations were made in the context of proton radiography or tomography using different kinds of set-ups. We will specifically explore the effects of unbalanced scattering in single tracking set-ups.

Studies have been conducted to assess the impact or even correct heterogeneities in the MLP framework, although only longitudinal heterogeneities (tissue variations as a function of depth) have been considered until now. Wong et al. (2009) have studied the impact of longitudinal heterogeneities on the MLP. Their results showed no significant systematic error caused by longitudinal heterogeneities, i.e. the MLP estimate was still correct. However, the RMS error was 20% higher since bone slabs were added in the hetergeneous phantom which would increase the scattering. More recently, Collins-Fekete et al. (2017a) have extended the MLP formalism by including prior knowledge on the medium composition and density. The proposed method is based on an MLP formalism that models MCS for longitudinal heterogeneities, but does not take into account transverse ones. Their results showed that the heterogeneous formalism did not reduce the RMS error inside the object compared with the conventional MLP formalism.

4.1.3 Preliminary observations

We observed the effect of unbalanced scattering around transverse heterogeneities experimentally: proton beam profiles acquired with a pair of strip detectors (Krah et al., 2018c) at the Curie Institute - Proton Therapy Center in Orsay (France) showed non Gaussian distributions when the protons traversed interfaces (e.g. water/bone or water/lung) of the CIRS electron density phantom. The skewness (i.e. the asymmetry) of these profiles, defined as

$$\text{skewness} = \frac{\text{mean} - \text{mode}}{\text{standard deviation}} \tag{4.1}$$

is shown in Figure 4.1. Two maps, corresponding to the horizontal and vertical strip detectors are represented, where each pixel corresponds to the skewness of a fluence profile. The edges of the inserts of bone and lung in the water phantom are associated with either high positive or negative skewness values, corresponding to right or left non-Gaussian tails. This depends on the "order" of the interface, e.g. water/bone or bone/water. It is not the purpose of this work to quantitatively analyse the measured beam profiles. They serve as illustrative evidence of the effect of material heterogeneities on MCS.

In the following work, we investigate the effects of tissue heterogeneities, and particularly transverse heterogeneities, on the proton path prediction. For this purpose, we have used Monte Carlo simulated proton tracks to determine a reference MLP against which the conventional MLP formalism of Schulte et al. (2008) was evaluated. Specifically, we study the kind and degree of deflection caused by transverse heterogeneities and its impact on the MLP and on the energy spectra of the protons.

4.2 Materials and methods

4.2.1 Theoretical MLP

In what follows, the term “theoretical MLP” refers to the approximate MLP calculated with the formalism of Schulte et al. (2008) and “real MLP” means the MLP derived from the Monte Carlo (MC) results. We remind the formula to compute the theoretical MLP

$$\mathbf{y}_{\text{MLP,theo}}(w_1) = (\mathbf{\Sigma}_1^{-1} + \mathbf{R}_1^T \mathbf{\Sigma}_2^{-1} \mathbf{R}_1)^{-1} (\mathbf{\Sigma}_1^{-1} \mathbf{R}_0 \mathbf{y}_0 + \mathbf{R}_1^T \mathbf{\Sigma}_2^{-1} \mathbf{y}_2), \tag{4.2}$$

and its uncertainty matrix

$$\mathbf{\Sigma}_{\text{MLP}}(w_1) = (\mathbf{\Sigma}_1^{-1} + \mathbf{R}_1^T \mathbf{\Sigma}_2^{-1} \mathbf{R}_1)^{-1}, \tag{4.3}$$

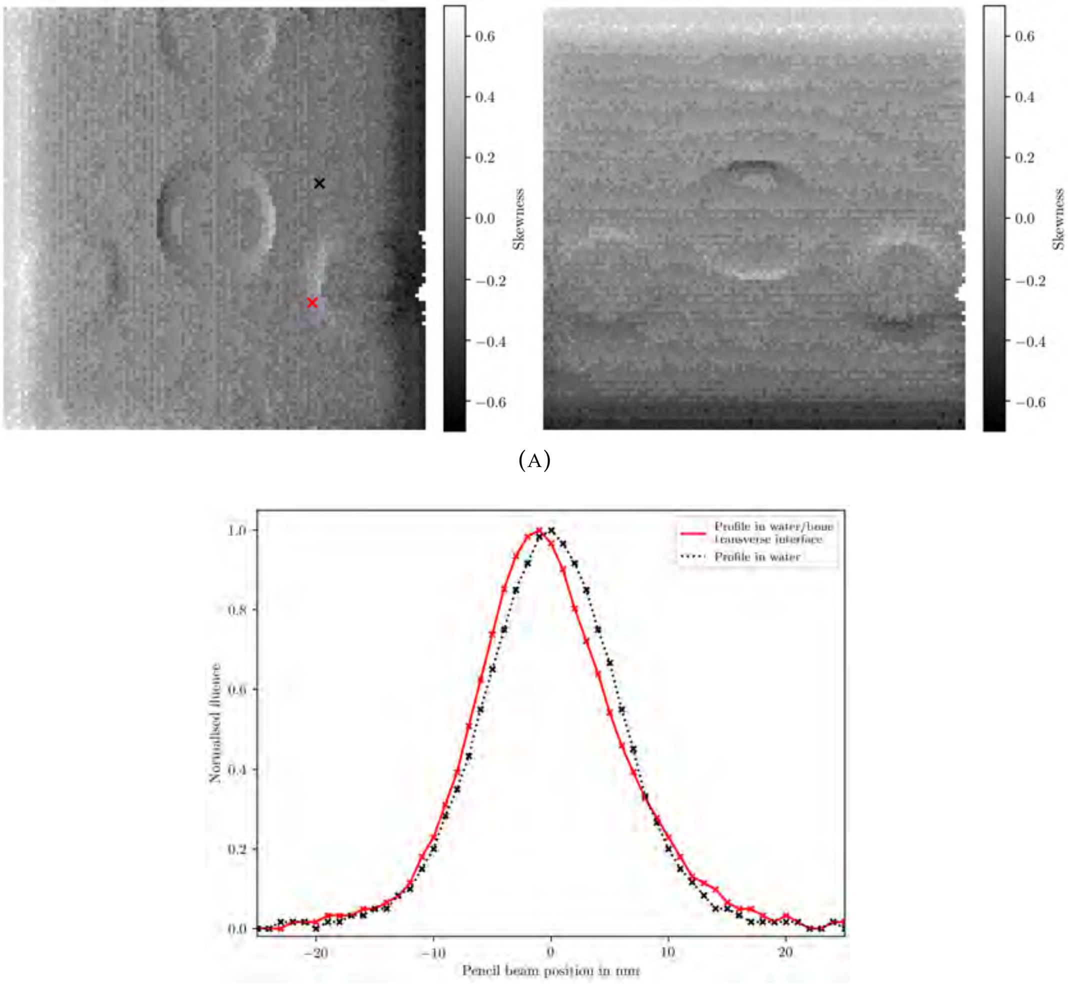

(A)

(B)

FIGURE 4.1 – (A) 2D maps of the skewness of each beam profile in a CIRS phantom with inserts and (B) fluence profiles measured in a homogeneous region and near a water/bone interface. The crosses indicate the pencil beam positions for which the profiles are shown.

both given in the previous chapter. As mentioned in the introduction, the scattering is calculated using the radiation length X_0 of water and a momentum-velocity ratio $1/p^2v^2$ estimated in water.

A theoretical MLP taking into account a depth dependent heterogeneity was also calculated using the same formula but replacing the position/angle scattering variances by

$$\sigma^2_{u_1}(w_1) = E_0^2\Big(1 + 0.038\ln\Big(\int_{w_{\text{in}}}^{w_1}\frac{dw}{X_0(w)}\Big)\Big)^2\int_{w_{\text{in}}}^{w_1}\frac{(w_1-w)^2}{p^2(w)v^2(w)}\frac{dw}{X_0(w)}, \tag{4.4}$$

$$\sigma^2_{\theta_1}(w_1) = E_0^2\Big(1 + 0.038\ln\Big(\int_{w_{\text{in}}}^{w_1}\frac{dw}{X_0(w)}\Big)\Big)^2\int_{w_{\text{in}}}^{w_1}\frac{1}{p^2(w)v^2(w)}\frac{dw}{X_0(w)}, \tag{4.5}$$

$$\sigma^2_{w_1\theta_1}(w_1) = E_0^2\Big(1 + 0.038\ln\Big(\int_{w_{\text{in}}}^{w_1}\frac{dw}{X_0(w)}\Big)\Big)^2\int_{w_{\text{in}}}^{w_1}\frac{w_1-w}{p^2(w)v^2(w)}\frac{dw}{X_0(w)}, \tag{4.6}$$

where an integral of the radiation lengths of the traversed tissues along the depth is used instead of the constant X_0 value for water. The matrices were computed using ground truth knowledge of the radiation length; and the momentum-velocity ratio was estimated from Monte Carlo simulations in the known geometry of the heterogeneous phantom. Unlike Collins-Fekete et al. (2017a), we used $E_0 = 13.6$ MeV instead of 14.1 and the constant 0.038 instead of 1/9 as recommended in Schulte et al. (2008). This was done for a more homogeneous comparison with Schulte's formalism.

4.2.2 Real MLP

4.2.2.1 Monte Carlo simulations

We have used GATE v8.0 (Jan et al., 2011) to simulate proton paths in different phantoms:

- a homogeneous water phantom (A),
- a heterogeneous phantom with a longitudinal bone/water interface (B),
- a heterogeneous phantom with a transverse bone/water interface (C),
- an International Commission on Radiological Protection (ICRP) head phantom (ICRP, 2009) with $1.775 \times 1.775 \times 4.84$ mm^3 voxels.

The first three phantoms, shown in Figure 4.2, were used to study the effects of heterogeneities in simple conditions. Although these phantoms exaggerate heterogeneities compared with interfaces found in the human body, they were used to quantify the maximum MLP error. The anthropomorphic head phantom was used to quantify the MLP in realistic conditions. We identified the regions with the largest and longest heterogeneities by computing the projections of the derivative of the $1/X_0$ map of the ICRP phantom. We selected two transverse regions : a 3.4 cm long interface between air ($X_0 = 6.3 \times 10^{11}$ cm) and the top of the head ($X_0 = 43.4$ cm), and a 7.7 cm long interface between the teeth ($X_0 = 9.0$ cm) and the mandible ($X_0 = 29.4$ cm). For the first heterogeneity, the beam was positioned at $u = 803.4$ mm and for the second one it was at $u = 634.0$ mm (see Figure 4.6).

A 250 MeV monoenergetic proton source was simulated to traverse these phantoms as some heterogeneities included large regions of tissues with a high stopping power. A non-divergent beam geometry was used to keep the protons tangent to the transverse interface. For the three phantoms in Figure 4.2, an infinitely narrow point source was used at different entry positions (see section 4.2.2.2). For the ICRP phantom, we simulated a uniform rectangular 4×4 mm proton source. We have simulated 10^7 protons for each tested path and for each particle the trajectory was tracked inside the phantom. In addition, two ideal position and direction detectors were positioned 40 cm upstream and downstream from the isocenter. The protons' kinetic energy was also recorded since an asymmetry in the spatial and angular distributions would also affect the energy distribution. Results using the *emstandard* physics list – used to simulate electromagnetic processes only – and the *QGSP_BIC* physics list – used to simulate all interaction processes – were compared.

4.2.2.2 Data post-processing

To compute the real MLP of protons going through each phantom, we first selected the trajectories of a subset of protons whose entry and exit coordinates, $\mathbf{y}_0$ and $\mathbf{y}_2$, lay within a small interval around chosen values, (u_0, θ_0) and (u_2, θ_2). Specifically, we filtered out protons whose angle and position would be experimentally indistinguishable by using windows of size 200 µm for the position and 3.4 mrad

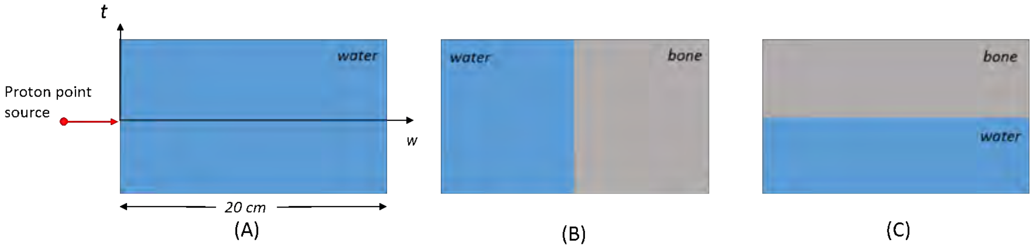

FIGURE 4.2 – Phantoms used in the simulations. The blue material is water and the grey one is bone.

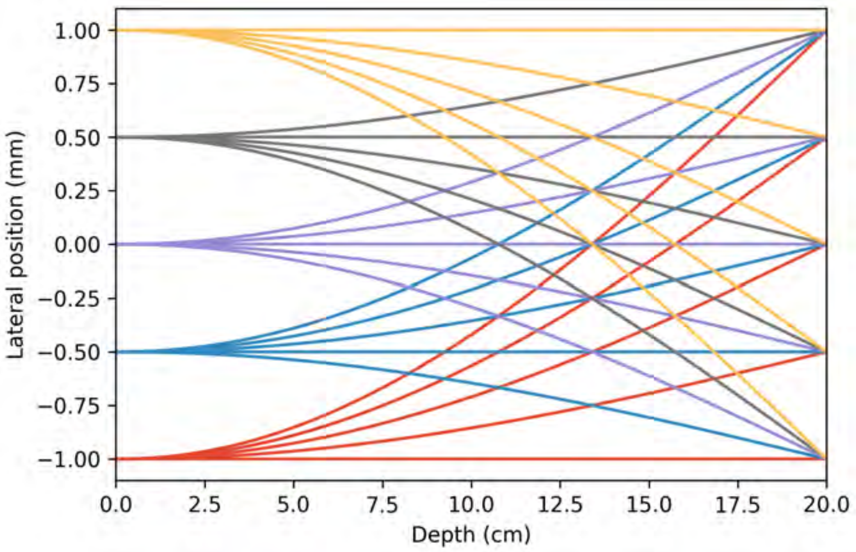

FIGURE 4.3 – Theoretical MLPs for all tested entry and exit coordinates. Different colors were used depending on the entry position for a clear visualization. The exit angles θ_2 are equal to 0, ±4, ±8, ±12, and ±16 mrad for lateral deviations Δu equal to 0, ±0.5, ±1.0, ±1.5, and ±2.0 mm, respectively. The axes' scales are different for a better visualization.

for the angle. These thresholds reflect the typical spatial and angular resolution of detectors used in pCT (Bopp et al., 2014). Since the proton sources were simulated without initial angular deviation, the entry angle θ_0 was not filtered. In addition, for the three test phantoms (A), (B) and (C), there was no need to filter the entrance position as we used a point source.

We have tested several combinations of entry and exit coordinates to find the maximum bias created by heterogeneities. Different values for u_0 were used in the simulation, while θ_0 was set to zero, and the values for u_2 and θ_2 were filtered. For θ_2, we took the most probable angle corresponding to each u_2 calculated in the case of a homogeneous phantom in order to keep paths with enough protons. The theoretical MLPs for the tested entry and exit coordinates are shown in Figure 4.3. For each case, we compared the theoretical MLP to the real MLP.

To estimate the real MLP, we have built a histogram of the transverse positions at different intermediate depths in the phantom and fitted a two-term Gaussian distribution to it:

$$f(u) = \frac{A_1}{\sigma_1\sqrt{2\pi}} e^{-\frac{(u-\mu_1)^2}{2\sigma_1^2}} + \frac{A_2}{\sigma_2\sqrt{2\pi}} e^{-\frac{(u-\mu_2)^2}{2\sigma_2^2}}, \tag{4.7}$$

as directly using the histogram data would have given a noisy result. We found that a two-term Gaussian was more suitable than a simple Gaussian since the distribution could be asymmetric in the case of transverse heterogeneities. The distributions were smoothed using a Gaussian filter of $\sigma = 3 \times 10^{-2}$ mm before fitting, as the two-term Gaussian could be sensitive to noise, especially in the cases where the distribution was very nearly Gaussian. We determined the real MLP at a given depth as the mode of the fitted distribution, that is the position of the maximum. We compared this real MLP to the theoretical MLP computed with Equation 4.2, and the real MLP's uncertainty envelope to the theoretical uncertainty given by Equation 4.3. The maximum absolute bias defined as

$$\max_{w} \quad |u_{\text{MLP,real}}(w) - u_{\text{MLP,theo}}(w)| \tag{4.8}$$

was used to characterize the accuracy of the theoretical MLP formalism. We estimated the uncertainty envelope of the real MLP using the 16th and 84th percentiles of the fitted distribution. When the distribution is symmetric, this is equivalent to one standard deviation from the mean. Otherwise, we obtain an asymmetric envelope which reflects the skewness of the distribution.

4.3 Results

4.3.1 Unfiltered spatial, angular and energy distributions

The two upper plots of Figure 4.4 represent the exit spatial and angular distributions of protons 20 cm downstream of the three phantoms (A), (B) and (C) without any filtering. Both distributions are Gaussian for phantoms (A) and (B), although the peak is more spread out for the heterogeneous phantom as the scattering power of bone is larger. The position and angle distributions for phantom (C) are not symmetric, with peak positions at $u = -3.8$ mm and $\theta = -12.5$ mrad, respectively, meaning the protons are scattered primarily towards the less dense material, i.e. water. The results including nuclear interactions are close to the profiles with electromagnetic (EM) interactions only. The difference lies in the presence of tails towards large angles, but the position of the maximum, i.e. the most probable position/angle, is the same.

Regarding the energy distributions, their shape is similar for phantoms (A) and (B), except that protons have traversed bone in case of phantom (B) and have consequently lost more energy. The peak energy is 163 MeV for phantom (A) and 121 MeV for phantom (B). As for phantom (C), the distribution shows two peaks at 161 MeV and 66 MeV, corresponding to protons that traversed mostly water and bone, respectively. The amplitude of the high energy peak is three times greater than that of the low energy peak, thus confirming more protons have passed through the water region. In addition, the plateau region between the two peaks shows that a lot of protons have an intermediate energy after having traversed both materials.

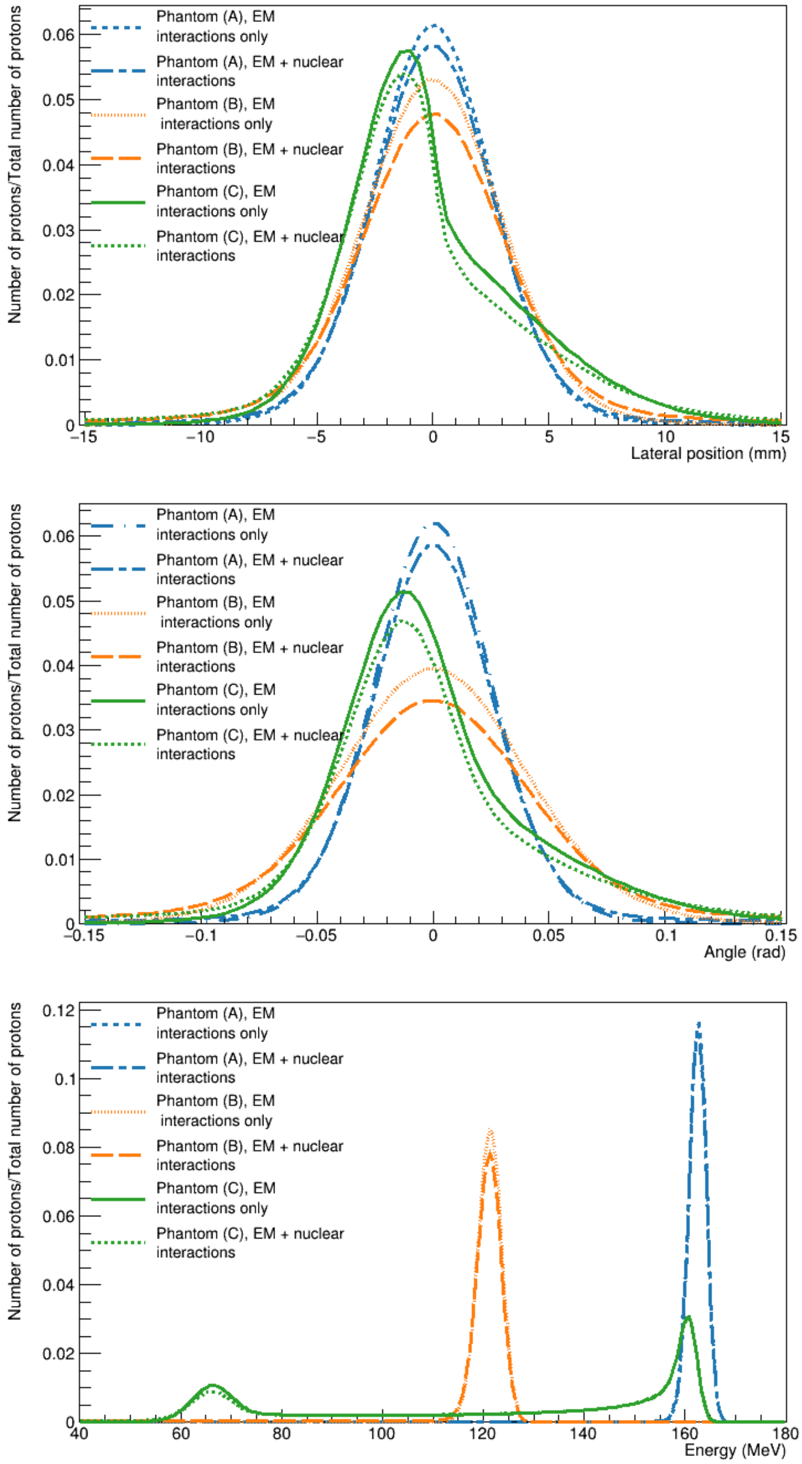

FIGURE 4.4 – Exit spatial (top), angular (middle) and energy (bottom) distributions of unfiltered protons (bottom) with initial position $t_0 = 0$ mm.

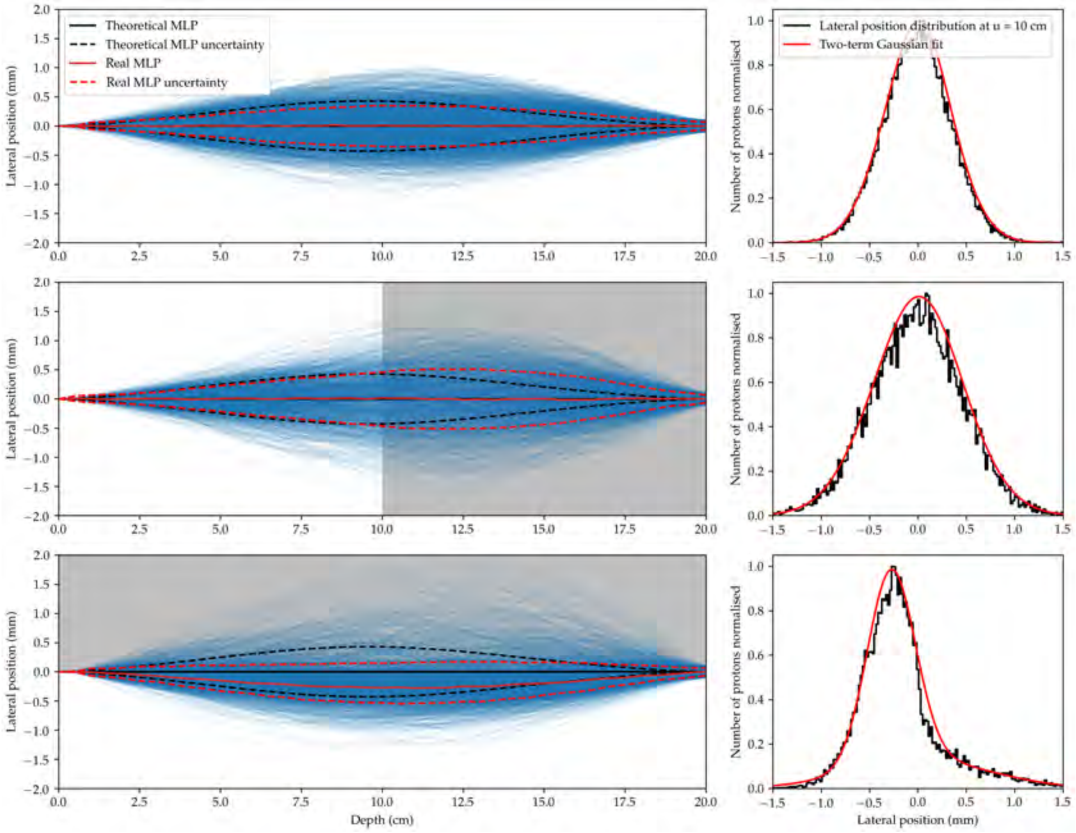

FIGURE 4.5 – Trajectories of filtered protons (left) going through phantoms A (top), B (middle) and C (bottom) and an example fit used to compute the real MLP (right). The shaded grey areas correspond to bone.

4.3.2 Real MLP estimation

Figure 4.5 shows proton trajectories in the three different phantoms in the case of a theoretical straight line path ($\mathbf{y}_0 = \mathbf{y}_2 = (0,0)$) and an example of the two-term Gaussian fit used to compute the real MLP. The real MLP computed from the most probable position at each depth does not differ from the theoretical MLP for phantoms (A) and (B). The uncertainty envelopes are also close to the theory, except that the envelope is wider in the bone region for phantom (B). For the transverse heterogeneity, the real MLP is deflected towards the water part of the phantom. In this case, the deviation reaches about -0.28 mm, but is still of the same magnitude as the uncertainty envelope. The uncertainty envelope of the real MLP is asymmetric with the larger side of the envelope situated towards the bone part of the phantom.

Regarding the distributions used to compute the real MLP, they are symmetric for phantoms (A) and (B) and skewed for phantom (C). Although the two-term Gaussian is not a perfect fit to the skewed distribution, it worked well enough to locate the most probable position. Also, we note the data could be quite noisy due to the filtering of the trajectories. Indeed, the cuts on the exit coordinates filter out more than 99% of protons. The number of filtered protons is lower in case of heterogeneous phantoms as materials with a higher density — in our case, bone — scatter protons with larger angles.

Figure 4.6 shows the Monte Carlo simulated trajectories of protons along the two

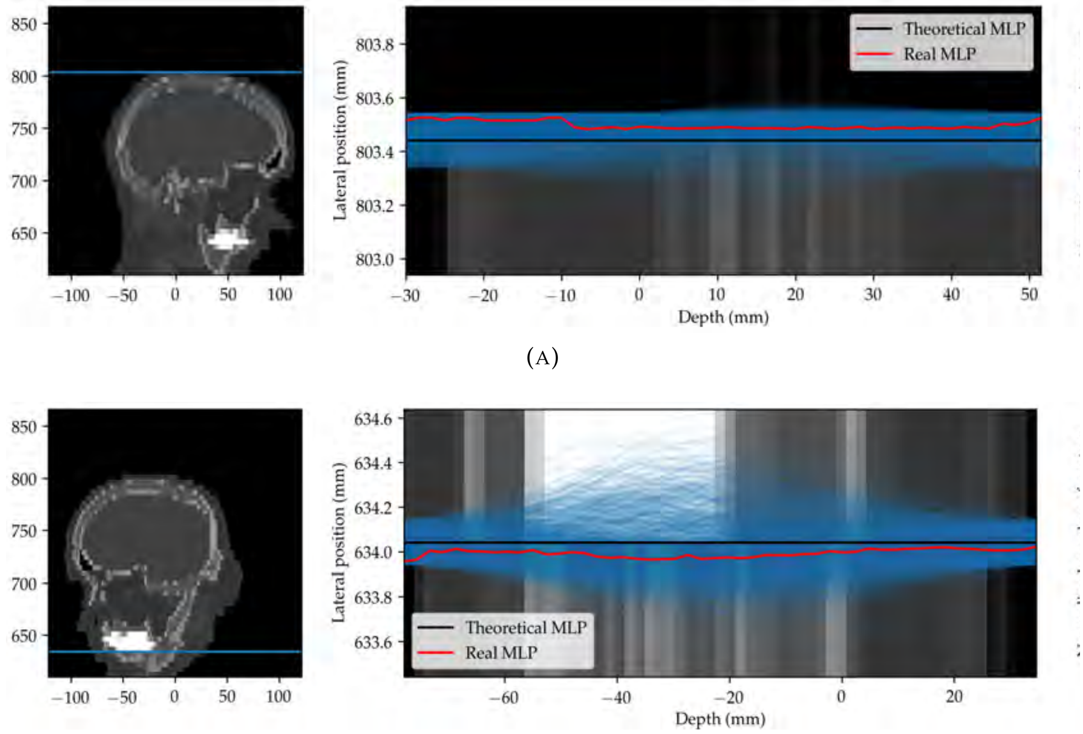

(A)

(B)

FIGURE 4.6 – Proton trajectories along two transverse heterogeneities. On the left, the beam position is shown on the $1/X_0$ map, in the middle, the trajectories are shown on a zoomed area of the same map. Most small longitudinal heterogeneities are just an effect of the spline interpolation done to rotate the image for visualization. On the right are represented the energy distributions on the exit detector.

selected transverse heterogeneities in the ICRP phantom. For the first interface between air and head, we observe that the majority of protons pass through air, where they are hardly scattered. We note that the entry and exit coordinates for the real and theoretical MLP are different since the source is not a point and a majority of protons satisfying $\mathbf{y}_0 = \mathbf{y}_2 = (0, 0)$ have started in air. The shape of the real MLP follows a quasi linear curve in the air region then gets closer to the theoretical MLP as protons are scattered in the head region. A maximum bias of 0.085 mm is reached around the entry and exit of the phantom. The real MLP for the second heterogeneity resembles the one observed for Phantom (C). The maximum bias between the theoretical and real MLP was measured at a depth of -34 mm and reached 0.075 mm.

4.3.3 MLP with prior knowledge

In Figure 4.7, the RMS error of the theoretical MLP for the same subset of protons used in Figure 4.5 (protons filtered with $\mathbf{y}_0 = \mathbf{y}_2 = (0, 0)$) is shown. The theoretical MLP was estimated for the three phantoms using the conventional formalism and the heterogeneous formalism of Collins-Fekete et al. (2017a). The maximum RMS, calculated using the homogeneous formalism, reaches 0.51 mm for phantom (B) and 0.46 mm for phantom (C), compared to 0.34 mm for the homogeneous phantom. The maximum is shifted towards the bone region for phantom (B). For both phantoms (B) and (C), the RMS error calculated using the heterogeneous formalism is almost identical to the one assuming a water medium.

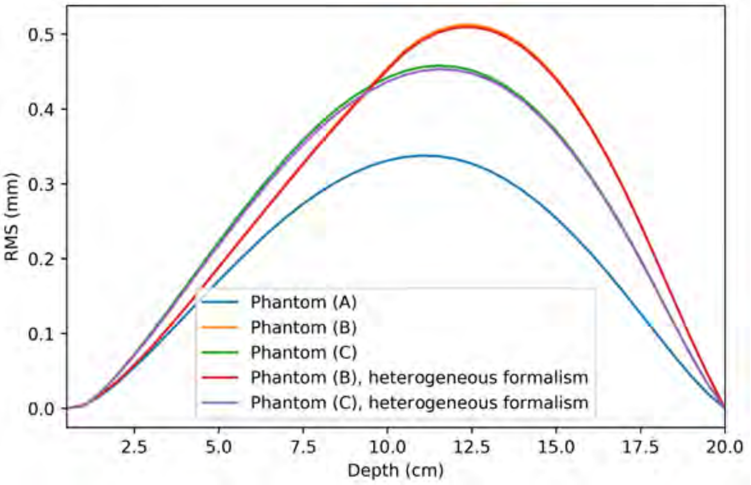

FIGURE 4.7 – RMS error of the theoretical MLP for the three phantoms. There is an overlap between the orange and red curves corresponding to phantom (B).

In Figure 4.8, we show the real and theoretical MLP for different exit coordinates in the three phantoms. We observe there is a systematic error on the MLP of phantom (B) when the path diverges from a straight line, although this error is smaller than the bias measured for phantom (C). The heterogeneous MLP formalism allows to effectively correct for this bias.

4.3.4 MLP near transverse interfaces for different trajectories

The unfiltered exit spatial and energy distributions for proton beams starting at $u_0 = \{-1, -0.5, 0, 0.5, 1\}$ mm in phantom (C) are shown in Figure 4.9. The distributions for beams starting in the bone region (at $u_0 = 0.5$ mm and 1 mm) are bimodal as two peaks are clearly distinguishable. The other distributions are skewed but have a single maximum.

Figure 4.10 shows an example of MLP when the distribution is bimodal. The positions (μ_1 and μ_2) and amplitudes (A_1 and A_2) of both peaks of the fitted distribution are represented, as well as the position of the global maximum. We observe that the position of the global maximum, which is usually used to represent the MLP, abruptly changes from 0.6 to -0.1 mm at $u = 14$ cm. The spatial distribution is Gaussian in the first centimeters, with a single visible peak. Then, this first peak declines and a second one appears as more and more protons transition to the water region. The path obtained using the most probable position at each depth is discontinuous, while the one following the center of the first Gaussian stays close to the theoretical MLP.

Figure 4.11 summarizes the different biases obtained in phantom (C) and the ICRP phantom for different entry and exit coordinates. The results for phantom (C) show that protons with entry and exit coordinates in the same medium (top-left and bottom-right quarters) have biases that are lower than protons whose entry and exit positions are in different tissues or exactly at the interface between the two media (bottom-left and top-right quarters). In addition, the bias is larger when protons start their path in the denser tissue since they are more likely to transition to a different medium. The maximum bias of 0.5 mm is found for protons starting in the bone region and exiting at the interface.

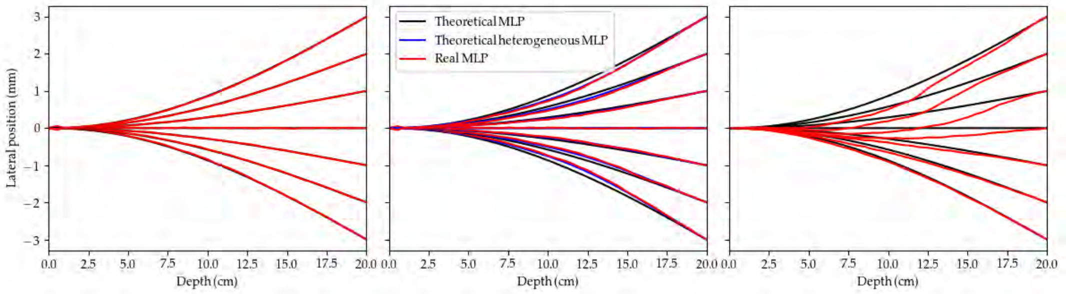

(A)

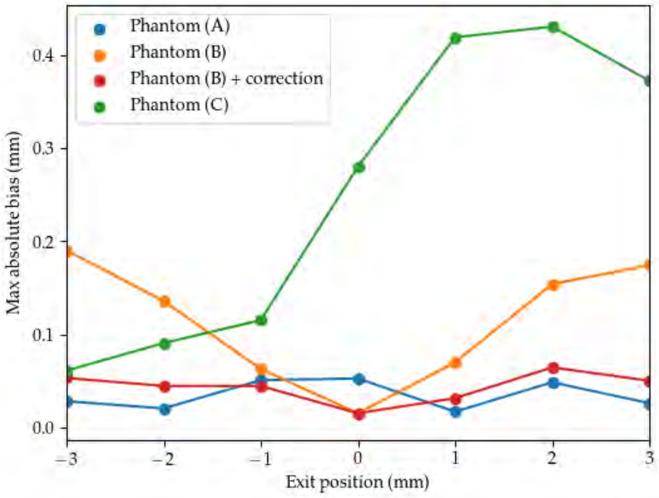

(B)

FIGURE 4.8 – Comparison of the theoretical and real MLP for different exit positions : (A) MLPs in phantoms (A), (B) and (C), from left to right, (B) maximum absolute difference between real and theoretical paths. For phantom (B), the theoretical MLP computed using ground truth knowledge of the tissues was additionally computed.

In the ICRP phantom, the bias for some trajectories could not be quantified near the air/head interface as such trajectories were followed by only a very small number of protons due to the lack of scattering in air. These cases correspond to the hatched regions in the figure. All measured biases, for both heterogeneities, were quite small compared to the ones calculated using phantom (C). The largest bias was 0.10 mm for the air/head interface and 0.13 mm for the teeth/mandible interface.

4.4 Discussion

4.4.1 Impact of transverse heterogeneities on MLP

We have shown that the Gaussian assumption on the spatial and angular distribution functions used to compute the MLP of protons is not valid when unbalanced scattering occurs due to transverse heterogeneities. When protons traverse two different tissues, the tissue with the higher scattering power will scatter the particles with larger angles, thus more protons will end up in the adjacent tissue. This causes skewed or even double peaked distributions as seen in figures 4.4 and 4.9a.

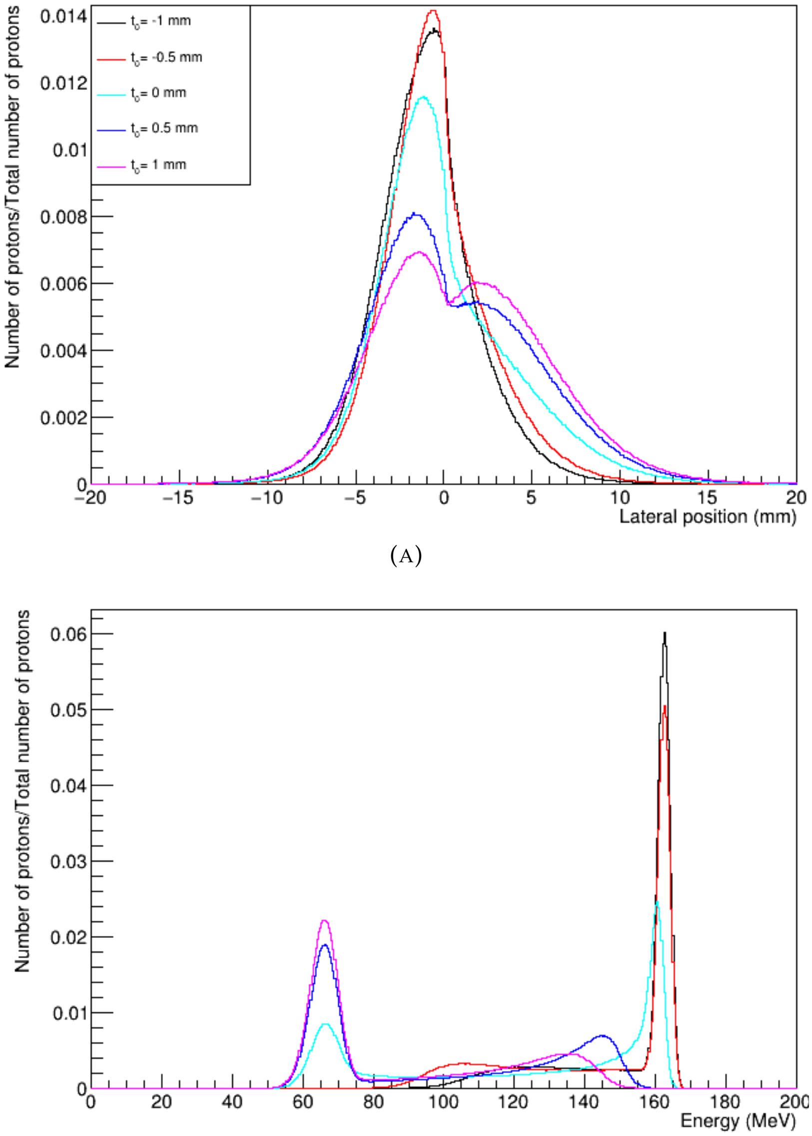

(A)

(B)

FIGURE 4.9 – Exit spatial (a) and energy (b) distributions for beams starting at different positions, without any selection on the exit position/angle. Negative t values are in water, positive ones are in bone.

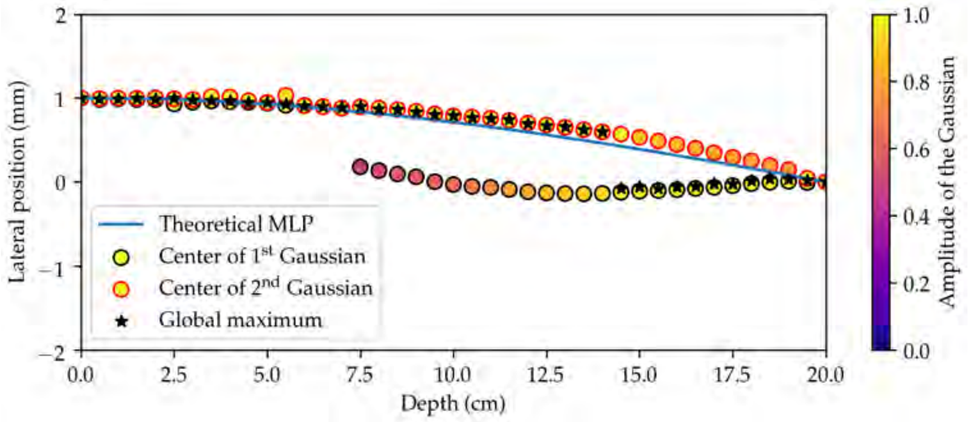

(A)

FIGURE 4.10 – Theoretical and real MLP for protons starting at $u_0 =$ 1 mm and exiting at $u_2 = 0$ mm.

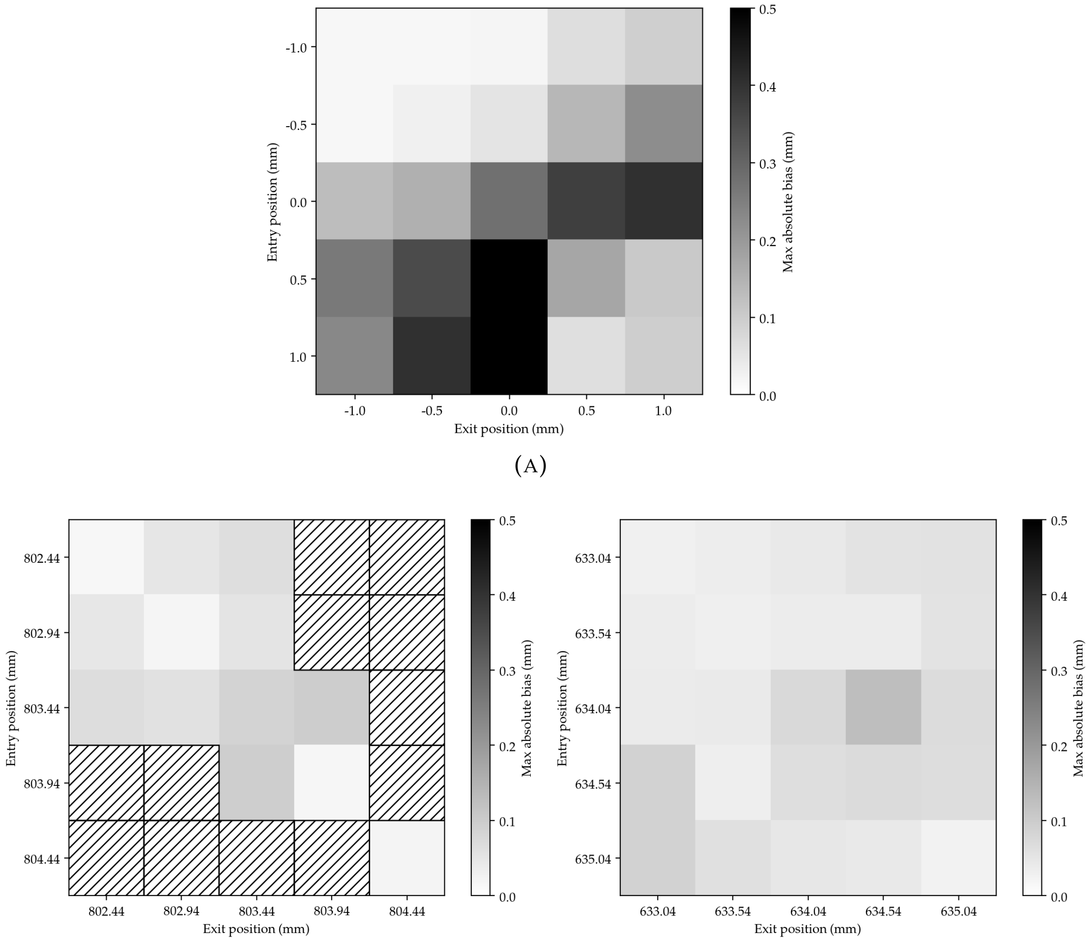

(A)

(B)

(C)

FIGURE 4.11 – (a) Maximum bias in phantom (C) for different entry and exit positions, negative positions are in water, positive values are in bone. (b) and (c) Maximum bias reached near the air/head and the teeth/mandible interfaces, respectively. The hatched areas correspond to paths for which the number of protons was too small for statistical analysis.

This asymmetry creates a bias between the MLP obtained from MC simulations and the theoretical MLP assuming a Gaussian distribution. For example, the theoretical MLP might predict a straight path while the real MLP near a transverse heterogeneity is in fact leaning towards the less scattering medium of the interface (figures 4.5 and 4.6). The unbalanced scattering also leads to asymmetrical error envelopes. The maximum bias measured in phantom (C) is 0.5 mm (Figure 4.11a). However, it was also shown that in cases when the distribution is not unimodal (when there is more than one peak, as seen when protons start their trajectory in bone in Figure 4.9), the MLP estimated using the lateral position distribution major mode (the most probable position) may produce a discontinuous trajectory. Therefore, in theses cases, the bias does not reflect the difference between the real MLP and theoretical MLP but rather the difference between the most probable position and the theoretical MLP. If we only consider the cases with unimodal distributions (three first rows of Figure 4.11a), the maximum bias reaches 0.45 mm. This is slightly larger than the maximum MLP uncertainty which reaches 0.43 mm in water. The maximum measured bias for a realistic heterogeneity only reached 0.13 mm (Figure 4.11c). We note that the choice of spatial and angular filter values was small enough to consider the exit positions constant and large enough to keep a sufficient number of protons for our analysis; reducing these thresholds did not alter our results.

4.4.2 Bimodal scattering distributions

Our results call into question the definition of the MLP in heterogeneous media. Usually, the MLP is defined as the junction of the most likely transverse positions determined independently as a function of depth. While this representation is a valid path in the case of a unimodal distribution of the proton positions, the set of most likely positions does not define a realistic and continuous path in the case of a distribution with more than one peak (Figure 4.10). For such cases, the MLP should better be understood as Most Likely Positions rather than Most Likely Path, and we can imagine several competing paths. In the particular case shown in Figure 4.10, there are two main proton populations: the first one is composed of protons that stayed in the same medium – in this case, bone – and the second one of protons that transitioned into water. Therefore, the path associated with the first Gaussian (Eq. 4.7) corresponds to protons having spent their entire trajectory in the bone region, which explains its proximity to the theoretical path (the difference should be due to the water assumption only). The path from the second Gaussian is harder to interpret. It corresponds to protons that passed in the water region, although not all protons transition at the same depth.

It could be of interest to develop an alternative definition of the MLP without assuming a Gaussian distribution of the scattering angles and positions to take into account transverse heterogeneities. However, one must keep in mind that the measured biases for realistic heterogeneities only reached 0.13 mm at the most. In addition, out of the many protons recorded and used for a full proton CT reconstruction, only a few will have entry and exit coordinates that suggest they have grazed a density interface. Therefore, a correction of the bias might not significantly improve the spatial resolution in pCT.

Also, we must acknowledge that our results are entirely based on Monte Carlo simulations, and what we refer to as "real MLP" is only the result of simulated proton trajectories. However, experimental tracking of proton trajectories inside a target would not have been feasible. The simulated proton tracks depend on the physics models used in Geant4 and on the simulation parameters. Therefore, we have verified our results were not considerably impacted by the chosen physics list or step size. A simulation such as the one used in Figure 4.5 was performed in phantom (C) using a maximum step size of either 100 µm and 5 mm, which resulted in the same real MLP.

4.4.3 Impact of prior knowledge on MLP

We were able to verify that an adaptation of the formalism including a depth-dependent radiation length and momentum-velocity (Collins-Fekete et al., 2017a) is sufficient to correct for the bias in a longitudinally heterogeneous phantom. Using ground-truth knowledge of the composition of phantom (B), we were able to correct the bias induced by the water assumption (Figure 4.8).

Also, we have confirmed that the RMS is not a satisfactory metric to evaluate the impact of heterogeneities on the accuracy of the MLP. Indeed, the RMS error is impacted by the systematic bias in the MLP estimate but also the uncertainty around this estimation, which depends on the scattering power of the medium. For example, the RMS is higher in bone although there is no bias in the MLP. Using other metrics such as the mean or maximum error allows for a better assessment of the MLP accuracy. Collins-Fekete et al. (2017a) considered the fact that no difference was seen in terms of RMS between the conventional MLP formalism and their adapted formalism indicated that the increase of RMS in heterogeneous phantoms was only due to an increased scattering. Our results show this holds true for longitudinal heterogeneities : since there was no systematic error in the MLP (at least for straight line paths, and the bias for other trajectories was small compared with the one for transverse heterogeneities), the rise in the RMS was essentially caused by MCS, thus the use of the heterogeneous formalism did not reduce the RMS error.

4.4.4 Impact on energy distributions

It might be interesting to investigate the effects of transverse heterogeneities on the protons' exit energy (see figures 4.4 and 4.9) and whether they can lead to artifacts during the reconstruction as protons having the same theoretical MLP would end up with a wide range of different energy losses.

We have shown that close to a transverse interface, the real MLP will lean towards the less scattering material. In terms of tomographic reconstruction, this means that protons will be backprojected along a path in one material (e.g. bone) whereas they actually traveled partly in another material (water, air, etc.), which would result in an underestimation of the relative stopping power of the bone tissue near the interface. We expect the reconstructed interface to be slightly shifted towards the bone region. We have yet to confirm these assumptions, but the impact of transverse heterogeneities during reconstruction could explain some of the artifacts observed in other works. For example, Wang, Mackie, and Tomé (2010) noted a dark ring artifact around object boundaries on reconstructed images. While the authors attribute this artifact to an issue with the Geant4 energy loss model, it could be related to transverse heterogeneities.

Furthermore, energy profiles such as the ones shown in Figures 4.4 and 4.9 would complicate the energy cuts used to filter nuclear events. Usually, 3σ data cuts on the exit energy allow to eliminate inelastic nuclear collisions, but such cuts on the observed distributions would probably be less efficient as the distribution is constituted of several peaks. In this case, it would be hard to distinguish between low energy protons that underwent nuclear collisions in water and protons that traversed mostly bone, for example.

4.5 Conclusion

In this chapter, we studied the impact of heterogeneities on the assumption that scattering distributions are Gaussian and how this could lead to systematic errors in the MLP prediction. It was demonstrated that transverse heterogeneities induce non Gaussian spatial and angular distributions. Depending on the trajectory along the interface, the distributions can resemble a skewed Gaussian or a two-term Gaussian. In the first case, there is a systematic error on the theoretical MLP as protons will be more likely to traverse the less scattering medium. In the second case, as the distributions of the transverse positions have several modes, the notion of a single most likely path is not fitting. The maximum bias between the theoretical MLP and the MLP derived from Monte Carlo simulated trajectories reaches 0.45 mm for a 20 cm long water/bone interface, and 0.13 mm for a more realistic interface in a head phantom. We have observed that longitudinal heterogeneities induce a very small systematic error on the MLP, which can be corrected by using prior knowledge of the object's tissue composition. Although the impact of heterogeneities on the MLP is small, combined with the impact on the energy distributions, it could lead to artifacts during reconstruction.

Chapter 5

A two-dimensional directional ramp filter

In this chapter, we propose a filter adapted to proton CT direct (non iterative) reconstruction in order to improve spatial resolution of pCT images. We derive its expression and test it on xCT and pCT data. Incidentally, this filter can be used to reconstruct 2D tilted projections in xCT. This chapter is adapted from Khellaf et al. (2020a).

5.1 Introduction

Filtered backprojection (FBP) is the reference algorithm to reconstruct tomographic data. It consists in (1) filtering the projections with a 1D ramp filter and (2) backprojecting the result in the image domain. An alternative method, the backproject-filter or backproject first (BPF), starts with the backprojection before filtering in the 2D image domain. BPF approaches can be useful when dealing with certain modalities to avoid resampling. For example, in proton CT, starting by backprojecting the protons along their non-linear paths could improve spatial resolution, compared with binning the list-mode data into projections (Zeng, 2007; Poludniowski et al., 2014; Rit et al., 2015). Similarly, time-of-flight (TOF) information of PET can be accounted for in the image domain (Watson, 2007) (Figure 5.1). Our objective is to develop such an approach by extending the usual 1D ramp filter in 2D. BPF methods usually rely on 2D radial filters (Zeng and Gullberg, 1994; Poludniowski et al., 2014). However, the backprojected image has an infinite support which is problematic during convolution since the computed backprojection matrix must have a finite size. The truncation will cause an offset in the reconstructed values, which can be minimized by using a very large backprojection matrix. Another possible backproject-first approach is based on the Hilbert transform inversion (Noo, Clackdoyle, and Pack, 2004; Zeng, 2007; Rit et al., 2015), and involves a differentiation step.

In this work, the idea is to (1) smear each single projection in the image space, (2) filter the smeared projection with a 2D version of the 1D ramp filter and (3) integrate over all projection angles. A similar 2D version of the ramp filter has been proposed by Watson (2007) in the context of TOF PET, although the filter was sampled directly in the frequency domain causing sampling artifacts. A variation of this filter, also proposed by Watson (2007) and called CRG-CW (Convolved Ramp and Gaussian with Confidence Weighting), has been used for TOF direct reconstruction (Kao, 2008; Kao et al., 2010; Guo, Kao, and Xie, 2011; Conti, Eriksson, and Westerwoudt, 2013). Similarly to what is done for the 1D ramp filter, we will sample the 2D ramp filter in the spatial domain to avoid sampling artifacts. We start by defining the 2D ramp filter in the case of parallel xCT, derive its expression in the spatial domain,

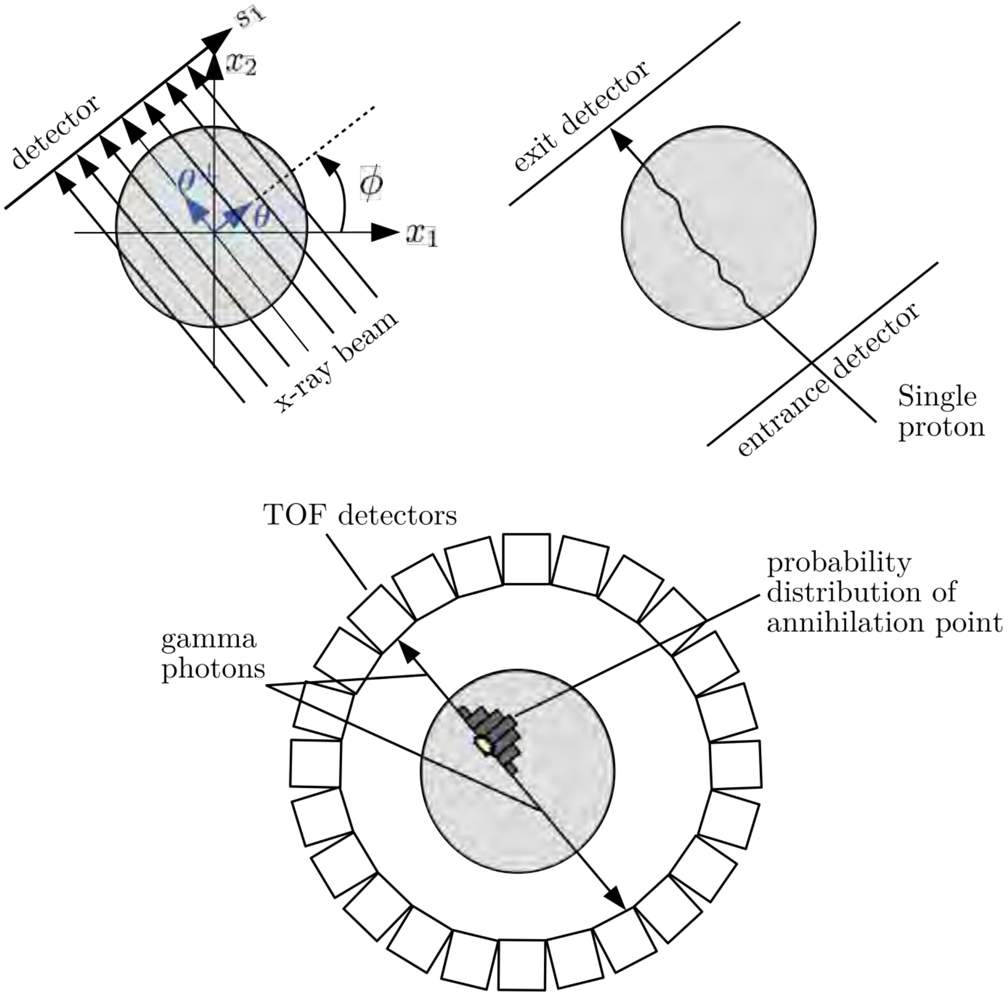

FIGURE 5.1 – Parallel xCT geometry (top left), pCT single tracking setup (top right), and TOF PET setup (bottom).

before applying this method to simulated xCT and pCT data. Although the main application in mind for this method is pCT, the filter is mathematically demonstrated in a conventional xCT setting for simplicity, and then applied to proton CT data.

5.2 Materials and Methods

5.2.1 Parallel FBP and 1D ramp filter

An image $f(x_1, x_2)$, with (x_1, x_2) the spatial coordinates, can be reconstructed from its parallel projections

$$p_\phi(s_1) = \int_{\mathbb{R}} f(s_1\boldsymbol{\theta} + s_2\boldsymbol{\theta}^\perp)\,\mathrm{d}s_2, \tag{5.1}$$

where s_1 is the distance of the projection line from the center, s_2 is the position along the projection line, $\boldsymbol{\theta} = (\cos\phi, \sin\phi)$ and $\boldsymbol{\theta}^\perp = (-\sin\phi, \cos\phi)$ (see Figure 5.1). Using a filtered backprojection method, the image is reconstructed by

$$f(x_1, x_2) = \int_0^\pi \tilde{p}_\phi(x_1\cos\phi + x_2\sin\phi)\,\mathrm{d}\phi, \tag{5.2}$$

where

$$\tilde{p}_\phi(s_1) = \int_{\mathbb{R}} P_\phi(\sigma_1)|\sigma_1|e^{i2\pi\sigma_1 s_1}\,\mathrm{d}\sigma_1, \tag{5.3}$$

with $P_\phi(\sigma_1)$ defined as the Fourier transform (FT) of $p_\phi(s_1)$.

In practice, the filtered projections $\tilde{p}_\phi(s_1)$ are obtained using a band-limited version of the 1D ramp filter. A common choice proposed by Bracewell and Riddle (1967) and Ramachandran and Lakshminarayanan (1971) is

$$H(\sigma_1) = \begin{cases} |\sigma_1| & \text{if } -W < \sigma_1 < W \\ 0 & \text{otherwise,} \end{cases} \tag{5.4}$$

with W the Nyquist frequency defined as $W = 1/2\tau$ with τ the sampling period of the projections p_ϕ. Directly discretizing this expression to filter the projections in the frequency domain would cause an underestimation of the entire reconstructed values, because of the zero value attributed to the zero frequency bin (Kak and Slaney, 1988; Crawford, 1991). In order to avoid this issue, the impulse response of the filter is calculated by taking its inverse Fourier transform

$$\begin{aligned} h(s_1) &= \int_{\mathbb{R}} H(\sigma_1)e^{i2\pi\sigma_1 s_1}\,\mathrm{d}\sigma_1 \\ &= \frac{1}{2\tau^2}\mathrm{sinc}\left(\frac{2\pi s_1}{2\tau}\right) - \frac{1}{4\tau^2}\mathrm{sinc}^2\left(\frac{\pi s_1}{2\tau}\right) \end{aligned} \tag{5.5}$$

and subsequently discretized by replacing $s_1 = n\tau$, which yields

$$h[n] = \begin{cases} \dfrac{1}{4\tau^2}, & \text{if } n = 0 \\ 0, & \text{if } n \text{ even} \\ \dfrac{-1}{n^2\pi^2\tau^2}, & \text{if } n \text{ odd,} \end{cases} \tag{5.6}$$

as was proposed by Ramachandran and Lakshminarayanan (1971). The discrete Fourier transform (DFT) of this impulse response does not have a zero value at its zero frequency and allows an accurate reconstruction of the image values (Kak and Slaney, 1988). Equation 5.6 is used to compute the 1D ramp filter used for FBP.

5.2.2 From the 1D ramp filter to a 2D directional ramp filter

From Equation 5.2, we see that the projections are filtered then smeared in the image space using the variable change $s_1 = x_1 \cos\phi + x_2 \sin\phi$. We want to apply a 2D version of the ramp filter on the already smeared projections, i.e. do the variable change before filtering.

We recall that (σ_1, σ_2) are the Fourier variables corresponding to (s_1, s_2) in the spatial domain. We introduce the Dirac δ function, using the property $\int_{\mathbb{R}} \delta(\sigma_2)e^{i2\pi\sigma_2 s_2}\,\mathrm{d}\sigma_2 = 1$, in Equation 5.3

$$\tilde{p}_\phi(s_1) = \int_{\mathbb{R}}\int_{\mathbb{R}} \delta(\sigma_2)P_\phi(\sigma_1)|\sigma_1|e^{i2\pi(\sigma_1 s_1 + \sigma_2 s_2)}\,\mathrm{d}\sigma_1\,\mathrm{d}\sigma_2 \tag{5.7}$$

and, given the expression of the Fourier transform $P_\phi(\sigma_1)$ and the fact that formally $\delta(\sigma_2) = \int_{\mathbb{R}} e^{-i2\pi\sigma_2 s_2}\,\mathrm{d}s_2$, note that

$$\delta(\sigma_2)P_\phi(\sigma_1) = \int_{\mathbb{R}}\int_{\mathbb{R}} p_\phi(s_1)e^{-i2\pi(\sigma_1 s_1+\sigma_2 s_2)}\,\mathrm{d}s_1\,\mathrm{d}s_2. \tag{5.8}$$

We use the following vector notations for $s_1 = \boldsymbol{x}\cdot\boldsymbol{\theta}$, $s_2 = \boldsymbol{x}\cdot\boldsymbol{\theta}^\perp$ and the corresponding Fourier variables $\sigma_1 = \boldsymbol{\xi}\cdot\boldsymbol{\theta}$ and $\sigma_2 = \boldsymbol{\xi}\cdot\boldsymbol{\theta}^\perp$, where $\boldsymbol{x} = (x_1, x_2)$ and $\boldsymbol{\xi} = (\xi_1, \xi_2)$. We also define $b_\phi : \mathbb{R}^2 \to \mathbb{R}$, the backprojection of one projection, as

$$b_\phi(\boldsymbol{x}) = p_\phi(\boldsymbol{x}\cdot\boldsymbol{\theta}), \tag{5.9}$$

and $B_\phi(\boldsymbol{\xi})$ its Fourier transform. We call $b_\phi(\boldsymbol{x})$ a smeared projection. Using these definitions, we note that Equation 5.8 is the expression of the Fourier transform of $b_\phi(\boldsymbol{x})$, and Equation 5.7 becomes

$$\tilde{b}_\phi(\boldsymbol{x}) = \int_{\mathbb{R}^2} B_\phi(\boldsymbol{\xi})|\boldsymbol{\xi}\cdot\boldsymbol{\theta}|e^{i2\pi\boldsymbol{\xi}\cdot\boldsymbol{x}}\,\mathrm{d}\boldsymbol{\xi}. \tag{5.10}$$

The image can then be reconstructed from

$$f(\boldsymbol{x}) = \int_0^\pi \tilde{b}_\phi(\boldsymbol{x})\,\mathrm{d}\phi. \tag{5.11}$$

This equation allows reconstructing the image in three steps

1. Smear each projection in the image space, i.e. compute a 2D image $b_\phi(\boldsymbol{x})$ for each projection angle;
2. Filter each 2D image $b_\phi(\boldsymbol{x})$ with the corresponding 2D filter $|\boldsymbol{\xi}\cdot\boldsymbol{\theta}|$ to obtain $\tilde{b}_\phi(\boldsymbol{x})$;
3. Sum $\tilde{b}_\phi(\boldsymbol{x})$ over all angles ϕ.

Note that this 2D version of the ramp filter depends on ϕ, hence the name directional ramp (DR) filter. By definition, the backprojection operation consists in smearing each projection in the image space, i.e. interpolating $b_\phi(\boldsymbol{x})$ from $p_\phi(s_1)$ using $b_\phi(\boldsymbol{x}) = p_\phi(\boldsymbol{x}\cdot\boldsymbol{\theta})$, and summing over all projection angles, i.e. computing $\int_0^\pi b_\phi(\boldsymbol{x})d\phi$. In the proposed method, we break these two steps apart: steps (1) and (3) correspond to the backprojection and step (2) to the filtering. This method resembles a BPF approach since we start by smearing the projections in the image space, however the angular sum to compute the backprojected image is the last step as in an FBP.

The usual 2D cone filter used in BPF methods is $\|\boldsymbol{\xi}\|$. Unlike the DR filter which must be used before the angular sum as it depends on the projection angle, the cone filter is applied after the full backprojection since it is not direction dependent. We mentioned in the introduction that a similar filter to the 2D DR, called transverse ramp, had been proposed to reconstruct TOF PET data (Watson, 2007). It was directly sampled in the frequency domain, causing sampling artifacts due to the zero values along the line $\boldsymbol{\xi}\cdot\boldsymbol{\theta} = 0$. We choose to calculate the filter's impulse response as in the 1D case to avoid such artifacts.

5.2.3 Impulse response of the 2D directional ramp filter

A band-limited version of the 2D DR filter is given by

$$H_\phi(\boldsymbol{\xi}) = \begin{cases} |\boldsymbol{\xi} \cdot \boldsymbol{\theta}| & \text{if } \mid \xi_1 \mid, \mid \xi_2 \mid < W \\ 0 & \text{otherwise.} \end{cases} \tag{5.12}$$

The corresponding kernel in the direct space is obtained by taking the inverse Fourier transform of this directional filter:

$$h_\phi(\boldsymbol{x}) = \int_{\mathbb{R}^2} H_\phi(\boldsymbol{\xi}) e^{i2\pi\boldsymbol{\xi}\cdot\boldsymbol{x}} \,\mathrm{d}\boldsymbol{\xi}. \tag{5.13}$$

For $\phi \in [-\pi/4, \pi/4]$, the integral can be split into two parts,

$$\begin{aligned} h_\phi(x_1, x_2) = \int_{-W}^{W} \Big[\int_{-W}^{-\xi_2 \tan\phi} & -(\xi_1 \cos\phi + \xi_2 \sin\phi) e^{i2\pi(\xi_1 x_1 + \xi_2 x_2)} \,\mathrm{d}\xi_1 \\ & + \int_{-\xi_2 \tan\phi}^{W} (\xi_1 \cos\phi + \xi_2 \sin\phi) e^{i2\pi(\xi_1 x_1 + \xi_2 x_2)} \,\mathrm{d}\xi_1 \Big] \,\mathrm{d}\xi_2, \end{aligned} \tag{5.14}$$

knowing that $\boldsymbol{\xi} \cdot \boldsymbol{\theta}$ is negative below the line given by $\xi_1 = -\xi_2 \tan\phi$ and positive above it. These integrals lead to

$$\begin{aligned} h_\phi(x_1, x_2) = \Big(& - x_2 \cos\phi \,\mathrm{sinc}\Big(\frac{\pi(x_1 \tan\phi - x_2)}{\tau}\Big) - x_1 \sin\phi \cos\Big(\frac{\pi x_1}{\tau}\Big) \cos\Big(\frac{\pi x_2}{\tau}\Big) \\ & + (x_1 \sin\phi + x_2 \cos\phi) \,\mathrm{sinc}\Big(\frac{\pi x_2}{\tau}\Big) \cos\Big(\frac{\pi x_1}{\tau}\Big)\Big) \\ & \times \frac{1}{2\tau(\pi x_1)^2 x_2} + \frac{\cos\phi}{2\tau^3} \,\mathrm{sinc}\Big(\frac{\pi x_1}{\tau}\Big) \,\mathrm{sinc}\Big(\frac{\pi x_2}{\tau}\Big). \end{aligned} \tag{5.15}$$

The discretized impulse response, with $x_1 = m\tau$ and $x_2 = n\tau$, is given by

$$h_\phi[m,n] = \begin{cases} \dfrac{1}{2\pi^2\tau^3}\Big(\dfrac{-\cos\phi}{m^2}\mathrm{sinc}(\pi(m\tan\phi - n)) \\ \quad - \cos(\pi n)\cos(\pi m)\dfrac{\sin\phi}{nm}\Big) & \text{if } m, n \neq 0 \\ \dfrac{\sin^2\phi}{2\pi^2 n^2 \tau^3 \cos\phi}\cos(\pi n) & \text{if } m = 0, n \neq 0 \\ \dfrac{\cos\phi}{2\pi^2 m^2 \tau^3}(\cos(\pi m) - \mathrm{sinc}(\pi m \tan\phi)) & \text{if } m \neq 0, n = 0 \\ \dfrac{2\cos^2\phi + 1}{12\tau^3\cos\phi} & \text{if } m = 0, n = 0. \end{cases} \tag{5.16}$$

The expressions for m and/or n equal to zero are found by setting x_1 and/or x_2 to zero in Equation 5.14. The expression can be extended to angles $\phi \notin [-\pi/4, \pi/4]$ using $h_{\phi+\pi}[m,n] = -h_\phi[m,n]$ and $h_{\phi+\pi/2}[m,n] = h_{-\phi}[n,m]$. Note that setting $\phi = 0$ in Equation 5.16 gives the expression of the 1D ramp filter multiplied by $1/\tau$ on the line $n = 0$, and zero elsewhere. It should also be noted that the impulse response of the filter (Equation 5.15) has infinite support, such that sampling the filter in the frequency domain would always result in aliasing artifacts according to the sampling theorem (Crawford, 1991).

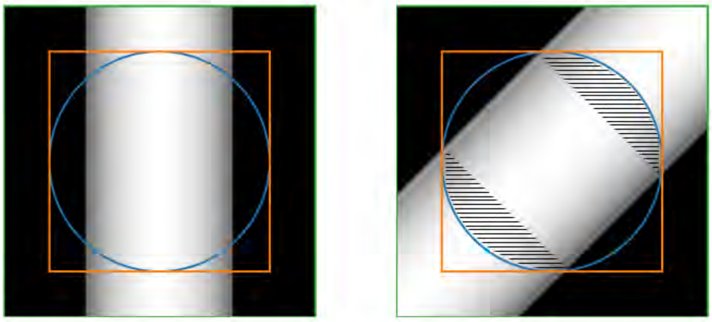

FIGURE 5.2 – Smeared projection for angle $\phi = 0$ (left) and $\phi = -\pi/4$ (right). The field of view is represented by the blue circle and the reconstructed region by the orange square. The shaded areas represent the regions where the image is truncated in the direction of $\boldsymbol{\theta}$. The green square represents the region needed to accurately filter the smeared projection for all angles. For $\phi = 0$, the data inside the orange square is sufficient for accurate reconstruction inside the FOV, while a larger region is needed for oblique angles, with the largest area being for $\phi = \pi/4 + k\pi/2$.

5.2.4 Size of the backprojection region

In order for the 2D filtered smeared projections to be equivalent to the 1D filtered projections, we need non-truncated images $b_\phi(\boldsymbol{x})$ along the direction $\boldsymbol{\theta}$ inside the FOV (Figure 5.2). We do not need the full projections outside the FOV since the DR filter tends to a Dirac along $\boldsymbol{\theta}^\perp$ in the direct space (since it is constant in the Fourier space), such that the projection lines outside the FOV do not contribute to the reconstruction. By taking a backprojection region (region where the projections will be smeared) of the same size as the reconstruction region, part of the data near the borders will be truncated for angles $\phi \neq k\pi/2$, $k \in \mathbb{Z}$. In order to keep the full projections inside a circular FOV for all angles, one should set $M = \sqrt{2}N$, where the backprojection region is $M \times M$ and the reconstruction region is $N \times N$.

5.2.5 Simulations

We generated parallel ray projections of the 2D Shepp Logan phantom (Shepp and Logan, 1974) using RTK (Rit et al., 2014) in order to test the filter. 804 projections were acquired over a 180 degree range, with a detector of 512 pixels. The phantom was reconstructed using grids of 512×512 pixels and 1024×1024 pixels. Poisson noise was applied to the idealized projections, using an initial fluence of 10^7 photons per detector pixel, and weighting the line integrals with 0.01879 mm^{-1}, the linear attenuation coefficient of water at 75 keV, to work with physical attenuation values.

A proton CT simulation was performed using the Monte Carlo platform GATE (Jan et al., 2011). A “single tracking" setup was used, consisting of two ideal detectors measuring position, direction and energy, located upstream and downstream from the phantoms. A 200 MeV rotating fan-beam proton source was positioned 1 m away from the object center, with a flux of 225 protons·mm^{-2}·projection^{-1} at the isocenter, for a total of 720 projections over a 360 degree range. Protons were paired between the two detectors, and each proton’s path was estimated using the MLP formalism, after excluding protons with nuclear interactions using 3σ angle and energy cuts (Schulte et al., 2008). The list-mode data was binned into parallel geometry images $b_\phi(\boldsymbol{x})$ using the same binning as the one of Rit et al. (2015), described in detail in the next chapter. The object was reconstructed in a grid of 1000×1000 pixels with a pixel spacing of 0.25 mm. We simulated a spiral phantom, consisting of a disk of water of diameter 20 cm with aluminum inserts (Figure 5.6) to take into account the spatial dependence of the spatial resolution in pCT.

5.2.6 Spatial resolution

The spatial resolution was obtained by extracting edge profiles and estimating the corresponding MTF. The MTF was calculated in the spiral phantom using each aluminium insert's radial edge spread function (ESF), as recommended by Richard et al. (2012).

Assuming a Gaussian line spread function (LSF), the ESF is given by the integral of a Gaussian, which is the error function (erf). Therefore, the following function with parameters μ and σ was fitted to radial edge profiles for each insert

$$\mathrm{ESF}(x) \propto \frac{1}{2}\left(1+\mathrm{erf}\left(\frac{x-\mu}{\sigma}\right)\right), \tag{5.17}$$

with

$$\mathrm{erf}(x) = \frac{2}{\sqrt{\pi}}\int_0^x \exp(-t^2)\,\mathrm{d}t. \tag{5.18}$$

The MTF is simply the modulus of the Fourier transform of the LSF, which yields

$$\mathrm{MTF}(f) \propto \exp\left(-2\pi^2(\sigma f)^2\right), \tag{5.19}$$

therefore it can be directly calculated from the fitted parameter of the ESF function. The frequency corresponding to an MTF value of 10%, given by

$$f_{\mathrm{MTF10\%}} = \sqrt{\frac{\ln 10}{2}}\frac{1}{\pi\sigma}, \tag{5.20}$$

was used to quantify the spatial resolution. The uncertainty on $f_{\mathrm{MTF10\%}}$ was derived from the standard deviation of the error function fit.

5.3 Results

Figure 5.3 shows the "pseudo-continuous" filter, i.e. the oversampled filter calculated from the continuous impulse response (Equation 5.15) by setting $x_1 = m\tau'$ and $x_2 = n\tau'$ with $\tau' \ll \tau$. After discretization, for the case $\phi = 0$ (left), the samples outside the central horizontal line lie exactly on the zero crossings. For the case $\phi = \pi/3$ (right), the filter is not zero outside the filtering line $n = m\tan\phi$. The DFT of the filters looks like the usual 1D ramp filter duplicated along the direction $\boldsymbol{\theta}^{\perp}$.

Figure 5.4 shows the central line profile of the Shepp Logan phantom reconstructed using the 2D DR filter sampled in the frequency domain or in the spatial domain. The reconstructed values using the frequency sampling are underestimated. The bias is constant and equal to -0.017.

The reconstructions of the Shepp-Logan phantom using different parameters are shown in Figure 5.5. Except for the reconstruction using a frequency sampled filter, the rest of the reconstructions are very similar. Some artifacts are visible near the outer edges of the phantom in the case of the non-apodized DR filter (third and forth columns) for idealized projections. This is better visualized on the difference

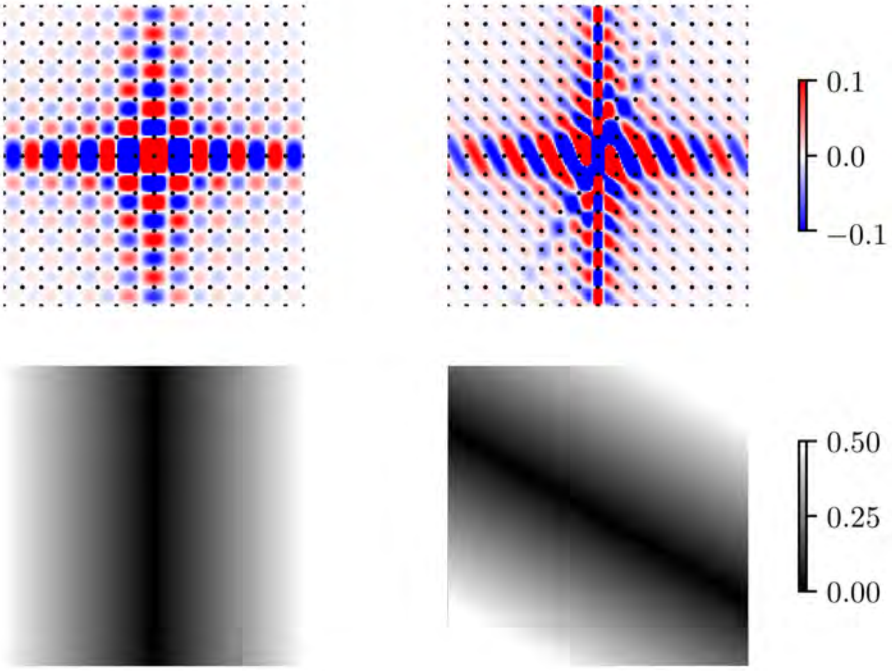

FIGURE 5.3 – Top : Pseudo-continuous impulse response of the 2D DR filter for $\phi = 0$ (left) and $\phi = \pi/3$ (right). The discrete samples are overlayed as black dots. Bottom : Fourier transform of the discrete impulse response.

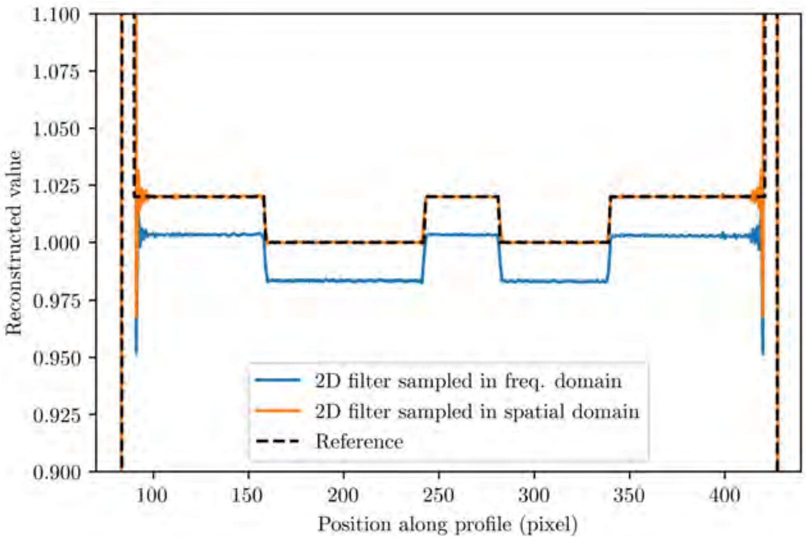

FIGURE 5.4 – Central line profile of the reference and the reconstructed Shepp-Logan phantom using the 2D DR filter sampled in the frequency domain or the spatial domain.

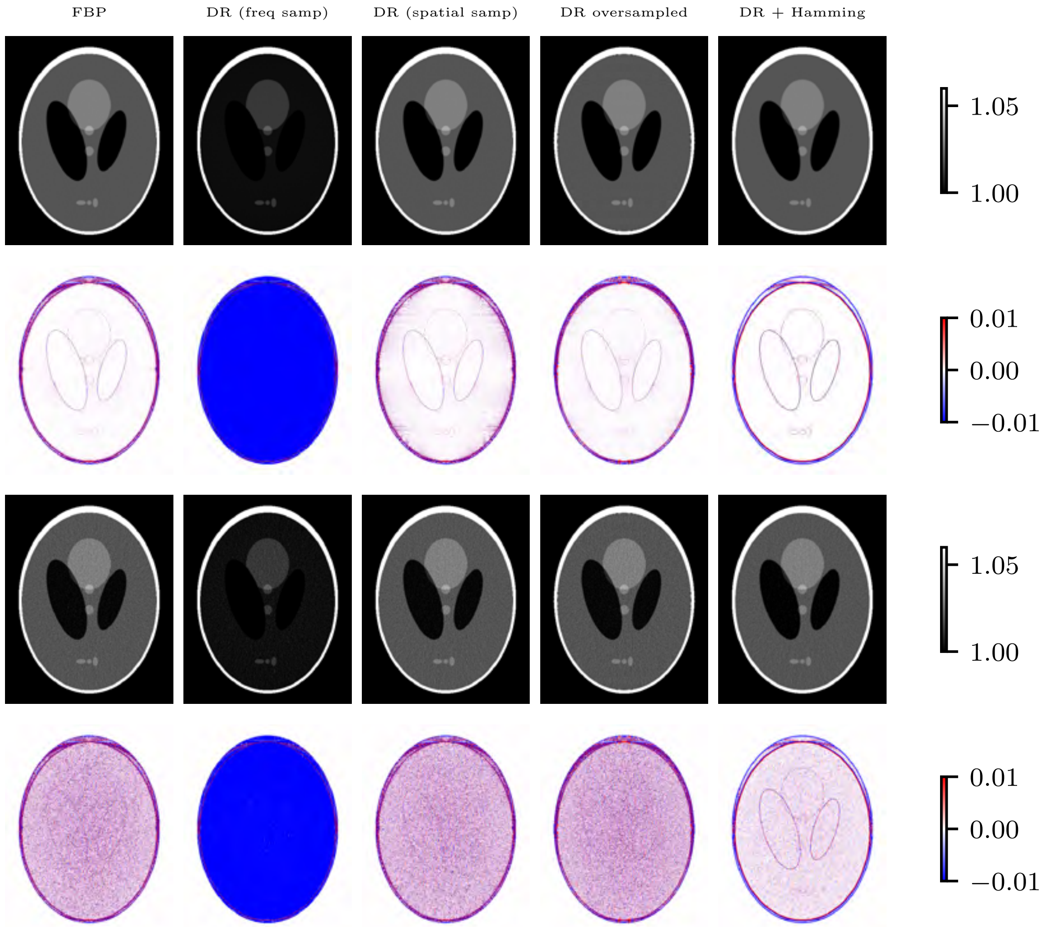

FIGURE 5.5 – Shepp-Logan phantom reconstructed using, from left to right, an FBP, the DR filter sampled in the frequency and spatial domain, the oversampled DR filter (N=1024), and the filter apodized with a Hamming window. The first two rows correspond to the results (reconstruction and difference with reference) for idealised projections and the two bottom rows to the results for noisy projections.

maps, where the DR reconstructed image is slightly noisier for idealized projections, although this is only visible with a tight color scale ($[-0.01, 0.01]$). Using an oversampled backprojection (but keeping the same sampling for the projections) reduces the noise, and apodizing the filter with a Hamming window completely suppresses the artifacts. The reconstructions from noisy projections show the DR filter performs as well as the 1D ramp filter, and that the amplitude of the previous artifacts is small compared with the statistical noise as they are not visible anymore.

The reconstructions of proton CT data are shown in Figure 5.6. The spatially sampled DR filter, without resampling or apodization, was used for reconstruction. There is no visible difference between the image reconstructed with an FBP and with the DR filter. The spatial resolution $f_{\mathrm{MTF10\%}}$ as a function of each bead's distance to the center of the phantom is represented. The difference between the resolution for the FBP and the DR algorithms reaches 0.8 lp/mm for the outermost bead.

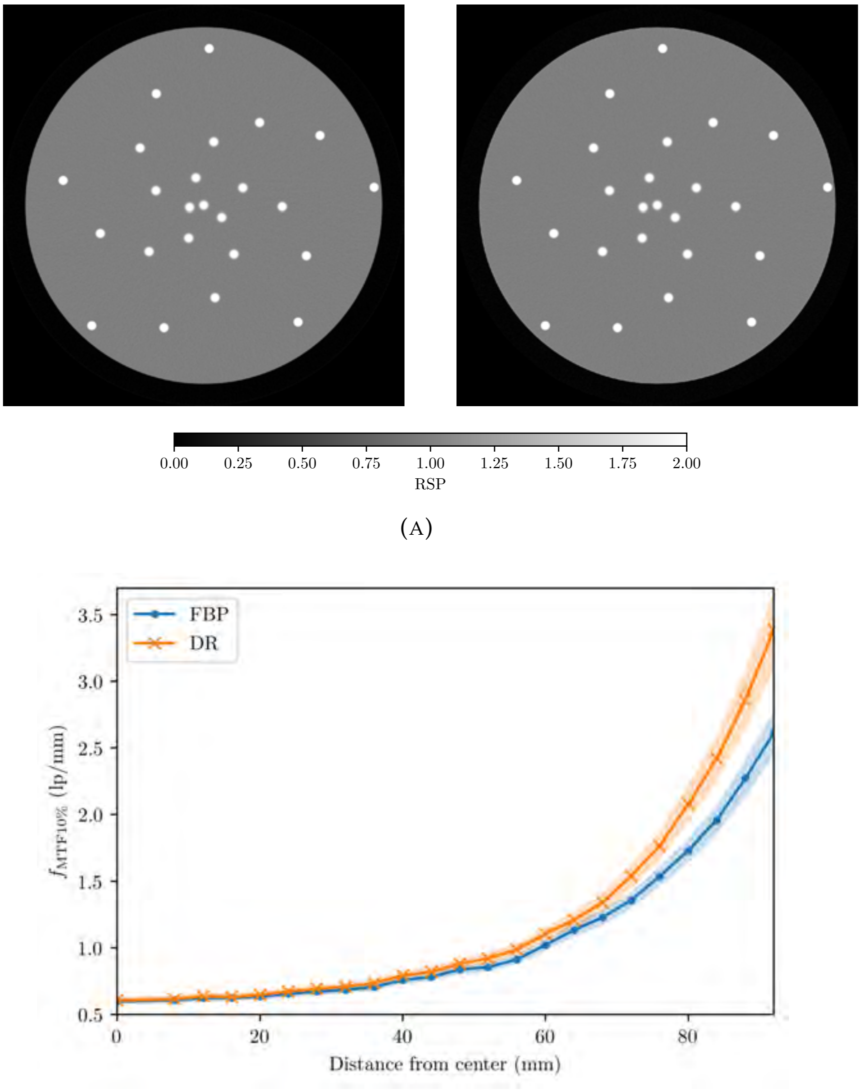

(A)

(B)

FIGURE 5.6 – (a) Proton CT reconstructions of the RSP map of the spiral phantom using an FBP (left) and the DR filter (right). (b) Spatial resolution of the inserts in the spiral phantom. The shaded areas correspond to $\pm 3\sigma$ where σ is the uncertainty on the spatial resolution.

5.4 Discussion

Our results show that the 2D DR filter, sampled in the spatial domain, allows accurate reconstruction of xCT and pCT data, although some artifacts are apparent in the case of reconstructions from noiseless xCT projections.

As was observed for the 1D ramp filter by Crawford (1991) and Kak and Slaney (1988), sampling in the frequency domain will cause aliasing artifacts (an underestimation in the spatial domain) due to the infinite support of the impulse response. In the direct space, the DR filter should look like a Dirac in the direction $\boldsymbol{\theta}^{\perp}$ for the 2D convolution to be equivalent to the 1D one. However, apodizing the filter with a square window in Equation 5.12 results in a convolution with a 2D sinc function, which explains the shape of the filter in Figure 5.3. While the discretized filter is a Dirac for angles $\phi = k\pi/2, k \in \mathbb{Z}$, since all samples outside the central line are zero, this is not the case for other angles, meaning there will be interferences from other lines during convolution. In Fourier space, this translates in a discontinuity of the FT at the Nyquist frequency. This is visible in Figure 5.3 where the DFT of the DR filter for $\phi = \pi/3$ has very thin black lines on its bottom left corner. This could explain the remaining artifacts visible in Figure 5.5. A similar issue with the continuity of the FT was reported by Schöndube, Stierstorfer, and Noo (2010), where the authors define a 2D inverse Hilbert transform. The image reconstructed using this filter suffered from ring artifacts. One of the proposed solutions is to apodize the filter in the Fourier space using a Hamming window to deal with the discontinuity. Our results show that the apodization effectively suppresses artifacts, although it also causes a slight loss of spatial resolution. An alternative is to increase the sampling of the backprojected image, which also reduces the noise as seen in Figure 5.5. Since the artifacts are related to the sampling of the 2D DR filter, taking more samples i.e. increasing the filter's band limit, will make the reconstruction less noisy. However, this artifact is not visible when using projections with a realistic level of noise.

In the case of simple line integrals, such as in xCT, using the 2D DR filter should give the same result as a standard FBP but is computationally less effective. The DR filter could rather be used with modalities such as proton CT or TOF PET, where the projections are respectively integrals along non-linear paths due to multiple Coulomb scattering or integrals along weighted lines due to time resolution of the detector. In xCT, the projections are constant along the direction $\boldsymbol{\theta}^{\perp}$, therefore using 1D projections and the 1D ramp filter makes sense. Both pCT and TOF PET add a new dimension, the depth of the proton or the time-of-flight, such that the smeared projections vary along $\boldsymbol{\theta}^{\perp}$ (see Figure 5.1). Filtering the 2D smeared projections $b_{\phi}(\boldsymbol{x})$ requires either rotating each image so that its samples are aligned with the 1D filter, then performing a line-by-line filtering; or using a directional 2D ramp filter. The DR filter could present some notable advantages in this case: as in BPF methods, the filtering is done in the image space so that we avoid rotations that can cause a loss of spatial resolution; at the same time, unlike other BPF approaches, there is no bias due to the truncation of the backprojection region which does not need to be approximated using very large matrices (2 to 4 times the reconstruction region in Poludniowski et al. (2014) versus $\sqrt{2}$-times). A drawback is that the DR filter is different for each projection angle, but it can be pre-computed for a given image grid and set of projection angles.

Our results for proton CT data (Figure 5.6) have confirmed that the DR filter can improve spatial resolution compared with an FBP algorithm. This improvement was observed only for inserts close to the edge of the spiral phantom because at the

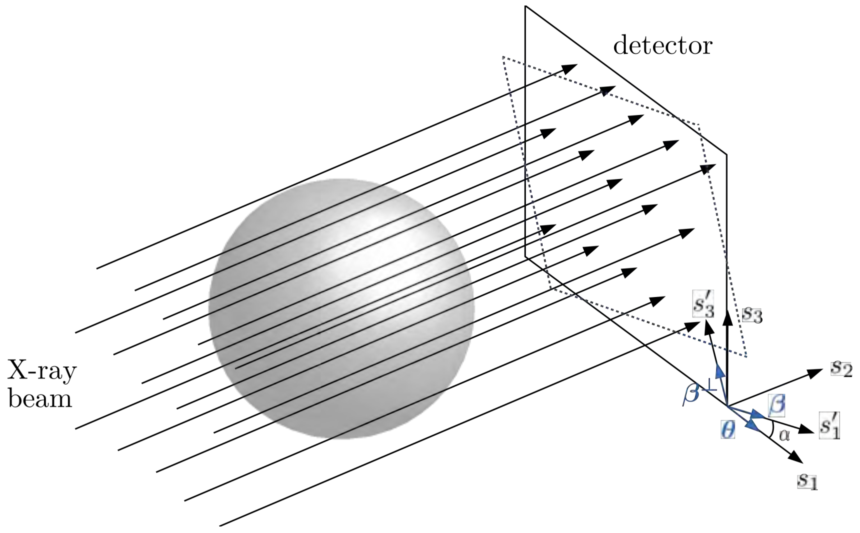

FIGURE 5.7 – Scheme of the geometry for tilted 2D projections. The tilted detector is represented in dotted lines. It corresponds to a rotation of the aligned detector by angle α around the s_2-axis.

center of the object, the image is too blurry due to Coulomb scattering to see any enhancement of spatial resolution. Additionally, no sampling artifacts were observed as the pCT image noise was dominated by energy straggling of the protons, multiple Coulomb scattering and statistical noise.

While this method is theoretically demonstrated for parallel geometries only, the acquisitions can be done in another setup as long as the data is rebinned into parallel geometry, which is straightforward for list-mode pCT data, as was done for our own pCT simulations. It may be possible to derive an expression for the ramp filter in the case of fan beam data, for example; however, this might prove to be more difficult as the transform from the sinogram domain to the image domain is not a simple rotation as for parallel data.

5.5 Application to tilted X-ray CT projections

In this section, we present a different application of the DR filter in the case of 2D parallel projections in xCT, when the detector is rotated by an in-plane angle α (see Figure 5.7). The projections would need to be realigned with the reconstructed image grid before filtering. To avoid this interpolation, the 2D DR filter, computed for the in-plane angle α, could be used on each 2D projection before backprojection. Unlike the previous application, the same filter direction would be used on all 2D projections, which reduces the computational cost of this operation.

Let us redefine $\boldsymbol{x} \in \mathbb{R}^3$ and $\boldsymbol{\theta} = (\cos\phi, \sin\phi, 0)$. The tilted vectors $\boldsymbol{\beta}$ and $\boldsymbol{\beta}^\perp$ are given by

$$\boldsymbol{\beta} = \begin{pmatrix} \cos\alpha\cos\phi \\ \cos\alpha\sin\phi \\ \sin\alpha \end{pmatrix}, \tag{5.21}$$

and

$$\boldsymbol{\beta}^\perp = \begin{pmatrix} -\sin\alpha\cos\phi \\ -\sin\alpha\sin\phi \\ \cos\alpha \end{pmatrix}, \tag{5.22}$$

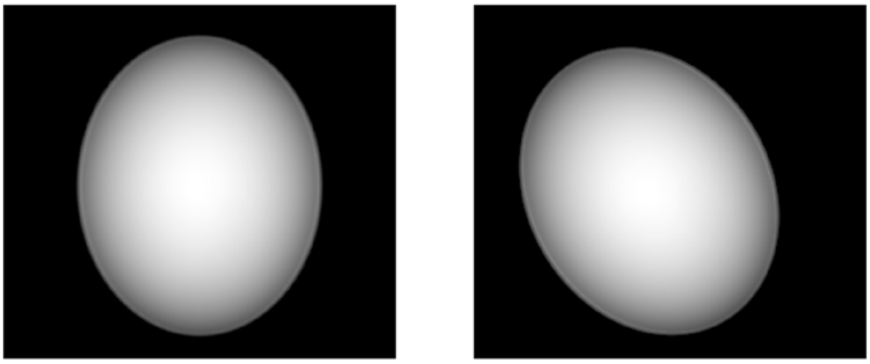

FIGURE 5.8 – Example of one projection at $\phi = 25°$ of the Shepp-Logan phantom, with in-plane angle $\alpha = 0$ (left) and $\alpha = \pi/6$ (right).

which yields $s_1' = \boldsymbol{x} \cdot \boldsymbol{\beta}$ and $s_3' = \boldsymbol{x} \cdot \boldsymbol{\beta}^{\perp}$. We wish to filter the projections $p_\phi(s_1', s_3')$. An example of such 2D projections for the Shepp-Logan phantom is shown in Figure 5.8. Instead of interpolating $p_\phi(s_1, s_3)$ from $p_\phi(s_1', s_3')$ in order to filter the projection line-by-line, the DR filter can directly perform the ramp filtering. The reconstructed image is given by

$$f(\boldsymbol{x}) = \int_0^{\pi} (p_\phi * h_\alpha)(\boldsymbol{x} \cdot \boldsymbol{\beta}, \boldsymbol{x} \cdot \boldsymbol{\beta}^{\perp})\, \mathrm{d}\phi, \tag{5.23}$$

with h_α the DR filter for angle α and $*$ the 2D convolution operator.

5.5.1 Simulations

In order to test the filter, we generated 3D projections of a Shepp Logan phantom using RTK (Rit et al., 2014) with a parallel beam. 360 projections of 1000×1000 pixels were acquired with in-plane angles of $\pi/6$, $\pi/4$ and $\pi/3$, over a 180° range. The central slice was reconstructed, using a grid of 1000×1000 pixels of size 0.5×0.5 mm^2. The data was reconstructed either by rotating the projections then performing a standard filtered backprojection with the 1D ramp filter, or by using the directional ramp filter.

5.5.2 Results

Figure 5.9 shows the reconstructed Shepp-Logan phantom from projections acquired with in-plane angles of $\phi = \pi/6$, $\pi/4$ and $\pi/3$ using the 2D directional ramp filter without apodization. All reconstructions show ringing-like artifacts, although they are only visible with a tight colorscale. We also observe that the shape of the artifacts depends on the direction of the filter. The spatial resolution is not significantly different between the three reconstructions.

Figure 5.10 shows the reconstructions achieved using the directional ramp filter from projections acquired with an in-plane angle of $\phi = \pi/3$, compared to the usual reconstruction with the 1D ramp filter after rotation and without apodization. Using a Hamming window completely suppresses the ringing artifacts, although a loss in spatial resolution is visible. The directional ramp filter apodized with a Tukey window offers a trade-off between artifact suppression (some ringing artifatcts are

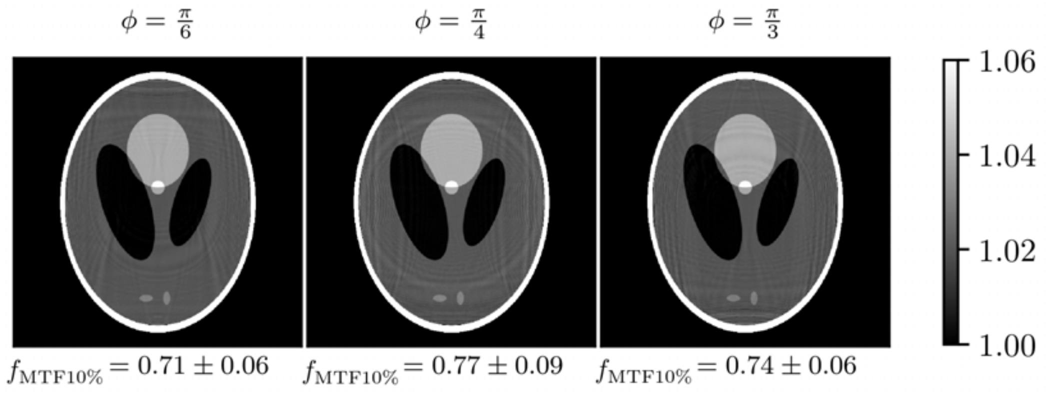

FIGURE 5.9 – Reconstructions of the central slice of the Shepp-Logan phantom using the non-apodized directional ramp filter, from projections acquired with different in-plane angles.

still visible near the object borders) and spatial resolution. The amplitude of the artifacts can be assessed on the vertical and horizontal profiles.

Figure 5.11 shows the MTFs in the Shepp-Logan phantom reconstructed using a rotation and 1D ramp filter, or the 2D DR filter with different apodizations. Results show the reconstruction with the non-apodized directional ramp filter has the best MTF although the associated uncertainty is quite high compared with the other reconstructions due to the artifacts. Apodizing the filter with a Tukey window gives a better resolution than the reconstruction after rotation while suppressing most artifacts, while the Hamming window causes a significant resolution loss. The resolution $f_{\mathrm{MTF10\%}}$ reaches 0.56 lp/mm for the reconstruction after rotation, 0.74 lp/mm for the 2D ramp, 0.66 lp/mm for the Tukey apodized DR and 0.42 lp/mm with the Hamming apodization.

5.5.3 Discussion

Our results show that the 2D directional ramp filter allows to reconstruct x-ray CT images from tilted projections without resorting to a rotation. The resulting reconstructed images benefit from a better spatial resolution, with an increase from 0.56 to 0.74 lp/mm. However, this improvement in terms of spatial resolution comes with ringing-like artifacts visible in Figure 5.9. The images reconstructed with the directional ramp filter are therefore noisier, which explains the larger uncertainty on the MTF compared to an apodized filter or a rotation (Figure 5.11).

We observed that the artifacts' shape depends on the direction of the filter. Since these artifacts are caused by the discontinuity of the DFT, each filter direction will produce a different discontinuity which will have different effects on the image in the direct space. To remove these artifacts, apodization windows like Hamming or Tukey are effective. The Tukey window offers a good alternative since it removes most of the artifacts except some over- and undershoots at the edges and still preserves the spatial resolution. We have shown the results using a Tukey window parameter of 0.5, but the window can be adjusted according to the severity of the artifacts. We also note that the artifacts are more important for this application than the previous one. This might be due to the fact that a single filter direction is used for all projections, such that the artifacts for different directions cannot even out.

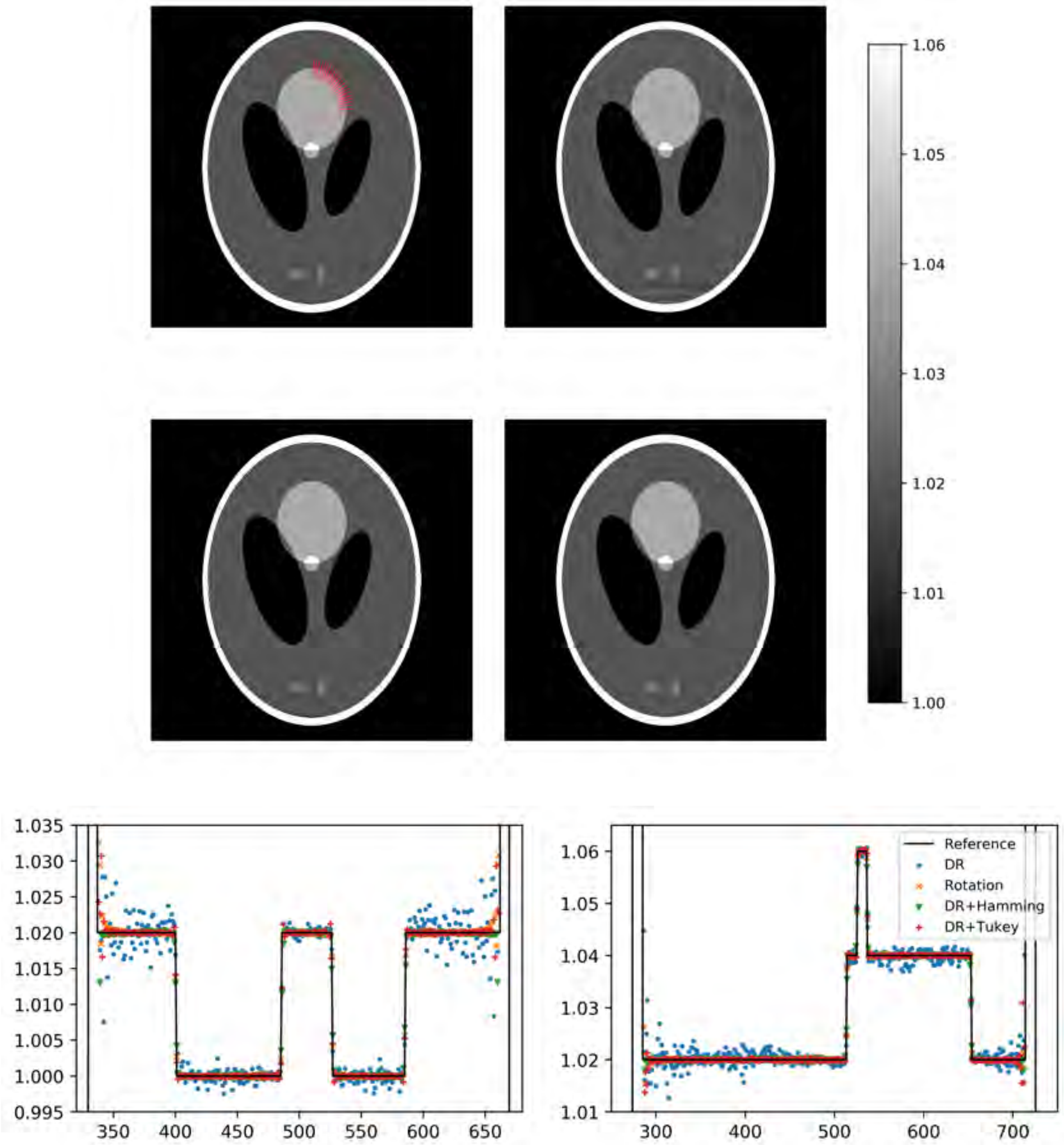

FIGURE 5.10 – Reconstructed central slice of the Shepp-Logan phantom from tilted projections, with rotation and 1D ramp filtering (top left), 2D directional ramp filter (top right), 2D directional filter apodized with a Tukey window (middle left) and a Hamming window (middle right). The edge profiles used to compute the spatial resolution are shown in red in the top left image. Horizontal (bottom left) and vertical (bottom right) central profiles are drawn for the four reconstructions.

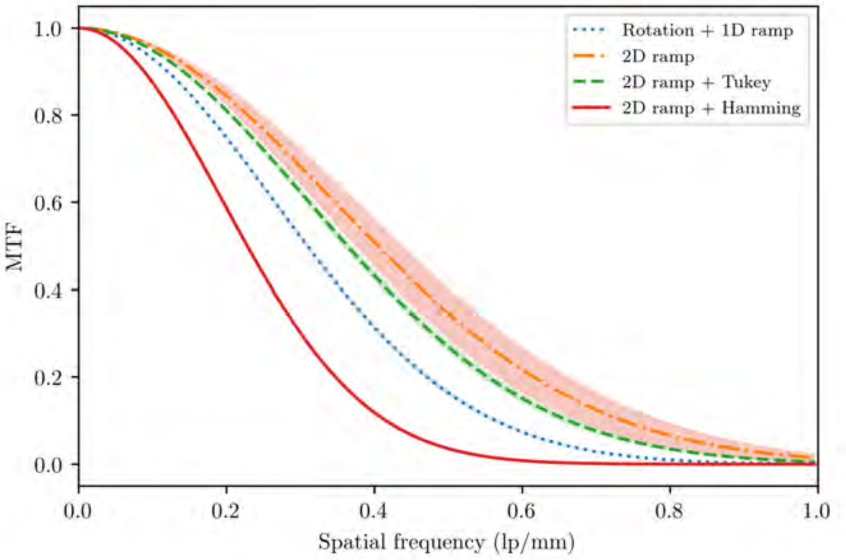

FIGURE 5.11 – Modulation transfer functions for the four different reconstructions. The filled envelopes represent the 3σ uncertainty on the MTF.

5.6 Conclusion

We have proposed a 2D version of the ramp filter, called directional ramp filter, and showed two possible applications. First, this filter can be used in place of the 1D ramp to take into account the depth dimension of pCT data. This reconstruction method starts by smearing each individual projection in the image space, performing the direction-dependent filtering, and finally summing over all projection angles. This allows an accurate reconstruction of pCT images and can be used to avoid an interpolation which would degrade spatial resolution. In the next chapter, this method will be more throughly compared to other pCT reconstruction methods in terms of spatial resolution and RSP accuracy.

Second, we have shown a different application in the context of 2D X-ray CT projections using tilted detectors. Again, the filter can be useful to preserve spatial resolution when used in place of a rotation, although special care must be taken to avoid introducing artifacts in the reconstructed image.

Chapter 6

A comparison of direct reconstruction algorithms in proton CT

In this chapter, we conduct a comparison of several non-iterative reconstruction algorithms for pCT, including the directional ramp method, in terms of spatial resolution and RSP accuracy. This chapter is adapted from Khellaf et al. (2020b).

6.1 Introduction

The inverse problem in pCT is similar to that in X-ray CT as it consists in reconstructing an image from line integrals. What makes it different are the non-linear integration lines representing the proton path estimates. We have briefly introduced the different reconstruction methods proposed to account for this non-linearity in pCT images in section 3.6.2. The MLP information can be included in iterative or analytical reconstruction algorithms to improve spatial resolution. In this chapter, we focus on analytical methods, although we prefer to call them "direct" rather than analytical, since there is no actual mathematical inversion for proton trajectories and all solutions are heuristic.

Iterative algorithms have advantages, e.g. including priors to improve image reconstruction (Hansen et al., 2014b), however, their computational cost is generally an order of magnitude larger than direct methods (Hansen, Sørensen, and Rit, 2016). A comparison between several iterative and one direct reconstruction methods was conducted by Hansen, Sørensen, and Rit (2016). However, no comparison between direct reconstruction methods was reported in the literature. The purpose of this work is to compare five different direct algorithms based on spatial resolution as well as RSP accuracy. Although some of the direct methods are quite close, they use different kinds of approximations which could impact spatial resolution and/or RSP accuracy. For instance, as discussed in the previous chapter, backproject-filter approaches fit the list-mode data more naturally and might give a better spatial resolution, but some of these methods also require the computation of correction terms that might degrade the RSP accuracy. By comparing these methods, this work aims to select the algorithm giving the best spatial resolution while keeping a high RSP accuracy (relative error about 0.1% to 0.5% (Penfold et al., 2009; Poludniowski et al., 2014)) with a reasonable computational cost.

6.2 Materials and Methods

The aim of pCT reconstruction is to build an RSP map from the protons' energy loss. We remind the inverse problem of pCT for a given proton i

$$\mathrm{WEPL}_i \equiv \int_{\boldsymbol{\Gamma}_i(t_i^{\mathrm{in}})}^{\boldsymbol{\Gamma}_i(t_i^{\mathrm{out}})} \mathrm{RSP}(\boldsymbol{\Gamma}_i(t))\,\mathrm{d}\boldsymbol{\Gamma}_i(t) \approx \int_{E_i^{\mathrm{out}}}^{E_i^{\mathrm{in}}} \frac{\mathrm{d}E}{S_{\mathrm{water}}(E)} \tag{6.1}$$

where $\boldsymbol{\Gamma}_i(t) \in \mathbb{R}^3$ is the proton path parametrized by $t \in \mathbb{R}$, t_i^{in} and t_i^{out} are the entrance and exit times, $\mathrm{RSP}(\boldsymbol{\Gamma}_i(t))$ is the stopping power relative to water at position $\boldsymbol{\Gamma}_i(t)$, E_i^{in} and E_i^{out} are the entrance and exit proton energies, and $S_{\mathrm{water}}(E)$ is the stopping power of water for energy E.

The WEPL can be computed by numerically integrating the right-hand side of Equation 6.1 using the measured entrance and exit energies and the Bethe-Bloch formula to estimate $S_{\mathrm{water}}(E)$. The MLP $\hat{\boldsymbol{\Gamma}}_i$ is computed using the formalism of Schulte et al. (2008). The difference between the reconstruction algorithms described below is in the method to invert the RSP integral along the MLP.

The following sections summarize the five algorithms included in this comparison: the distance-driven (DD) binning algorithm, the ML algorithm, the backprojection-then-filtering (BTF) method, the differentiated backprojection (DBP) method, and the directional ramp which will not be detailed as it is already presented in the previous chapter. All algorithms are presented in a parallel beam set-up for simplicity, although they can all be used with other geometries after appropriate rebinning of the list-mode data.

6.2.1 Distance-driven algorithm

It is the first direct reconstruction algorithm incorporating the MLP that was proposed in the literature (Rit et al., 2013). It consists in binning the protons into projections on a series of planes parallel to the detectors according to the estimated proton path, rather than binning just in the detector plane. The projection binning is done at several distances, hence the name of the algorithm.

The MLP formalism yields the coordinates $u_i(w)$ and $v_i(w)$ for each proton i, where w is the depth of the proton, following Equation 3.14. In practice, we compute this trajectory at a discrete number of distances w_k with $k \in \{1, ..., K\}$ such that $u_{i,k} = u_i(w_k)$ and $v_{i,k} = v_i(w_k)$ (Figure 6.1). The 3D proton trajectory at the time when proton i crosses the plane parallel to the detectors at distance w_k is written $\hat{\boldsymbol{\Gamma}}_i(t_{i,k}) \in \mathbb{R}^3$ such that

$$\begin{cases} u_{i,k} = \hat{\boldsymbol{\Gamma}}_i(t_{i,k}) \cdot \boldsymbol{e}_u \\ v_{i,k} = \hat{\boldsymbol{\Gamma}}_i(t_{i,k}) \cdot \boldsymbol{e}_v \\ w_k = \hat{\boldsymbol{\Gamma}}_i(t_{i,k}) \cdot \boldsymbol{e}_w. \end{cases} \tag{6.2}$$

Without loss of generality, we use the 3D path to bin the list-mode data into projections, but only the 2D central slice is considered in the following. The value in the sinogram for pixel j and source position p is given by

$$g_{j,p} = \frac{\sum_{i \in \mathbb{I}_p} \sum_k \zeta_j(u_{i,k}, v_{i,k}, w_k) \mathrm{WEPL}_i}{\sum_{i \in \mathbb{I}_p} \sum_k \zeta_j(u_{i,k}, v_{i,k}, w_k)} \tag{6.3}$$

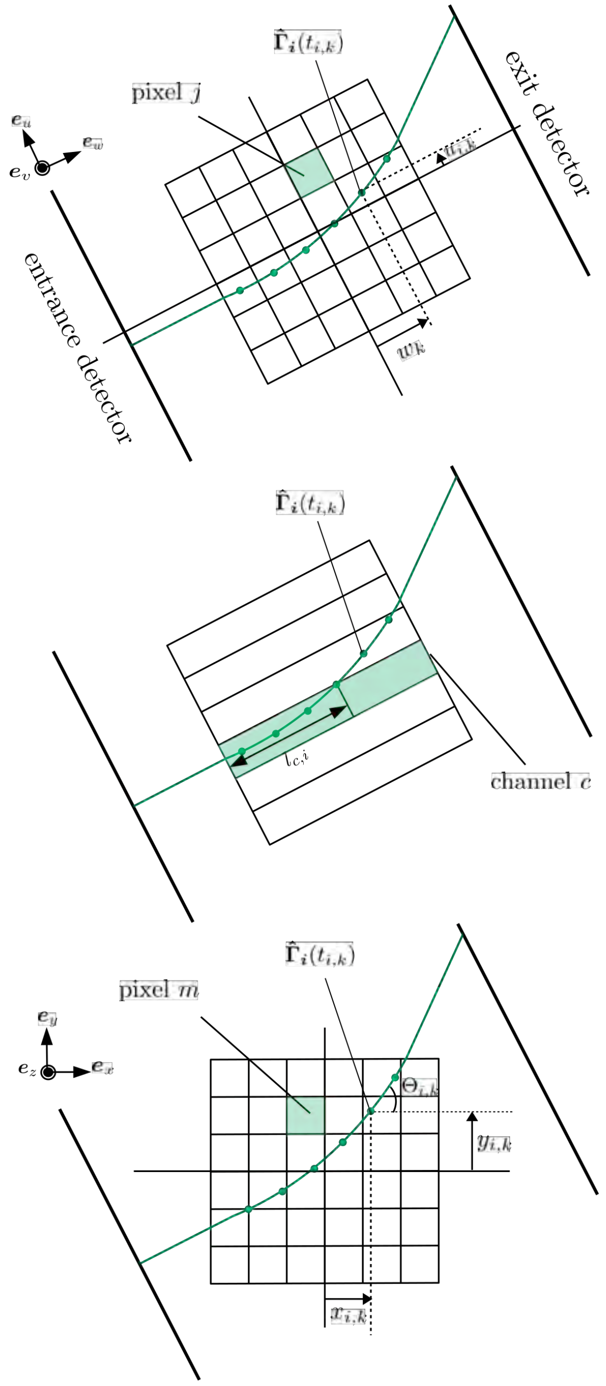

FIGURE 6.1 – pCT set-up with a parallel proton beam. The top figure corresponds to the geometry in the frame of reference of the source/detector used for the distance-driven binning, i.e. the unit vectors $(\boldsymbol{e}_u, \boldsymbol{e}_v, \boldsymbol{e}_w)$ define a coordinate system with $\boldsymbol{e}_u$ defining the detector surface, $\boldsymbol{e}_w$ the proton beam direction and $\boldsymbol{e}_v$ the axial direction. The middle figure corresponds to the geometry used in the ML method. The bottom figure corresponds to the geometry in the frame of reference of the object used for the backprojection binning, with $(\boldsymbol{e}_x, \boldsymbol{e}_y, \boldsymbol{e}_z)$ a fixed coordinate system.

where ζ_j is the indicator function for pixel j defined as

$$\zeta_j(\boldsymbol{y}) = \begin{cases} 1 & \text{if } \boldsymbol{y} \in \mathbb{R}^3 \text{ is in pixel } j, \\ 0 & \text{otherwise,} \end{cases} \tag{6.4}$$

and $\mathbb{I}_p$ is the subset of protons emitted from the same source position p. Note that the sinogram for a single slice is in 3D since it depends on the source position and the 2D pixel index. The filtering and backprojection steps are the same as in a standard filtered backprojection algorithm, except that a voxel-specific backprojection is used to select which distance w to use, instead of the usual pixel-specific backprojection. Specifically, we define the 2D projections $g_p(u,w) : \mathbb{R}^2 \to \mathbb{R}$ as

$$g_p(u,w) = \sum_j g_{j,p}\psi_j(u,w), \tag{6.5}$$

with $\psi_j(u,w)$ a given interpolation function. The reconstructed image $f^{\mathrm{DD}}(\boldsymbol{x}) : \mathbb{R}^2 \to \mathbb{R}$ is then given by

$$f^{\mathrm{DD}}(\boldsymbol{x}) = \sum_p \tilde{g}_p(\boldsymbol{x}\cdot\boldsymbol{e}_u, \boldsymbol{x}\cdot\boldsymbol{e}_w)\Delta\theta \tag{6.6}$$

with $\boldsymbol{x} = (x,y) \in \mathbb{R}^2$, $\tilde{g}_p$ the ramp-filtered projection g_p, and $\Delta\theta$ the constant angular spacing between consecutive projections.

6.2.2 Maximum likelihood algorithm

This method proposes to maximize the likelihood of the water equivalent thickness (WET) in proton radiographs, i.e. on the projection level, in order to improve their spatial resolution (Collins-Fekete et al., 2016). These optimized radiographs are then used to reconstruct a pCT image using a standard FBP. Specifically, the WET's likelihood is maximized for each so-called "channel" c in a radiograph, where a channel is the volume defined by the pixel corners along the source direction (see Figure 6.1). The WET value for channel c and source position p is obtained given the measured WEPL and the estimated trajectory for each proton using

$$\mathrm{WET}_{c,p} = \frac{\sum_{i\in\mathbb{I}_p} \frac{l_{c,i}^2}{L_i^2}\mathrm{WEPL}_i}{\sum_{i\in\mathbb{I}_p} \frac{l_{c,i}^2}{L_i^2}} \tag{6.7}$$

with $l_{c,i}$ the length of the i-th proton in channel c and L_i its total path length. This is similar to the DD algorithm, except that the WEPL is integrated along the w direction to form a single projection per source position while the DD uses a series of depth dependent projections. Also, the weights for the ML correspond to proportions of proton trajectories spent in a given channel ($\frac{l_{c,i}^2}{L_i^2}$) while for the DD method, the weighting function ζ_j is binary. To reconstruct the pCT image, the radiographs $\mathrm{WET}_{c,p}$ are simply fed to a standard filtered backprojection algorithm (Feldkamp, Davis, and Kress, 1984). As in the DD, we define interpolated projections

$$\mathrm{WET}_p(u) = \sum_c \mathrm{WET}_{c,p}\psi_c(u), \tag{6.8}$$

giving the following reconstructed image

$$f^{\mathrm{ML}}(\boldsymbol{x}) = \sum_p \widetilde{\mathrm{WET}}_p(\boldsymbol{x} \cdot \boldsymbol{e}_u)\Delta\theta, \tag{6.9}$$

where $\widetilde{\mathrm{WET}}_p(u)$ is the filtered projection $\mathrm{WET}_p(u)$.

6.2.3 Backprojection-then-filtering algorithm

This algorithm inverts the order of the backprojection and the filtering so that we directly backproject the protons along their MLPs, instead of binning them into a sinogram first (Poludniowski et al., 2014). The following coordinates in the image space are used for the backprojection (Figure 6.1)

$$\begin{cases} x_{i,k} = \hat{\boldsymbol{\Gamma}}_i(t_{i,k}) \cdot \boldsymbol{e}_x \\ y_{i,k} = \hat{\boldsymbol{\Gamma}}_i(t_{i,k}) \cdot \boldsymbol{e}_y \\ z_{i,k} = \hat{\boldsymbol{\Gamma}}_i(t_{i,k}) \cdot \boldsymbol{e}_z. \end{cases} \tag{6.10}$$

An intermediate step for calculating the backprojection from the list-mode data is a pixel-wise and direction-wise binning in the image space,

$$b_{m,n} = \frac{\sum_{i,k} \zeta_m(x_{i,k}, y_{i,k}, z_{i,k})\xi_n(\Theta_{i,k})\mathrm{WEPL}_i}{\sum_{i,k} \zeta_m(x_{i,k}, y_{i,k}, z_{i,k})\xi_n(\Theta_{i,k})}, \tag{6.11}$$

with indicator functions

$$\zeta_m(\boldsymbol{y}) = \begin{cases} 1 & \text{if } \boldsymbol{y} \in \mathbb{R}^3 \text{ is in pixel } m, \\ 0 & \text{otherwise,} \end{cases} \tag{6.12}$$

and

$$\xi_n(\Theta_{i,k}) = \begin{cases} 1 & \text{if } \Theta_{i,k} \in \mathbb{R} \text{ is in angular bin } n, \\ 0 & \text{otherwise.} \end{cases} \tag{6.13}$$

This binning was first presented in Rit et al. (2015). The WEPL for each proton is smeared along the corresponding path in the image grid using ζ_m, an indicator function for pixel m, and ξ_n, an indicator function for angular bin θ_n. $\Theta_{i,k}$ is the angle of proton i at depth w_k with respect to $\boldsymbol{e}_x$ (Figure 6.1). This binning was also used for the differentiated backprojection algorithm and the directional ramp filter method. Note that $b_{m,n}$ is not strictly speaking a backprojection but rather an average of the WEPL of protons passing through pixel m with an angle $\simeq \theta_n$. This direction-wise binning allows to rebin the data into parallel geometry (in case another geometry is used) as it uses the proton's angle $\Theta_{i,k}$ with respect to $\boldsymbol{e}_x$ rather than the subsets $\mathbb{I}_p$ as in the previous methods. We interpolate an image $b_n(\boldsymbol{x}) : \mathbb{R}^2 \to \mathbb{R}$ defined as

$$b_n(\boldsymbol{x}) = \sum_m b_{m,n}\psi_m(\boldsymbol{x}), \tag{6.14}$$

giving the backprojected image

$$B(\boldsymbol{x}) = \sum_n b_n(\boldsymbol{x})\Delta\theta. \tag{6.15}$$

In the backprojection-then-filtering (BTF) method, the image is reconstructed by convolving the backprojection with a 2D cone filter defined in the Fourier space as

$$C(\rho = \|\boldsymbol{\nu}\|) = \begin{cases} \rho & \text{if } \rho < 1/(2\tau) \\ 0 & \text{otherwise} \end{cases} \tag{6.16}$$

where $\boldsymbol{\nu}$ is the Fourier vector corresponding to $\boldsymbol{x}$ in the direct space, and τ is the pixel spacing. The expression of the filter in the direct space is obtained by taking the inverse Fourier transform of $C(\rho)$, yielding

$$c(r = \|\boldsymbol{x}\|) = \begin{cases} \dfrac{1}{4\pi^2 r^3}\left[\left(\dfrac{\pi r}{\tau}\right)^2 J_1\left(\dfrac{\pi r}{\tau}\right) - \phi\left(\dfrac{\pi r}{\tau}\right)\right] & \text{if } r \neq 0 \\ \dfrac{\pi}{12\tau^3} & \text{if } r = 0 \end{cases} \tag{6.17}$$

with $\phi(x) = \dfrac{\pi x}{2}[J_1(x)H_0(x) - J_0(x)H_1(x)]$, where J_n and H_n are the nth order Bessel and Struve functions. Ideally, the reconstruction can be computed using

$$f^{\mathrm{BTF}}(\boldsymbol{x}) = (B * c)(\boldsymbol{x}). \tag{6.18}$$

Since the backprojection B has an infinite support, its computation as a finite size matrix will cause artifacts, namely a constant offset of the reconstructed values. In order to mitigate the effects of truncating B during the convolution, the backprojection is computed on a very large matrix (for a reconstruction region of size $N \times N$, the backprojection region can be $2N \times 2N$ or $4N \times 4N$). We chose to use a size of $2N \times 2N$ to keep a reasonable computation time. This reduces the bias but a correction is still needed. The contribution of distant data of B to the reconstruction is approximated by a factor

$$\Delta(\boldsymbol{x}) \approx \int_{\Omega_f} f^{\mathrm{BTF}}(\boldsymbol{x}')\,\mathrm{d}\boldsymbol{x}' \int_{\Omega_{ob}} \frac{c(\boldsymbol{x} - \boldsymbol{x}')}{r'}\,\mathrm{d}\boldsymbol{x}', \tag{6.19}$$

with Ω_f the reconstruction region and Ω_{ob} the region outside the computed backprojection matrix. While this second integral is over an infinite domain, in practice, the filter $c(\boldsymbol{x})$ is computed on an even larger matrix than the backprojection matrix (we used a size of $8N \times 8N$). Since the shift in the reconstructed values caused by truncation is constant (i.e. pixel independent), the correction is calculated only for the central pixel and then the same factor is applied to all pixels.The final image is given by

$$f^{\mathrm{BTF},\Delta} = f^{\mathrm{BTF}} + \Delta. \tag{6.20}$$

6.2.4 Differentiated backprojection algorithm

This algorithm is based on the two-step Hilbert transform method (Noo, Clackdoyle, and Pack, 2004) originally proposed for X-ray CT. It relies on the relationship between the backprojection of the derivative of the projections and the Hilbert transform of the image. The image is reconstructed from

$$f(x, y) = \mathcal{H}^{-1} \int_0^{\pi} \frac{\partial}{\partial s} p(s, \theta)\big|_{s = -x\sin\theta + y\cos\theta}\,\mathrm{d}\theta, \tag{6.21}$$

with $\mathcal{H}^{-1}$ the inverse of the Hilbert transform and $p(s,\theta)$ an X-ray CT projection at angle θ. Basically, the ramp filter used in an FBP approach is equivalent to a combination of a differentiation and a Hilbert transform. A formula for the inverse Hilbert transform of a function $g(s)$ known inside $[L,U]$, given that $\mathcal{H}^{-1}g(s)$ is zero outside $[L+\epsilon, U-\epsilon]$, is

$$\mathcal{H}^{-1}g(s) = \frac{-1}{\sqrt{(s-L)(U-s)}}\left(\int_L^U \sqrt{(s'-L)(U-s')}\frac{g(s')}{\pi(s-s')}\,\mathrm{d}s' + C\right). \tag{6.22}$$

The constant C is obtained by using points where $\mathcal{H}^{-1}g(s) = 0$ and solving Equation 6.22. The result is averaged over several points satisfying this condition for a better accuracy. Therefore, the convex hull of the object must be known to select these points (an information which is also used in our implementation of the MLP). This inversion is done line-by-line on the backprojected image since the inverse Hilbert transform is a 1D operator. The advantage of this approach is that, as the backprojection of the derivative is related to a 1D operator, truncated data can still be reconstructed in cases when points are lying on at least one line segment having its two end points in the field of view and outside the object to reconstruct, i.e. satisfying the conditions to be able to compute the inverse Hilbert transform. This method was adapted to work with list-mode data by inverting the order of the differentiation and the backprojection steps (Zeng, 2007), giving the following reconstruction formula

$$f^{\mathrm{DBP}}(x,y) = \mathcal{H}^{-1}\left(\frac{\partial}{\partial x}B^s(x,y) + \frac{\partial}{\partial y}B^c(x,y)\right). \tag{6.23}$$

Due to the partial differentiation, two intermediate weighted backprojections must be computed

$$B^s(\boldsymbol{x}) = -\sum_n b_n(\boldsymbol{x}) \sin\theta_n \Delta\theta, \tag{6.24}$$

$$B^c(\boldsymbol{x}) = \sum_n b_n(\boldsymbol{x}) \cos\theta_n \Delta\theta. \tag{6.25}$$

This method was applied to pCT data by Rit et al. (2015).

6.2.5 Simulations

The same simulation setup as the one described in section 5.2.5 was used in GATE (Jan et al., 2011) to generate pCT data. Three phantoms were imaged: the CTP528 module of the Catphan phantom (The Phantom Laboratory, NY) with aluminium line pairs of different resolutions in a 20 cm diameter water cylinder (unlike the original phantom where the line pairs are cast into epoxy, they are cast into water here); the spiral phantom, consisting of aluminium cylinders placed along a spiral in a 20 cm diameter water cylinder (Rit et al., 2015), and the Gammex 467 tissue characterization phantom with different tissues inserts inside a 33 cm diameter water cylinder (Figure 6.2). The phantoms used for spatial resolution assessment (Catphan and spiral) were reconstructed in images of 1000 × 1000 pixels with a pixel spacing of 0.25 mm. The Gammex 467 was reconstructed on a grid of 800 × 800 pixels of spacing 0.5 mm and required a beam energy of 250 MeV because of its larger diameter, instead of 200 MeV for the other two phantoms.

In order to estimate the impact of detector uncertainties on spatial resolution, an uncertainty on the simulated position and direction data was added using the

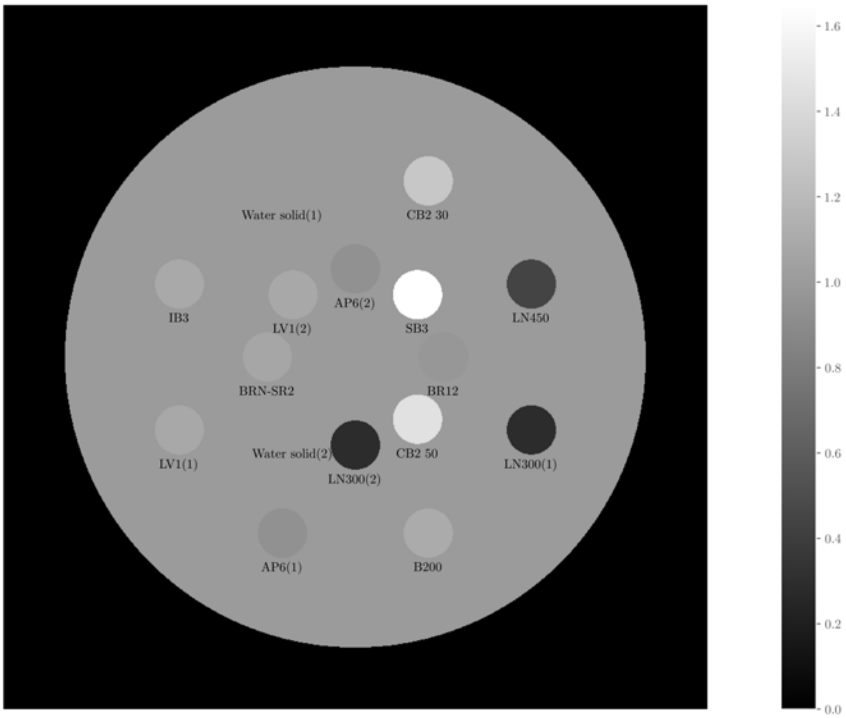

FIGURE 6.2 – RSP map of the Gammex 467 tissue characterization phantom.

formalism of Krah et al. (2018c). The parameters were chosen to reflect a typical pCT prototype. In particular, the detector resolution (pitch of strips) was characterized by a Gaussian of $\sigma_p = 0.15$ mm, the distance between the trackers was set to $d_T = 10$ cm (each real detector consists of a pair of trackers), the distance between the trackers and the object border to 20 cm, and the material budget to $x/X_0 = 5 \times 10^{-3}$.

The energy resolution of the detectors and the spread of the incident beam were omitted for simplicity as scintillating detectors (Bashkirov et al., 2016a) are capable of achieving a WEPL resolution close to the limit due to proton range straggling (measured WEPL resolution of 3 mm for a range straggling of 2.85 mm, for 200 MeV protons in water), although we note the beam spread can contribute to the WEPL variance up to 20% (Dickmann et al., 2019). Electromagnetic interactions are taken into account in the simulation and are responsible for the RSP resolution of the reconstructed images.

6.2.6 Image quality metrics

Both spatial resolution and RSP accuracy were evaluated. The spatial resolution was assessed qualitatively using the Catphan phantom and quantitatively with the spiral phantom. The same method as the one presented in section 5.2.6 was used to evaluate the spatial resolution in the spiral phantom. In addition, we measured the radial and azimuthal resolutions defined as in Plautz et al. (2016) in order to assess the (an)isotropy of the spatial resolution. The radial resolution was measured using ESFs along the direction from the isocenter to the center of the bead and the azimuthal resolution was measured from profiles along the direction perpendicular to the radial direction. Profiles were sampled and averaged for angles in a range of $\pm 10^{\circ}$ around these two directions.

Each algorithm's RSP accuracy was evaluated by computing the mean value in each insert of the Gammex phantom. A region of interest (ROI) of radius 8 mm was used (the radius of the inserts is 14 mm) so that the measured RSP value would not be impacted by the inserts' spatial resolution. The uncertainty on the measured RSP is computed using the 95% confidence limits of the mean, i.e. $\pm 1.96\sigma_{\text{ROI}}/\sqrt{N_{\text{ROI}}}$, with σ_{ROI} the standard deviation of the RSP values in the ROI and N_{ROI} the number of pixels inside the ROI.

6.3 Results

The reconstructed images of the Catphan and spiral phantoms are shown in Figure 6.3. For the Catphan phantom, the five reconstructions are quite similar, as confirmed by the line profiles drawn in Figure 6.4. All algorithms underestimate the RSP of aluminium in the Catphan phantom due to the impact of axial resolution (the height of the line pairs is 2 mm). The ML reconstruction leads to a lower resolution, causing a larger underestimation of the RSP value of the aluminium inserts. Regarding the spiral phantom reconstructed from data simulated with ideal trackers (middle column of Figure 6.3), the central beads appear much blurrier than the outer beads for all algorithms. This is expected because the MLP uncertainty is largest for those inserts. A slight artifact is seen for the ML reconstruction where the outer beads appear smeared along the azimuthal direction. This is visible on the zoomed insets, although it is exaggerated by using a color scale with a small range. Figure 6.5 shows the spatial resolution as a function of each bead's distance to the centre of the spiral phantom, for reconstructions with ideal trackers and realistic trackers. For ideal trackers, resolution is about a factor 4 to 6 higher for beads near the phantom borders compared with the resolution at the centre. The resolution of the ML algorithm is lower than other algorithms: it only reaches 1 lp/mm for the outermost bead and is also smaller for central beads. Differences in spatial resolution among the other four algorithms are much smaller, especially below a distance of about 80 mm from the center. Beyond that distance, i.e. closer to the phantom edge, the DR and BTF algorithms reach similar resolutions (up to 3.5 and 3.3 lp/mm, respectively), while the DBP and DD methods both reach about 2.7 lp/mm. Figure 6.6 presents a more extensive analysis of the ideal spatial resolution, discriminating between the radial and azimuthal resolutions. The azimuthal resolution is higher than the radial resolution for all algorithms except ML.

The right column of Figure 6.3 shows that the resolution with realistic trackers is considerably lower than with ideal ones. In Figure 6.5, we observe that the maximum resolution for all algorithms only reaches between 0.39 and 0.42 lp/mm, and that the difference of spatial resolution between the center and the borders is much less important than with ideal detectors. For example, for the DD algorithm, it only increases by a factor of 1.3 between the central bead and the outer bead, versus a factor of 4.6 with ideal detectors. In addition, the differences in spatial resolution observed between the algorithms are mostly insignificant considering the uncertainty on the MTF. Only the ML algorithm still shows a slightly lower resolution although it is much closer to other algorithms compared to the ideal case.

Table 6.1 shows the relative error on the RSP value in each insert of the reconstructed Gammex phantom. The most accurate algorithms are the DR and DD, with a mean relative error of 0.07% and 0.08% respectively, followed by the BTF with an error of 0.11%, the DBP with 0.19%, and the ML with a mean error of 0.25%. The uncertainty in Figure 6.7 shows that the majority of the reconstructed RSP values are

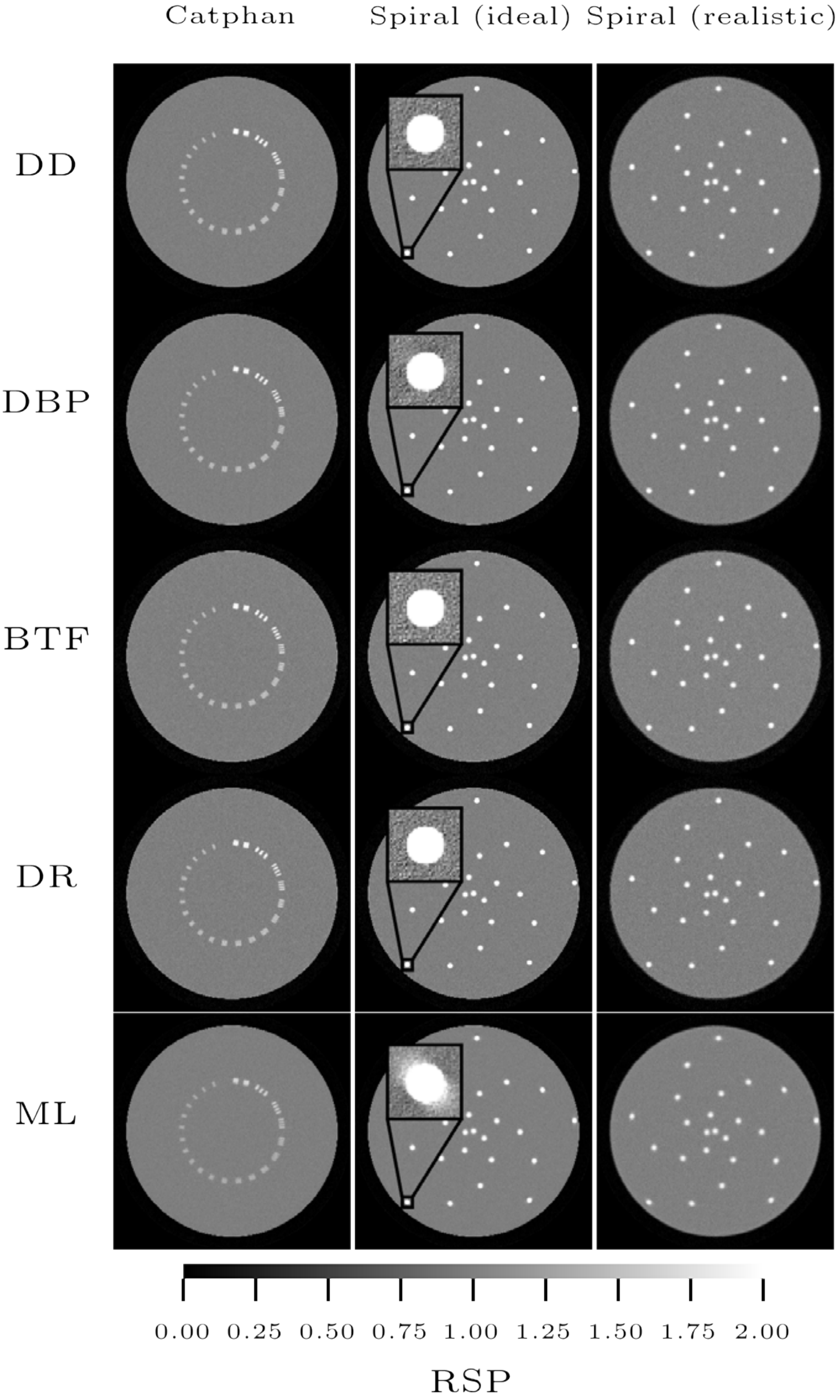

FIGURE 6.3 – Reconstructions of the Catphan and spiral phantoms for the five algorithms. The Catphan is reconstructed from idealized data. Zoomed insets of a peripheral bead are shown to appreciate the artifact reconstructed by the ML algorithm. The extent of the color scale in the insets is [0.7,1.3] to highlight the artifact.

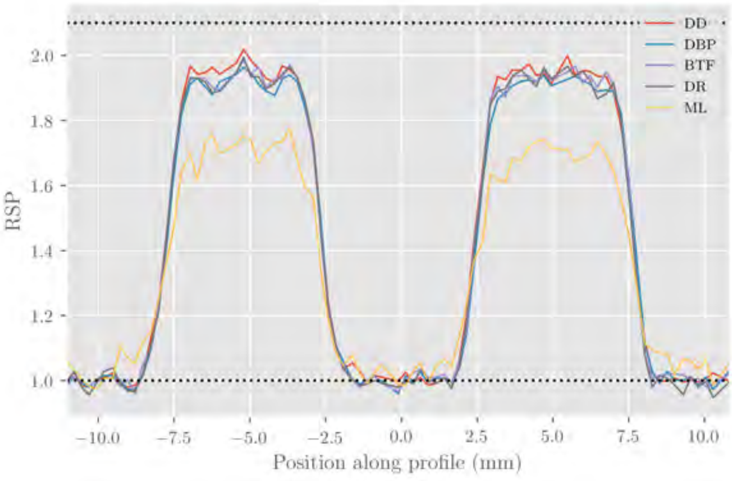

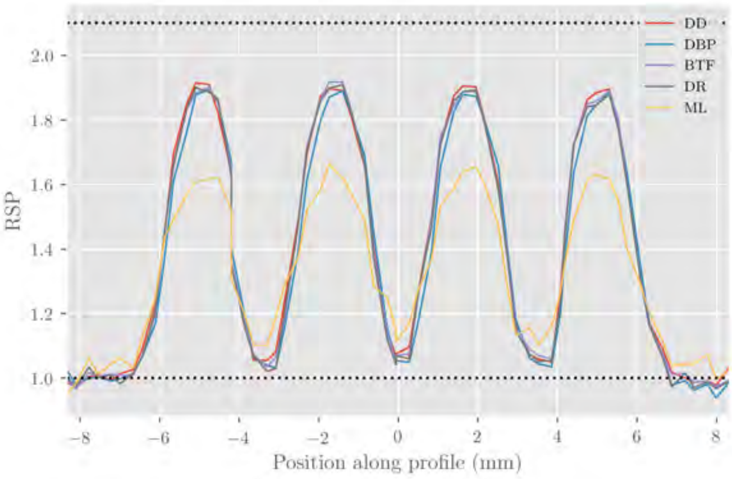

FIGURE 6.4 – Line profiles along first (top) and third (bottom) line pairs in the Catphan phantom. The dotted lines represent the theoretical RSP values of water (RSP=1) and aluminium (RSP=2.1).

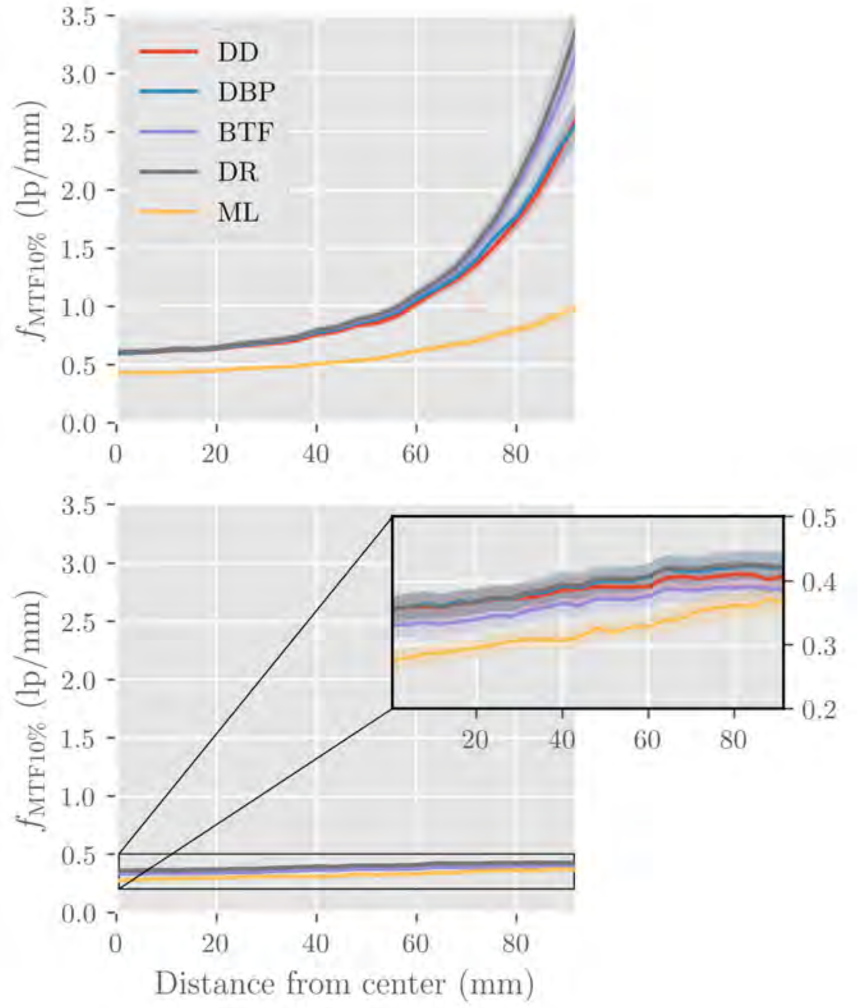

FIGURE 6.5 – Spatial resolution measured as the frequency for an MTF value of 10% in function of distance from the isocenter, for ideal trackers (top) and realistic trackers (bottom). The shaded areas represent the uncertainty on the MTF estimation.

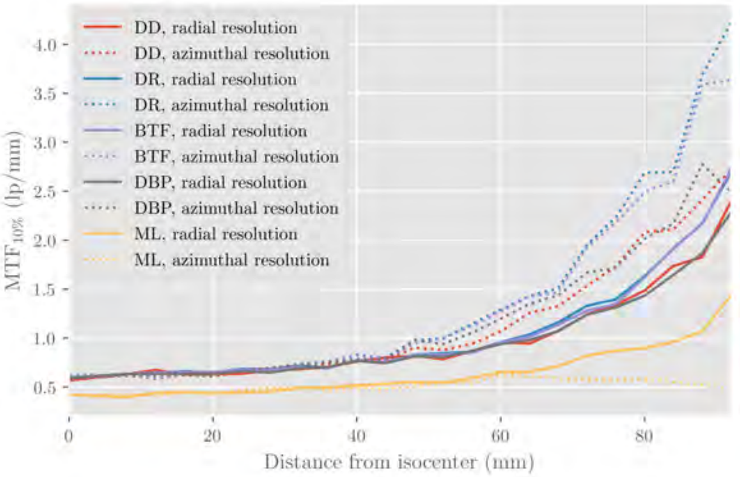

FIGURE 6.6 – Spatial resolution for ideal trackers computed on profiles along the normal and tangent directions to the edge. Error bars were omitted for clarity.

TABLE 6.1 – Relative error on the measured RSP values.

Insert	Reference	DD	BTF	DBP	ML	DR
LN300(1)	0.295	-0.15%	0.02%	-0.44%	1.32%	-0.21%
IB3	1.094	-0.04%	0.02%	-0.19%	-0.02%	-0.03%
LV1 (1)	1.084	-0.03%	0.05%	-0.21%	-0.03%	-0.01%
LN450	0.443	-0.27%	-0.06%	-0.24%	0.54%	-0.21%
B200	1.103	-0.04%	0.06%	-0.18%	-0.17%	<0.01%
Water_Solid (1)	1.005	-0.03%	0.06%	-0.16%	0.05%	-0.01%
CB2_30	1.286	0.04%	0.10%	-0.14%	-0.13%	0.07%
AP6 (1)	0.940	0.04%	0.08%	-0.15%	0.03%	0.02%
BR12	0.974	-0.01%	-0.17%	-0.15%	-0.03%	0.01%
BRN-SR2	1.073	0.08%	-0.06%	-0.05%	0.01%	0.07%
CB2_50	1.449	-0.11%	-0.18%	-0.25%	-0.13%	-0.08%
SB3	1.649	-0.16%	-0.19%	-0.20%	-0.13%	-0.08%
LN300 (2)	0.295	0.05%	-0.59%	-0.30%	1.16%	-0.07%
AP6 (2)	0.940	0.14%	<0.01%	0.19%	0.18%	0.18%
LV1 (2)	1.084	0.04%	-0.08%	-0.06%	0.06%	0.07%
Water_Solid (2)	1.005	0.06%	-0.06%	-0.11%	0.06%	0.07%
Mean abs error		0.08%	0.11%	0.19%	0.25%	0.07%

very close, with differences within the confidence intervals of the mean. The RSP error in the lung inserts, however, reaches over 1% for the ML method.

6.4 Discussion

The aim of this work was to compare the performance of five direct reconstruction algorithms in terms of spatial resolution and RSP accuracy. Spatial resolution in pCT is impacted by various factors. A first factor is MCS which is mitigated to some extent by modeling the MLP (Schulte et al., 2008). This greatly improves spatial resolution compared to naive straight line trajectories, although the effect of scattering is still important especially at the center of the phantoms where the MLP estimate is most uncertain. We have observed that the resolution at the center of a 20 cm wide phantom is about $0.5 - 0.6$ lp/mm with ideal trackers. For the DR method, the resolution is improved by a factor of 6 between the center and the border of the spiral phantom. Since the center of the object corresponds to the largest uncertainty on the MLP, differences in spatial resolution between the algorithms are not significant near the center.

Another consequence of proton scatter is the anisotropy of the spatial resolution. As expected, the azimuthal resolution gets higher than the radial resolution with the distance to the center. Due to scatter, the uncertainty on the MLP of protons traversing the same region will depend on the thickness of material traversed, i.e. on their initial direction. For central beads, the variation of the traversed thickness depending on direction will be small because of the cylindrical shape of the phantom, such that resolution is isotropic at the center. The only algorithm for which the azimuthal resolution is poor is the ML algorithm, due to the artifact observed in Figure 6.3. This artifact can be explained by the uncertainty on the MLP. We mentioned that the ML method basically consists in integrating the DD's binning along the w direction. We know that the projections that are farthest from the detectors will be the most blurry due to a large uncertainty on the MLP. For the outer beads of the spiral phantom, the most blurry projection contributing to their reconstruction is the one where protons have had the longest trajectory inside the phantom, i.e. the ones that contribute to

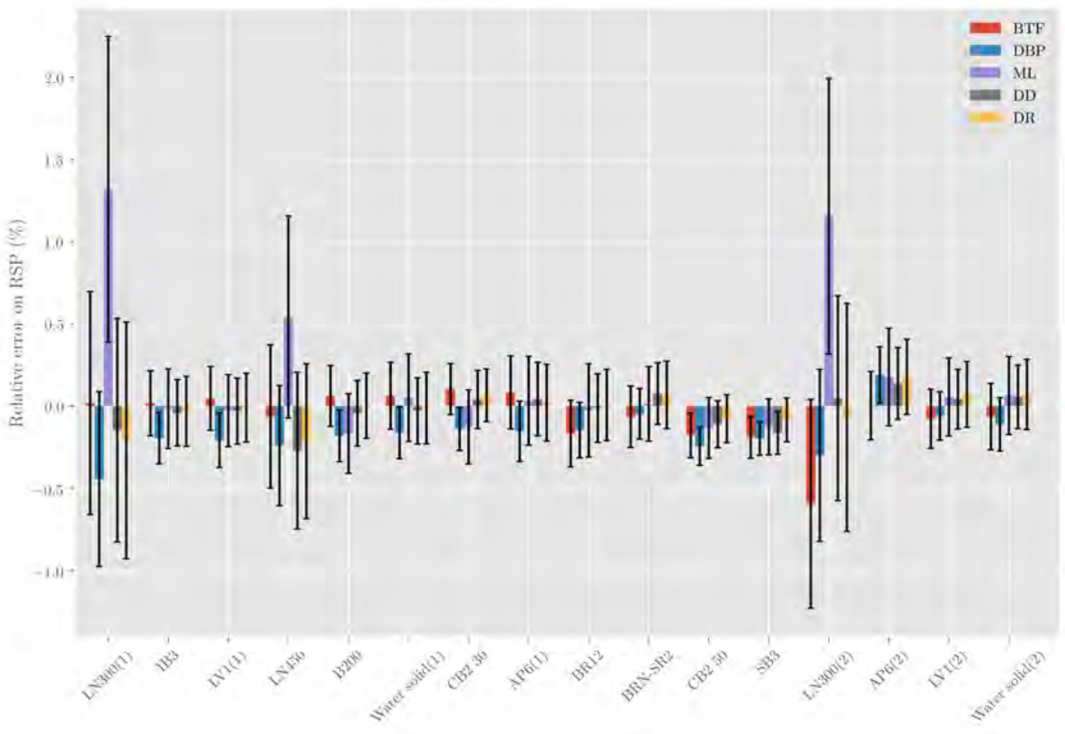

FIGURE 6.7 – Relative error on RSP with confidence limits.

the azimuthal resolution. This explains why the outer beads seem smeared on the ML reconstruction.

Another factor of resolution loss is the tracker uncertainties which have a significant impact as can be seen in Figure 6.5. Adding an uncertainty on the position and direction measurements dramatically lowers the spatial resolution compared to ideal simulated data. It should be noted that those results were obtained for a distance of 20 cm between the trackers and the borders of the phantom. Using larger distances would further reduce resolution.

Finally, the choice of the algorithm also has an impact on the resolution as different binnings and interpolations are involved. For example, using ideal detectors, the resolution 96 mm away from the center for the DR method is 250% higher than the ML algorithm's resolution (only 25% at the center), and 26% higher than the DD algorithm's resolution (1% at the center). Our results show that the best performing algorithms in terms of spatial resolution away from the center are the DR and BTF, suggesting that backprojecting the protons before filtering can improve spatial resolution. Indeed, filter-first methods imply two interpolations that can reduce spatial resolution: the projection binning and the backprojection. On the other hand, only one is needed for backproject-first methods. This could preserve the spatial information of proton paths and therefore the resolution. However, we have seen that the DBP method, which starts with the backprojection, has the same spatial resolution as the DD. A possible explanation is that the discrete differentiation computed in the DBP algorithm, using differences of adjacent pixels, may cause a loss of spatial resolution. The ML algorithm shows the worst spatial resolution as it attempts to account for MLPs in the 2D projections, but they can only be described in 3D space. This method might be better suited for proton radiography than CT. Overall, the impact of the choice of the algorithm is negligible compared with MLP and tracker uncertainty.

In terms of RSP, the DR, DD and BTF show good accuracy with mean absolute errors close to 0.1%. The DBP method is slightly less accurate, which can be linked to the computation of a constant during the Hilbert transform inversion (Noo, Clackdoyle, and Pack, 2004), as it is the result of averaging points outside the support of the object (Equation 6.22). However, this error is not significant with respect to the 95% confidence interval of the mean (Figure 6.7).The ML algorithm overestimates the RSP value in the lung inserts compared with the other methods, resulting in a higher mean error. An explanation is that as it uses channels instead of pixels, the WEPL value of a proton that has not traversed a lung insert can still be attributed to it. While this would happen for all inserts, lung inserts would be more impacted because the difference between the RSP of the lung and the rest of the phantom is larger than for other inserts.

The computational cost of each algorithm is an important factor when several algorithms reach similar levels of resolution and RSP accuracy. The binning of the list-mode data is the most costly operation as the MLP of each proton has to be computed. The binning steps to compute projections as in Equation 6.3 or partial backprojections as in Equation 6.11 are mostly similar in terms of computational cost. This cost increases with the number of protons and the number of evaluations of the MLP. As we have used a high fluence (288×10^6 protons in total) and a small spacing for the MLP evaluation (0.25 mm or 0.5 mm depending on the phantom), our binning is orders of magnitude slower than the other reconstruction steps (for the DD, 8 s/projection × 720 projections for the binning, and 42 s for the filtering and backprojection). Both the BPF and DR methods require the backprojection region to be larger than the reconstructed image region, increasing the computation time of the binning. While the DR method requires backprojecting the list-mode data in a region larger by a factor of $\sqrt{2}$, the BPF method needs a matrix of at least two times the reconstruction matrix. They are therefore the most computationally expensive methods. The cost of the filtering step varies a lot depending on the algorithm. For example, for the DD, a 3D sinogram needs to be filtered (for each slice) compared with the usual 2D sinogram for the ML. However, as we stated above, the cost of the filtering step is quite negligible compared with the cost of the binning step.

6.5 Conclusion

We have studied the spatial resolution and RSP accuracy of five different algorithms used to reconstruct proton list-mode data. The results show that, using ideal trackers, two of the methods that bin the list-mode data directly in the image space (DR and BTF) offer a better spatial resolution at the borders of the object, with a maximum of 3.5 lp/mm at the borders of a 20 cm thick object. However, considering realistic measurement uncertainties, the impact of the choice of the algorithm on spatial resolution becomes negligible. Furthermore, the DR, DD, and BTF methods show the best RSP accuracy with a mean error close to 0.1%. While the DR and BTF methods have a slight advantage regarding spatial resolution as well as a good accuracy, they are also the most computationally expensive. For faster reconstructions, the DD algorithm offers the same accuracy and an equivalent spatial resolution considering detector uncertainties, and the DBP, while being somewhat less accurate, offers a good spatial resolution and can be used for reconstruction with truncated data. The ML, as it works in the projection level, is well suited for proton radiography.

Chapter 7

A deconvolution method to improve spatial resolution in pCT

In this chapter, we propose a method to deconvolve the uncertainty on the proton path due to MCS and tracker resolution, in order to improve the spatial resolution of the reconstructed image. Unlike other contributions (chapters 4, 5 and 6), this chapter has not been presented before. The work on the impact of tracker resolution on the MLP uncertainty was published in Krah et al. (2018a).

7.1 Introduction

The spatial resolution of pCT is mainly impacted by MCS of the protons and tracker resolution. As was observed in the previous chapter, the spatial resolution in the reconstructed image is shift-variant and anisotropic. The uncertainty on the proton path only depends on the depth of the proton inside the object (Equation 4.3), and not on the measured entrance/exit transverse positions and directions. For given entrance and exit depths, the uncertainty on the MLP is the largest near the center of the path, where the proton is the farthest away from the trackers. It is slightly shifted towards the exit of the phantom due to the energy loss term in the scattering estimation. In addition, the longer the proton path inside the object, the larger the uncertainty envelope, such that the uncertainty depends on the shape of the object and the projection angle as the entrance/exit depths are given by the intersection of the object contours with the proton entrance/exit paths. The addition of tracker resolution will only increase this uncertainty. As the reconstructed image is a combination of the filtered projections, the blur in each image pixel is also the result of a combination of different uncertainties.

In this work, we try to deconvolve the pCT blur due to MCS and detector uncertainties by using an estimate of the MLP uncertainty. Deconvolution is conducted at the projection level to better take into account the space variance and asymmetry of the spatial resolution. Using the MLP uncertainty to improve spatial resolution has been mentioned by Williams (2004) and Schulte et al. (2008). Wang, Mackie, and Tomé (2010) have tried to include this uncertainty in the projection matrix and performed reconstruction using ART. However, their results did not show an improvement of spatial resolution compared with the use of the MLP without uncertainty information. We propose a method to deconvolve distance-driven projections for reconstruction with the method presented by Rit et al. (2013). In order to account for tracker resolution, we use the formalism of Krah et al. (2018a) who extended the usual MLP formalism to include tracker resolution for different kinds of set-ups. In particular, they give an expression for the MLP uncertainty taking into account the trackers' spatial and angular resolution. In the following section, we start by presenting the model for the shift-variant blur in the distance-driven projections, we use the formalism of Krah et al. (2018a) to compute distance-driven uncertainty maps, and deconvolve the uncertainty using a truncated singular value decomposition (TSVD) (Hansen, Nagy, and O'Leary, 2006).

7.2 Materials and methods

7.2.1 Shift variant deconvolution

We consider the binned projections $g_p(u,w)$ described in section 6.2.1, with u the lateral coordinate along the detector, w the depth, and p the source position. The blur in these projections will depend on w since the deeper the proton is inside the phantom, the larger the uncertainty on the MLP, and on u and p since protons entering and exiting the object through different depths will have different uncertainties. As the blur occurs in the (u,v) plane, we consider the distance-driven projections distance-by-distance, i.e., for each w. Therefore, we deal with a sequence of small 1D problems, which allows the singular value decomposition (SVD) approach described below. If the blur were not spatially variant, the measured projection would be the result of the convolution of an ideal projection $\hat{g}_p(u,w)$ with a constant convolution kernel h. However, as the blur depends on the position u, the measured projection is the result of a shift-variant operation

$$g_p(u,w) = \int h[u-u', \sigma_p(u',w)]\hat{g}_p(u',w)\,\mathrm{d}u' \tag{7.1}$$

where $\sigma_p(u',w)$ represents the MLP uncertainty of protons with source position p at depth w and position u'. The kernel function is a Gaussian due to the Gaussian model used for the MLP uncertainty

$$h[u-u', \sigma_p(u',w)] \propto \exp\Big(-\frac{(u-u')^2}{2\sigma_p(u',w)^2}\Big). \tag{7.2}$$

In matrix notation, we have

$$\mathbf{g}_w = \mathbf{H}_w\hat{\mathbf{g}}_w \tag{7.3}$$

where $\mathbf{g}_w$ is a vector containing one distance w of the distance-driven projection, $\mathbf{H}_w$ is the shift-variant system matrix for this distance, and $\hat{\mathbf{g}}_w$ is one distance of the deconvolved projection. The deconvolved projection is obtained by inverting $\mathbf{H}_w$

$$\hat{\mathbf{g}}_w = \mathbf{H}_w^{-1}\mathbf{g}_w. \tag{7.4}$$

This inversion has to be done for all distances and all projections before reconstruction. In practice, directly inverting $\mathbf{H}_w$ is impractical because of noise. The singular value decomposition (SVD) corresponds to a factorization of a matrix into a product of matrices, which can be useful to compute the inverse of a matrix (Hansen, Nagy, and O'Leary, 2006). The SVD of a square matrix $\mathbf{H}_w \in \mathbb{R}^{N\times N}$ is

$$\mathbf{H}_w = \mathbf{USV}^T \tag{7.5}$$

where $\mathbf{U}$ and $\mathbf{V}$ are orthogonal matrices such that $\mathbf{U}^T\mathbf{U} = \mathbf{I}_N$ and $\mathbf{V}^T\mathbf{V} = \mathbf{I}_N$; and $\mathbf{S} = \mathrm{diag}(s_1, ..., s_N)$ is a diagonal matrix with

$$s_1 \geq ... \geq s_N \geq 0. \tag{7.6}$$

The values s_i are called the singular values. The column vectors of $\mathbf{U} = [\mathbf{u}_1 ... \mathbf{u}_N]$ are called the left singular vectors, and the column vectors of $\mathbf{V} = [\mathbf{v}_1 ... \mathbf{v}_N]$ are the right singular vectors. The inverse of $\mathbf{H}_w$ is then given by

$$\begin{aligned} \mathbf{H}_w^{-1} &= \mathbf{V}\mathbf{S}^{-1}\mathbf{U}^T \\ &= \sum_{i=1}^{N} \frac{1}{s_i} \mathbf{v}_i \mathbf{u}_i^T \end{aligned} \tag{7.7}$$

We write the solution as a weighted sum of the singular vectors $\mathbf{v}_i$

$$\hat{\mathbf{g}}_w = \sum_{i=1}^{N} \frac{\mathbf{u}_i^T \mathbf{g}_w}{s_i} \mathbf{v}_i. \tag{7.8}$$

In order to leave out high-frequency noise, we choose a cut-off value $N_c < N$

$$\hat{\mathbf{g}}_w = \sum_{i=1}^{N_c} \frac{\mathbf{u}_i^T \mathbf{g}_w}{s_i} \mathbf{v}_i. \tag{7.9}$$

In practice, we chose a truncation level α to keep only the N_c singular values that verify $\dfrac{s_i}{\max(s_1, ..., s_N)} > \alpha$.

7.2.2 MLP uncertainty

In this section, we describe the formalism used to evaluate the σ values of the shift-variant kernel. The MLP formalism described in section 3.6 allows to compute the proton path and the associated uncertainty. The derivation assumes perfectly known entrance and exit parameters $\mathbf{y}_{\text{in}}$ and $\mathbf{y}_{\text{out}}$. In practice, the spatial and angular resolution of the trackers will result in an uncertainty on the measured parameters. Krah et al. (2018a) have included the impact of detector resolution on the MLP uncertainty envelope. We briefly introduce their formalism and give the formulas used to compute the σ values.

First, we redefine the joint probability that a proton passes through $\mathbf{y}_1$ and $\mathbf{y}_2 = \tilde{\mathbf{y}}_{\text{out}}$ given $\tilde{\mathbf{y}}_{\text{in}}$, with $\tilde{\mathbf{y}}_{\text{in}}$ and $\tilde{\mathbf{y}}_{\text{out}}$ the measured entrance and exit coordinates,

$$\begin{aligned} L(\mathbf{y}_1, \mathbf{y}_2 = \tilde{\mathbf{y}}_{\text{out}} | \tilde{\mathbf{y}}_{\text{in}}) = \int L(\mathbf{y}_1 | \mathbf{y}_{\text{in}}) L_{\text{meas}}(\tilde{\mathbf{y}}_{\text{in}} | \mathbf{y}_{\text{in}}) \, \mathrm{d}\mathbf{y}_{\text{in}} \\ \times \int L(\mathbf{y}_{\text{out}} | \mathbf{y}_1) L_{\text{meas}}(\tilde{\mathbf{y}}_{\text{out}} | \mathbf{y}_{\text{out}}) \, \mathrm{d}\mathbf{y}_{\text{out}} \end{aligned} \tag{7.10}$$

where $L_{\text{meas}}(\tilde{\mathbf{y}}_{\text{in}} | \mathbf{y}_{\text{in}})$ and $L_{\text{meas}}(\tilde{\mathbf{y}}_{\text{out}} | \mathbf{y}_{\text{out}})$ represent the probability of measuring $\tilde{\mathbf{y}}_{\text{in}} / \tilde{\mathbf{y}}_{\text{out}}$ given the true parameters $\mathbf{y}_{\text{in}} / \mathbf{y}_{\text{out}}$, respectively. The probabilities L_{meas} are also modeled with a Gaussian distribution as it describes well the statistical error in experimental practice. Solving this equation gives an expression for the MLP and an uncertainty matrix that takes into account measurement uncertainties. Krah et al. (2018a) give the following expression for the error matrix

$$\mathbf{\Sigma}_{\text{MLP}}(w) = \mathbf{C}_1 (\mathbf{C}_1 + \mathbf{C}_2)^{-1} \mathbf{C}_2 \tag{7.11}$$

with w the depth of the proton and

$$\mathbf{C}_1 = \mathbf{R}_0 \mathbf{S}_{\text{in}} \mathbf{\Sigma}_{\text{in}} \mathbf{S}_{\text{in}}^T \mathbf{R}_0^T + \mathbf{\Sigma}_1 \tag{7.12}$$

$$\mathbf{C}_2 = \mathbf{R}_1^{-1}\mathbf{S}_{\text{out}}^{-1}\mathbf{\Sigma}_{\text{out}}(\mathbf{S}_{\text{out}}^{-1})^T(\mathbf{R}_1^{-1})^T + \mathbf{R}_1^{-1}\mathbf{\Sigma}_2(\mathbf{R}_1^{-1})^T. \tag{7.13}$$

The uncertainty on the MLP position σ_{MLP} is given by the element in the first row and first column of $\mathbf{\Sigma}_{\text{MLP}}$. The expressions for $\mathbf{R}_0, \mathbf{R}_1, \mathbf{\Sigma}_1, \mathbf{\Sigma}_2$ are the ones used in the usual MLP formalism and have been given in section 3.6.1.1. The matrices $\mathbf{S}_{\text{in}}$ and $\mathbf{S}_{\text{out}}$ are simply used to project the measured positions from the detector to the object surface

$$\mathbf{S}_{\text{in}} = \begin{pmatrix} 1 & d_{\text{entry}} \\ 0 & 1 \end{pmatrix}, \ \mathbf{S}_{\text{out}} = \begin{pmatrix} 1 & d_{\text{exit}} \\ 0 & 1 \end{pmatrix}, \tag{7.14}$$

with d_{entry} the distance from the position on the front tracker to the entrance position and d_{exit} the distance from the rear tracker to the exit position. The matrices $\mathbf{\Sigma}_{\text{in}}$ and $\mathbf{\Sigma}_{\text{out}}$ describe experimental uncertainties, i.e. the impact of the spatial and angular resolution of the trackers. They are given by the sum of the uncertainty due to the spatial resolution of the trackers σ_t and the error due to scattering inside the trackers

$$\mathbf{\Sigma}_{\text{in}} = \sigma_t^2 \mathbf{T}_{\text{in}}\mathbf{T}_{\text{in}}^T + \mathbf{\Sigma}_{\text{sc,in}} \tag{7.15}$$

$$\mathbf{\Sigma}_{\text{out}} = \sigma_t^2 \mathbf{T}_{\text{out}}\mathbf{T}_{\text{out}}^T + \mathbf{\Sigma}_{\text{sc,out}} \tag{7.16}$$

where $\mathbf{T}_{\text{in}}$ and $\mathbf{T}_{\text{out}}$ are the matrices relating the positions measured by the two detectors in each pair to the position/direction parameters:

$$\mathbf{T}_{\text{in}} = \begin{pmatrix} 0 & 1 \\ -1/d_T & 1/d_T \end{pmatrix}, \mathbf{T}_{\text{out}} = \begin{pmatrix} 1 & 0 \\ -1/d_T & 1/d_T \end{pmatrix}, \tag{7.17}$$

with d_T the distance between the trackers. Finally, the matrices $\mathbf{\Sigma}_{\text{sc,in}}/\mathbf{\Sigma}_{\text{sc,out}}$ represent the impact of the scattering inside the trackers on the direction uncertainty

$$\mathbf{\Sigma}_{\text{sc,in}} = \begin{pmatrix} 0 & 0 \\ 0 & \sigma_{\text{sc,in}}^2 \end{pmatrix}, \mathbf{\Sigma}_{\text{sc,out}} = \begin{pmatrix} 0 & 0 \\ 0 & \sigma_{\text{sc,out}}^2 \end{pmatrix}, \tag{7.18}$$

with

$$\sigma_{\text{sc,in}} = \frac{13.6}{p(E_{\text{in}})v(E_{\text{in}})}\sqrt{\frac{x}{X_0}}\left[1 + 0.038 \ln \frac{x}{X_0}\right], \tag{7.19}$$

$$\sigma_{\text{sc,out}} = \frac{13.6}{p(E_{\text{out}})v(E_{\text{out}})}\sqrt{\frac{x}{X_0}}\left[1 + 0.038 \ln \frac{x}{X_0}\right]. \tag{7.20}$$

Equation 7.11 allows to compute the MLP uncertainty for each proton. In order to use this information to deconvolve the uncertainty in the binned distance-driven projections, similarly to Equation 6.3, we perform a binning of the MLP uncertainty:

$$\sigma_{j,p} = \sqrt{\frac{\sum_{i \in \mathbb{I}_p} \sum_k \zeta_j(u_{i,k}, v_{i,k}, w_k)\sigma_{\text{MLP},i}^2(w_k)}{\sum_{i \in \mathbb{I}_p} \sum_k \zeta_j(u_{i,k}, v_{i,k}, w_k)}} \tag{7.21}$$

with $\sigma_{\text{MLP},i}^2(w_k)$ the MLP error of proton i at distance w_k. The value $\sigma_{j,p}$ represents the average error on the MLP for protons with source position p passing in pixel j, with j the 2D pixel index in the (u, w) plane.

7.2.3 Simulations

We use the same simulation for the spiral phantom as the one described in the previous chapters (see section 5.2.5). We remind the reader that a 200 MeV fan beam with a fluence of 225 protons$\cdot$mm$^{-2}\cdot$projection^{-1} at the isocenter is simulated. In

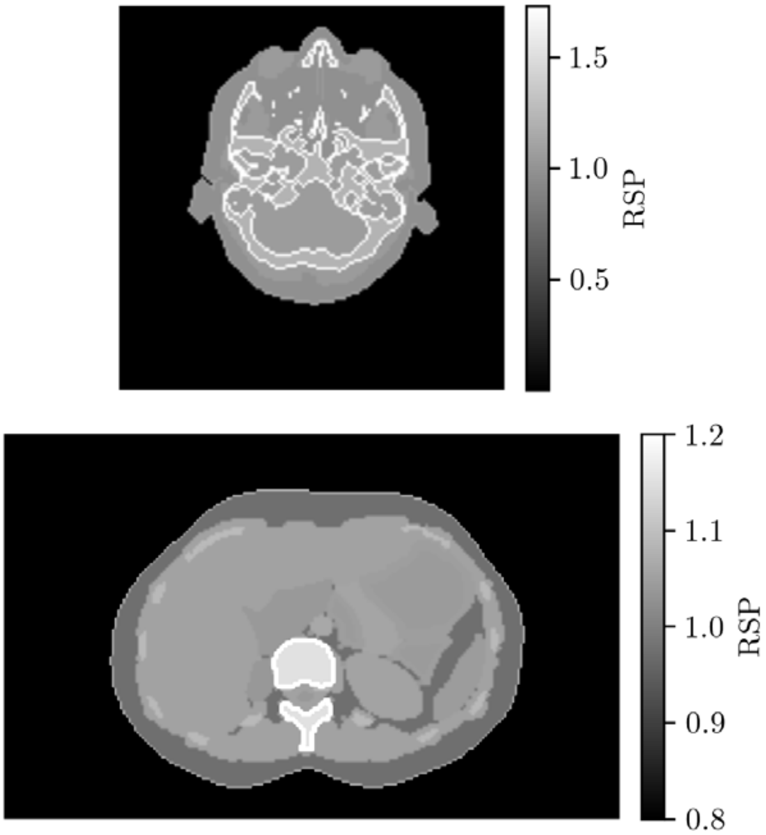

FIGURE 7.1 – Reference RSP maps of the reconstructed slices.

addition, we simulate an acquisition using an ICRP female phantom (ICRP, 2009). A 250 MeV beam energy was used to traverse the phantom volume, with a flux of 190 protons·mm^{-2}·projection^{-1} as a wider beam was used to cover the whole volume. A total of 720 projections over 360° were acquired. Two slices, near the head and near the pelvis, were reconstructed (Figure 7.1). To compute the MLP and its uncertainty, the convex hull of the spiral phantom was known and that of the head and pelvis was approximated by an ellipse for fast detection of the intersection between the patient and the proton path before and after the patient. The images were reconstructed on grids of 500×500 pixels of size 0.5×0.5 mm^2 for the spiral and the head phantoms, and 800×800 pixels of size 0.5×0.5 mm^2 for the pelvis phantom.

Tracker uncertainties were included using a spatial resolution of $\sigma_t = 0.066$ mm corresponding to a strip pitch of 228 µm, a material budget of $x/X_0 = 5 \times 10^{-3}$ and a distance $d_T = 10$ cm between the detectors in each pair. The detectors were placed at a distance of 30 cm from the isocenter for the spiral phantom simulation, and at a distance of 40 cm for the ICRP phantom. Images were reconstructed from ideal trackers using the standard formalism to compute the uncertainty; and from realistic trackers using the extended formalism to compute the uncertainty maps. Spatial resolution was measured in the spiral phantom using the frequency corresponding to an MTF value of 10%, as explained in section 5.2.6.

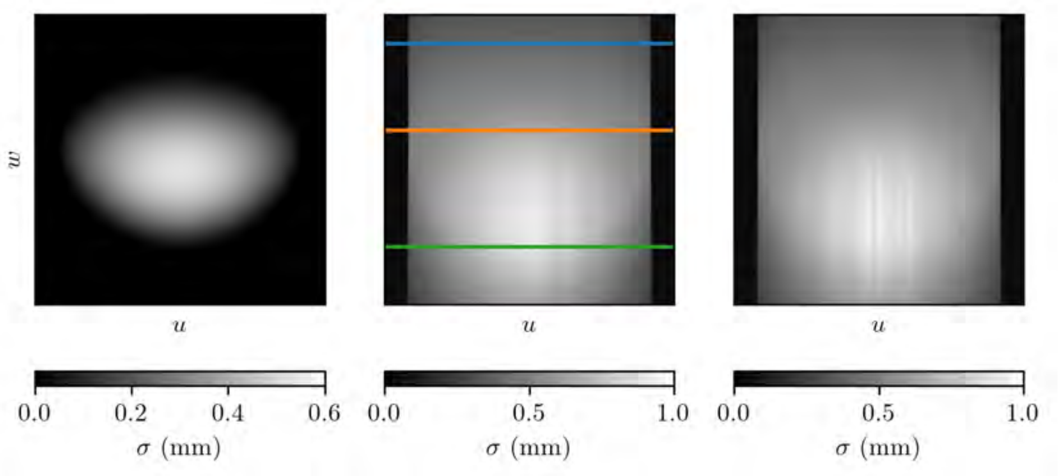

FIGURE 7.2 – Uncertainty maps of one projection of the spiral phantom: uncertainty without tracker resolution (left) and uncertainty including tracker resolution for projection angle 0° and 90° (middle and right). The vertical axis represents the depth w and the horizontal axis is the transverse position u. The colored lines represent the profiles used in Figure 7.4.

7.3 Results

7.3.1 MLP uncertainty maps

Figure 7.2 shows uncertainty maps for the spiral phantom, with and without tracker uncertainties. Note that the support of the uncertainty function is not circular like the shape of the phantom because the uncertainty maps are shown in the projection space and, as a fan beam was used to acquire the data, there is a magnification factor for each distance of the projection. The uncertainty due to MCS reaches its maximum of about 0.6 mm when the protons traverse the widest part of the object. However, the maximum is not exactly at the central depth due to the energy loss term in the computation of the scattering. Given that the object is circular, the MLP uncertainty due to scatter in the object only is not projection-dependent, such that uncertainty maps without tracker resolution are equal for all projection angles. Adding tracker uncertainties increases the maximum σ value to about 1 mm. We observe high uncertainty streaks near the end of the path, corresponding to the aluminium inserts, as protons with lower energy will scatter more in the rear tracker.

Figure 7.3 shows uncertainty maps for the pelvis phantom for three different projections, with and without tracker resolution. There is a large variability in terms of the range of σ values between different projections due to the elliptical shape of the pelvis (axes of 19 and 27 cm). The maximum MLP uncertainty in the projection at 0° (traversing the left-right axis of the patient) reaches 1/1.3 mm depending on whether tracker resolution is included, while the maximum for the projection at 90° (traversing the antero-posterior axis of the patient) is 0.5/0.8 mm. There are not as many streaks as in the spiral phantom since the pelvis region is mostly homogeneous in terms of RSP values, except for the spine. The uncertainty maps are not shown for the head phantom as they are in between the spiral and pelvis phantoms' maps, since the convex hull for the head is closer to a circle (axes of 15 and 17 cm).

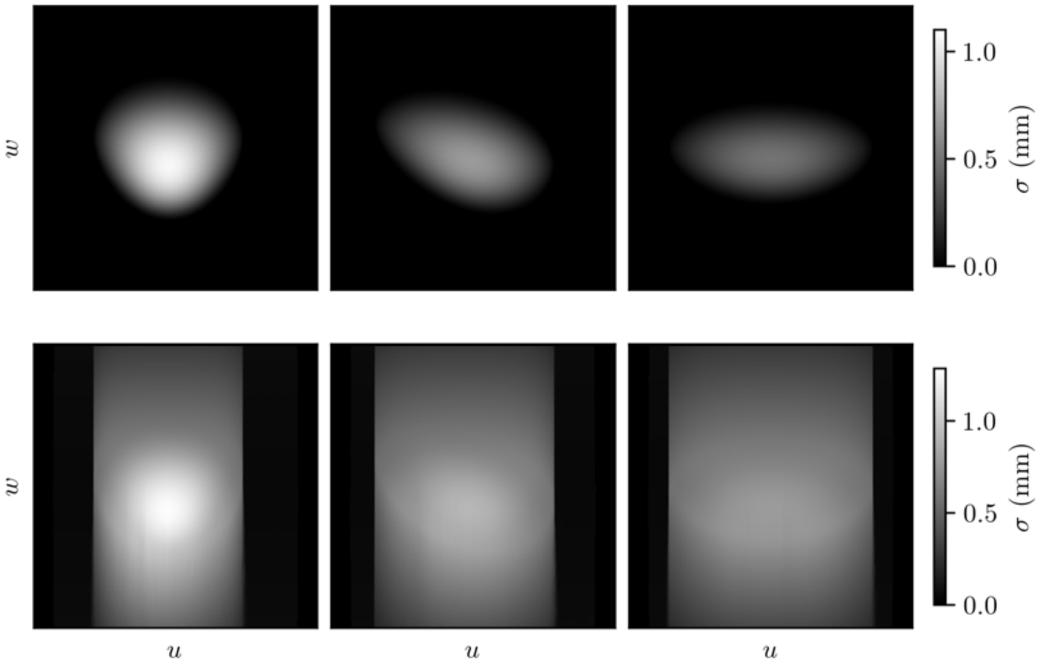

FIGURE 7.3 – Uncertainty maps without tracker resolution (top) and with tracker resolution (bottom) for the pelvis phantom for three different source positions corresponding to 0°, 45°, and 90°.

7.3.2 Truncated singular value decomposition

Figure 7.4 represents three profiles at different depths in the uncertainty map of one projection of the spiral phantom, with the singular values of the corresponding shift-variant deconvolution matrix. We observe that for distances w corresponding to high uncertainty values, the singular values decay to zero faster. Using a truncation relative to the maximum singular value, we see that the SVD corresponding to high uncertainties are more truncated to remove small singular values.

Figure 7.5 shows the number of protons per pixel in a distance-driven projection of the spiral phantom to evaluate the noise level in the projections. Due to MCS, higher distances are associated with a lower proton density, i.e. more noise, which means noise amplification during the inversion will be more problematic for these distances.

7.3.3 Reconstructions

The reconstructions of the spiral phantom are shown in Figure 7.6, and the corresponding spatial resolutions in Figure 7.7. Regarding the results for realistic trackers, both deconvolved reconstructions have a better resolution with an average increase of +37% for the TSVD with $\alpha = 10\%$ and +32% for the TSVD with $\alpha = 30\%$. The maximum increase of the spatial resolution is for the central beads, and reaches +45% and +38% for the TSVD with $\alpha = 10\%$ and $\alpha = 30\%$, respectively. The difference between the spatial resolution of the two deconvolved images is not significant. For the image deconvolved with a truncation level $\alpha = 10\%$, the noise has been considerably amplified compared with the original reconstruction, which is reflected by the larger error bars on the MTF. The results with ideal trackers also show an increase of spatial resolution, with an average gain of 23% and 30%, and a maximum gain of

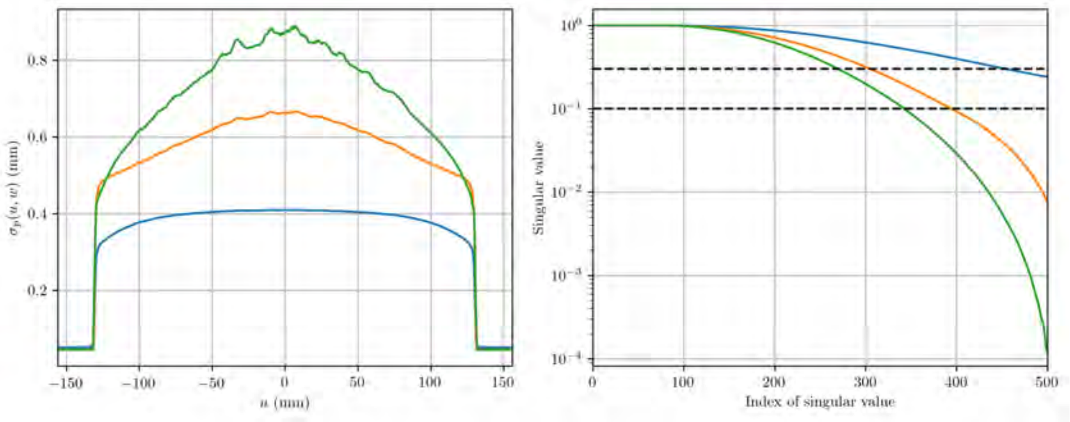

FIGURE 7.4 – Three profiles at different depths (see Figure 7.2 middle) of the uncertainty map for a projection of the spiral phantom (left) and the singular values of the corresponding system matrix (right). The dotted lines represent the truncation levels $\alpha = 10\%$ and $\alpha = 30\%$.

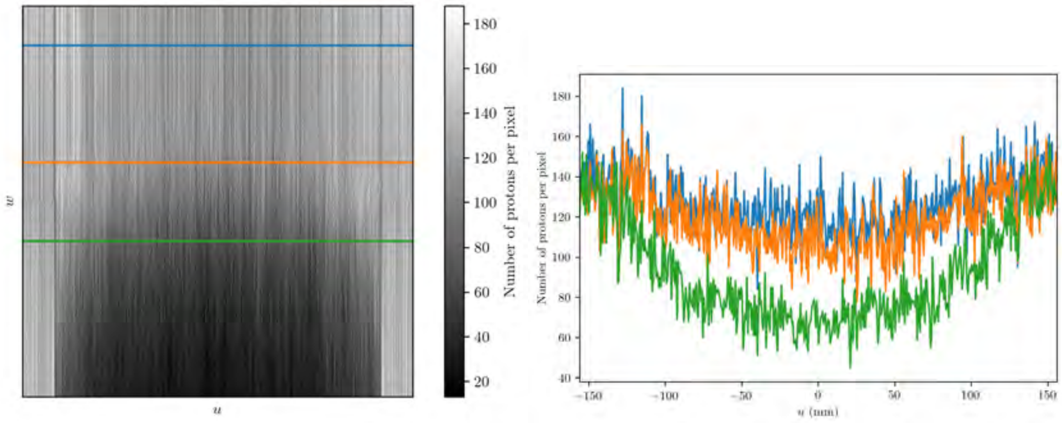

(A)

(B)

FIGURE 7.5 – Image of number of counts for one distance-driven projection of the spiral phantom (A) (the vertical axis represents the depth w and the horizontal axis is the transverse position u) and three profiles at different distances w (B).

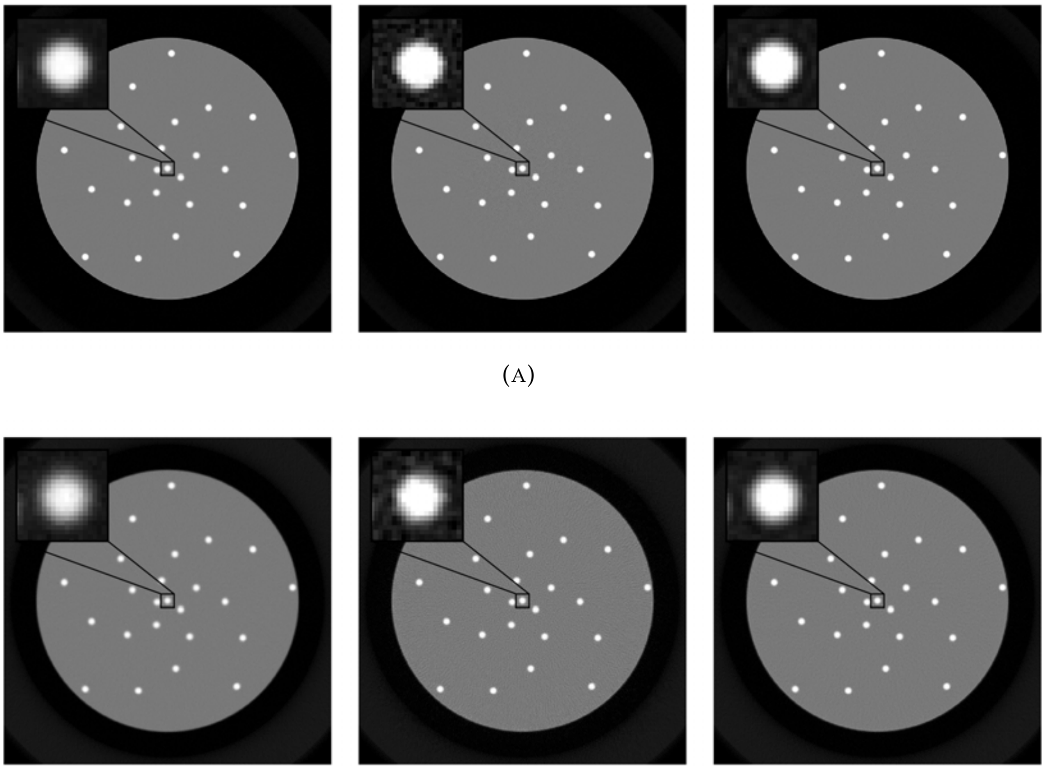

(A)

(B)

FIGURE 7.6 – pCT reconstruction of the spiral phantom: without deconvolution (left), with deconvolution at $\alpha = 10\%$ (middle), with deconvolution $\alpha = 30\%$ (right), for ideal trackers (top) and realistic trackers (bottom). The zoomed inset represents the central bead. The color scale of the image is $[0 - 2.1]$, and that of the inset is $[0.9 - 2]$.

40% and 59% for the deconvolution with $\alpha = 30\%$ and $\alpha = 10\%$, respectively. The average increase is lower compared to the results with tracker resolution because there is no improvement for the farthest beads.

The histogram of the RSP values in the water region of the spiral phantom is shown in Figure 7.7. The RSP distributions for ideal trackers do not vary much, although we observe that the distribution for TSVD 10% is wider. As can be seen in the reconstructed image, the noise mainly affects the central part of the image, and the borders look similar for all reconstructions. For realistic trackers, the reconstruction with TSVD 10% shows a considerably larger standard deviation of the RSP values. The distribution of the RSP values for the TSVD 30% is similar to the distribution for the original reconstruction without deconvolution.

The reconstructions for the head and pelvis phantoms using realistic trackers are shown in Figure 7.8. The deconvolved reconstructions show a better spatial resolution, which is particularly visible on the difference maps where the error near edges is considerably reduced. As the head phantom contains more high contrast edges, the improvement is more noticeable. On the pelvis phantom, the approximative ellipse used as convex hull appears on the difference map. Regarding the results with ideal trackers in Figure 7.9, there is no visible improvement of spatial resolution for both slices.

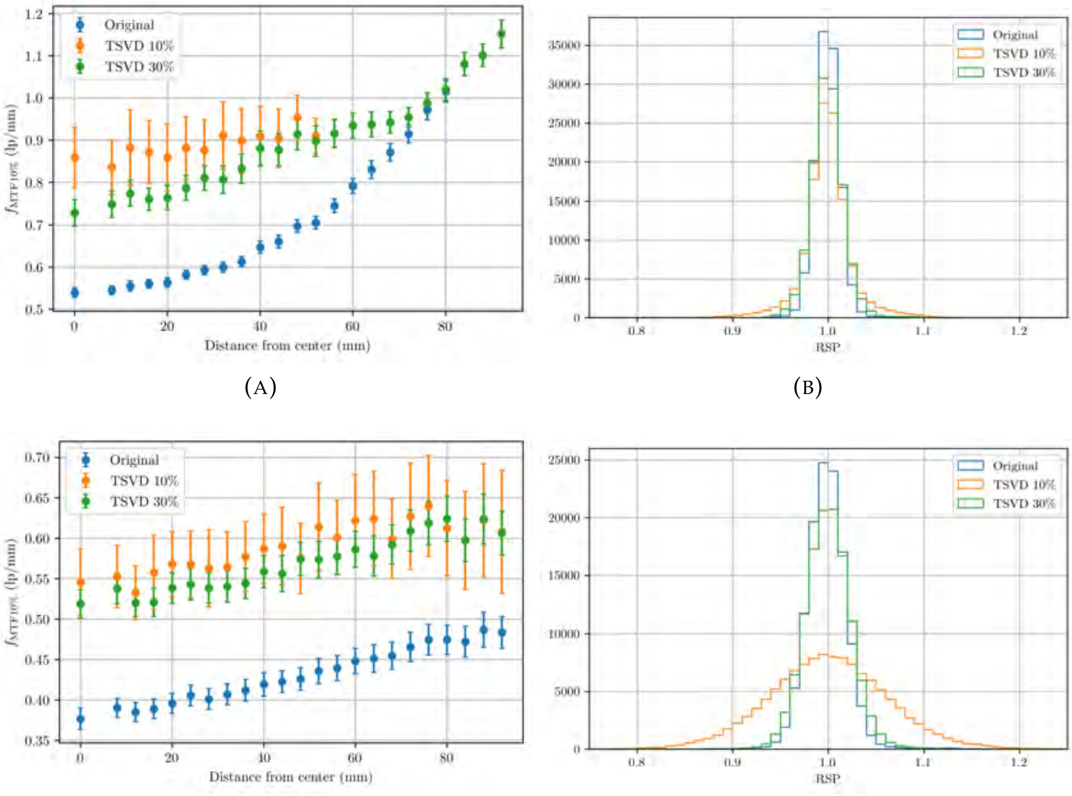

(A) (B)

(C) (D)

FIGURE 7.7 – Spatial resolution of the three reconstructions of the spiral phantom in function of the distance from the center (left) and histogram of the RSP values in the water region of the phantom (right). Results for ideal trackers are shown in the first row, and those for realistic trackers in the second row.

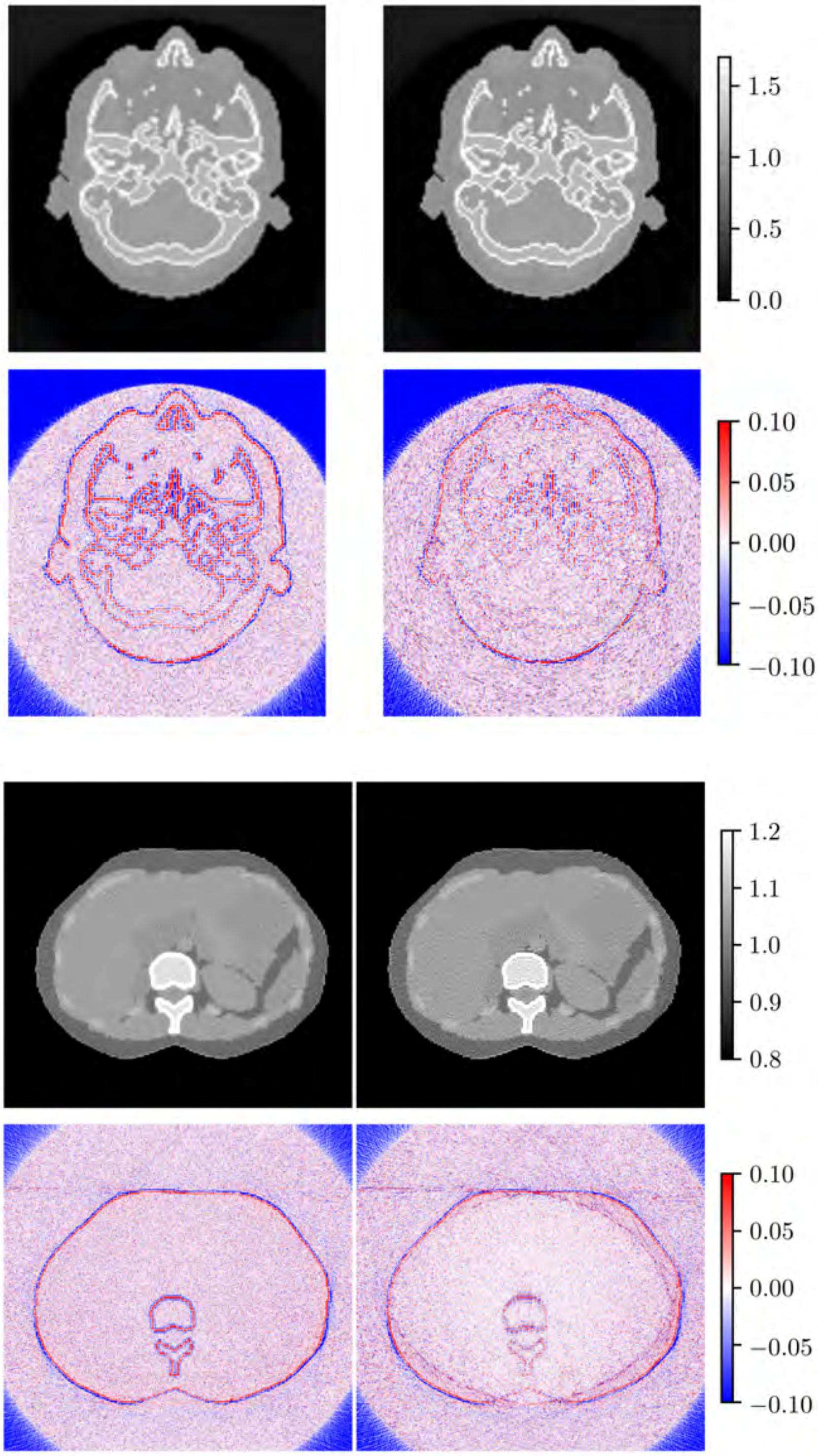

FIGURE 7.8 – Reconstruction of the head and pelvis slices without deconvolution (left) and with deconvolution with $\alpha = 30\%$ (right) using realistic trackers. The difference maps with the reference RSP images are also shown with a blue to red color scale.

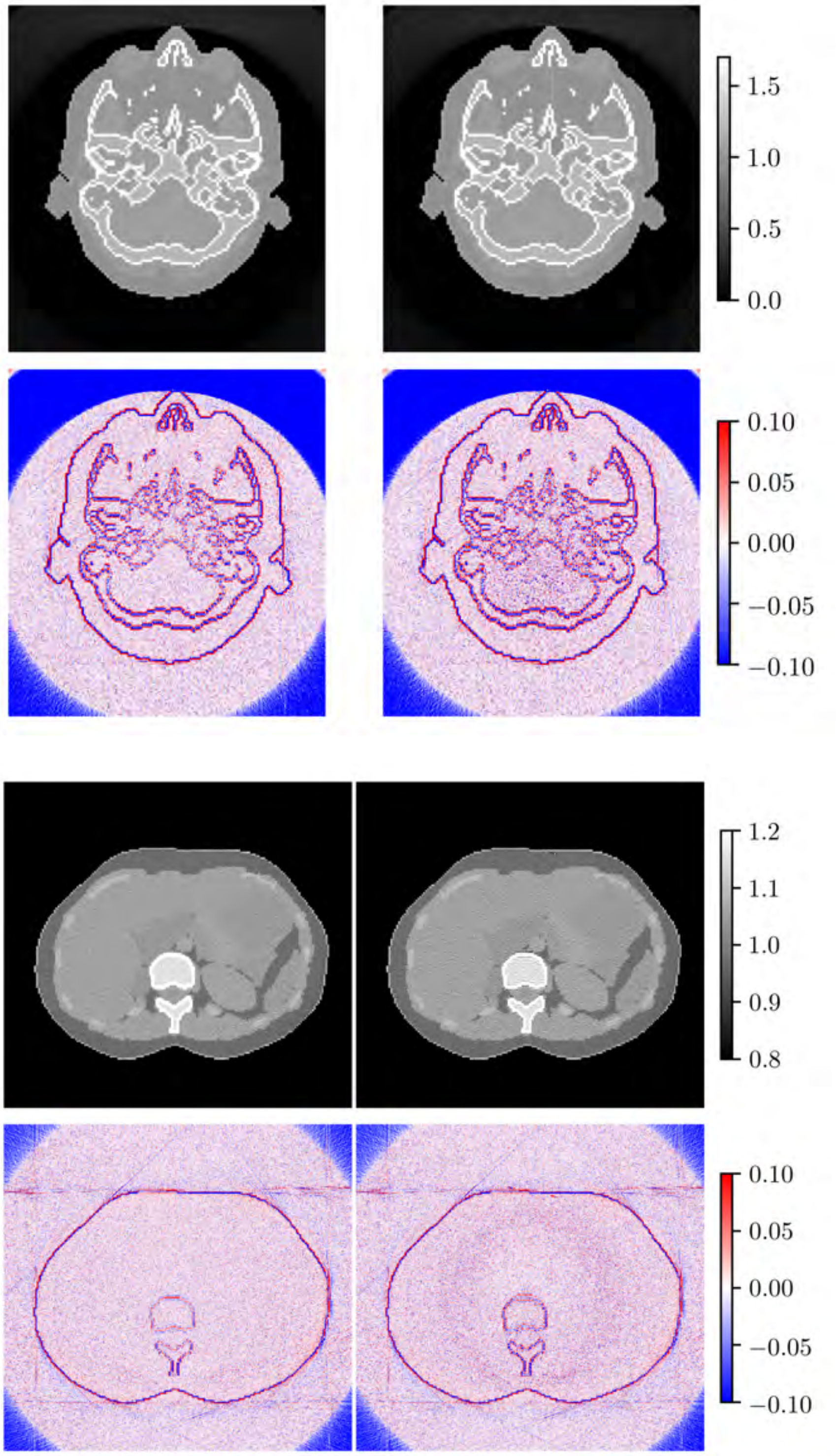

FIGURE 7.9 – Reconstruction of the head and pelvis slices without deconvolution (left) and with deconvolution with $\alpha = 30\%$ (right) using ideal trackers. The difference maps with the reference RSP images are also shown with a blue to red color scale.

7.4 Discussion

The purpose of this work was to investigate the use of the MLP uncertainty to improve spatial resolution. First, we have generated uncertainty maps for each distance-driven projection. The uncertainty maps will depend on the shape of the object, the projection angle, and the heterogeneities in the object. The uncertainty varies in a single projection in function of depth and transverse position, but it is also different between each projection. Specifically, the contribution to the uncertainty of MCS inside the object (without tracker resolution) is projection-dependent when the phantom is not perfectly circular. For the pelvis phantom, there was a factor 2 between the maximum uncertainty for protons traversing the large axis of the object and those traversing the small axis (Figure 7.3). Adding tracker resolution increases the range of the σ maps and allows to introduce an additional information about heterogeneities. Although both the standard and the extended MLP formalisms assume a homogeneous medium, heterogeneities inside the phantom are taken into account through the energy term used for the computation of the scattering inside the rear detector. Particularly, in the case of the spiral phantom, protons that traversed aluminium had lower exit energies and scattered more in the rear tracker, therefore inducing visible uncertainty streaks (Figure 7.2).

The reconstructed images for the spiral phantom showed an increase of spatial resolution in the centre of the object up to 38%/45% with realistic trackers depending on the SVD truncation level. Similarly, the reconstructions for the ICRP phantom taking into account tracker resolution showed a visible improvement of spatial resolution. The results with ideal trackers for the spiral phantom showed an improvement of spatial resolution only at the center of the object. At the borders, the uncertainty of the MLP tends to zero such that the blurring kernel is nearly a Dirac. Due to the sampling of the kernel, i.e. the pixel size in the projections, there is a limit on the σ under which all kernels are Diracs. That is why there is no difference in spatial resolution or noise far away from the center. The results for the ICRP phantoms with ideal trackers show no visible improvement of spatial resolution. We could expect an improvement at the center where the uncertainty reaches about 0.5 mm in the head. However, we recall that the pixel size for the original ICRP phantom used in the simulations was 1.775 mm, which is quite large compared with the impact of MCS alone. This imposes a limit on the maximum achievable resolution, which would explain the lack of improvement after deconvolution. We note that we used an approximative ellipse as a convex hull for the head and pelvis phantoms which would cause an error on the σ values used to compute the system matrix $\mathbf{H}$. The deconvolution is therefore not completely optimal for these two phantoms. Particularly for the pelvis phantom, the chosen ellipse was too small and is visible on the difference map in Figure 7.8.

We have observed that the truncation level must be adapted to the noise in the projections. The pCT data for the ICRP data was acquired with a slightly lower fluence (190 protons$\cdot$mm$^2\cdot$projection versus 225 protons$\cdot$mm$^2\cdot$projection for the spiral phantom) due to the larger volume of the body phantom, which might have required a higher truncation level. In addition, for the same acquisition, the noise will vary depending on the distance in the distance-driven projection due to MCS, such that a constant truncation level α might not be ideal. In this work, the truncation level was heuristically adapted by testing different values. A better understanding of the relationship between the noise in the projections and the truncation level of the SVD might allow for a better and more precise regularization of the reconstructed images.

Although computing a single SVD is not too computationally demanding, this has to be done for each distance and each projection, which can quickly increase the computational load. This operation could, however, be parallelized. Investigating a different method to perform the matrix inversion could improve the computational cost, and/or allow for a better regularization of the deconvolution. Fast algorithms for convolution integrals with shift-variant kernels (Gilad and Von Hardenberg, 2006) might be used to accelerate the computation. In addition, as tracker resolution reduces the shift-variance of the σ values in the uncertainty maps, using a single kernel per projection or for all projections might still improve resolution, depending on the phantom shape and heterogeneities, while being more practical. It could also be possible to do the deconvolution in the image space, after reconstruction. We would need to approximate the uncertainty value in each pixel of the reconstructed image. It could be interesting to compare the results between projection-based and image-based deconvolution. We expect that, depending on the phantom, results could be similar between both methods. For example, the pelvis phantom presents a large variability between the maps for different angles such that the approximation of the uncertainty in one pixel of the reconstructed image would be the combination of very different values. For the head or spiral phantom, since the contribution to the uncertainty in a pixel would be similar for all projection angles, we expect an image-based deconvolution to produce similar results.

This work was conducted using a distance-driven projection binning algorithm. It can be used similarly with other direct methods by deconvolving projections or partial backprojections. Since it is projection-based, direct application to iterative methods is not straightforward. Although Wang, Mackie, and Tomé (2010) have tried to include MLP uncertainty in their projection model, their results did not show any improvement of spatial resolution. Specifically, they used the whole uncertainty envelope in the projection operator, which corresponds to the convolution of the MLP with the Gaussian uncertainty, to iteratively reconstruct a pCT image. Alternatively, a deconvolution after reconstruction would be done independently of the reconstruction method.

7.5 Conclusion

The purpose of this work was to investigate whether including MLP uncertainty in a deconvolution framework might improve spatial resolution in pCT reconstruction. We have generated uncertainty maps for a distance-driven sinogram and performed a shift-variant deconvolution using a TSVD approach. It was shown that including MLP error to perform deconvolution of blurred distance-driven projections can significantly increase spatial resolution of pCT images. Particularly, the resolution in a spiral phantom was increased by 38% while keeping a similar noise level as in the reconstruction without deconvolution, when tracker resolution was included. Reconstructions of realistic phantoms also showed an enhancement of spatial resolution. The choice of the truncation level of the SVD was not optimized in this work, and should be better adapted to the noise level in the projections.

Conclusions

The objective of this thesis was to explore list-mode proton CT reconstruction and improve image quality in pCT. In a proton CT single tracking set up, each proton's entry and exit position and direction is measured in order to estimate its trajectory using a most likely path formalism. Several aspects were investigated, from the accuracy of the MLP formalism to the different reconstruction pCT algorithms to the deconvolution of the MLP uncertainty. We were particularly interested in direct (i.e. non iterative) algorithms. Those are heuristic solutions since there is no known analytic inversion for the MLP curved trajectories. Specifically, during the course of this thesis, we have

1. studied the impact of heterogeneities on the MLP;
2. proposed a different method to filter pCT data;
3. compared different direct algorithms for pCT reconstruction;
4. proposed a method to deconvolve distance-driven projections using the MLP uncertainty.

First, we have studied the accuracy of the MLP formalism in different heterogeneous configurations. By comparing the theoretical MLP to Monte Carlo simulations, we have shown that there is a systematic error on the MLP estimate near transverse interfaces. While prior knowledge about longitudinal heterogeneities can be included in the current MLP formalism to improve the path estimate, this is not the case for transverse heterogeneities. The Gaussian approximation of the spatial and angular distributions is not valid in this case, and the measured distributions resemble skewed Gaussians or two-term Gaussians. It could be interesting to develop an MLP formalism that does not assume a Gaussian model. However, with bimodal distributions, even the concept of a single MLP is debatable as it appears there are several preferred paths. Additionally, we expect the error due to realistic transverse heterogeneities to be small. We have also observed that the non Gaussian shape of the energy distributions that could have an impact on the reconstructed RSP value, and complicates the 3σ energy cuts used to exclude non-elastic nuclear reactions. Further investigations about the energy distributions and the impact on the reconstruction could explain some of the artifacts previously reported. Also, the initial energy of the proton beam could have an impact on the amplitude of the MLP error as scattering is more important for lower energies. Reconstructing a phantom with a transverse heterogeneity could confirm the assumptions on the impact of the skewed spatial and energy distributions on the final image.

Secondly, we have proposed an alternative filter to reconstruct pCT data. We have defined and found the band-limited expression for a 2D directional ramp filter. The objective was to filter the data directly in the image space to avoid an interpolation and preserve the spatial information of the MLP. The reconstruction procedure using this filter is (1) perform a partial backprojection binning, (2) filter the data using the directional ramp and (3) sum over all projection angles. Since the list-mode data is binned in the image space and no interpolation is needed to apply the directional ramp filter, a slight gain in spatial resolution is observed compared with an approach where the data is binned into projections. The 2D directional ramp filter was developed assuming a parallel geometry. It may be possible to derive an equivalent filter for other geometries such as fan beam, although we expect its expression to be more difficult to derive, as the variable change from the sinogram space to the image space for fan beam is not a simple rotation as for a parallel geometry. Although it is straightforward to rebin list-mode pCT data to a parallel geometry, this rebinning could be more complicated for integration mode pCT set-ups.

We have conducted a comparison of all the direct methods used to reconstruct pCT data. Results were compared in terms of spatial resolution and RSP accuracy. The different algorithms were (1) the distance-driven algorithm extending the FBP to non-linear paths, (2) the maximum likelihood algorithm working with optimized radiographs, (3) the backprojection-then-filtering which inverts the filtering and backprojection steps, (4) the differentiated backprojection and (5) the directional ramp method. Results have shown minor differences between the different algorithms. In general, algorithms that start by backprojecting the data in the image space allow for a superior spatial resolution. Most differences in spatial resolution were noticeable at the border of the reconstructed phantom. Elsewhere, spatial resolution was dominated by MCS and tracker resolution. The computational cost is therefore a major factor for the choice of the reconstruction algorithm. Some backproject first methods require to compute the backprojection beyond the limits of the reconstruction region which increases the computational load. Also, the ability of the differentiated backprojection to deal with truncated projections can make it the preferred solution in certain cases.

Finally, we proposed a shift-variant deconvolution method to deconvolve the MLP uncertainty from distance-driven projections. First, we compute distance-driven uncertainty maps for each projection using the MLP formalism with tracker resolution. Then, we use a truncated singular value decomposition to invert the corresponding shift-variant system matrix for each distance and each projection. Results have a shown a significant gain of spatial resolution in simple and realistic phantoms when tracker resolution is included. This benefit is most significant in regions with a lot of heterogeneities in terms of RSP value, e.g. the head. On the reconstructed slices, it was observed that the spatial distribution of the noise was different after deconvolution. The truncation level of the TSVD has to be adapted to the noise in the projections, which we did heuristically. Adjusting the noise level more carefully might improve the current results.

This method is quite slow since SVD must be calculated for each distance and each projection angle. It could be possible, in order to speed up the deconvolution, to use the same uncertainty map for all projection angles. This could be reasonable for circular objects with few heterogeneities, i.e. objects where there is little variability in terms of MLP uncertainty as a function of projection angle. Alternatively, a single matrix per projection could work when there is little variability as a function of distance. This could be a reasonable approximation as adding tracker uncertainty reduces the variability of each uncertainty map. Also, it would be interesting to compare this method with an image based deconvolution method, where deconvolution would be done after the reconstruction. This could give satisfactory results in cases when the uncertainty map does not vary much as a function of projection angle. While this would mean deconvolving a single 2D image instead of a whole 3D sinogram, the shift-variant blurring kernels would be in 2D which currently makes TSVD unusable for such a large problem. Other deconvolution methods could also be used for faster calculations and a better control of the noise. More sophisticated regularization schemes might reduce the noise level while keeping a high spatial resolution. Although this method was tested on list-mode data, the MLP formalism computing the uncertainty on the path estimate has been extended to integration mode set-ups. Therefore, the same method can be used to deblur projections acquired using different kinds of set-ups. We expect the gain of spatial resolution to be greater for integration set-ups since resolution of the reconstructed image is more impacted by tracker uncertainty. It would be interesting to compare the spatial resolution after deconvolution between list-mode and integration mode set-ups.

During this thesis, all studies were based on Monte Carlo simulations. While we have taken into account tracker resolution using an approximative model, there are several aspects that have been idealized. For example, the resolution of the energy detector was assumed to be perfect, the reconstruction of the proton track in the front and rear trackers used knowledge of a particle identification number, there were no motion artifacts, etc. Experimental set-ups have to deal with tracking errors, electronic noise, limited detection rate and resolution, etc. Therefore, our findings need to be confirmed on real data. Still, by proposing different solutions to improve spatial resolution and conducting a comprehensive comparison of pCT reconstruction algorithms, our work contributes to the development of this imaging modality.

There are still limitations to the clinical use of pCT such as the maximum beam energy delivered by the medical accelerator, the scan time, or the incorporation into the clinical workflow. Additionally, while our work has focused on list-mode set-ups as they achieve the best spatial resolution, integration mode set-ups might be easier to implement clinically. There have been several hardware developments such that detectors with spatial and energy resolution of the same order as MCS and energy straggling are possible. However, the increased complexity, cost and scan time of this type of equipment makes the investigation of integration-mode systems worthwhile. Improving the spatial resolution of pCT data acquired with integration set-ups might be possible by dual modality image reconstruction, for example. The combination of X-ray CT with pCT or multi-projection proton radiographies has been studied by Wang, Mackie, and Tomé (2012), Hansen et al. (2014a), and Zhang et al. (2019). Dual modality image reconstruction has also been considered to overcome the range limit imposed by the maximum energy of the accelerator. The principle is to use only projections acquired at angles where the proton range is sufficient to traverse the patient and complete the missing data using X-ray CT. Although increasing the energy of the proton beam might be physically possible, it might not be economically justified if it is for the purpose of reconstructing pCT images only.

While there are still challenges to the clinical implementation of pCT, clinical prototypes for proton radiography and CT are currently under development, notably the pRad system of ProtonVDA is being medically certified.

Résumé étendu

Avec environ 18 millions de nouveaux cas et 9.5 millions de décès dans le monde en 2018, le cancer est l'une des pathologies les plus répandues et les plus létales. Environ la moitié des cas requièrent un traitement par radiothérapie, seul ou en combinaison avec d'autres traitements tels que la chirurgie et/ou la chimiothérapie. La radiothérapie standard utilise des rayons X à haute énergie afin d'endommager les cellules cancéreuses. L'utilisation des protons au lieu des rayons X pour la thérapie contre le cancer a été proposée car elle offre des avantages en matière de conformité de dose, c'est-à-dire qu'elle permet de maximiser la dose administrée à la tumeur tout en minimisant la dose reçue par les tissus sains environnants. L'exploitation du pic de Bragg du proton - un pic de dose localisé peu avant l'arrêt des protons - permet de traiter les tumeurs profondes tout en épargnant les structures critiques, ce qui est essentiel pour les cancers de la tête et du cou, de la prostate, les cancers pédiatriques, etc. La position du pic de Bragg (appelée *range*) peut être ajustée via l'énergie du faisceau de protons.

La planification d'une thérapie proton nécessite l'acquisition d'une image CT afin de prédire le *range* des protons et donc la dose absorbée par le patient. Plus précisément, une carte du pouvoir d'arrêt des tissus traversés est nécessaire pour estimer le *range* des protons. Cependant, l'utilisation d'une image CT à rayons X pour calculer le pouvoir d'arrêt introduit des incertitudes car les interactions des photons et des protons avec la matière sont très différentes. Cette incertitude, additionnée à d'autres erreurs dues à l'alignement du patient, aux mouvements respiratoires, etc., obligent les praticiens à utiliser des marges de sécurité autour du volume de traitement au détriment de la protection des tissus sains. Dans ce contexte, l'imagerie CT proton est une solution intéressante car la quantité reconstruite est directement le pouvoir d'arrêt du proton, c'est-à-dire qu'aucune calibration n'est nécessaire à partir d'une image CT à rayons X. L'utilisation de l'imagerie CT proton pour la planification des traitements de thérapie proton peut donc aider à réduire les incertitudes de *range* et ainsi améliorer la conformité de dose.

L'objectif de cette thèse était d'améliorer la qualité d'image en reconstruction CT proton en mode liste. Dans une configuration en mode liste, chaque proton est suivi individuellement, et son énergie, sa position et sa direction sont mesurées en amont et en aval du patient. Comme les trajectoires des protons ne sont pas linéaires en raison de la diffusion coulombienne multiple, les configurations en mode liste permettent une meilleure estimation de la trajectoire des protons et une amélioration de la résolution spatiale. Les algorithmes de reconstruction tomographique en imagerie CT proton doivent donc être adaptés pour prendre en compte la non-linéarité des chemins des protons. Le problème de reconstruction consiste alors à retrouver une carte du pouvoir d'arrêt à partir des données en mode liste.

Le chapitre 1 commence par présenter les différentes interactions des protons avec la matière, à savoir la perte d'énergie, la diffusion coulombienne multiple et les interactions nucléaires. Le chapitre 2 présente les bases de la thérapie proton et la justification clinique de l'imagerie proton dans le contexte de la planification des thérapies proton. Le chapitre 3 est une revue de l'imagerie CT proton, depuis les débuts de l'imagerie proton jusqu'aux développements hardware et aux techniques de reconstruction contemporains. Les chapitres 4 à 7 présentent nos contributions originales. Dans un premier temps, une étude de l'impact des hétérogénéités sur la trajectoire du proton est réalisée à l'aide de simulations Monte Carlo. Plus précisément, le most likely path (MLP) théorique est comparé à une trajectoire simulée dans différentes configurations hétérogènes. Dans le chapitre 5, une extension du filtre rampe en deux dimensions pour améliorer la résolution spatiale en pCT est proposée. Cette méthode, ainsi que quatre autres algorithmes de reconstruction directe, est évaluée en matière de résolution spatiale et de précision du pouvoir d'arrêt dans le chapitre 6. Une dernière contribution est présentée dans le chapitre 7 : il s'agit d'une méthode de déconvolution shift-variante prenant en compte l'incertitude sur la trajectoire du proton afin d'améliorer la résolution spatiale.

I Interactions proton-matière

Un proton est une particule subatomique positivement chargée, souvent noté p ou p^+. Pour des protons dans le régime d'énergie utilisé en imagerie proton (60-300 MeV), on distingue trois processus d'interactions différents :

- La perte d'énergie par des interactions coulombiennes non-élastiques avec les électrons atomiques ;
- La diffusion multiple de Coulomb, qui correspond à la déviation de la trajectoire du proton via des interactions coulombiennes entre les charges du proton et du noyau ;
- Les interactions nucléaires élastiques et non-élastiques.

I.1 Perte d'énergie

Les protons perdent de l'énergie principalement via des interactions électromagnétiques avec les électrons atomiques. La multiplication de ces interactions microscopiques fait perdre de l'énergie au proton jusqu'à ce qu'il s'arrête. On suppose que les protons perdent leur énergie continûment le long de leurs trajectoires à un taux donné par le pouvoir d'arrêt S, exprimé comme une perte d'énergie moyenne par unité de longueur. Le pouvoir d'arrêt dépend du milieu traversé ainsi que de l'énergie du proton, et est calculé par la formule de Bethe-Bloch pour des énergies supérieures à 2 MeV (Equation 1.2). La dose libérée par les protons est directement proportionnelle au pouvoir d'arrêt. Lorsque le proton avance dans le milieu, il perd de plus en plus d'énergie, ce qui donne lieu au pic de dose à la fin de sa trajectoire, appelé pic de Bragg.

Étant donné que la perte d'énergie est un processus statistique, un faisceau parfaitement monoénergétique aura toujours une distribution en énergie après avoir traversé un médium. Dans le cas d'absorbeurs épais, si la perte d'énergie est faible, la distribution en énergie en sortie est gaussienne ; sinon il s'agit d'une distribution de Tschalar (Tschalär, 1968b,a ; Tschalär et Maccabee, 1970).

I.2 Diffusion multiple de Coulomb

Les protons dévient de leur trajectoire initiale due à la multiplication d'interactions électromagnétiques élastiques avec les noyaux. La distribution angulaire après diffusion est approximativement gaussienne, avec une queue vers les grands angles de diffusion. Bien qu'il existe une théorie plus précise pour décrire cette distribution, 98% des protons rentrent dans le cadre du modèle gaussien. En pratique, dans le contexte de l'imagerie proton, les protons présentant des angles de diffusion particulièrement importants sont exclus afin de respecter l'approximation gaussienne.

I.3 Interactions nucléaires

Alors que les interactions électromagnétiques sont bien comprises, il est plus difficile de modéliser les interactions impliquant des forces nucléaires. Ces interactions sont moins fréquentes que les interactions électromagnétiques mais ne doivent pas être négligées pour autant. Il existe des interactions nucléaires élastiques (sans perte d'énergie) et non-élastiques (avec perte d'énergie). Ces dernières conduisent à la créations de particules secondaires tels que des protons, neutrons, particules alpha, etc.

II Proton thérapie

La radiothérapie est un traitement contre le cancer dont l'objectif est l'arrêt, ou au moins le ralentissement, de la croissance des cellules tumorales via la dégradation de leur ADN. Un point fondamental en radiothérapie est la conformité de la dose, c'est-à-dire la maximisation de la dose administrée à la tumeur et la minimisation de la dose administrée aux tissus sains. L'objectif de la proton thérapie est d'améliorer la conformité de la dose par rapport aux traitements conventionnels utilisant des photons, en exploitant le profil de dose des protons et leur efficacité radiobiologique.

II.1 Justification clinique

L'existence des protons, particules subatomiques chargées positivement, fut démontrée par Rutherford (1919). Wilson (1946) fut le premier à proposer l'utilisation des protons à la place des photons dans le cadre de la radiothérapie. Il suggéra de tirer parti de leur profil de dose caractérisé par une faible dose superficielle et un pic de dose en profondeur afin de viser des tumeurs entourées de tissu sain. Depuis, ce sont plus de 190,000 patients qui ont été traités par proton thérapie, principalement aux États-Unis, en Europe et au Japon.

Comme évoqué plus haut, le profil de dose des protons est avantageux étant donné qu'il se caractérise par un pic de dose fin, le pic de Bragg, situé à la fin du parcours des protons, et d'une dose quasi-nulle après ce pic. En modulant la position du pic, qui dépend de l'énergie initiale des protons et du pouvoir d'arrêt des tissus traversés, il est possible de cibler très précisément une tumeur en profondeur. Afin de couvrir la totalité du volume de la tumeur, plusieurs pics situés à différentes profondeurs sont superposés.

De nombreuses études ont démontré l'avantage de la proton thérapie en matière de distribution de dose, particulièrement dans le cas de tumeurs proches de structures sensibles (tête et cou, oeil, prostate, etc.) et de cancers pédiatriques, étant donné que les individus jeunes présentent un plus grand risque de développer des cancers secondaires radio-induits. Cependant, la transposition de cet avantage dosimétrique en bénéfices cliniques mesurables n'est pas encore démontrée pour tous les sites de traitement. Plusieurs études cliniques à grande échelle sont actuellement en cours. Les résultats de ces études pourront également aider à avoir une estimation plus robuste du rapport bénéfices-coûts de la thérapie proton. En effet, les centres de thérapie proton sont bien plus coûteux que les centres de radiothérapie (facteur de 2-3 par fraction).

II.2 Planification des traitements de proton thérapie

Afin de sculpter la distribution de dose et de couvrir la tumeur uniformément, l'acquisition d'une image du patient est essentielle. La prise en compte des variations des tissus du patient permet d'éviter un sous- ou surdosage. Le système de planification des traitements utilise une image CT afin de calculer la dose absorbée en convertissant les unités Hounsfield en pouvoir d'arrêt du proton. En comparant cette carte de dose à la dose prescrite, les paramètres du système sont optimisés.

Afin d'exploiter pleinement le profil de dose des protons, la position du pic de Bragg doit être précisément connue. Même une erreur de quelques millimètres peut induire un grave sous-dosage de la tumeur et/ou un surdosage des organes à risque. Il existe plusieurs sources d'incertitude en thérapie proton, comme la conversion des unités HU en pouvoir d'arrêt, le choix de l'algorithme de calcul de dose, les mouvements du patient, un mauvais alignement, etc. Afin de compenser l'erreur due à ces incertitudes, des marges de sécurité autour de la tumeur sont utilisées, au dépend de la conformité de dose. Ces marges sont nécessaires afin de s'assurer que la dose prescrite a bien été délivrée à la tumeur.

L'objectif de l'imagerie proton est de réduire l'erreur due à la conversion des unités HU en pouvoir d'arrêt. Selon plusieurs études, les incertitudes en matière de *range* dues à cette calibration varient entre 1.1%-1.8% (Schaffner et Pedroni, 1998) et 3.0%-3.5% (Moyers et al., 2010; Yang et al., 2010). D'autres modalités d'images, tels que la DECT ou la radiographie proton, sont étudiées afin d'améliorer la calibration HU/RSP. Cependant, seule l'imagerie proton CT permet de s'affranchir totalement de cette calibration en reconstruisant directement une carte de RSP.

III Tomographie proton

III.1 Débuts de l'imagerie proton

L'idée d'utiliser des protons pour l'imagerie médicale fut initialement proposée par Cormack (1963), il y a plus de cinquante ans. La première radiographie proton fut rapportée par Koehler (1968). La fluence des protons était mesurée afin de produire une image offrant un contraste supérieur. D'autres publications explorèrent les capacités de la radiographie proton en matière de contraste, mais ce mode d'imagerie basé sur la mesure de fluence a peu progressé depuis les années 1970.

Les premières expériences en proton CT furent conduites par Cormack et Koehler (1976). Plus tard, dans les années 1970 et 1980, Hanson a continué d'explorer cette modalité d'imagerie au laboratoire national de Los Alamos (Hanson et al., 1978; Hanson, 1979; Hanson et al., 1981, 1982). Il utilise des détecteurs pour mesurer la position des protons afin d'améliorer la résolution. Plusieurs de ses idées sont aujourd'hui utilisées dans les prototypes de scanners pCT.

Ces premières études se sont focalisées sur le potentiel avantage en matière de dose de l'imagerie pCT plutôt que sur son utilisation dans le cadre de la thérapie proton, car l'usage de celle-ci était encore limité. Dû aux avancées en imagerie CT à rayons X à faible dose et aux coûts importants des accélérateurs de particule nécessaires à la pCT, l'intérêt pour l'imagerie pCT diminua.

Ainsi, bien que la faisabilité de l'imagerie pCT fut démontrée dès le début des années 1980, il fallut attendre les années 1990 et l'expansion de la thérapie proton pour que l'imagerie proton suscite à nouveau l'intérêt des scientifiques.

III.2 Conception et détecteurs

Afin de bien appréhender les développements technologiques actuels, il est important de comprendre la conception d'un scanner pCT. Ici, seuls les systèmes en mode liste — c'est-à-dire les configurations où chaque proton est mesuré individuellement — seront étudiés, étant donné que la grande partie des recherches actuelles se concentrent sur ce type de systèmes. Le cahier des charges pour un scanner pCT est le suivant :

- Une résolution spatiale de l'ordre de 1 mm (Schulte et al., 2004). Celle-ci est limitée par la diffusion multiple de Coulomb, et par la résolution du détecteur.
- La résolution du WEPL doit être inférieure à 1% (Schulte et al., 2004). Elle est limitée par le straggling en énergie, la distribution en énergie du faisceau incident, la résolution du détecteur, et le MCS (Dickmann et al., 2019).
- Un taux de détection important afin de scanner le patient en un temps raisonnable. Étant donné qu'il faut environ 100 protons par mm^3 par angle de projection, cela correspond à un taux de 2 MHz pour un scan d'une durée de 6 min.
- Une haute efficacité de détection car les protons non détectés participent à l'irradiation du patient sans contribuer à la formation de l'image.

D'autres critères sont à noter, tels que la gamme d'énergie du faisceau incident, la taille des détecteurs, et la résistance des détecteurs aux irradiations. En ce qui concerne l'énergie du faisceau de protons, elle doit être assez grande afin que les protons puissent traverser le patient. Cela correspond à une énergie de 200 MeV au niveau de la tête, et au moins 250 MeV au niveau de l'abdomen.

Deux types de détecteurs sont nécessaires afin de satisfaire le cahier des charges ci-dessus : un détecteur d'énergie/*range* résiduels afin de mesurer le WEPL des protons, et des trackers afin de mesurer la position et l'angle et estimer la trajectoire des protons pour améliorer la résolution spatiale. En ce qui concerne les trackers, des détecteurs à base de bandes de silicone sont souvent utilisés car dotés d'une bonne résolution spatiale et efficacité, compacts, et faciles à calibrer. Par ailleurs, il existe deux types de détecteurs d'énergie : les calorimètres, et les *range telescopes*. Les calorimètres sont des détecteurs non segmentés mesurant l'énergie des protons. D'autre part, le *range telescope* consiste en de multiples couches sensibles (entre 60 et 100 couches idéalement), et le *range* est obtenu par la position de la couche où le proton s'est arrêté. Plus récemment, un troisième type de détecteur hybride, le scintillateur multi-couches, a été proposé (Bashkirov et al., 2016a).

III.3 Développements contemporains

Dans les années 1990, avec l'expansion de la thérapie proton, l'imagerie proton a connu un regain d'intérêt avec l'idée de l'utiliser afin de planifier les thérapies. Schneider et Pedroni (1994, 1995) de l'institut Paul Sherrer ont investigué la radiographie proton. En 2000, Zygmanski et al. (2000) a évalué un système d'imagerie pCT avec un faisceau conique, sans mesurer chaque proton individuellement afin de réduire le temps d'acquisition. Cependant, ce type de systèmes offre une résolution spatiale limitée due à l'effet du MCS. Bien que ces configurations continuent d'être étudiées dû à leur simplicité et faible coût, la plupart des développements utilisent des configurations en mode liste.

Depuis 2002, une collaboration informelle entre LLUMC et UCSC a conduit à la publication d'un grand nombre d'articles sur la pCT. Un premier concept de scanner a été proposé par Schulte et al. (2004), et, quelques années plus tard, un prototype capable d'imager des phantomes de la taille d'une petite tête fut installé à LLUMC (Hurley et al., 2012). Ce système est basé sur des détecteurs à bandes de silicone et un calorimètre. Il a été conçu afin de fonctionner à un taux d'acquisition limité, ce qui fait que le temps de scan était de plusieurs heures. Par conséquent, en 2011, une collaboration entre LLUMC, UCSC, et California State University San Bernardino, a conçu un scanner pCT de phase-II. Ce dernier prototype a permis l'acquisition de données de grande qualité avec un temps d'acquisition entre 6 et 10 minutes (Bashkirov et al., 2016b). D'autres améliorations sont en cours afin de réduire ce temps à 2-3 minutes.

En 2013, le consortium PRaVDA a entrepris le développement du premier système pCT entièrement à état solide. Dans leur design final, les trackers ainsi que le détecteur d'énergie sont tous deux à base de bandes de silicone. Ce scanner a permis l'acquisition d'une image avec un taux de 2×10^8 protons/s (Esposito et al., 2018).

D'autres prototypes ont été construits par ailleurs : en Italie avec le projet PRIMA (Cirrone et al., 2007a ; Menichelli et al., 2010 ; Sipala et al., 2011 ; Scaringella et al., 2013 ; Vanzi et al., 2013), au Japon (Saraya et al., 2014), en Norvège (Pettersen et al., 2017 ; Pettersen et al., 2019), etc. Enfin, protonVDA a entrepris d'implanter des systèmes d'imagerie proton en clinique. Un système de radiographie proton est actuellement en train d'être certifié, et un scanner pCT est en développement.

III.4 Modalités d'imagerie proton alternatives

Bien que la plupart des développement en imagerie proton concernent l'imagerie basée sur la perte d'énergie, certains travaux portent sur la reconstruction d'image à partir d'informations différentes. Par exemple, Bopp et al. (2013, 2015) et Quinones, Létang et Rit (2016) ont étudié l'utilisation de la déviation angulaire et/ou du taux de transmission des protons. Ces modalités permettent la reconstruction d'un contraste différent, mais souffrent d'un bruit statistique important. Par ailleurs, Saudinos et al. (1975) ont proposé d'utiliser la diffusion nucléaire de protons à haute énergie (500 MeV à 1 GeV) afin de reconstruire des objets sans rotation du faisceau ou de l'objet. Il s'agit de mesurer des protons ayant été déviés par diffusion nucléaire et de retrouver le point d'interaction. Cette technique est limitée par le besoin d'un accélérateur à haute énergie, une faible résolution spatiale, et un mauvais rapport signal sur bruit étant donné que les réactions nucléaires sont plus rares que les interactions électromagnétiques. Des projets similaires ont plus récemment étudié l'utilisation de cette méthode dans le cadre de la thérapie carbone, étant donné que les interactions nucléaires sont plus fréquentes pour les ions carbone que pour les protons (Amaldi et al., 2010).

III.5 Reconstruction en proton CT

III.5.1 Estimation de la trajectoire

Afin d'améliorer la résolution spatiale, le chemin le plus vraisemblable d'un proton, sachant la position et direction en entrée/sortie, peut être dérivé en utilisant une approximation gaussienne du MCS. Schulte et al. (2008) ont proposé un formalise compact, basé sur des matrices, et pouvant fonctionner même dans le cas d'une information partielle sur la position/direction du proton. Afin de rentrer dans le cadre de l'approximation gaussienne, un filtrage en fonction de l'angle de sortie est effectué afin d'éliminer les protons avec un angle de déviation trop important. Un filtrage en fonction de l'énergie de sortie est également pratiqué afin d'exclure les interactions nucléaires non-élastiques et d'améliorer la résolution en densité. Bien que le formalisme du MLP donne la meilleure estimation de la trajectoire du proton, il est coûteux en matière de temps de calcul comparé à des méthodes plus simples. L'estimation la plus simple est de supposer une trajectoire linéaire reliant la position d'entrée à la position de sortie, mais cela conduit à une mauvaise résolution spatiale. Par ailleurs, une trajectoire spline cubique est un compromis intéressant car son calcul est moins coûteux que celui du MLP et elle permet une nette amélioration de la résolution spatiale.

III.5.2 Algorithmes de reconstruction

Le problème de reconstruction d'image à partir de projections est bien connu et a été largement étudié. En imagerie CT à rayons X, les mesures correspondent à des intégrales le long de lignes droites à différents angles. L'ensemble de ces intégrales correspond à la transformée de Radon de l'image. La reconstruction de l'image à partir d'intégrales de lignes peut-être effectué analytiquement, l'algorithme de rétroprojection filtrée (Kak et Slaney, 1988) étant l'une des solutions les plus populaires. Par ailleurs, des méthodes itératives, bien que plus coûteuses en matière de calculs, offrent de sérieux avantages concernant la réduction de dose et d'artefacts, et deviennent donc de plus en plus populaires afin de produire des images à faible dose. Dans ce cas, la reconstruction revient à résoudre un système d'équations linéaires. Dû à la grande taille du système et à l'impact du bruit, une simple inversion de matrice n'est pas envisageable. Ainsi, différents types d'algorithmes itératifs ont été développés, le plus simple étant l'algorithme ART (Gordon, Bender et Herman, 1970).

De prime abord, les méthodes itératives semblent plus adaptées à l'imagerie pCT. Les méthodes analytiques supposent en effet des lignes droites, et il n'y a pas de solution mathématique afin d'inverser une intégrale le long d'une trajectoire curviligne, à l'exception des trajectoires circulaires. Les méthodes itératives peuvent être plus facilement redéfinies pour résoudre un problème de pCT. Ainsi, différents méthodes ont été testées dans le cadre de l'imagerie pCT (Li et al., 2006 ; Wang, Mackie et Tomé, 2010 ; Penfold et al., 2010b ; Hansen et al., 2014b ; Hansen, Sørensen et Rit, 2016). Par ailleurs, différentes façons d'adapter les algorithmes analytiques à la proton CT ont été proposées. Par exemple, l'algorithme de FBP peut être combiné à un filtrage des protons pour ne garder que des trajectoires quasi-linéaires, bien que cela donne des images limitées en matière de résolution spatiale et augmente la dose et le temps d'acquisition. Alternativement, l'algorithme de FBP a été heuristiquement adapté aux trajectoires curvilignes en effectuant un binning en fonction de la distance du proton à l'intérieur de l'objet à reconstruire (Rit et al., 2013). D'autres approches directes ont ensuite été développées (Poludniowski, Allinson et Evans, 2014 ; Rit et al., 2015 ; Collins-Fekete et al., 2016). Une comparaison entre plusieurs algorithmes directs et itératifs en pCT a été effectuée par Hansen, Sørensen et Rit (2016). Les résultats ont démontré que les méthodes directs produisent des images de qualité comparable aux méthodes itératives, même à faible dose, tout en étant beaucoup plus rapides.

IV Trajectoire des protons en milieu hétérogène

IV.1 Introduction

Le formalisme du MLP suppose un milieu homogène, ce qui est approximatif pour plusieurs raisons. Premièrement, la longueur de radiation X_0 est nécessaire pour calculer les matrices de diffusion. Étant donné que la composition de l'objet est inconnue, une valeur constante, correspondant à la longueur de radiation de l'eau, est assignée. De plus, le ratio $1/p^2v^2$ est approximé à partir de l'énergie perdue par un proton dans l'eau. Or, l'énergie perdue dépend des tissus traversés, ce qui introduit également des inexactitudes dans l'estimation de la diffusion coulombienne. Enfin, l'hétérogénéité des tissus remet également en cause l'hypothèse d'une distribution gaussienne des positions et angles de diffusion. Même dans le cas homogène, la diffusion à grand angle et les interactions nucléaires induisent des queues non gaussiennes dans les distributions spatio-angulaires. Mais l'impact de ces évènements est atténué par l'application de filtres en angle et en énergie. On peut donc considérer que l'approximation gaussienne est valide dans le cas homogène. À vrai dire, elle est valide tant que les tissus varient uniquement en fonction de la profondeur, mais pas en fonction de la direction perpendiculaire au faisceau. Dans le cas d'une hétérogénéité transverse, on s'attend à une distribution asymétrique étant donné que le pouvoir de diffusion dépendrait de la position latérale. Ce type d'hétérogénéités transverses pourrait causer des erreurs systématiques du MLP si elles sont assez conséquentes. Contrairement à l'approximation sur la valeur de la longueur de radiation ou le ratio $1/p^2v^2$, cette asymétrie ne pourrait pas être simplement corrigée en introduisant une information sur les tissus traversés, mais demanderait une reformulation du formalisme du MLP.

Des observations de diffusion asymétrique ont été rapportées par West et Sherwood (1972, 1973) qui avaient remarqué des franges dans la distribution de la fluence des protons à proximité d'hétérogénéités transverses. Cet effet avait été exploité en imagerie proton basée sur la fluence afin d'améliorer la résolution en densité. Cependant, en imagerie CT proton basée sur la perte d'énergie, cela est considéré comme une cause de détérioration de la qualité d'image. Quelques études ont été menées afin d'évaluer l'impact, ou même de prendre en considération, les hétérogénéités dans le formalisme du MLP. Mais seules les hétérogénéités longitudinales ont été considérées jusqu'à présent. Wong et al. (2009) ont étudié l'impact des hétérogénéités longitudinales sur le MLP. Leurs résultats n'ont pas démontré d'erreur systématique sur le MLP, seulement une augmentation du RMS étant donné que des inserts d'os avaient été ajoutés. Collins-Fekete et al. (2017a) ont étendu le formalisme du MLP en incluant une information sur la composition des tissus, mais leur formalisme suppose toujours une distribution symétrique du MCS. Leurs résultats ont démontré que leur formalisme étendu ne permet pas de réduire le RMS comparé au formalisme standard.

Nous avons observé l'effet d'une diffusion asymétrique à proximité d'hétérogénéités transverses expérimentalement : des profils acquis à l'institut Curie - Centre de thérapie proton à Orsay (France) ont montré des distributions non gaussiennes lorsque les protons traversent des interfaces dans un fantôme CIRS. Les bords des inserts d'os et de poumon sont associés avec des valeurs d'asymétrie importantes. Nos travaux étudient les effets des hétérogénéités, et plus particulièrement les hétérogénéités transverses, sur l'estimation de la trajectoire du proton. Pour cela, nous avons utilisé des trajectoires simulées par Monte Carlo afin de définir un MLP de référence, et l'avons comparé au formalisme conventionnel du MLP.

IV.2 Matériels et méthodes

Nous avons comparé le MLP théorique proposé par Schulte et al. (2008) à un MLP simulé. La plateforme GATE (Jan et al., 2011) a été utilisée afin de simuler des trajectoires de proton dans différents fantômes :

- un fantôme homogène composé d'eau (A),
- un fantôme hétérogène avec une interface longitudinale os/eau (B),
- un fantôme hétérogène avec une interface transverse os/eau (C),
- la tête d'un fantôme réaliste (ICRP, 2009) avec des voxels de $1.775 \times 1.775 \times 4.84$ mm^3.

Les trois premiers fantômes ont été utilisés pour étudier les effets des hétérogénéités dans des conditions simples. Bien que ces fantômes exagèrent les hétérogénéités comparés aux interfaces trouvées dans le corps humain, ils ont été utilisés pour quantifier l'erreur maximale sur le MLP. Le fantôme de tête anthropomorphe a été utilisé pour quantifier l'erreur sur le MLP dans des conditions réalistes. Nous avons identifié les régions avec les hétérogénéités les plus importantes en calculant les projections de la dérivée de la carte $1/X_0$ du fantôme ICRP. Nous avons sélectionné deux régions présentant une hétérogénéité transversale : une interface entre l'air ($X_0 = 6.3 \times 10^{11}$ cm) et le sommet de la tête ($X_0 = 43.4$ cm) de longueur 3.4 cm, et une interface de 7.7 cm de long entre les dents ($X_0 = 9.0$ cm) et la mandibule ($X_0 = 29.4$ cm).

Une source de protons monoénergétiques de 250 MeV a été simulée pour traverser ces fantômes. Un faisceau non-divergent a été utilisé pour garder les protons tangents à l'interface transversale. Pour les trois premiers fantômes, une source ponctuelle a été utilisée à différentes positions d'entrée. Pour le fantôme ICRP, nous avons simulé une source de protons rectangulaire uniforme de taille 4 × 4 mm. Nous avons simulé 10^7 protons pour chaque trajet testé, et pour chaque particule la trajectoire était suivie à l'intérieur du fantôme. De plus, deux détecteurs idéaux mesurant le position et la direction ont été positionnés à 40 cm en amont et en aval de l'isocentre. L'énergie cinétique des protons a également été enregistrée car une asymétrie dans les distributions spatio-angulaires affecte également la distribution en énergie. Les résultats utilisant la liste de physique *emstandard* – utilisée pour simuler les processus électromagnétiques uniquement – et la liste $QGSP\_BIC$ – utilisée pour simuler tous les processus d'interaction – ont été comparés.

Pour calculer le MLP réel des protons passant par chaque fantôme, nous avons d'abord sélectionné les trajectoires d'un sous-ensemble de protons dont les coordonnées d'entrée et de sortie sont très proches. Les intervalles utilisés pour sélectionner ces sous-ensembles reflètent la résolution spatiale et angulaire typique des détecteurs utilisé en pCT (Bopp et al., 2014). Nous avons testé plusieurs combinaisons de coordonnées d'entrée et de sortie pour trouver le biais maximal créé par les hétérogénéités. Pour chaque cas, nous avons comparé le MLP théorique au MLP réel. Pour estimer le MLP réel, nous avons construit l'histogramme des positions transversales à différentes profondeurs dans le fantôme et ajusté une somme de deux gaussiennes à cet histogramme. Nous avons déterminé le MLP réel à chaque profondeur comme étant le mode de la distribution, c'est-à-dire la position du maximum. Le biais absolu maximal a été utilisé afin de caractériser la justesse du formalisme de MLP théorique.

IV.3 Résultats et discussion

Nos résultats ont montré que l'hypothèse d'une distribution spatiale et angulaire gaussienne, utilisée pour calculer le MLP des protons, n'est pas valide en cas d'asymétrie dans la diffusion due à des hétérogénéités transversales. Lorsque les protons traversent deux tissus différents en même temps, le tissu avec le pouvoir de diffusion le plus élevé dispersera les particules avec des angles plus grands. Ainsi, un plus grand nombre de protons se retrouvera dans le tissu adjacent. Ceci provoque des distributions asymétriques, voire des distributions avec plusieurs pics. Cette asymétrie crée un biais entre le MLP obtenu à partir de simulations Monte Carlo et le MLP théorique, qui suppose une distribution gaussienne. Par exemple, le MLP théorique peut prédire un chemin droit tandis que le MLP réel près d'une hétérogénéité transverse penche vers le milieu le moins diffusant de l'interface. Le biais maximal que nous avons mesuré est de 0.5 mm. Cependant, il a également été montré que dans les cas où la distribution n'est pas unimodale (lorsqu'il y a plus d'un pic), le MLP estimé en utilisant la pic majeur peut produire une trajectoire discontinue. Dans ce cas, le biais ne reflète pas la différence entre le MLP réel et théorique mais plutôt la différence entre la position la plus probable et le MLP théorique. Si on ne considère que les cas avec des distributions unimodales, le biais maximal atteint 0.45 mm. Pour une hétérogénéité réaliste, ce biais n'atteint que 0.13 mm.

Nos résultats remettent en cause la définition du MLP en milieu hétérogène. Habituellement, le MLP est défini comme la jonction des positions transversales les plus probables en fonction de la profondeur. Bien que cette représentation produise des trajectoires valides dans le cas d'une distribution spatiale unimodale, les positions les plus probables ne définissent pas une trajectoire réaliste et continue dans le cas de distributions à plusieurs pics. Dans de tels cas, le MLP devrait être interprété comme les positions les plus probables plutôt que comme le chemin le plus probable. Il pourrait être intéressant de développer une définition alternative du MLP sans supposer une distribution gaussienne des angles et des positions de diffusion. Cependant, il faut garder à l'esprit que les biais mesurés pour des hétérogénéités réalistes n'atteignent au plus que 0.13 mm. De plus, parmi les nombreux protons enregistrés et utilisés pour reconstruire une image pCT, seuls quelques-uns auront des coordonnées d'entrée et de sortie suggérant qu'ils ont traversé une interface transverse. Par conséquent, une correction du biais n'apporterait probablement pas d'amélioration significative en matière de résolution spatiale.

Nous avons pu vérifier qu'une adaptation du formalisme incluant une longueur de radiation et un produit moment-vélocité dépendant de la profondeur (Collins-Fekete et al., 2017a) est suffisante pour corriger le biais dans un fantôme longitudinalement hétérogène. De plus, nous avons confirmé que le RMS n'est pas une métrique satisfaisante pour évaluer l'impact des hétérogénéités sur la précision du MLP. En effet, l'erreur RMS est impactée par le biais systématique de l'estimation du MLP mais aussi par l'incertitude autour cette estimation, qui dépend du pouvoir de diffusion du milieu. L'utilisation d'autres métriques telles que l'erreur moyenne ou maximale permet une meilleure évaluation de la jutesse du MLP.

Il pourrait être intéressant d'étudier les effets des hétérogénéités transverses sur l'énergie de sortie des protons afin de vérifier si elles peuvent conduire à des artefacts pendant la reconstruction, étant donné que des protons ayant le même MLP théorique auraient des énergies de sortie différentes. Nous avons montré qu'à proximité d'une interface transversale, le véritable MLP penchera vers le matériau le moins diffusant. Nous nous attendrions donc à ce que l'interface reconstruite soit légèrement décalée vers la région avec le plus fort pouvoir de diffusion. De plus, des profils énergétiques tels que ceux que nous avons observés compliqueraient le filtrage énergétique utilisé pour filtrer les événements nucléaires.

IV.4 Conclusion

Dans ce chapitre, nous avons étudié l'impact des hétérogénéités sur les distributions de diffusion spatio-angulaires, et comment cela peut conduire à des erreurs systématiques dans la prédiction du MLP. Il a été démontré que les hétérogénéités transverses induisent des distributions non gaussiennes. En fonction de la trajectoire le long de l'interface, les distributions ressemblent à des gaussiennes asymétriques ou à une somme de deux gaussiennes. Dans le premier cas, il y a une erreur systématique sur le MLP théorique car les protons sont plus susceptibles de traverser le milieu le moins diffusant. Dans le second cas, la notion d'un seul chemin probable n'est pas adapté. Le biais maximal entre le MLP théorique et le MLP dérivé des trajectoires simulées atteint 0.45 mm pour une interface eau/os de 20 cm de long et 0.13 mm pour une interface au niveau de la tête d'un fantôme anthropomorphe. Nous avons observé que les hétérogénéités longitudinales induisent une très faible erreur systématique sur le MLP, qui peut être corrigée en utilisant une connaissance préalable de la composition tissulaire de l'objet. Bien que l'impact des hétérogénéités sur le MLP soit faible, combiné à l'impact sur les distributions en énergie, il pourrait conduire à des artefacts pendant la reconstruction.

V Filtre rampe directionnel en 2D

V.1 Introduction

La rétroprojection filtrée (FBP) est l'algorithme de référence pour reconstruire des données tomographiques. Il consiste à (1) filtrer les projections avec un filtre rampe 1D et (2) rétroprojecter le résultat dans le domaine de l'image. Une méthode alternative, le backproject-filter ou backproject first (BPF), commence par la rétroprojection avant d'effectuer le filtrage dans le domaine de l'image 2D. Les approches BPF peuvent se révéler utiles dans certains cas pour éviter un ré-échantillonnage. Par exemple, en proton CT, commencer par rétroprojecter les protons le long de leurs trajectoires non linéaires pourrait améliorer la résolution spatiale, comparé au binning des données en mode liste en projections (Zeng, 2007; Poludniowski, Allinson et Evans, 2014; Rit et al., 2015). De même, le temps de vol (TOF) en imagerie PET peut être pris en compte dans le domaine de l'image (Watson, 2007). Notre objectif est de développer une approche similaire en étendant le filtre rampe 1D en deux dimensions. Les méthodes BPF reposent généralement sur des filtres radiaux 2D. Cependant, l'image rétroprojectée a un support infini, ce qui est problématique lors de la convolution avec le filtre car la matrice de rétroprojection calculée a une taille finie. La troncature de la rétroprojection entraîne un offset dans les valeurs reconstruites, qui peut être minimisé en calculant de grandes matrices de rétroprojection. Une autre approche possible est basée sur l'inversion de la transformée de Hilbert (Noo, Clackdoyle et Pack, 2004; Zeng, 2007; Rit et al., 2015).

Dans ce travail, l'idée est de (1) "étaler" chaque projection dans l'espace image, (2) filtrer la projection étalée avec une version 2D du filtre rampe et (3) faire la somme de toutes les projections filtrées. Une version 2D similaire du filtre à rampe a été proposée par Watson (2007) pour l'imagerie TOF PET, bien que le filtre ait été échantillonné directement dans le domaine fréquentiel provoquant des artefacts d'échantillonnage. De la même manière que pour le filtre rampe 1D, nous allons échantillonner notre filtre 2D dans le domaine spatial pour éviter les artefacts d'échantillonnage. Nous commencerons par définir le filtre rampe 2D dans le cas de l'imagerie xCT parallèle, puis nous dériverons son expression dans le domaine spatial, avant d'appliquer cette méthode à des données xCT et pCT simulées. Bien que la principale application de ce filtre soit l'imagerie pCT, le filtre est mathématiquement dérivé dans le contexte de l'imagerie xCT pour plus de simplicité, puis appliqué à des données pCT.

V.2 Matériels et méthodes

V.2.1 Dérivation du filtre

Une image $f(x_1, x_2)$, où (x_1, x_2) sont les coordonnées spatiales, peut être reconstruite depuis ses projections parallèles

$$p_\phi(s_1) = \int_{\mathbb{R}} f(s_1\boldsymbol{\theta} + s_2\boldsymbol{\theta}^\perp)\,\mathrm{d}s_2, \tag{7.22}$$

où s_1 est la distance entre le centre et la ligne de projection, s_2 est la position le long de la ligne de projection, $\boldsymbol{\theta} = (\cos\phi, \sin\phi)$ et $\boldsymbol{\theta}^\perp = (-\sin\phi, \cos\phi)$. Selon la méthode de la rétroprojection filtrée, l'image est reconstruite par

$$f(x_1, x_2) = \int_0^\pi \tilde{p}_\phi(x_1\cos\phi + x_2\sin\phi)\,\mathrm{d}\phi, \tag{7.23}$$

avec

$$\tilde{p}_\phi(s_1) = \int_{\mathbb{R}} P_\phi(\sigma_1)|\sigma_1|e^{i2\pi\sigma_1 s_1}\,\mathrm{d}\sigma_1, \tag{7.24}$$

où $P_\phi(\sigma_1)$ est défini comme étant la transformée de Fourier (FT) de $p_\phi(s_1)$.

Les projections sont filtrées puis rétroprojetées dans l'image en utilisant le changement de variable $s_1 = x_1\cos\phi + x_2\sin\phi$. Nous souhaitons appliquer une version 2D du filtre rampe sur les projections déjà rétroprojetées, c'est-à-dire faire le changement de variable avant le filtrage.

On rappelle que (σ_1, σ_2) sont les variables de Fourier correspondant à (s_1, s_2) dans le domaine spatial. On introduit la fonction Dirac δ, en utilisant la propriété $\int_{\mathbb{R}} \delta(\sigma_2)e^{i2\pi\sigma_2 s_2}\,\mathrm{d}\sigma_2 = 1$, dans l'équation 7.24

$$\tilde{p}_\phi(s_1) = \int_{\mathbb{R}}\int_{\mathbb{R}} \delta(\sigma_2)P_\phi(\sigma_1)|\sigma_1|e^{i2\pi(\sigma_1 s_1 + \sigma_2 s_2)}\,\mathrm{d}\sigma_1\,\mathrm{d}\sigma_2 \tag{7.25}$$

et, étant donné l'expression de la transformée de Fourier $P_\phi(\sigma_1)$ et le fait que $\delta(\sigma_2) = \int_{\mathbb{R}} e^{-i2\pi\sigma_2 s_2}\,\mathrm{d}s_2$, on note que

$$\delta(\sigma_2)P_\phi(\sigma_1) = \int_{\mathbb{R}}\int_{\mathbb{R}} p_\phi(s_1)e^{-i2\pi(\sigma_1 s_1 + \sigma_2 s_2)}\,\mathrm{d}s_1\,\mathrm{d}s_2. \tag{7.26}$$

On utilise les notations vectorielles suivantes $s_1 = \boldsymbol{x}\cdot\boldsymbol{\theta}$, $s_2 = \boldsymbol{x}\cdot\boldsymbol{\theta}^\perp$, et pour les variables de Fourier correspondantes $\sigma_1 = \boldsymbol{\xi}\cdot\boldsymbol{\theta}$ et $\sigma_2 = \boldsymbol{\xi}\cdot\boldsymbol{\theta}^\perp$, où $\boldsymbol{x} = (x_1, x_2)$ et $\boldsymbol{\xi} = (\xi_1, \xi_2)$. On définit également $b_\phi : \mathbb{R}^2 \to \mathbb{R}$, la rétroprojection d'une seule projection, comme

$$b_\phi(\boldsymbol{x}) = p_\phi(\boldsymbol{x}\cdot\boldsymbol{\theta}), \tag{7.27}$$

et $B_\phi(\boldsymbol{\xi})$ sa transformée de Fourier. On appelle $b_\phi(\boldsymbol{x})$ une projection étalée. À partir de ces définitions, on note que l'équation 7.26 est l'expression de la transformée de Fourier de $b_\phi(\boldsymbol{x})$, et l'équation 7.25 devient

$$\tilde{b}_\phi(\boldsymbol{x}) = \int_{\mathbb{R}^2} B_\phi(\boldsymbol{\xi}) |\boldsymbol{\xi} \cdot \boldsymbol{\theta}| e^{i2\pi\boldsymbol{\xi}\cdot\boldsymbol{x}} \, \mathrm{d}\boldsymbol{\xi}. \tag{7.28}$$

L'image peut alors être reconstruite à partir de

$$f(\boldsymbol{x}) = \int_0^\pi \tilde{b}_\phi(\boldsymbol{x}) \, \mathrm{d}\phi. \tag{7.29}$$

Cette équation permet de reconstruire l'image à partir de trois étapes

1. Étaler chaque projection dans l'espace image, c'est-à-dire calculer l'image 2D $b_\phi(\boldsymbol{x})$ pour chaque angle de projection ;
2. Filtrer chaque image 2D $b_\phi(\boldsymbol{x})$ avec le filtre correspondant $|\boldsymbol{\xi} \cdot \boldsymbol{\theta}|$ afin d'obtenir $\tilde{b}_\phi(\boldsymbol{x})$;
3. Calculer la somme des images $\tilde{b}_\phi(\boldsymbol{x})$ sur tous les angles ϕ.

Il est à noter que cette version 2D du filtre rampe dépend de ϕ, d'où le nom filtre directionnel. Par définition, l'opération de rétroprojection consiste à étaler chaque projection dans le domaine image, c'est-à-dire interpoler $b_\phi(\boldsymbol{x})$ à partir de $p_\phi(s_1)$ en utilisant $b_\phi(\boldsymbol{x}) = p_\phi(\boldsymbol{x} \cdot \boldsymbol{\theta})$, et calculer la somme sur tous les angles de projection, c'est-à-dire calculer $\int_0^\pi b_\phi(\boldsymbol{x}) d\phi$. Dans la méthode proposée ici, ces deux étapes sont séparées : les étapes (1) et (3) correspondent à la rétroprojection et l'étape (2) au filtrage. Cette méthode ressemble à une approche BPF étant donné qu'elle commence par étaler les projections dans l'espace image, cependant la somme angulaire afin de calculer la rétroprojection est la dernière étape comme dans les approches FBP.

Le filtre conique 2D habituellement utilisé dans les approches BPF est $\|\boldsymbol{\xi}\|$. Contrairement au filtre directionnel qui doit être utilisé avant la somme angulaire étant donné qu'il dépend de l'angle de projection, le filtre conique est appliqué après la rétroprojection complète car il n'est pas dépendent de la direction. Il a été mentionné dans l'introduction qu'un filtre similaire au filtre directionnel a été proposé pour la reconstruction de données TOF PET (Watson, 2007). Ce filtre a été échantillonné directement dans le domaine fréquentiel, causant des artefacts d'échantillonnage. Ici, on calcule la réponse impulsionnelle du filtre comme dans le cas 1D afin d'éviter ces artefacts.

Une version limitée en bande de fréquence du filtre directionnel 2D est donnée par

$$H_\phi(\boldsymbol{\xi}) = \begin{cases} |\boldsymbol{\xi} \cdot \boldsymbol{\theta}| & \text{si } \mid \xi_1 \mid, \mid \xi_2 \mid < W \\ 0 & \text{sinon.} \end{cases} \tag{7.30}$$

Le kernel correspondant dans l'espace direct est obtenu en calculant la transformée de Fourier inverse de ce filtre directionnel :

$$h_\phi(\boldsymbol{x}) = \int_{\mathbb{R}^2} H_\phi(\boldsymbol{\xi}) e^{i2\pi\boldsymbol{\xi}\cdot\boldsymbol{x}} \, \mathrm{d}\boldsymbol{\xi}. \tag{7.31}$$

La réponse impulsionnelle discrète est donnée dans l'équation 5.16.

V.2.2 Simulations

Nous avons généré des projections parallèles du fantôme 2D de Shepp Logan (Shepp et Logan, 1974) en utilisant RTK (Rit et al., 2014). Un total de 804 projections ont été acquises sur une plage de 180 degrés, avec un détecteur de 512 pixels. Le fantôme a été reconstruit sur des grilles de 512×512 pixels et 1024×1024 pixels. Du bruit Poissonien a été appliqué aux projections idéales, en utilisant une fluence initiale de 10^7 photons par pixel, et en pondérant les intégrales de ligne avec 0.01879 mm^{-1}, le coefficient d'atténuation linéaire de l'eau à 75 keV.

Une simulation proton CT a été réalisée à l'aide de la plateforme Monte Carle GATE (Jan et al., 2011). Une configuration en mode liste a été utilisée, composée de deux détecteurs idéaux mesurant la position, la direction et l'énergie, situés en amont et en aval des fantômes. Un faisceau en éventail de protons à 200 MeV a été positionné à 1 m du centre de l'objet, avec un flux de 225 $\text{protons}\cdot\text{mm}^{-2}\cdot\text{projection}^{-1}$ à l'isocentre, pour un total de 720 projections sur une plage de 360 degrés. La trajectoire de chaque proton a été estimée en utilisant le formalisme MLP, après exclusion des protons ayant subi des interactions nucléaires (Schulte et al., 2008). Les données en mode liste ont été binnées en images $b_\phi(x)$ en utilisant la même procédure que celle décrite par Rit et al. (2015). L'image a été reconstruite sur une grille de 1000×1000 pixels de taille 0.25 mm. Un fantôme en spirale a été simulé, constitué d'un disque d'eau de 20 cm avec des inserts d'aluminium afin de prendre en compte la dépendance spatiale de la résolution spatiale. La résolution spatiale a été définie comme la fréquence correspondant à une MTF de 10%.

V.3 Résultats et discussions

Nos résultats montrent que le filtre directionnel 2D, échantillonné dans le domaine spatial, permet de reconstruire des données xCT et pCT, bien que certains artefacts soient apparents dans le cas de reconstructions à partir de projections xCT idéales. Comme cela a été observé pour le filtre rampe 1D par Crawford (1991) et Kak et Slaney (1988), l'échantillonnage dans le domaine fréquentiel provoque des artefacts d'aliasing en raison du support infini de la réponse impulsionnelle. Dans l'espace direct, le filtre DR devrait ressembler à un Dirac dans la direction $\boldsymbol{\theta}^{\perp}$ pour que la convolution 2D soit équivalente à celle en 1D. Cependant, le fait d'apodiser le filtre entraîne une convolution avec une fonction sinc 2D. Cela qui signifie qu'il y aura des interférences entre les différentes lignes pendant la convolution. Dans l'espace de Fourier, cela se traduit par une discontinuité de la transformée de Fourier à la fréquence de Nyquist. Cela pourrait expliquer les artefacts observés sur certaines reconstructions. Un problème similaire avec la continuité de la FT a été rapporté par Schöndube, Stierstorfer et Noo (2010), qui définissent une transformée de Hilbert inverse en 2D. L'image reconstruite à l'aide de ce filtre présentait des artefacts en anneau. L'une des solutions proposées est d'apodiser le filtre dans l'espace de Fourier en utilisant une fenêtre de Hamming. Nos résultats montrent que l'apodisation supprime les artefacts, même si elle provoque une légère perte de résolution spatiale. Une alternative consiste à augmenter la fréquence d'échantillonnage de l'image rétroprojectée, ce qui réduit également le bruit. Cependant, ces artefacts ne sont pas visibles lorsque des projections avec un niveau de bruit réaliste sont utilisées.

Dans le cas d'intégrales de ligne simples, comme pour le cas de l'imagerie xCT, l'utilisation du filtre DR 2D donne le même résultat qu'un algorithme de FBP standard mais est moins efficace en matière de calcul. Ainsi, le filtre DR a plutôt vocation a être utilisé avec des modalités telles que la proton CT ou la TOF PET, où les projections sont respectivement des intégrales le long de chemins non linéaires ou des intégrales le long de lignes pondérées en raison de la résolution temporelle du détecteur. En imagerie xCT, les projections sont constantes selon la direction $\boldsymbol{\theta}^{\perp}$, il est donc sensé de traiter les projections dans l'espace 1D. En imagerie pCT ou TOF PET, une nouvelle dimension est ajoutée, la profondeur du proton ou le temps de vol, de telle sorte que les projections varient selon $\boldsymbol{\theta}^{\perp}$. Le filtrage des projections 2D $b_{\phi}(x)$ nécessite soit de faire pivoter chaque image pour que ses échantillons soient alignés avec le filtre 1D, puis d'effectuer un filtrage ligne par ligne; soit d'utiliser un filtre rampe 2D directionnel. Ce filtre pourrait alors présenter des avantages : comme dans les méthodes BPF, le filtrage se fait dans l'espace image afin d'éviter des rotations qui peuvent provoquer une perte de résolution spatiale; et en même temps, contrairement aux autres approches BPF, il n'y a pas de biais dû à la troncature de la région de rétroprojection. Un inconvénient est que le filtre DR est différent pour chaque angle de projection, mais il peut être pré-calculé pour une grille et un ensemble d'angles de projection donnés.

Nos résultats pour les données proton CT ont confirmé que le filtre DR permet d'améliorer la résolution spatiale par rapport à un algorithme FBP. Cette amélioration n'a été observé que pour des inserts proches du bord du fantôme en spirale car au centre de l'objet, l'image est trop floue en raison de la diffusion de Coulomb. De plus, aucun artefact d'échantillonnage n'a été observé étant donné que le bruit de l'image pCT était dominé par le straggling en énergie des protons, la diffusion coulombienne et le bruit statistique. Bien que cette méthode ne soit théoriquement démontrée que pour les géométries parallèles, d'autres géométries peuvent être utilisées lors de l'acquisition tant que les données sont rebinnées en géométrie parallèle, ce qui est simple pour les données pCT en mode liste.

V.4 Conclusion

Nous avons proposé une version 2D du filtre rampe, appelé filtre rampe directionnel. Ce filtre peut être utilisé à la place du filtre rampe 1D pour prendre en compte la dimension de profondeur des données pCT. Cette méthode de reconstruction commence par étaler chaque projection dans l'espace de l'image, puis effectue un filtrage direction-dépendent, et enfin calcule la somme sur toutes les directions. Cette méthode permet de reconstruire des images pCT et peut être utilisée pour éviter une interpolation qui dégraderait la résolution spatiale. Par la suite, cette méthode sera plus rigoureusement comparée aux autres méthodes de reconstruction pCT en termes de résolution spatiale et de précision du RSP.

VI Comparaison d'algorithmes de reconstruction directs en tomographie proton

VI.1 Introduction

Le problème inverse en imagerie pCT est similaire à celui en tomographie à rayons X étant donné qu'il consiste à reconstruire une image à partir d'intégrales de ligne. Ce qui distingue les deux problèmes est qu'en pCT, les lignes d'intégration qui représentent les trajectoires des protons ne sont pas linéaires. Nous avons brièvement présenté les différentes méthodes de reconstruction en imagerie pCT dans l'introduction. Le MLP peut être inclus dans des algorithmes itératifs ou analytiques pour améliorer la résolution spatiale. Dans ce chapitre, nous nous concentrons sur les méthodes analytiques, que nous appellerons plutôt méthodes "directes" car il n'y a pas d'inversion mathématique pour les trajectoires des protons, toutes les solutions étant heuristiques. Bien que les algorithmes itératifs présentent des avantages, par exemple l'inclusion d'à priori pour améliorer la reconstruction (Hansen et al., 2014b), leur coût de calcul est généralement plus grand que pour les méthodes directes d'un ordre de grandeur (Hansen, Sørensen et Rit, 2016). Une comparaison entre plusieurs méthodes de reconstruction itératives et une méthode directe a été publiée par Hansen, Sørensen et Rit (2016). Cependant, aucune comparaison entre les méthodes de reconstruction directes n'a été rapportée dans la littérature. Le but de ce travail consiste à comparer cinq algorithmes directs différents, en se basant sur des métriques comme la résolution spatiale et la précision du RSP. Bien que certaines des méthodes directes soient assez proches, elles utilisent différents types d'approximations qui pourraient avoir un impact sur la résolution spatiale et/ou la précision du RSP. Par exemple, comme indiqué dans le chapitre précédent, les approches backproject-filter s'adaptent plus naturellement aux données en mode liste et pourraient donner une meilleure résolution spatiale. Mais certaines de ces méthodes nécessitent également le calcul de termes de correction qui pourraient dégrader la précision du RSP. En comparant ces méthodes, ce travail vise à sélectionner l'algorithme donnant la meilleure résolution spatiale tout en gardant une précision de RSP élevée et un temps de calcul raisonnable.

VI.2 Matériels et méthodes

Les algorithmes étudiés sont ceux proposés par Rit et al. (2013), Collins-Fekete et al. (2016), Poludniowski, Allinson et Evans (2014), Rit et al. (2015) et Khellaf et al. (2020a).

La même configuration que celle utilisée pour la contribution précédente a été simulée dans GATE (Jan et al., 2011) pour générer des données pCT. Trois fantômes ont été imagés : le module CTP528 du fantôme Catphan (The Phantom Laboratory, NY) avec des paires de lignes en aluminium de résolutions différentes dans un cylindre d'eau de 20 cm de diamètre ; le fantôme en spirale composé de cylindres en aluminium placés le long d'une spirale dans un cylindre d'eau de 20 cm de diamètre ; et le fantôme de caractérisation tissulaire Gammex 467 avec différents inserts de tissus à l'intérieur d'un cylindre d'eau de 33 cm de diamètre. Les fantômes utilisés pour l'évaluation de la résolution spatiale (Catphan et Spiral) ont été reconstruits sur des grilles de 1000 × 1000 pixels de 0.25 mm. Le fantôme Gammex 467 a été reconstruit sur une grille de 800 × 800 pixels de 0.5 mm, et a nécessité l'utilisation d'une énergie initiale 250 MeV en raison de son plus grand diamètre, au lieu de 200 MeV pour les deux autres fantômes. Afin d'estimer l'impact des incertitudes du détecteur sur la résolution spatiale, une incertitude sur la position et la direction mesurées a été ajoutée à l'aide du formalisme de Krah et al. (2018a). Les paramètres ont été choisis pour refléter un détecteur de pCT typique. En particulier, la résolution du détecteur a été caractérisée par une gaussienne de $\sigma_p = 0.15$ mm, la distance entre les trackers a été fixée à $d_T = 10$ cm, la distance entre les trackers et les bords de l'objet à 20 cm, et le *material budget* à $x/X_0 = 5 \times 10^{-3}$. La résolution énergétique des détecteurs et la dispersion du faisceau incident ont été omis par simplicité, étant donné que les détecteurs utilisés en pCT (Bashkirov et al., 2016a) sont capables d'atteindre une résolution de WEPL proche de la limite du *range straggling* des protons (résolution de WEPL mesurée de 3 mm pour un straggling de 2.85 mm, pour des protons de 200 MeV dans l'eau), même s'il est noté que la dispersion du faisceau peut contribuer à la variance du WEPL jusqu'à 20% (Dickmann et al., 2019). Les interactions électromagnétiques sont prises en compte dans la simulation et sont responsables de la résolution du RSP des images reconstruites.

VI.3 Résultats et discussion

L'objectif de ce travail était de comparer les performances de cinq algorithmes de reconstruction directes en matière de résolution spatiale et de précision de RSP. La résolution spatiale en pCT est influencée par divers facteurs. Un premier facteur est le MCS qui est atténué par la prise en compte du MLP. Ceci entraîne une amélioration considérable de la résolution spatiale par rapport à l'utilisation de trajectoires en ligne droite, bien que l'effet de la diffusion soit toujours important au centre des fantômes. Nous avons observé que la résolution au centre d'un fantôme de largeur 20 cm est d'environ $0.5 - 0.6$ lp/mm avec des trackers idéaux. Pour la méthode DR, le résolution est améliorée d'un facteur 6 entre le centre et la bordure du fantôme spirale. Puisque le centre de l'objet correspond à la plus grande incertitude sur le MLP, la différence de résolution spatiale entre les algorithmes n'est pas significative au centre. Une autre conséquence de la diffusion des protons est l'anisotropie de la résolution spatiale. Ainsi, la résolution azimutale devient supérieure à la résolution radiale en s'éloignant du centre. En raison du MCS, l'incertitude sur le MLP des protons traversant la même région dépendra de l'épaisseur du matériau traversé, c'est-à-dire de leur direction initiale. Pour les billes centrales, l'épaisseur traversée en fonction de la direction varie peu en raison de la forme cylindrique du fantôme, tel que la résolution est isotrope au centre. Le seul algorithme pour lequel la résolution azimutale est mauvaise est l'algorithme ML, en raison d'un artefact observé dans la reconstruction.

Un autre facteur de perte de résolution est l'incertitude du tracker qui a un impact significatif. Ainsi, l'ajout d'une incertitude sur la position et la direction dégrade considérablement la résolution spatiale par rapport aux données idéales. Il est à noter que ces résultats ont été obtenus avec une distance de 20 cm entre les trackers et les bords du fantôme. L'utilisation d'une plus grande distance réduirait davantage la résolution. Enfin, le choix de l'algorithme a également un impact sur la résolution car différents binnings et interpolations sont impliqués. Par exemple, en utilisant des détecteurs idéaux, la résolution à 96 mm du centre pour la méthode DR est 250% plus élevée que la résolution pour l'algorithme ML (seulement 25% au centre) et 26% plus élevée que la résolution pour l'algorithme DD (1% au centre). Nos résultats montrent que algorithmes les plus performants en matière de résolution spatiale loin du centre sont le DR et le BTF, ce qui suggère que la rétroprojection des protons avant le filtrage peut améliorer la résolution spatiale. En effet, les méthodes de filtrage en premier impliquent deux interpolations qui peuvent réduire résolution : le binning pour calculer les projections et la rétroprojection. En comparaison, une seule interpolation est nécessaire pour les méthodes backproject-first. Cela peut aider à préserver l'information spatiale de la trajectoire du proton, et donc de la résolution. Cependant, nous observé que la méthode DBP, qui commence par la rétroprojection, a la même résolution spatiale que l'algorithme DD. Cela peut s'expliquer par le calcul de la dérivée dans l'algorithme DBP qui peut entraîner une perte de résolution. L'algorithme ML produit la pire résolution spatiale, étant donné qu'il tente de prendre en compte les MLPs à travers des projections 2D, alors qu'ils ne peuvent être décrits que dans l'espace 3D. Cette méthode serait mieux adaptée à la radiographie proton qu'à la tomographie. Dans l'ensemble, l'impact du choix de l'algorithme est négligeable par rapport au MLP et à l'incertitude des trackers.

En matière de RSP, les algorithmes DR, DD et BTF montrent une bonne précision avec une erreur absolue moyenne proche de 0.1%. La méthode DBP est légèrement moins précise, ce qui peut être lié au calcul d'une constante lors de l'inversion de la transformée de Hilbert (Noo, Clackdoyle et Pack, 2004). L'algorithme ML surestime la valeur du RSP dans les inserts de poumon par rapport aux autres méthodes, ce qui induit une erreur moyenne plus élevée.

Le coût de calcul de chaque algorithme est un facteur important lorsque plusieurs algorithmes atteignent des niveaux de résolution et de justesse de RSP similaires. Le binning des données en mode liste est l'opération la plus coûteuse en matière de temps de calcul car le MLP de chaque proton doit être estimé. Les étapes de projection ou rétroprojection sont similaires en matière de temps de calcul. Ce temps augmente avec le nombre de protons et le nombre d'évaluations du MLP. Comme nous avons utilisé une fluence élevée (288×10^6 protons au total) et un échantillonnage fin pour l'évaluation du MLP (0.25 mm ou 0.5 mm selon le fantôme), le binning est beaucoup plus lent que les autres étapes de la reconstruction (pour la méthode DD, 8 s/projection × 720 projections pour le binning, et 42 s pour le filtrage et la rétroprojection). Les méthodes BPF et DR nécessitent que la région de rétroprojection soit plus grande que la taille de l'image reconstruite, ce qui augmente le temps de calcul du binning. Alors que la méthode DR nécéssite une région plus grande d'un facteur $\sqrt{2}$, la méthode BPF nécessite une matrice d'au moins deux fois la taille de l'image reconstruite. Ces méthodes sont donc les plus coûteuses en matière de calcul. Le coût de l'étape de filtrage varie beaucoup en fonction de l'algorithme. Par exemple, pour l'algorithme DD, un sinogramme 3D doit être filtré (pour chaque slice), alors qu'un sinogramme 2D est utilisé dans l'algorithme ML. Cependant, comme nous l'avons indiqué ci-dessus, le coût du l'étape de filtrage est assez négligeable par rapport au coût de l'étape de binning.

VI.4 Conclusion

Nous avons étudié la résolution spatiale et la précision du RSP de cinq algorithmes différents utilisés pour reconstruire des données proton en mode liste. Les résultats montrent qu'en utilisant des trackers idéaux, deux des méthodes qui effectuent le binning des données directement dans l'espace image (DR et BTF) offrent une meilleure résolution spatiale aux bords de l'objet, avec un maximum de 3.5 lp/mm aux bords d'un objet de 20 cm d'épaisseur. Cependant, compte tenu des incertitudes de mesure pour des trackers réalistes, l'impact du choix de l'algorithme sur la résolution spatiale devient négligeable. De plus, les méthodes DR, DD et BTF montrent la meilleure précision du RSP avec une erreur moyenne proche de 0.1%. Si les méthodes DR et BTF présentent un léger avantage en matière de résolution spatiale ainsi qu'une bonne précision, elles sont également les plus coûteuses en matière de temps de calcul. Pour des reconstructions plus rapides, l'algorithme DD offre la même précision et une résolution spatiale équivalente compte tenu des incertitudes du détecteur, et la méthode DBP, bien qu'un peu moins précise, offre une bonne résolution spatiale et peut être utilisée pour la reconstruction de données tronquées. La méthode ML est mieux adaptée pour la radiographie proton.

VII Déconvolution pour l'amélioration de la résolution spatiale en pCT

VII.1 Introduction

La résolution spatiale en pCT est principalement impactée par le MCS des protons et la résolution des trackers. Comme cela a été observé dans le chapitre précédent, la résolution spatiale dans l'image reconstruite est shift-variante et anisotrope. L'incertitude sur le trajet du proton ne dépend que de la profondeur du proton à l'intérieur de l'objet, et non des positions et directions transversales d'entrée/sortie mesurées. Pour des profondeurs d'entrée et de sortie données, l'incertitude sur le MLP est la plus grande près du centre de l'objet, là où le proton est le plus éloigné des trackers. Le maximum est légèrement décalé vers la sortie du fantôme en raison du terme de perte d'énergie. De plus, plus le trajet du proton à l'intérieur de l'objet est long, plus l'enveloppe d'incertitude est grande, de sorte que l'incertitude dépend de la forme de l'objet et de l'angle de projection car les profondeurs d'entrée/sortie sont données par l'intersection des contours de l'objet avec le chemins d'entrée/sortie des protons. L'ajout de la résolution des trackers ne fait qu'augmenter cette incertitude. Comme l'image reconstruite est une combinaison des projections filtrées, le flou dans chaque pixel de l'image est aussi le résultat d'une combinaison d'incertitudes différentes.

Dans ce travail, nous essayons de déconvoluer le flou en pCT dû aux incertitudes du MCS et du détecteur à partir d'une estimation de l'incertitude du MLP. La déconvolution est effectuée au niveau de la projection pour mieux prendre en compte la variance spatiale et l'asymétrie de la résolution spatiale. L'utilisation de l'incertitude du MLP pour améliorer la résolution spatiale a été mentionnée par Williams (2004) et Schulte et al. (2008). Wang, Mackie et Tomé (2010) ont tenté d'inclure cette incertitude dans la matrice de projection et ont effectué une reconstruction à l'aide de l'algorithme itératif ART. Cependant, leurs résultats n'ont pas montré d'amélioration de la résolution spatiale par rapport à l'utilisation du MLP sans l'incertitude. Nous proposons une méthode de déconvolution des projections distance-driven utilisées dans la méthode présentée par Rit et al. (2013). Afin de tenir compte de la résolution des trackers, nous utilisons le formalisme de Krah et al. (2018a) qui ont étendu le formalisme du MLP habituel pour inclure la résolution des trackers pour différents types de configurations. En particulier, ils proposent une expression de l'incertitude du MLP en tenant compte de la résolution spatiale et angulaire des trackers. Dans la section suivante, nous commençons par présenter le modèle de flou shift-variant des projections, puis nous utilisons le formalisme de Krah et al. (2018a) pour calculer des cartes d'incertitude, enfin nous déconvoluons l'incertitude en utilisant une décomposition en valeurs singulières tronquée (TSVD) (Hansen, Nagy et O'Leary, 2006).

VII.2 Matériels et méthodes

Nous considérons les projections $g_p(u,w)$, avec u la coordonnée latérale le long du détecteur, w la profondeur et p la position de la source. Le flou dans ces projections dépend de w car plus le proton est en profondeur à l'intérieur du fantôme, plus l'incertitude sur le MLP est importante ; et de u et p puisque les protons entrant et sortant de l'objet via différentes profondeurs auront des incertitudes différentes. Comme le flou se produit dans le plan (u,v), nous considérons les projections distance par distance, c'est-à-dire pour chaque w. Par conséquent, nous traitons une séquence de problèmes 1D, ce qui permet d'utiliser l'approche par décomposition en valeurs singulières (SVD) décrite ci-dessous. La projection mesurée est le résultat du floutage d'une projection idéale par un noyau gaussien shift-variant. La déviation standard du kernel gaussien représente l'incertitude du MLP pour les protons avec même position de source, profondeur et position latérale. La déconvolution consiste à inverser la matrice représentant cette opération shift-variante. Cette inversion a été effectuée via une SVD tronquée.

On utilise les simulations du fantôme en spirale décrites dans les sections précédentes. On rappelle qu'un faisceau de 200 MeV avec une fluence de 225 protons$\cdot$mm$^{-2}\cdot$projection^{-1} à l'isocentre est simulé. De plus, une acquisition à l'aide d'un fantôme ICRP (ICRP, 2009) a été simulée. Une énergie de faisceau de 250 MeV a été utilisée pour traverser tout le volume du fantôme, avec un flux de 190 protons$\cdot$mm$^{-2}\cdot$projection^{-1} car un faisceau plus large a été utilisé pour couvrir tout le volume. Au total, 720 projections sur une plage de 360 degrés ont été acquises. Deux coupes, près de la tête et près du bassin, ont été reconstruites. Pour calculer le MLP et son incertitude, la coque convexe du fantôme en spirale était connue et celle de la tête et du bassin a été approximée par une ellipse pour une détection rapide de l'intersection entre le patient et le trajet du proton. Les images ont été reconstruites sur des grilles de 500×500 pixels de taille 0.5×0.5 mm^2 pour la spirale et le fantôme de la tête et sur une grille de 800×800 pixels de taille 0.5×0.5 mm^2 pour le fantôme du bassin.

Les incertitudes du tracker ont été incluses en utilisant une résolution spatiale de $\sigma_t = 0.066$ mm correspondant à une largeur de bande de détection de 228 µm, un "material budget" $x/X_0 = 5 \times 10^{-3}$, et une distance $d_T = 10$ cm entre les détecteurs de chaque paire. Les détecteurs ont été placés à une distance de 30 cm de l'isocentre pour la simulation du fantôme en spirale, et à une distance de 40 cm pour le fantôme ICRP. Les images ont été reconstruites à partir de trackers idéaux en utilisant le formalisme standard pour calculer l'incertitude ; et à partir de trackers réalistes en utilisant le formalisme étendu. La résolution spatiale a été mesurée dans le fantôme en spirale en utilisant la fréquence correspondant à une valeur de MTF de 10%.

VII.3 Résultats et discussion

Le but de ce travail était d'utiliser l'incertitude sur le MLP afin d'améliorer la résolution spatiale des images en pCT. Premièrement, nous avons généré des cartes d'incertitude pour chaque distance-driven projection. Les cartes d'incertitude dépendent de la forme de l'objet, de l'angle de projection et des hétérogénéités dans l'objet. L'incertitude varie dans une seule projection en fonction de la profondeur et de la position transversale, mais elle est aussi différente entre chaque projection. Plus précisément, la contribution à l'incertitude du MCS à l'intérieur de l'objet (sans résolution du tracker) dépend de la projection lorsque le fantôme n'est pas parfaitement circulaire. Pour le fantôme au niveau du bassin, il y avait un facteur 2 entre l'incertitude maximale pour les protons traversant le grand axe de l'objet et ceux traversant le petit axe. L'ajout de la résolution du tracker augmente les valeurs d'incertitude et permet d'introduire une information supplémentaire sur les hétérogénéités. Bien que les formalismes MLP standard et étendu supposent un milieu homogène, les hétérogénéités à l'intérieur du fantôme sont prises en compte à travers le terme d'énergie utilisé pour le calcul de la diffusion dans le détecteur en sortie. En particulier, dans le cas du fantôme en spirale, les protons qui traversaient les inserts d'aluminium avaient des énergies de sortie plus faibles et se dispersaient davantage dans le tracker arrière, induisant ainsi des bandes de forte incertitude dans la projection.

Les images reconstruites pour le fantôme en spirale ont montré une augmentation de la résolution spatiale au centre de l'objet jusqu'à 38%/45% avec des trackers réalistes en fonction du niveau de troncature de la SVD. De même, les reconstructions du fantôme ICRP prenant en compte la résolution du tracker ont montré une amélioration visible de la résolution spatiale. Les résultats avec des trackers idéaux pour le fantôme en spirale ont montré une amélioration de la résolution spatiale uniquement au centre de l'objet. Aux bords, l'incertitude du MLP tend vers zéro, de sorte que le noyau est presque un Dirac. En raison de l'échantillonnage du kernel, c'est-à-dire de la taille des pixels dans les projections, il y a une limite au dessous de laquelle tous les noyaux sont des Diracs. C'est pourquoi il n'y a pas de différence de résolution spatiale ou de bruit loin du centre par rapport aux résultats non déconvolués. Les résultats pour les fantômes ICRP avec des trackers idéaux ne montrent aucune amélioration visible de la résolution spatiale. On pourrait s'attendre à une amélioration au centre où l'incertitude atteint environ 0.5 mm dans la tête. Cependant, nous rappelons que la taille de pixel pour le fantôme ICRP utilisé dans les simulations était de 1.775 mm, ce qui est assez grand par rapport à l'impact du MCS seul. Ceci impose une limite sur la résolution maximale pouvant être reconstruite, ce qui expliquerait le manque d'amélioration après déconvolution. Nous notons que nous avons utilisé une ellipse approximative comme coque convexe pour les fantômes de la tête et du bassin, ce qui provoque une erreur sur les valeurs d'incertitude utilisées pour calculer la matrice $\mathbf{H}$. La déconvolution n'est donc pas totalement optimale pour ces deux fantômes. En particulier pour le fantôme du bassin, l'ellipse choisie était trop petite.

Nous avons observé que le niveau de troncature doit être adapté au bruit dans les projections. Les données pCT pour le fantôme ICRP ont été acquises avec une fluence légèrement inférieure (190 protons$\cdot$mm$^2\cdot$projection^{-1} contre 225 protons$\cdot$mm$^2\cdot$projection^{-1} pour le fantôme en spirale) en raison du plus grand volume du fantôme ICRP, ce qui aurait pu nécessiter un niveau de troncature plus élevé. De plus, pour la même acquisition, le bruit variera en fonction de la distance dans la projection *distance-driven* en raison du MCS, de sorte qu'un niveau de troncature constant ne serait pas optimal. Dans ce travail, le niveau de troncature a été adapté de manière heuristique en testant différentes valeurs. Une meilleure compréhension de la relation entre le bruit dans les projections et le niveau de troncature de la SVD pourrait permettre une meilleure régularisation des images reconstruites.

Bien que le calcul d'une seule SVD ne soit pas trop coûteux, cette décomposition doit être faite pour chaque distance et chaque projection, ce qui peut rapidement augmenter la charge de calcul. Cette opération peut cependant être parallélisée. L'étude d'une méthode différente pour effectuer l'inversion de matrice pourrait améliorer le coût de calcul, et/ou permettre une meilleure régularisation de la déconvolution. Des algorithmes rapides pour la convolution shift-variante (Gilad et Von Hardenberg, 2006) pourraient être utilisés pour accélérer le calcul. De plus, comme la résolution du tracker réduit la variation spatiale des valeurs d'incertitude, l'utilisation d'un seul noyau par projection ou pour toutes les projections pourrait éventuellement améliorer la résolution – en fonction de la forme du fantôme et des hétérogénéités – tout en étant plus pratique. Il pourrait également être possible de faire la déconvolution dans l'espace image, après reconstruction. Pour cela, nous aurions besoin d'approximer la valeur d'incertitude dans chaque pixel de l'image reconstruite. Il pourrait être intéressant de comparer les résultats entre la déconvolution dans le domaine des projections et dans le domaine image. Nous nous attendons à ce que, selon le fantôme, les résultats soient similaires entre les deux méthodes. Par exemple, le fantôme du bassin présente une grande variabilité entre les cartes d'incertitude pour des angles différents de sorte que l'approximation de l'incertitude dans un pixel de l'image reconstruite serait la combinaison de valeurs très différentes. Pour la tête ou le fantôme en spirale, puisque la contribution à l'incertitude d'un pixel serait similaire pour tous les angles de projection, nous nous attendons à ce qu'une déconvolution basée sur l'image produise des résultats similaires.

Ce travail a été réalisé à l'aide d'un algorithme de distance-driven binning. La méthode peut être utilisée de la même manière avec d'autres algorithmes directs en déconvoluant les projections ou les rétroprojections partielles. Puisqu'il est basé dans le domaine des projections, l'application directe aux méthodes itératives n'est pas évidente. Bien que Wang, Mackie et Tomé (2010) aient essayé d'inclure l'incertitude du MLP dans leur modèle de projection, leurs résultats n'ont pas montré d'amélioration de la résolution spatiale. Alternativement, une déconvolution après reconstruction pourrait être effectuée indépendamment de la méthode de reconstruction.

VII.4 Conclusion

Le but de ce travail était d'évaluer si l'utilisation de l'incertitude sur le MLP dans un algorithme de reconstruction pCT pouvait améliorer la résolution spatiale. Nous avons généré des cartes d'incertitude pour un sinogramme "distance-driven" et effectué une déconvolution shift-variante en utilisant une approche TSVD. Il a été démontré que l'inclusion de l'incertitude sur le MLP pour effectuer la déconvolution de projections peut augmenter considérablement la résolution spatiale des images pCT. En particulier, la résolution dans un fantôme en spirale a été augmentée de 38% tout en conservant un niveau de bruit similaire à celui dans la reconstruction sans déconvolution. Les reconstructions de fantômes réalistes ont également montré une amélioration de la résolution spatiale. Le choix du niveau de troncature de la SVD n'a pas été optimisé dans ce travail, et devrait être mieux adapté au niveau de bruit dans les projections.

VIII Conclusions

L'objectif de cette thèse était d'explorer la reconstruction tomographique proton CT en mode liste et d'améliorer la qualité d'image en pCT. Dans une configuration en mode liste, la position et la direction d'entrée et de sortie de chaque proton sont mesurées afin d'estimer la trajectoire du proton via un formalisme de MLP (chemin le plus vraisemblable). Plusieurs aspects ont été étudiés, de la justesse du formalisme MLP aux différents algorithmes de reconstruction en pCT, en passant par la déconvolution de l'incertitude sur le MLP. Nous nous sommes particulièrement intéressés aux algorithmes directs (c'est-à-dire non itératifs). Il s'agit de solutions heuristiques car il n'y a pas d'inversion analytique connue pour les trajectoires de type MLP. Plus précisément, au cours de cette thèse, nous avons

- étudié l'impact des hétérogénéités sur le MLP ;
- proposé une nouvelle méthode pour filtrer les données pCT ;
- comparé différents algorithmes directs pour la reconstruction en pCT ;
- proposé une méthode pour déconvoluer les projections en utilisant l'incertitude sur le MLP.

Tout d'abord, nous avons étudié la précision du formalisme MLP dans différents fantômes hétérogènes. En comparant le MLP théorique aux résultats de simulations Monte Carlo, nous avons montré qu'il y a une erreur systématique sur l'estimation du MLP près d'interfaces transversales. Alors que des à-priori sur les hétérogénéités longitudinales peuvent être inclus dans le formalisme du MLP pour améliorer l'estimation de la trajectoire, ce n'est pas le cas des hétérogénéités transverses. L'approximation gaussienne des distributions spatiales et angulaires n'est plus valide dans ce cas, et les distributions mesurées ressemblent à des gaussiennes asymétriques ou à une somme de deux gaussiennes. Il pourrait être intéressant de développer un formalisme MLP qui ne pré-suppose pas de modèle gaussien. Cependant, avec certaines distributions bimodales, le concept même d'un MLP unique est discutable car il apparaît qu'il existe plusieurs chemins probables. De plus, l'erreur à proximité d'hétérogénéités réalistes reste faible. Nous avons également observé que les distributions d'énergie non gaussiennes pouvent avoir un impact sur le RSP, et compliquer les filtres énergétiques utilisés pour exclure les réactions nucléaires non élastiques. Des observations complémentaires des distributions en énergie et de leur impact sur la reconstruction pourraient expliquer certains des artefacts rapportés dans d'autres travaux. Reconstruire un fantôme avec une hétérogénéité transversale pourrait confirmer les hypothèses sur l'impact de distributions spatiales et énergétiques asymétriques sur l'image finale.

Deuxièmement, nous avons proposé un nouveau filtre pour reconstruire les données pCT. Nous avons défini et trouvé l'expression d'un filtre rampe directionnel 2D. L'objectif était de filtrer les données directement dans l'espace image pour éviter une interpolation et préserver l'information spatiale du MLP. La procédure de reconstruction à partir de ce filtre consiste à (1) effectuer un binning en rétroprojections partielles, (2) filtrer les données en utilisant le filtre rampe directionnel et (3) calculer la somme sur tous les angles de projection. Étant donné que les données en mode liste sont binnées dans l'espace image et qu'aucune interpolation n'est nécessaire pour appliquer le filtre rampe directionnel, un léger gain de résolution spatiale est observé par rapport à une approche où les données sont binnées dans l'espace des projections. Le filtre rampe directionnel 2D a été développé en supposant une géométrie parallèle. Il peut être possible de dériver un filtre équivalent pour d'autres géométries telles qu'un faisceau en éventail, bien que son expression serait moins simple à dériver, car le changement de variable de l'espace du sinogramme à l'espace image pour le faisceau en éventail n'est pas une simple rotation comme pour une géométrie parallèle. Bien qu'il soit simple de rebinner les données pCT en mode liste vers une géométrie parallèle, ce rebinning pourrait être plus compliqué pour les configurations pCT en mode intégration.

Nous avons effectué une comparaison de toutes les méthodes directes utilisées pour reconstruire des données pCT. Les résultats ont été comparés en matière de résolution spatiale et de précision du RSP. Les différents algorithmes étaient (1) l'algorithme "distance-driven" étendant la FBP aux trajectoires non linéaires, (2) l'algorithme "maximum likelihood" basé sur des radiographies optimisées, (3) la rétroprojection-puis-filtrage qui inverse les étapes de filtrage et de rétroprojection, (4) la rétroprojection différenciée et (5) la méthode du filtre rampe directionnel. Les résultats ont montré des différences mineures entre les différents algorithmes. En général, les algorithmes qui commencent par rétroprojecter les données dans l'espace image permettent une résolution spatiale supérieure. La plupart des différences de résolution spatiale étaient perceptibles aux bords du fantôme reconstruit. Ailleurs, la résolution spatiale était principalement dégradée par le MCS et la résolution du tracker. Le coût computationnel est donc un facteur majeur pour le choix de l'algorithme de reconstruction. Certaines méthodes "backproject first" nécessitent de calculer la rétroprojection au-delà des limites de la région de reconstruction, ce qui augmente le temps de calcul. De plus, la capacité de la rétroprojection différenciée à traiter des projections tronquées peut en faire la solution préférée dans certains cas.

Enfin, nous avons proposé une méthode de déconvolution shift-variante pour déconvoluer des projections en utilisant l'incertitude du MLP. D'abord, nous avons calculé des cartes d'incertitude pour chaque projection en utilisant le formalisme MLP incluant la résolution des détecteurs. Ensuite, nous utilisons une décomposition en valeurs singulières tronquée pour inverser la matrice shift-variante pour chaque distance et chaque projection. Les résultats ont montré un gain significatif de résolution spatiale dans des fantômes simples et réalistes lorsque la résolution du tracker est incluse. Ce bénéfice est plus important dans des régions très hétérogènes en matière de RSP, par ex. la tête. Sur les coupes reconstruites, il a été observé que la distribution spatiale du bruit était différente après déconvolution. Le niveau de troncature de la TSVD doit être adapté au bruit dans les projections, ce que nous avons fait de manière heuristique. Un réglage plus précis du niveau de troncature pourrait améliorer les résultats actuels. Il pourrait être possible, afin de faciliter la déconvolution, d'utiliser la même carte d'incertitude pour tous les angles de projection. Cela serait raisonnable pour des objets circulaires avec peu d'hétérogénéités, c'est-à-dire des objets où il y a peu de variabilité en matière d'incertitude du MLP en fonction de l'angle de projection. Alternativement, une seule matrice par projection pourrait fonctionner lorsqu'il y a peu de variabilité en fonction de la distance. Cela pourrait être une approximation raisonnable car l'ajout de l'incertitude du tracker réduit la variabilité de chaque carte d'incertitude. Aussi, il serait intéressant de comparer cette méthode avec une méthode de déconvolution dans l'espace image, où la déconvolution serait effectuée après la reconstruction. Cela pourrait donner des résultats satisfaisants dans les cas où la carte d'incertitude ne varie pas beaucoup en fonction de l'angle de projection. Bien que cela signifierait déconvoluer une seule image 2D au lieu d'un sinogramme 3D entier, les noyaux shift-variants seraient en 2D, ce qui rendrait l'utilisation de la TSVD pour en faire l'inversion très coûteuse. D'autres méthodes de déconvolution pourraient également être utilisées pour accélérer les calculer et mieux contrôler le bruit. Des méthodes de régularisation plus sophistiquées pourraient réduire le niveau de bruit tout en conservant une résolution spatiale élevée. Bien que cette méthode ait été testée sur des données en mode liste, le formalisme MLP calculant l'incertitude sur l'estimation de la trajectoire a été étendu aux modes intégration. Par conséquent, la même méthode peut être utilisée pour supprimer le flou des projections acquises en utilisant différents types de configurations. Nous nous attendons à ce que le gain de résolution spatiale soit plus important pour les données en mode intégration car la résolution de l'image reconstruite est plus affectée par l'incertitude du tracker. Il serait intéressant de comparer la résolution spatiale après déconvolution entre les configurations en mode liste et en mode intégration.

Au cours de cette thèse, toutes les études étaient basées sur des simulations Monte Carlo. Bien que nous ayons pris en compte la résolution des trackers à l'aide d'un modèle approximatif, plusieurs aspects ont été idéalisés. Par exemple, la résolution du détecteur d'énergie a été supposée parfaite, l'appariement des protons dans les trackers avant et arrière était sans erreur, il n'y avait pas d'artefacts de mouvement, etc. Les données expérimentales sont aussi affectées par du bruit électronique, un taux de détection et une résolution limités, etc. Par conséquent, nos résultats doivent être confirmés sur des données réelles. Il reste que, en proposant différentes solutions pour améliorer la résolution spatiale et en effectuant une comparaison complète des algorithmes de reconstruction pCT, nos travaux contribuent au développement de cette modalité d'imagerie.

Il existe encore des limites à l'utilisation clinique de l'imagerie pCT, telles que l'énergie maximale du faisceau fournie par l'accélérateur de particules, le temps d'acquisition ou l'intégration dans le workflow clinique. De plus, alors que notre travail s'est concentré sur les configurations en mode liste car elles permettent d'obtenir la meilleure résolution spatiale, les configurations en mode intégral pourraient être plus faciles à mettre en œuvre en clinique. Il y a eu nombre de développements matériels, tels que des détecteurs dotés d'une excellente résolution spatiale et énergétique sont aujourd'hui possibles. Cependant, la complexité, le coût, et le temps d'acquisition accrus de ce type d'équipement font que l'étude des systèmes en mode intégral reste digne d'intérêt. L'amélioration de la résolution spatiale des données pCT acquises avec des configurations en mode intégral pourrait être possible via l'utilisation d'images reconstruites à partir de deux modalités différentes, par exemple. La combinaison de données tomodensitométriques à rayons X avec des images pCT ou des radiographies proton a été étudiée par Wang, Mackie et Tomé (2012), Hansen et al. (2014a) et Zhang et al. (2019). Ce type de reconstruction a également été considéré pour surmonter la limite sur l'énergie maximale de l'accélérateur. Le principe est de n'utiliser que des projections acquises à des angles où l'énergie est suffisante pour que les protons traversent le patient, et de compléter les données manquantes via une image CT à rayons X. Bien que l'augmentation de l'énergie du faisceau de protons puisse être physiquement possible, elle serait difficile à justifier économiquement si elle était uniquement destinée à la reconstruction des images pCT.

Bien qu'il existe encore des obstacles à la mise en œuvre clinique de l'imagerie pCT, des prototypes cliniques pour la radiographie et la tomodensitométrie proton sont actuellement en cours de développement, notamment le système de radiographie de ProtonVDA qui est en cours de certification.

Bibliography

Agostinelli, S. et al. (2003). “GEANT4 – a simulation toolkit”. In: *Nuclear instruments and methods in physics research section A: Accelerators, Spectrometers, Detectors and Associated Equipment* 506.3, pp. 250–303. DOI: `10.1016/S0168-9002(03)01368-8`.

Ainsley, C. G. and C. M. Yeager (2014). “Practical considerations in the calibration of CT scanners for proton therapy”. In: *Journal of applied clinical medical physics* 15.3, pp. 202–220. DOI: `10.1120/jacmp.v15i3.4721`.

Amaldi, U. et al. (2010). “Advanced Quality Assurance for CNAO”. In: *Nuclear Instruments and Methods in Physics Research Section A: Accelerators, Spectrometers, Detectors and Associated Equipment* 617.1-3, pp. 248–249. DOI: `10.1016/j.nima.2009.06.087`.

Arbor, N et al. (2015). “Monte Carlo comparison of x-ray and proton CT for range calculations of proton therapy beams”. In: *Physics in Medicine & Biology* 60.19, p. 7585. DOI: `10.1088/0031-9155/60/19/7585`.

Archambeau, J. O. et al. (1992). “Role for proton beam irradiation in treatment of pediatric CNS malignancies”. In: *International Journal of Radiation Oncology* Biology* Physics* 22.2, pp. 287–294. DOI: `10.1016/0360-3016(92)90045-j`.

Barschall, H. et al. (1999). “Nuclear data for neutron and proton radiotherapy and for radiation protection”. In: *ICRU Report* 63.

Bashkirov, V. et al. (2016a). “Novel scintillation detector design and performance for proton radiography and computed tomography”. In: *Medical physics* 43.2, pp. 664–674. DOI: `10.1118/1.4939255`.

Bashkirov, V. et al. (2009). “Development of proton computed tomography for applications in proton therapy”. In: *AIP Conference Proceedings*. Vol. 1099. 1. American Institute of Physics, pp. 460–463. DOI: `10.1063/1.3120073`.

Bashkirov, V. A. et al. (2007). “Proton computed tomography: Update on current status”. In: *2007 IEEE Nuclear Science Symposium Conference Record*. Vol. 6. IEEE, pp. 4685–4688. DOI: `10.1109/nssmic.2007.4437152`.

Bashkirov, V. A. et al. (2016b). “Development of proton computed tomography detectors for applications in hadron therapy”. In: *Nuclear Instruments and Methods in Physics Research Section A: Accelerators, Spectrometers, Detectors and Associated Equipment* 809, pp. 120–129. DOI: `10.1016/j.nima.2015.07.066`.

Bazalova, M. et al. (2009). “Kilovoltage beam Monte Carlo dose calculations in submillimeter voxels for small animal radiotherapy”. In: *Medical physics* 36.11, pp. 4991–4999. DOI: `10.1118/1.3238465`.

Berger, M. et al. (1993). “Stopping powers and ranges for protons and alpha particles”. In: *ICRU Report* 49.

Besemer, A, H Paganetti, and B Bednarz (2013). “The clinical impact of uncertainties in the mean excitation energy of human tissues during proton therapy”. In: *Physics in medicine and biology* 58.4, p. 887. DOI: `10.1088/0031-9155/58/4/887`.

Bethe, H. A. (1953). “Molière’s theory of multiple scattering”. In: *Physical review* 89.6, p. 1256. DOI: `10.1103/physrev.89.1256`.

Bohr, N. (1948). *The penetration of atomic particles through matter*. Munksgaard Copenhagen.

Bopp, C et al. (2013). “Proton computed tomography from multiple physics processes”. In: *Physics in Medicine & Biology* 58.20, p. 7261. DOI: `10.1088/0031-9155/58/20/7261`.

Bopp, C et al. (2015). “Quantitative proton imaging from multiple physics processes: a proof of concept”. In: *Physics in Medicine & Biology* 60.13, p. 5325. DOI: `10.1088/0031-9155/60/13/5325`.

Bopp, C. et al. (2014). “The impact of tracking system properties on the most likely path estimation in proton CT”. In: *Physics in Medicine & Biology* 59.23, N197. DOI: `10.1088/0031-9155/59/23/n197`.

Bortfeld, T. (1997). “An analytical approximation of the Bragg curve for therapeutic proton beams”. In: *Medical physics* 24.12, pp. 2024–2033. DOI: `10.1118/1.598116`.

Bracewell, R. N. and A. Riddle (1967). “Inversion of fan-beam scans in radio astronomy”. In: *The Astrophysical Journal* 150, p. 427. DOI: `10.1086/149346`.

Brada, M., M. Pijls-Johannesma, and D. De Ruysscher (2007). “Proton therapy in clinical practice: current clinical evidence”. In: *Journal of clinical oncology* 25.8, pp. 965–970. DOI: `10.1200/jco.2006.10.0131`.

Chan, A. W. and N. J. Liebsch (2008). “Proton radiation therapy for head and neck cancer”. In: *Journal of surgical oncology* 97.8, pp. 697–700. DOI: `10.1002/jso.21013`.

Charpak, G. et al. (1976). “Further results in nuclear scattering radiography”. In: *Physics in Medicine & Biology* 21.6, p. 941. DOI: `10.1088/0031-9155/21/6/004`.

Cirrone, G. P. et al. (2007a). “Monte Carlo studies of a proton computed tomography system”. In: *IEEE Transactions on Nuclear Science* 54.5, pp. 1487–1491. DOI: `10.1109/tns.2007.906988`.

Cirrone, G. A. P. et al. (2007b). “The Italian project for a proton imaging device”. In: *Nuclear Instruments and Methods in Physics Research Section A: Accelerators, Spectrometers, Detectors and Associated Equipment* 576.1, pp. 194–197. DOI: `10.1016/j.nima.2007.01.151`.

Cirrone, G. A. P. et al. (2011). “Monte Carlo evaluation of the Filtered Back Projection method for image reconstruction in proton computed tomography”. In: *Nuclear Instruments and Methods in Physics Research Section A: Accelerators, Spectrometers, Detectors and Associated Equipment* 658.1, pp. 78–83. DOI: `10.1016/j.nima.2011.05.061`.

Civinini, C et al. (2013). “Recent results on the development of a proton computed tomography system”. In: *Nuclear Instruments and Methods in Physics Research Section A: Accelerators, Spectrometers, Detectors and Associated Equipment* 732, pp. 573–576. DOI: `10.1016/j.nima.2013.05.147`.

Civinini, C. et al. (2016). “Proof-of-Principle results of proton computed tomography”. In: *2016 IEEE Nuclear Science Symposium and Medical Imaging Conference*. IEEE, pp. 1–6. DOI: `10.1109/nssmic.2016.8069620`.

Clair, W. S. et al. (2004). “Advantage of protons compared to conventional X-ray or IMRT in the treatment of a pediatric patient with medulloblastoma”. In: *International Journal of Radiation Oncology* Biology* Physics* 58.3, pp. 727–734. DOI: `10.1016/s0360-3016(03)01574-8`.

Collins-Fekete, C.-A. et al. (2015). “Developing a phenomenological model of the proton trajectory within a heterogeneous medium required for proton imaging”. In: *Physics in Medicine & Biology* 60.13, p. 5071. DOI: `10.1088/0031-9155/60/13/5071`.

Collins-Fekete, C.-A. et al. (2016). “A maximum likelihood method for high resolution proton radiography/proton CT”. In: *Physics in Medicine & Biology* 61.23, p. 8232. DOI: `10.1088/0031-9155/61/23/8232`.

Collins-Fekete, C.-A. et al. (2017a). "Extension of the Fermi–Eyges most-likely path in heterogeneous medium with prior knowledge information". In: *Physics in Medicine & Biology* 62.24, p. 9207. DOI: `10.1088/1361-6560/aa955d`.

Collins-Fekete, C.-A. et al. (2017b). "Pre-treatment patient-specific stopping power by combining list-mode proton radiography and x-ray CT". In: *Physics in Medicine & Biology* 62.17, p. 6836. DOI: `10.1088/1361-6560/aa7c42`.

Conti, M., L. Eriksson, and V. Westerwoudt (2013). "Estimating image quality for future generations of TOF PET scanners". In: *IEEE Transactions on Nuclear Science* 60.1, pp. 87–94. DOI: `10.1109/tns.2012.2233214`.

Cormack, A. M. (1963). "Representation of a function by its line integrals, with some radiological applications". In: *Journal of Applied Physics* 34.9, pp. 2722–2727. DOI: `10.1063/1.1729798`.

Cormack, A. and A. Koehler (1976). "Quantitative proton tomography: preliminary experiments". In: *Physics in Medicine & Biology* 21.4, p. 560. DOI: `10.1088/0031-9155/21/4/007`.

Crawford, C. R. (1991). "CT filtration aliasing artifacts". In: *IEEE transactions on medical imaging* 10.1, pp. 99–102. DOI: `10.1109/42.75616`.

De Ruysscher, D. et al. (2012). "Charged particles in radiotherapy: a 5-year update of a systematic review". In: *Radiotherapy and Oncology* 103.1, pp. 5–7. DOI: `10.1016/j.radonc.2012.01.003`.

Dickmann, J. et al. (2019). "Prediction of image noise contributions in proton computed tomography and comparison to measurements". In: *Physics in Medicine & Biology* 64.14, p. 145016. DOI: `10.1088/1361-6560/ab2474`.

Doolan, P. et al. (2015). "Patient-specific stopping power calibration for proton therapy planning based on single-detector proton radiography". In: *Physics in Medicine & Biology* 60.5, p. 1901. DOI: `10.1088/0031-9155/60/5/1901`.

Draeger, E et al. (2018). "3D prompt gamma imaging for proton beam range verification". In: *Physics in Medicine & Biology* 63.3, p. 035019. DOI: `10.1088/1361-6560/aaa203`.

Duchazeaubeneix, J. et al. (1980). "Nuclear scattering radiography". In: *J. Comput. Assist. Tomography* 4.CERN-EP-80-52, pp. 803–818. DOI: `10.1097/00004728-198012000-00013`.

Durante, M., R. Orecchia, and J. S. Loeffler (2017). "Charged-particle therapy in cancer: clinical uses and future perspectives". In: *Nature Reviews Clinical Oncology* 14.8, p. 483. DOI: `10.1038/nrclinonc.2017.30`.

Enghardt, W et al. (1999). "The application of PET to quality assurance of heavy-ion tumor therapy". In: *Strahlentherapie und Onkologie* 175.2, pp. 33–36. DOI: `10.1007/bf03038884`.

Erdelyi, B (2009). "A comprehensive study of the most likely path formalism for proton-computed tomography". In: *Physics in Medicine and Biology* 54.20, pp. 6095–6122. DOI: `10.1088/0031-9155/54/20/005`.

Esposito, M. et al. (2015). "CMOS Active Pixel Sensors as energy-range detectors for proton Computed Tomography". In: *Journal of Instrumentation* 10.06, p. C06001. DOI: `10.1088/1748-0221/10/06/c06001`.

Esposito, M. et al. (2018). "PRaVDA: The first solid-state system for proton computed tomography". In: *Physica Medica* 55, pp. 149–154. DOI: `10.1016/j.ejmp.2018.10.020`.

Feldkamp, L., L. Davis, and J. Kress (1984). "Practical cone-beam algorithm". In: *J Opt Soc Am A* 1.6, pp. 612–619. DOI: `10.1364/josaa.1.000612`.

Fernández-Varea, J. et al. (1993). "On the theory and simulation of multiple elastic scattering of electrons". In: *Nuclear Instruments and Methods in Physics Research*

Section B: Beam Interactions with Materials and Atoms 73.4, pp. 447–473. DOI: 10.1016/0168-583x(93)95827-r.

Finck, C. et al. (2017). "Study for online range monitoring with the interaction vertex imaging method". In: *Physics in Medicine & Biology* 62.24, pp. 9220–9239. DOI: 10.1088/1361-6560/aa954e.

Frandes, M. et al. (2010). "A tracking Compton-scattering imaging system for hadron therapy monitoring". In: *IEEE Transactions on Nuclear Science* 57.1, pp. 144–150. DOI: 10.1109/tns.2009.2031679.

Fuss, M. et al. (1999). "Proton radiation therapy (PRT) for pediatric optic pathway gliomas: comparison with 3D planned conventional photons and a standard photon technique". In: *International Journal of Radiation Oncology* Biology* Physics* 45.5, pp. 1117–1126. DOI: 10.1016/S0360-3016(99)00337-5.

Gilad, E. and J. Von Hardenberg (2006). "A fast algorithm for convolution integrals with space and time variant kernels". In: *Journal of Computational Physics* 216.1, pp. 326–336. DOI: 10.1016/j.jcp.2005.12.003.

Global Cancer Observatory. https://gco.iarc.fr. Accessed: 2020-07-03.

Goitein, M. (1978). "Compensation for inhomogeneities in charged particle radiotherapy using computed tomography". In: *International Journal of Radiation Oncology* Biology* Physics* 4.5-6, pp. 499–508. DOI: 10.1016/0360-3016(78)90087-1.

— (1979). "Computed tomography in planning radiation therapy". In: *International Journal of Radiation Oncology* Biology* Physics* 5.3, pp. 445–447. DOI: 10.1016/0360-3016(79)91230-6.

Gordon, R., R. Bender, and G. T. Herman (1970). "Algebraic reconstruction techniques (ART) for three-dimensional electron microscopy and X-ray photography". In: *Journal of theoretical Biology* 29.3, pp. 471–481. DOI: 10.1016/0022-5193(70)90109-8.

Gottschalk, B et al. (1993). "Multiple Coulomb scattering of 160 MeV protons". In: *Nuclear Instruments and Methods in Physics Research Section B: Beam Interactions with Materials and Atoms* 74.4, pp. 467–490. DOI: 10.1016/0168-583x(93)95944-z.

Grichine, V. (2009). "A simple model for integral hadron–nucleus and nucleus–nucleus cross-sections". In: *Nuclear Instruments and Methods in Physics Research Section B: Beam Interactions with Materials and Atoms* 267.14, pp. 2460–2462. DOI: 10.1016/j.nimb.2009.05.020.

Guo, J., C.-M. Kao, and Q. Xie (2011). "Evaluation of windowed image reconstruction for time-of-flight PET". In: *2011 IEEE Nuclear Science Symposium Conference Record*. IEEE, pp. 4162–4166. DOI: 10.1109/nssmic.2011.6153796.

Hansen, D. C., T. S. Sørensen, and S. Rit (2016). "Fast reconstruction of low dose proton CT by sinogram interpolation". In: *Physics in Medicine & Biology* 61.15, p. 5868. DOI: 10.1088/0031-9155/61/15/5868.

Hansen, D. C. et al. (2014a). "Improved proton computed tomography by dual modality image reconstruction". In: *Medical physics* 41.3, p. 031904. DOI: 10.1118/1.4864239.

Hansen, D. C. et al. (2014b). "The image quality of ion computed tomography at clinical imaging dose levels". In: *Medical physics* 41.11, p. 111908. DOI: 10.1118/1.4897614.

Hansen, P. C., J. G. Nagy, and D. P. O'Leary (2006). *Deblurring images: matrices, spectra, and filtering*. Vol. 3. SIAM.

Hanson, K. (1979). "Proton Computed Tomography". In: *Nuclear Science, IEEE Transactions on* 26, pp. 1635 –1640. DOI: 10.1109/TNS.1979.4330455.

Hanson, K. et al. (1978). “The Application of Protons to Computed Tomography”. In: *Nuclear Science, IEEE Transactions on* 25, pp. 657–660. DOI: `10.1109/TNS.1978.4329389`.

Hanson, K. et al. (1981). “Computed tomography using proton energy loss”. In: *Physics in Medicine & Biology* 26.6, p. 965. DOI: `10.1088/0031-9155/26/6/001`.

Hanson, K. et al. (1982). “Proton computed tomography of human specimens”. In: *Physics in Medicine & Biology* 27.1, p. 25. DOI: `10.1088/0031-9155/27/1/003`.

Henriquet, P et al. (2012). “Interaction vertex imaging (IVI) for carbon ion therapy monitoring: a feasibility study”. In: *Physics in Medicine and Biology* 57.14, pp. 4655–4669. DOI: `10.1088/0031-9155/57/14/4655`.

Highland, V. L. (1975). “Some practical remarks on multiple scattering”. In: *Nuclear Instruments and Methods* 129.2, pp. 497–499. DOI: `10.1016/0029-554x(75)90743-0`.

Holliday, E. B. et al. (2016). “Dosimetric advantages of intensity-modulated proton therapy for oropharyngeal cancer compared with intensity-modulated radiation: a case-matched control analysis”. In: *Medical Dosimetry* 41.3, pp. 189–194. DOI: `10.1016/j.meddos.2016.01.002`.

Hurley, R. et al. (2012). “The phase I proton CT scanner and test beam results at LLUMC”. In: *Transactions of the American Nuclear Society* 106, p. 63.

ICRP (2009). *Adult Reference Computational Phantoms*. ICRP Publication 110. Ann. ICRP 39 (2).

Ito, A. and H. Koyama-Ito (1987). “Proton computed tomography applied to small biomedical samples”. In: *Biological trace element research* 13.1, pp. 423–423. DOI: `10.1007/bf02796653`.

Ivanchenko, V. N. et al. (2010). “Geant4 models for simulation of multiple scattering”. In: *Journal of Physics: Conference Series* 219.3, p. 032045. DOI: `10.1088/1742-6596/219/3/032045`.

Jan, S et al. (2011). “GATE V6: a major enhancement of the GATE simulation platform enabling modelling of CT and radiotherapy”. In: *Physics in Medicine & Biology* 56.4, p. 881. DOI: `10.1088/0031-9155/56/4/001`.

Janni, J. F. (1982). “Proton range-energy tables, 1 keV-10 GeV. Energy loss, range, path length, time-of-flight, straggling, multiple scattering, and nuclear interaction probability”. In: *Atomic Data and Nuclear Data Tables* 27.4-5, pp. 341–529. DOI: `10.1016/0092-640x(82)90005-5`.

Johnson, L et al. (2003). “Initial studies on proton computed tomography using a silicon strip detector telescope”. In: *Nuclear Instruments and Methods in Physics Research Section A: Accelerators, Spectrometers, Detectors and Associated Equipment* 514.1-3, pp. 215–223. DOI: `10.1016/j.nima.2003.08.108`.

Johnson, L. et al. (2002). “Monte Carlo studies on proton computed tomography using a silicon strip detector telescope”. In: vol. 2, pp. 916 –920. ISBN: 0-7803-7636-6. DOI: `10.1109/NSSMIC.2002.1239473`.

Johnson, R. P. (2017). “Review of medical radiography and tomography with proton beams”. In: *Reports on progress in physics* 81.1, p. 016701. DOI: `10.1088/1361-6633/aa8b1d`.

Johnson, R. P. et al. (2015). “A fast experimental scanner for proton CT: technical performance and first experience with phantom scans”. In: *IEEE transactions on nuclear science* 63.1, pp. 52–60. DOI: `10.1109/tns.2015.2491918`.

Johnson, R. et al. (2014). “Results from a pre-clinical head scanner for proton CT”. In: *2014 IEEE Nuclear Science Symposium and Medical Imaging Conference (NSS/MIC)*. IEEE, pp. 1–5. DOI: `10.1109/nssmic.2014.7430876`.

Kak, A. C. and M. Slaney (1988). *Principles of computerized tomographic imaging*. New York: IEEE Press.

Kao, C.-M. (2008). "Windowed image reconstruction for time-of-flight positron emission tomography". In: *Physics in Medicine & Biology* 53.13, p. 3431. DOI: `10.1088/0031-9155/53/13/002`.

Kao, C.-M. et al. (2010). "Analytic reconstruction methods for list-mode time-of-flight PET". In: *IEEE Nuclear Science Symposuim & Medical Imaging Conference*. IEEE, pp. 3492–3494. DOI: `10.1109/nssmic.2010.5874455`.

Khellaf, F. et al. (2019). "Effects of transverse heterogeneities on the most likely path of protons". In: *Physics in Medicine & Biology* 64.6, p. 065003.

Khellaf, F. et al. (2020a). "2D directional ramp filter". In: *Physics in Medicine & Biology* 65.8, 08NT01. DOI: `10.1088/1361-6560/ab7875`.

Khellaf, F. et al. (2020b). "A comparison of direct reconstruction algorithms in proton computed tomography". In: *Physics in Medicine & Biology* 65.10, p. 105010. DOI: `10.1088/1361-6560/ab7d53`.

Knopf, A.-C. and A. Lomax (2013). "In vivo proton range verification: a review". In: *Physics in Medicine & Biology* 58.15, R131. DOI: `10.1088/0031-9155/58/15/r131`.

Koehler, A. (1968). "Proton radiography". In: *Science* 160.3825, pp. 303–304. DOI: `10.1126/science.160.3825.303`.

Krah, N et al. (2018a). "A comprehensive theoretical comparison of proton imaging set-ups in terms of spatial resolution". In: *Physics in Medicine & Biology* 63.13, p. 135013. DOI: `10.1088/1361-6560/aaca1f`.

Krah, N et al. (2018b). "Proton radiography with a commercial range telescope detector using dedicated post processing methods". In: *Physics in Medicine & Biology* 63.20, p. 205016. DOI: `10.1088/1361-6560/aae043`.

— (2018c). "Proton radiography with a commercial range telescope detector using dedicated post processing methods". In: *Physics in Medicine & Biology* 63.20, p. 205016. DOI: `10.1088/1361-6560/aae043`.

Krah, N., J.-M. Létang, and S. Rit (2019). "Polynomial modelling of proton trajectories in homogeneous media for fast most likely path estimation and trajectory simulation". In: *Physics in Medicine & Biology* 64.19, p. 195014. DOI: `10.1088/1361-6560/ab3d0b`.

Krah, N. et al. (2019). "Regularised patient-specific stopping power calibration for proton therapy planning based on proton radiographic images". In: *Physics in Medicine & Biology* 64.6, p. 065008. DOI: `10.1088/1361-6560/ab03db`.

Kramer, S. et al. (1978). "Application of proton radiography to medical imaging". In: *64th Scientific Assembly and Annual Meeting of the Radiological Society of North America*. DOI: `10.2172/5883163`.

Krimmer, J et al. (2018). "Prompt-gamma monitoring in hadrontherapy: A review". In: *Nuclear Instruments and Methods in Physics Research Section A: Accelerators, Spectrometers, Detectors and Associated Equipment* 878, pp. 58–73. DOI: `10.1016/j.nima.2017.07.063`.

Lawrence, E. O. and N. E. Edlefsen (1930). "On the production of high speed protons". In: *Science* 72.1867, p. 376.

Lewis, H. W. (1950). "Multiple Scattering in an Infinite Medium". In: *Physical Review* 78.5, pp. 526–529. DOI: `10.1103/physrev.78.526`.

Li, T et al. (2003). "Reconstruction for proton computed tomography: a Monte Carlo study". In: *2003 IEEE Nuclear Science Symposium and Medical Imaging Conference*. Vol. 4. IEEE, pp. 2767–2770. DOI: `10.1109/nssmic.2003.1352460`.

Li, T. et al. (2006). "Reconstruction for proton computed tomography by tracing proton trajectories: A Monte Carlo study". In: *Medical physics* 33.3, pp. 699–706. DOI: `10.1118/1.2171507`.

Lievens, Y. and M. Pijls-Johannesma (2013). "Health economic controversy and cost-effectiveness of proton therapy". In: *Seminars in radiation oncology*. Vol. 23. 2. Elsevier, pp. 134–141. DOI: `10.1016/j.semradonc.2012.11.005`.

Lin, R. et al. (2000). "Conformal proton radiation therapy of the posterior fossa: a study comparing protons with three-dimensional planned photons in limiting dose to auditory structures". In: *International Journal of Radiation Oncology* Biology* Physics* 48.4, pp. 1219–1226. DOI: `10.1016/s0360-3016(00)00741-0`.

Lodge, M. et al. (2007). "A systematic literature review of the clinical and cost-effectiveness of hadron therapy in cancer". In: *Radiotherapy and Oncology* 83.2, pp. 110–122. DOI: `10.1016/j.radonc.2007.04.007`.

Lomax, A. J. et al. (1999). "A treatment planning inter-comparison of proton and intensity modulated photon radiotherapy". In: *Radiotherapy and Oncology* 51.3, pp. 257–271. DOI: `10.1016/s0167-8140(99)00036-5`.

Lynch, G. R. and O. I. Dahl (1991). "Approximations to multiple Coulomb scattering". In: *Nuclear Instruments and Methods in Physics Research Section B: Beam Interactions with Materials and Atoms* 58.1, pp. 6–10. DOI: `10.1016/0168-583x(91)95671-y`.

MacDonald, S. M. et al. (2008). "Proton radiotherapy for childhood ependymoma: initial clinical outcomes and dose comparisons". In: *International Journal of Radiation Oncology* Biology* Physics* 71.4, pp. 979–986. DOI: `10.1016/j.ijrobp.2007.11.065`.

Mattiazzo, S. et al. (2018). "iMPACT: An innovative tracker and calorimeter for proton computed tomography". In: *IEEE Transactions on Radiation and Plasma Medical Sciences* 2.4, pp. 345–352. DOI: `10.1109/trpms.2018.2825499`.

McGowan, S., N. Burnet, and A. Lomax (2013). "Treatment planning optimisation in proton therapy". In: *The British journal of radiology* 86.1021, pp. 20120288–20120288. DOI: `10.1259/bjr.20120288`.

McMillan, E. M. (1945). "The Synchrotron — A Proposed High Energy Particle Accelerator". In: *Physical Review* 68.5-6, p. 143.

Menichelli, D. et al. (2010). "Characterization of a silicon strip detector and a YAG:Ce calorimeter for a proton computed radiography apparatus". In: *IEEE Transactions on Nuclear Science* 57.1, pp. 8–16. DOI: `10.1109/tns.2009.2031869`.

Miller, C. et al. (2019). "Reconstructed and real proton radiographs for image-guidance in proton beam therapy". In: *Journal of Radiation Oncology* 8.1, pp. 97–101. DOI: `10.1007/s13566-019-00376-0`.

Min, C.-H. et al. (2006). "Prompt gamma measurements for locating the dose falloff region in the proton therapy". In: *Applied Physics Letters* 89.18, p. 183517. DOI: `10.1063/1.2378561`.

Mishra, M. V. et al. (2017). "Establishing evidence-based indications for proton therapy: an overview of current clinical trials". In: *International Journal of Radiation Oncology* Biology* Physics* 97.2, pp. 228–235. DOI: `10.1016/j.ijrobp.2016.10.045`.

Missaghian, J et al. (2010). "Beam test results of a CsI calorimeter matrix element". In: *Journal of Instrumentation* 5.06, P06001. DOI: `10.1088/1748-0221/5/06/p06001`.

Moffett, D. et al. (1975). "Initial test of a proton radiographic system". In: *IEEE Transactions on Nuclear Science* 22.3, pp. 1749–1751. DOI: `10.1109/tns.1975.4327982`.

Molière, G. (1947). “Theorie der Streuung schneller geladener Teilchen I Einzelstreuung am abgeschirmten Coulomb-feld”. In: *Zeitschrift für Naturforschung A* 2.3, pp. 133–145. DOI: 10.1515/zna-1947-0302.

— (1948). “Theorie der Streuung schneller geladener Teilchen II Mehrfach-und Vielfachstreuung”. In: *Zeitschrift für Naturforschung A* 3.2, pp. 78–97. DOI: 10.1515/zna-1948-0203.

Moyers, M. F. et al. (2010). “Ion stopping powers and CT numbers”. In: *Medical Dosimetry* 35.3, pp. 179–194. DOI: 10.1016/j.meddos.2009.05.004.

Mueller, K et al. (2003). “Reconstruction for proton computed tomography: A practical approach”. In: *2003 IEEE Nuclear Science Symposium and Medical Imaging Conference*. Vol. 5. IEEE, pp. 3223–3225. DOI: 10.1109/nssmic.2003.1352584.

Naimuddin, M. et al. (2016). “Development of a proton computed tomography detector system”. In: *Journal of Instrumentation* 11.02, p. C02012. DOI: 10.1088/1748-0221/11/02/c02012.

Newhauser, W. D. and R. Zhang (2015). “The physics of proton therapy”. In: *Physics in Medicine & Biology* 60.8, R155. DOI: 10.1088/0031-9155/60/8/r155.

Noo, F., R. Clackdoyle, and J. D. Pack (2004). “A two-step Hilbert transform method for 2D image reconstruction”. In: *Physics in Medicine & Biology* 49.17, p. 3903. DOI: 10.1088/0031-9155/49/17/006.

Ofuya, M. et al. (2019). “Systematic review of methodology used in clinical studies evaluating the benefits of proton beam therapy”. In: *Clinical and translational radiation oncology* 19, pp. 17–26. DOI: 10.1016/j.ctro.2019.07.002.

Oliphant, M. (1943). “The acceleration of particles to very high energies”. In: *Classified memo submitted to DSIR, University of Birmingham Archive*.

Olsen, D. R. et al. (2007). “Proton therapy–a systematic review of clinical effectiveness”. In: *Radiotherapy and oncology* 83.2, pp. 123–132. DOI: 10.1016/j.radonc.2007.03.001.

Paganetti, H. (2002). “Nuclear interactions in proton therapy: dose and relative biological effect distributions originating from primary and secondary particles”. In: *Physics in Medicine & Biology* 47.5, p. 747. DOI: 10.1088/0031-9155/47/5/305.

— (2012a). *Proton therapy physics*. CRC press.

— (2012b). “Range uncertainties in proton therapy and the role of Monte Carlo simulations”. In: *Physics in Medicine & Biology* 57.11, R99. DOI: 10.1088/0031-9155/57/11/r99.

Peeters, A. et al. (2010). “How costly is particle therapy? Cost analysis of external beam radiotherapy with carbon-ions, protons and photons”. In: *Radiotherapy and oncology* 95.1, pp. 45–53. DOI: 10.1016/j.radonc.2009.12.002.

Pemler, P et al. (1999). “A detector system for proton radiography on the gantry of the Paul-Scherrer-Institute”. In: *Nuclear Instruments and Methods in Physics Research Section A: Accelerators, Spectrometers, Detectors and Associated Equipment* 432.2-3, pp. 483–495. DOI: 10.1016/s0168-9002(99)00284-3.

Penfold, S. et al. (2010a). “Block-iterative and string-averaging projection algorithms in proton computed tomography image reconstruction”. In: pp. 347–367. ISBN: 978-1930524484.

Penfold, S. N. (2010). “Image reconstruction and Monte Carlo simulations in the development of proton computed tomography for applications in proton radiation therapy”. PhD thesis. University of Wollongong.

Penfold, S. et al. (2009). “A more accurate reconstruction system matrix for quantitative proton computed tomography”. In: *Medical physics* 36.10, pp. 4511–4518. DOI: 10.1118/1.3218759.

Penfold, S. et al. (2010b). “Total variation superiorization schemes in proton computed tomography image reconstruction”. In: *Medical physics* 37.11, pp. 5887–5895. DOI: `10.1118/1.3504603`.

Penfold, S. et al. (2011). “Geometrical optimization of a particle tracking system for proton computed tomography”. In: *Radiation Measurements* 46.12, pp. 2069–2072. DOI: `10.1016/j.radmeas.2011.04.032`.

Pettersen, H. E. S. (2018). “A digital tracking calorimeter for proton computed tomography”. PhD thesis. The University of Bergen.

Pettersen, H. E. S. et al. (2019). “Design optimization of a pixel-based range telescope for proton computed tomography”. In: *Physica Medica* 63, pp. 87–97. DOI: `10.1016/j.ejmp.2019.05.026`.

Pettersen, H. et al. (2017). “Proton tracking in a high-granularity Digital Tracking Calorimeter for proton CT purposes”. In: *Nuclear Instruments and Methods in Physics Research Section A: Accelerators, Spectrometers, Detectors and Associated Equipment* 860, pp. 51–61. DOI: `10.1016/j.nima.2017.02.007`.

Plautz, T. E. et al. (2016). “An evaluation of spatial resolution of a prototype proton CT scanner”. In: *Medical physics* 43.12, pp. 6291–6300. DOI: `10.1118/1.4966028`.

Poludniowski, G, N. Allinson, and P. Evans (2014). “Proton computed tomography reconstruction using a backprojection-then-filtering approach”. In: *Physics in Medicine & Biology* 59.24, p. 7905. DOI: `10.1088/0031-9155/59/24/7905`.

Poludniowski, G., N. Allinson, and P. Evans (2015). “Proton radiography and tomography with application to proton therapy”. In: *The British journal of radiology* 88.1053, p. 20150134. DOI: `10.1259/bjr.20150134`.

Poludniowski, G. et al. (2014). “Proton-counting radiography for proton therapy: a proof of principle using CMOS APS technology”. In: *Physics in Medicine & Biology* 59.11, p. 2569. DOI: `10.1088/0031-9155/59/11/2569`.

Presti, D. L. et al. (2014). “OFFSET: Optical Fiber Folded Scintillating Extended Tracker”. In: *Nuclear Instruments and Methods in Physics Research Section A: Accelerators, Spectrometers, Detectors and Associated Equipment* 737, pp. 195–202. DOI: `10.1016/j.nima.2013.11.049`.

Presti, D. L. et al. (2017). “An Innovative Proton Tracking System for Qualification of Particle Beam in Real-Time”. In: *IEEE Transactions on Radiation and Plasma Medical Sciences* 1.3, pp. 268–274. DOI: `10.1109/trpms.2017.2690842`.

Price, T, P. Consortium, et al. (2016). “PRaVDA: high energy physics towards proton computed tomography”. In: *Nuclear Instruments and Methods in Physics Research Section A: Accelerators, Spectrometers, Detectors and Associated Equipment* 824, pp. 226–227. DOI: `10.1016/j.nima.2015.12.013`.

Quinones, C., J. Létang, and S Rit (2016). “Filtered back-projection reconstruction for attenuation proton CT along most likely paths”. In: *Physics in Medicine & Biology* 61.9, p. 3258. DOI: `10.1088/0031-9155/61/9/3258`.

Radon, J (1917). “On the determination of functions from their integrals along certain manifolds”. In: *Ber. Verh, Sachs Akad Wiss.* 69, pp. 262–277.

Ramachandran, G. and A. Lakshminarayanan (1971). “Three-dimensional reconstruction from radiographs and electron micrographs: application of convolutions instead of Fourier transforms”. In: *Proc Natl Acad Sci USA* 68.9, pp. 2236–2240. DOI: `10.1073/pnas.68.9.2236`.

Rescigno, R. et al. (2015). “A pencil beam approach to proton computed tomography”. In: *Medical physics* 42.11, pp. 6610–6624. DOI: `10.1118/1.4933422`.

Richard, S. et al. (2012). “Towards task-based assessment of CT performance: system and object MTF across different reconstruction algorithms”. In: *Medical physics* 39.7, pp. 4115–4122. DOI: `10.1118/1.4725171`.

Rit, S. et al. (2013). "Filtered backprojection proton CT reconstruction along most likely paths". In: *Med Phys* 40.3, 031103, p. 031103. DOI: 10.1118/1.4789589.

Rit, S. et al. (2014). "The Reconstruction Toolkit (RTK), an open-source cone-beam CT reconstruction toolkit based on the Insight Toolkit (ITK)". In: *Journal of Physics: Conference Series*. Vol. 489. 1. IOP Publishing, p. 012079. DOI: 10.1088/1742-6596/489/1/012079.

Rit, S. et al. (2015). "List-mode proton CT reconstruction using their most likely paths via the finite Hilbert transform of the derivative of the backprojection". In: *The 13th International Meeting on Fully Three-Dimensional Image Reconstruction in Radiology and Nuclear Medicine*. Fully3D 2015 Conference Proceedings, pp. 324–327.

Rombi, B. et al. (2014). "Proton radiotherapy for pediatric tumors: review of first clinical results". In: *Italian Journal of Pediatrics* 40.1. DOI: 10.1186/s13052-014-0074-6.

Rossi, B. and K. Greisen (1941). "Cosmic-ray theory". In: *Reviews of Modern Physics* 13.4, p. 240. DOI: 10.1103/revmodphys.13.240.

Rutherford, E. (1919). "Collision of α-Particles with Light Atoms. I.-IV". In: *Journal of the Röntgen Society* 15.61, pp. 142–143. DOI: 10.1259/jrs.1919.0126.

Sadrozinski, H.-W. et al. (2003). "Issues in proton computed tomography". In: *Nuclear Instruments and Methods in Physics Research Section A: Accelerators, Spectrometers, Detectors and Associated Equipment* 511.1-2, pp. 275–281. DOI: 10.1016/S0168-9002(03)01806-0.

Sadrozinski, H.-W. et al. (2004). "Toward proton computed tomography". In: *IEEE Transactions on Nuclear Science* 51.1, pp. 3–9. DOI: 10.1109/TNS.2003.823044.

Sadrozinski, H.-W. et al. (2013). "Development of a head scanner for proton CT". In: *Nuclear Instruments and Methods in Physics Research Section A: Accelerators, Spectrometers, Detectors and Associated Equipment* 699, pp. 205–210. DOI: 10.1016/j.nima.2012.04.029.

Sadrozinski, H.-W. et al. (2016). "Operation of the preclinical head scanner for proton CT". In: *Nuclear Instruments and Methods in Physics Research Section A: Accelerators, Spectrometers, Detectors and Associated Equipment* 831, pp. 394–399. DOI: 10.1016/j.nima.2016.02.001.

Saraya, Y et al. (2014). "Study of spatial resolution of proton computed tomography using a silicon strip detector". In: *Nuclear Instruments and Methods in Physics Research Section A: Accelerators, Spectrometers, Detectors and Associated Equipment* 735, pp. 485–489. DOI: 10.1016/j.nima.2013.09.051.

Saudinos, J (1987). "Imaging with high energy particles". In: *Journal of optics* 18.4, p. 193. DOI: 10.1117/12.966760.

Saudinos, J. et al. (1975). "Nuclear scattering applied to radiography". In: *Physics in Medicine & Biology* 20.6, p. 890. DOI: 10.1088/0031-9155/20/6/002.

Scaringella, M et al. (2014). "A proton computed tomography based medical imaging system". In: *Journal of Instrumentation* 9.12, p. C12009. DOI: 10.1088/1748-0221/9/12/c12009.

Scaringella, M. et al. (2013). "The PRIMA (PRoton IMAging) collaboration: Development of a proton computed tomography apparatus". In: *Nuclear Instruments and Methods in Physics Research Section A: Accelerators, Spectrometers, Detectors and Associated Equipment* 730, pp. 178–183. DOI: 10.1016/j.nima.2013.05.181.

Schaffner, B and E Pedroni (1998). "The precision of proton range calculations in proton radiotherapy treatment planning: experimental verification of the relation between CT-HU and proton stopping power". In: *Physics in Medicine & Biology* 43.6, p. 1579. DOI: 10.1088/0031-9155/43/6/016.

Schneider, U. and E. Pedroni (1994). “Multiple Coulomb scattering and spatial resolution in proton radiography”. In: *Medical physics* 21.11, pp. 1657–1663. DOI: 10.1118/1.597212.

— (1995). “Proton radiography as a tool for quality control in proton therapy”. In: *Medical physics* 22.4, pp. 353–363. DOI: 10.1118/1.597470.

Schneider, U., E. Pedroni, and A. Lomax (1996). “The calibration of CT Hounsfield units for radiotherapy treatment planning”. In: *Physics in Medicine & Biology* 41.1, p. 111. DOI: 10.1088/0031-9155/41/1/009.

Schneider, U. et al. (2004). “First proton radiography of an animal patient”. In: *Medical physics* 31.5, pp. 1046–1051. DOI: 10.1118/1.1690713.

Schneider, U. et al. (2005). “Patient specific optimization of the relation between CT-Hounsfield units and proton stopping power with proton radiography”. In: *Medical physics* 32.1, pp. 195–199. DOI: 10.1118/1.1833041.

Schöndube, H., K. Stierstorfer, and F. Noo (2010). “Evaluations of a 2D inverse Hilbert Transform”. In: *1st International Conference on Image Formation in X-Ray Computed Tomography*. Salt Lake City, USA., p. 80.

Schulte, R. et al. (2004). “Conceptual design of a proton computed tomography system for applications in proton radiation therapy”. In: *IEEE Transactions on Nuclear Science* 51.3, pp. 866–872. DOI: 10.1109/tns.2004.829392.

Schulte, R. W. et al. (2005). “Density resolution of proton computed tomography”. In: *Medical physics* 32.4, pp. 1035–1046. DOI: 10.1118/1.1884906.

Schulte, R. et al. (2008). “A maximum likelihood proton path formalism for application in proton computed tomography”. In: *Medical physics* 35.11, pp. 4849–4856. DOI: 10.1118/1.2986139.

Schulte, R. et al. (2012). “Overview of the LLUMC/UCSC/CSUSB phase 2 proton CT project”. In: *Transactions of the American Nuclear Society* 106, p. 59.

Shepp, L. A. and B. F. Logan (1974). “The Fourier reconstruction of a head section”. In: *IEEE Transactions on nuclear science* 21.3, pp. 21–43. DOI: 10.1109/tns.1974.6499235.

Sipala, V. et al. (2011). “PRIMA: An apparatus for medical application”. In: *Nuclear Instruments and Methods in Physics Research Section A: Accelerators, Spectrometers, Detectors and Associated Equipment* 658.1, pp. 73–77. DOI: 10.1016/j.nima.2011.05.025.

Slater, J. M. et al. (1992). “The proton treatment center at Loma Linda University Medical Center: rationale for and description of its development”. In: *International Journal of Radiation Oncology, Biology, Physics* 22.2, pp. 383–389. DOI: 10.1016/0360-3016(92)90058-p.

Smith, A. R. (2006). “Proton therapy”. In: *Physics in Medicine & Biology* 51.13, R491. DOI: 10.1088/0031-9155/51/13/r26.

Steward, V. and A. Koehler (1973a). “Proton beam radiography in tumor detection”. In: *Science* 179.4076, pp. 913–914. DOI: 10.1126/science.179.4076.913.

— (1973b). “Proton radiographic detection of strokes”. In: *Nature* 245.5419, pp. 38–40. DOI: 10.1038/245038a0.

— (1974a). “Proton radiography in the diagnosis of breast carcinoma”. In: *Radiology* 110.1, pp. 217–221. DOI: 10.1148/110.1.217.

— (1974b). “Proton radiography of a human brain tumor within the skull: a preliminary report”. In: *Surgical neurology* 2.4, 283—284. ISSN: 0090-3019.

Symon, K. R. (1948). “Fluctuations in Energy Lost by High-energy Charged Particles in Passing Through Matter”. PhD thesis. Harvard University.

Takada, Y et al. (1988). “Proton computed tomography with a 250 MeV pulsed beam”. In: *Nuclear Instruments and Methods in Physics Research Section A: Accelerators, Spectrometers, Detectors and Associated Equipment* 273.1, pp. 410–422. DOI: `10.1016/0168-9002(88)90844-3`.

Takada, Y. and I. Abe (1987). “Multiple pencil beams for proton computed tomography”. In: *Nuclear Instruments and Methods in Physics Research Section A: Accelerators, Spectrometers, Detectors and Associated Equipment* 262.2-3, pp. 511–521. DOI: `10.1016/0168-9002(87)90893-x`.

Tanaka, S. et al. (2016). “Development of proton CT imaging system using plastic scintillator and CCD camera”. In: *Physics in Medicine & Biology* 61.11, p. 4156. DOI: `10.1088/0031-9155/61/11/4156`.

Tanaka, S. et al. (2018). “Improved proton CT imaging using a bismuth germanium oxide scintillator”. In: *Physics in Medicine & Biology* 63.3, p. 035030. DOI: `10.1088/1361-6560/aaa515`.

Taylor, J. et al. (2015). “Proton tracking for medical imaging and dosimetry”. In: *Journal of Instrumentation* 10.02, p. C02015. DOI: `10.1088/1748-0221/10/02/c02015`.

Taylor, J. et al. (2016a). “A new silicon tracker for proton imaging and dosimetry”. In: *Nuclear Instruments and Methods in Physics Research Section A: Accelerators, Spectrometers, Detectors and Associated Equipment* 831, pp. 362–366. DOI: `10.1016/j.nima.2016.02.013`.

Taylor, J. et al. (2016b). “An experimental demonstration of a new type of proton computed tomography using a novel silicon tracking detector”. In: *Medical physics* 43.11, pp. 6129–6136. DOI: `10.1118/1.4965809`.

Testa, M. et al. (2013). “Proton radiography and proton computed tomography based on time-resolved dose measurements”. In: *Physics in Medicine & Biology* 58.22, p. 8215. DOI: `10.1088/0031-9155/58/22/8215`.

Tobias, C. A. et al. (1955). “Irradiation hypophysectomy and related studies using 340-MeV protons and 190-MeV deuterons”. In:

Tschalär, C (1968a). “Straggling distributions of extremely large energy losses”. In: *Nuclear Instruments and Methods* 64.3, 237–243. ISSN: 0029-554X. DOI: `10.1016/0029-554X(68)90159-6`.

— (1968b). “Straggling distributions of large energy losses”. In: *Nuclear Instruments and Methods* 61.2, pp. 141–156. DOI: `10.1016/0029-554x(68)90535-1`.

Tschalär, C and H. Maccabee (1970). “Energy-straggling measurements of heavy charged particles in thick absorbers”. In: *Physical Review B* 1.7, p. 2863. DOI: `10.1103/physrevb.1.2863`.

Vanzi, E. et al. (2013). “The PRIMA collaboration: preliminary results in FBP reconstruction of pCT data”. In: *Nuclear Instruments and Methods in Physics Research Section A: Accelerators, Spectrometers, Detectors and Associated Equipment* 730, pp. 184–190. DOI: `10.1016/j.nima.2013.05.193`.

Vargas, C. et al. (2008). “Dose–volume comparison of proton therapy and intensity-modulated radiotherapy for prostate cancer”. In: *International Journal of Radiation Oncology* Biology* Physics* 70.3, pp. 744–751. DOI: `10.1016/j.ijrobp.2007.07.2335`.

Veksler, V. I. (1944). “A new method for the acceleration of relativistic particles”. In: *Doklady Akademii Nauk USSR*. Vol. 43. 8, pp. 346–348.

Verma, V., M. V. Mishra, and M. P. Mehta (2016). “A systematic review of the cost and cost-effectiveness studies of proton radiotherapy”. In: *Cancer* 122.10, pp. 1483–1501. DOI: `10.1002/cncr.29882`.

Wang, D., T. R. Mackie, and W. A. Tomé (2010). "On the use of a proton path probability map for proton computed tomography reconstruction a". In: *Medical physics* 37.8, pp. 4138–4145. DOI: 10.1118/1.3453767.

— (2012). "On proton CT reconstruction using MVCT-converted virtual proton projections". In: *Medical physics* 39.6Part1, pp. 2997–3008. DOI: 10.1118/1.4711752.

Watson, C. C. (2007). "An evaluation of image noise variance for time-of-flight PET". In: *IEEE Transactions on Nuclear Science* 54.5, pp. 1639–1647. DOI: 10.1109/tns.2007.901228.

Weber, D. C. et al. (2004). "A treatment planning comparison of intensity modulated photon and proton therapy for paraspinal sarcomas". In: *International Journal of Radiation Oncology* Biology* Physics* 58.5, pp. 1596–1606. DOI: 10.1016/j.ijrobp.2003.11.028.

Weber, D. C. et al. (2018). "Proton therapy for pediatric malignancies: Fact, figures and costs. A joint consensus statement from the pediatric subcommittee of PTCOG, PROS and EPTN". In: *Radiotherapy and Oncology* 128.1, pp. 44–55. DOI: 10.1016/j.radonc.2018.05.020.

Wentzel, G. (1926). "Zwei Bemerkungen über die Zerstreuung korpuskularer Strahlen als Beugungserscheinung". In: *Zeitschrift für Physik* 40.8, pp. 590–593. DOI: 10.1007/bf01390457.

West, D and A. Sherwood (1972). "Radiography with 160 MeV protons". In: *Nature* 239.5368, p. 157. DOI: 10.1038/239157b0.

— (1973). "Proton-scattering radiography". In: *Non-destructive Testing* 6.5, pp. 249–257. DOI: 10.1016/0029-1021(73)90072-8.

Williams, D. (2004). "The most likely path of an energetic charged particle through a uniform medium". In: *Physics in Medicine & Biology* 49.13, p. 2899. DOI: 10.1088/0031-9155/49/13/010.

Wilson, R. R. (1946). "Radiological use of fast protons". In: *Radiology* 47.5, pp. 487–491. DOI: 10.1148/47.5.487.

Wong, K. et al. (2009). "The effect of tissue inhomogeneities on the accuracy of proton path reconstruction for proton computed tomography". In: *AIP Conference Proceedings*. Vol. 1099. AIP, pp. 476–480. DOI: 10.1063/1.3120078.

Yang, M. et al. (2010). "Theoretical variance analysis of single-and dual-energy computed tomography methods for calculating proton stopping power ratios of biological tissues". In: *Physics in Medicine & Biology* 55.5, p. 1343. DOI: 10.1088/0031-9155/55/5/006.

Yang, M. et al. (2012). "Comprehensive analysis of proton range uncertainties related to patient stopping-power-ratio estimation using the stoichiometric calibration". In: *Physics in Medicine & Biology* 57.13, p. 4095. DOI: 10.1088/0031-9155/57/13/4095.

Yock, T. et al. (2005). "Proton radiotherapy for orbital rhabdomyosarcoma: clinical outcome and a dosimetric comparison with photons". In: *International Journal of Radiation Oncology* Biology* Physics* 63.4, pp. 1161–1168. DOI: 10.1016/j.ijrobp.2005.03.052.

Zatserklyaniy, A et al. (2014). "Track reconstruction with the silicon strip tracker of the proton CT Phase 2 scanner". In: *2014 IEEE Nuclear Science Symposium and Medical Imaging Conference (NSS/MIC)*. IEEE, pp. 1–4. DOI: 10.1109/nssmic.2014.7430749.

Zeng, G. L. (2007). "Image reconstruction via the finite Hilbert transform of the derivative of the backprojection". In: *Medical physics* 34.7, pp. 2837–2843. DOI: 10.1118/1.2739813.

Zeng, G. L. and G. T. Gullberg (1994). “Can the backprojection filtering algorithm be as accurate as the filtered backprojection algorithm?” In: *Proceedings of 1994 IEEE Nuclear Science Symposium*. Vol. 3. IEEE, pp. 1232–1236. DOI: `10.1109/nssmic.1994.474603`.

Zhang, R. et al. (2017a). “Improvement of single detector proton radiography by incorporating intensity of time-resolved dose rate functions”. In: *Physics in Medicine & Biology* 63.1, p. 015030. DOI: `10.1088/1361-6560/aa9913`.

Zhang, R. et al. (2019). “Iterative optimization of relative stopping power by single detector based multi-projection proton radiography”. In: *Physics in Medicine & Biology* 64.6, p. 065022. DOI: `10.1088/1361-6560/aaf976`.

Zhang, W. et al. (2017b). “Intensity-modulated proton therapy and osteoradionecrosis in oropharyngeal cancer”. In: *Radiotherapy and Oncology* 123.3, pp. 401–405. DOI: `10.1016/j.radonc.2017.05.006`.

Zhu, J. and S. N. Penfold (2016). “Dosimetric comparison of stopping power calibration with dual-energy CT and single-energy CT in proton therapy treatment planning”. In: *Medical physics* 43.6Part1, pp. 2845–2854. DOI: `10.1118/1.4948683`.

Zygmanski, P. et al. (2000). “The measurement of proton stopping power using proton-cone-beam computed tomography”. In: *Physics in Medicine & Biology* 45.2, p. 511. DOI: `10.1088/0031-9155/45/2/317`.

FOLIO ADMINISTRATIF

THESE DE L'UNIVERSITE DE LYON OPEREE AU SEIN DE L'INSA LYON

NOM : KHELLAF DATE de SOUTENANCE : 21/09/2020
(avec précision du nom de jeune fille, le cas échéant)

Prénoms : Feriel

TITRE : List-mode proton CT reconstruction

NATURE : Doctorat Numéro d'ordre : AAAALYSEIXXXX

Ecole doctorale : Électronique, Électrotechnique, Automatique

Spécialité : Traitement du Signal et de l'Image

RESUME :

La thérapie proton est utilisée dans le cadre du traitement contre le cancer afin de parvenir à une meilleure distribution de dose en exploitant les propriétés du proton. Les systèmes de planification de thérapie proton requièrent une carte du pouvoir d'arrêt des tissus du patient afin de calculer la dose absorbée. En clinique, cette image est générée à partir d'une conversion des unités Hounsfield d'une image tomodensitométrique (CT) rayons X au pouvoir d'arrêt relatif (RSP) du proton. Cette calibration induit des incertitudes, ce qui va mener à l'utilisation de marges de sécurité et à la réduction de la conformité de dose. Afin de réduire ces incertitudes, l'imagerie proton CT a été proposée puisque la quantité reconstruite est directement le RSP. En plus de la perte d'énergie, les protons interagissent également via la diffusion multiple de Coulomb (MCS) qui induit des trajectoires non linéaires, ce qui rend le problème de reconstruction en proton CT différent de la reconstruction CT rayons X.
L'objectif de cette thèse est l'amélioration de la qualité d'image en reconstruction proton CT en mode liste. L'utilisation du formalisme du chemin le plus probable (MLP) afin de prendre en compte les effets du MCS a permis d'améliorer la résolution spatiale en proton CT. Ce formalisme suppose un milieu homogène. La première contribution de cette thèse est une étude sur les trajectoires des protons en milieux hétérogènes: la justesse du MLP a été évaluée en comparaison avec un MLP obtenu par simulations Monte Carlo dans différentes configurations. Les résultats en matière de distribution spatiale, angulaire, et énergétique ont été analysés afin d'évaluer l'impact sur l'image reconstruite. La seconde contribution est un filtre rampe directionnel 2D utilisé dans le cadre de la reconstruction proton CT. Il s'agit d'une méthode intermédiaire entre la rétroprojection filtrée et le filtrage de la rétroprojection, basée sur l'extension du filtre rampe en 2D afin de préserver l'information spatiale sur le MLP. Une expression pour une version 2D limitée en bande de fréquence du filtre rampe a été dérivée et testée sur des données pCT simulées. Ensuite, une comparaison de différents algorithmes de reconstruction directs en matière de résolution spatiale et justesse du RSP a été menée. Cinq algorithmes, incluant le filtre rampe directionnel, ont été testés afin de reconstruire différents fantômes. Les résultats obtenus à partir de données acquises avec des détecteurs idéaux ou réalistes ont été comparés. Enfin, la dernière contribution est une méthode de déconvolution qui utilise l'information sur l'incertitude du MLP afin d'améliorer la résolution des images proton CT.

MOTS-CLÉS : imagerie proton, reconstruction tomographique, proton thérapie

Laboratoire (s) de recherche : CREATIS

Directeur de thèse: Jean Michel Létang

Président de jury :

Composition du jury : Reinhard Schulte (Rapporteur), Claude Comtat (Rapporteur), Katia Parodi (Examinatrice), Françoise Peyrin (Examinatrice), Jean Michel Létang (Directeur de thèse), Simon Rit (Co-directeur de thèse), Nils Krah (Invité), Ilaria Rinaldi (Invitée)